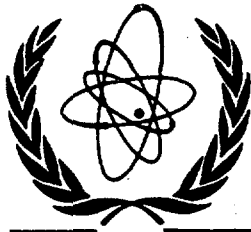


XA9642726-737



International Atomic Energy Agency

INDC(NDS)-338



XA9642726

---

**INDC**

**INTERNATIONAL NUCLEAR DATA COMMITTEE**

---

**FUSION BENCHMARKS  
FOR NUCLEAR DATA VALIDATION STUDIES**

Texts of Papers presented at an IAEA Consultants' Meeting  
Vienna, Austria, 13 to 16 December 1993

Compiled  
by

S. Ganesan  
IAEA Nuclear Data Section  
Vienna, Austria

December 1994

---

**IAEA NUCLEAR DATA SECTION, WAGRAMERSTRASSE 5, A-1400 VIENNA**

**VOL 28 No 01**

**FUSION BENCHMARKS  
FOR NUCLEAR DATA VALIDATION STUDIES**

Texts of Papers presented at an IAEA Consultants' Meeting  
Vienna, Austria, 13 to 16 December 1993

Compiled  
by

S. Ganesan  
IAEA Nuclear Data Section  
Vienna, Austria

**Abstract**

The report contains eleven papers on benchmark experiments and nuclear data uncertainty studies for the purpose of integral validation of the Fusion Evaluated Nuclear Data Library FENDL, with contributions from China, Germany, Italy, Japan, Russia, U.S.A.

December 1994

Reproduced by the IAEA in Austria  
July 1996

## Table of Contents

Introduction .....	4
(1) Jiang Wenmian, Chen yuan, Liu Rong, Guo Haiping and Shen Jian, Chengdu, China: "Systematic error studies in measurement of neutron multiplication." .....	5
(2) K. Seidel and S. Unholzer, Dresden, Germany: "Presentation of experimental benchmark data and their uncertainties." .....	15
(3) H. Giese, F. Kappler, U. von Möllendorff, Karlsruhe, Germany, and R. Tayama, Hitachi, Japan, and A. Alevra, H. Klein, Braunschweig, Germany: "Measurements of fusion neutron multiplication in spherical beryllium shells." .....	23
(4) U. von Möllendorff, U. Fischer, H. Giese, F. Kappler, E. Wiegner, Karlsruhe, Germany, and R. Tayama, Hitachi, Japan, and H. Klein, A. Alevra, Braunschweig, Germany: "The Karlsruhe neutron transmission experiment (KANT): Spherical shell transmission measurements with 14 MeV neutrons on beryllium." .....	35
(5) P. Batistoni, M. Angelone, M. Martone, M. Pillon and V. Rado, Frascati (Rome), Italy: "Bulk shield benchmark experiment on stainless steel at the Frascati neutron generator." .....	43
(6) Y. Oyama, JAERI, Japan: "Fusion integral experiments at FNS." .....	55
(7) J.E. White, Oak Ridge, Tennessee, U.S.A.: "Benchmark activities in the radiation shielding information center." .....	73
(8) S.P. Simakov, Obninsk, Kaluga Region, Russia: "Review of experiments and specifications on neutron leakage spectra from spherical shells." .....	123
(9) V.V. Afanasiev, A.G. Belevitin, V.V. Khromov, V.L. Romodanov, Yu.M. Verzilov, Moscow, Russia, and D.V. Markovskij, G.E. Shatalov, Moscow, Russia: "Benchmark experiments and analysis with hybrid reactor blanket mock-ups." .....	143
(10) C. Ichihara, K. Kobayashi, Osaka, Japan, and S.A. Hayashi, Kanagawa, Japan, and I. Kimura, Kyoto, Japan, and J. Yamamoto, A. Takahashi, Osaka, Japan: "Numerical data of leakage neutron spectra from various sphere piles with 14MeV neutrons." .....	187
(11) J. Yamamoto, T. Kanaoka, I. Murata, A. Takahashi and K. Sumita, Osaka, Japan: "Gamma-ray energy spectra emitted from spheres with 14 MeV neutron source." .....	205

## Introduction

An IAEA Consultants' Meeting on "Preparation of Fusion Benchmarks in Electronic Format for Nuclear Data Validation Studies" was convened by the International Atomic Energy Agency and held during 13 to 16 December 1993 at the IAEA Headquarters, Vienna. The main purpose of the meeting was to review the current status of work in the subject of compilation of fusion neutronic benchmarks for the purpose of integral validation of Fusion Evaluated Nuclear Data Libraries (FENDL working libraries). The compiled information in electronic format on fusion benchmarks will be used to integrally validate the working nuclear data libraries in processed form derived within the scope of the FENDL project of the Agency for neutron and photon transport. Since the meeting there have been many requests to make the texts of the presentations available in printed form. The texts are reproduced here, directly from the Authors' manuscripts or overhead transparencies with little or no editing, in the order in which the presentations were made at the meeting. The summary report containing the agenda, conclusions and recommendations of the meeting has been separately published as document INDC(NDS)-298.

Srinivasan GANESAN  
December 1994



IAEA Consultants Meeting on  
"preparation of fusion benchmarks in electronic format  
for nuclear data validation studies"

December 13–16, 1993 IAEA Headquarters, Vienna

## **SYSTEMATIC ERROR STUDIES IN MEASUREMENT OF NEUTRON MULTIPLICATION**

Jiang Wenmian, Chen yuan, Liu Rong,  
Guo Haiping and Shen Jian

(Southwest Institute of Nuclear Physics and Chemistry  
P.O. Box 525, Chengdu 610003, P.R.China)

### **ABSTRACT**

Systematic errors in measurement of neutron multiplication have been experimentally studied. The neutron multiplications in Pb, 15 cm in thickness, have been measured with the moderators of 41 cm and 46 cm thick. The validity of the experimental principle was verified with a small polyethylene sphere 10 cm in thickness. It is found that the reproducibility of TAD system is satisfactory. The flux perturbation of enriched Li glass detectors to neutron field was studied in detail. The corrections in the moderator were calculated and anew analyzed with 1-D ANISNcode and ENDF/B-VI library data.

### **1. INTRODUCTION**

Be and Pb are promising candidate elements as neutron multiplying materials in fusion-fission hybrid reactor or pure fusion reactor blanket and

used to increase production tritium rate due to their high (n, 2n) reaction cross section and no fissionability. Measurement and calculation of neutron multiplication in Be and Pb<sup>1-10</sup> have been carried out for more than ten years. In general, experimental results are still lower than calculated ones, except INEL's results. And there are differences among experimental results of the laboratories. To check nuclear parameters of beryllium and lead, it is necessary to obtain more accurate results of experiment. Hence it is very important to study systematic errors in measurement of neutron multiplication. Considering it, we have experimentally studied the systematic errors. At present, there are very few research reports in this respect.

## 2. EXPERIMENTAL PRINCIPLE

The principle of the experiment is detailed in Ref. 6. The total absorption method is used to measure neutron multiplication. The neutron moderator is the polyethylene sphere. The absorption of hydrogen in the moderator is proportional to that of a 1/v detector. The ratio,  $H_m / H_0$ , of hydrogen absorption is equal to the ratio,  $A_m / A_0$ , of 1/v detector absorption with and without multiplying material. Therefore apparent and true neutron multiplications are

$$M_a = \frac{H_m}{H_0} = \frac{A_m}{A_0} \quad (1)$$

and

$$M = M_a(1 - X_0 - L_0) + X_m + L_m + Pb(n,x) \quad (2)$$

where  $M_a$  is apparent neutron multiplication and  $M$  true neutron multiplication. Subscripts, m and 0, represent with and without multiplying material.  $H$  is the hydrogen absorption,  $A$  is the 1/v detector absorption,  $X$  is the nonhydrogen absorption,  $L$  is the leakage out of moderator,  $Pb(n,x)$  is lead net absorption of neutrons reflected by the moderator into lead sphere.  $M_a$  is obtained by experiment.  $X$ ,  $L$  and  $Pb(n,x)$  are calculated. Every term above is

normalized to one associated alpha particle, and integrated over the whole sphere.

### 3. EXPERIMENTAL SETUP

The polyethylene sphere is used as the total absorption detector (TAD). Its inner and outer diameters are 560 mm or 460 mm, and 1380 mm respectively, as shown in Fig.1. Inner and outer diameters of a lead sphere are 5 cm and 35 cm. The target chamber consists of a Ti-T target and beam drift tube <sup>(8)</sup>. The drift tube consists of two parts. The intensity of neutron source is  $\sim 10^9$  n / s. The fraction of D-D neutrons in source neutrons is less than 1%. The stability of neutron source is better than 2%.

Two <sup>6</sup>Li glasses were used in the experiment, as listed in Table 1. The structure of the <sup>6</sup>Li detector is described in detail in Ref.8.

**Table 1. <sup>6</sup>Li glass detectors**

Detector	Diameter(mm)	Thickness(mm)	Weight(mg)
<sup>6</sup> Li 1	2.62	0.22	2.818
<sup>6</sup> Li 2	1.66	0.50	2.621

The accuracy of <sup>6</sup>Li weight is  $\pm 0.001$  mg.

### 4. EXPERIMENTAL CONTENTS AND RESULTS

It is not very easy to find systematic errors from measuring data obtained by one kind of method. However, by changing conditions of measurement or using different kinds of methods to measure a physical quantity repeatedly, one may judge whether systematic errors in the measurement exist or not. In view of the reason, we have done the experiments described below.

The corrections were calculated using 1-D ANISN code and ENDF / B-VI library data, as shown in Table 2 <sup>(10)</sup>.

**Table 2. Calculated corrections**

Moderator Thickness	Material	Nonhydrogen Absorption	Leakage
28 / 69 cm	0	0.0592	0.1085
	Pb 2.5 / 17.5	0.0610 *	0.1513 *
		0.0233	0.1295
		0.0239 *	0.0472 *
	CH <sub>2</sub> 3.0 / 13.0	0.0349	0.0555
23 / 69 cm	0	0.0603	0.0761
	Pb 2.5 / 17.5	0.0235	0.0203

\* The calculations of L.Y.Liu.

#### 4.1. Increasing Moderator Thickness

To reduce the leakage neutrons, the CH<sub>2</sub>spherical shell 5 cm in thickness was put into the inner cavity of the moderator. The thickness of the moderator was increased to 46 cm from 41 cm. The apparent multiplication was measured, as listed in Table 3. The results were compared to ones with the moderator of 41 cm thick.

#### 4.2. Reproducibility

The reproducibility of multiplication measurement, using the total absorption method, was experimentally checked. The result is consistent with previous one within the range of experimental error with the moderator of 41 cm thick and lead sphere of 15 cm thick, as listed in Table 3.

**Table 3. Experimental results of neutron multiplications**

Moderator Thickness	Detector	M <sub>a</sub>	M	M *
28 / 69 <sup>Δ</sup> cm	<sup>6</sup> Li 1	1.823	1.507	—
	<sup>6</sup> Li 2	1.829	1.512	1.495
23 / 69 cm	<sup>6</sup> Li 1	1.659	1.447	—
	<sup>6</sup> Li 2	1.686	1.500	—

△ The corrections in the moderator of 41 cm thick were calculated by L.Y. Liu.

\* The previous result of experiment<sup>[8]</sup>

#### 4.3. Validity of Experimental Principle

A small 10-cm-thickness polyethylene sphere substituted for lead sphere to be used to measure multiplication. The moderator is 41 cm in thickness. The small CH<sub>2</sub>sphere doesn't multiply neutrons, thus

$$M + A_{\text{CH}_2} = 1 \quad (3)$$

where  $A_{\text{CH}_2}$  is neutron absorption of the small CH<sub>2</sub>sphere and obtained by calculation. The results are listed in Table 4.

Table 4. Experimental results with the small CH<sub>2</sub> sphere

Detector		<sup>6</sup> Li 1	<sup>6</sup> Li 2
Measured	INT <sub>m</sub>	810874	659123
	INT <sub>0</sub>	894470	730018
	M <sub>a</sub>	0.907	0.903
Calculated	A <sub>CH<sub>2</sub></sub>	0.1693	0.1693
	M	0.845	0.842
	M+A <sub>CH<sub>2</sub></sub>	1.015	1.011

INT<sub>m</sub>: the integrated counts with the small CH<sub>2</sub>sphere

INT<sub>0</sub>: the integrated counts without the small CH<sub>2</sub>sphere

It is quite evident that the principle of experiment is valid from Table 4 because the measured value of M+A<sub>CH<sub>2</sub></sub> is consistent with the relation (3) within the range of experimental error.

#### 4.4. Flux Perturbation of $^6\text{Li}$ Detectors

A  $^6\text{Li}$  glass detector placed in the moderator made the perturbation —self—shielding and flux depression —to the neutron field<sup>[11]</sup>. The flux perturbation in enriched  $^6\text{Li}$  glasses is mainly caused by the self—shielding. Flux perturbation depends on the neutronic and geometric parameters of the  $1/\nu$  detector and of the medium in which the flux is measured. In the experiment, ratio of weight of two  $^6\text{Li}$  glasses is 1.08. However, ratio of the integrated counts (per unit mass), over the whole sphere, of two  $^6\text{Li}$  glasses is about 1.21 that is average value of experiments mentioned above. The two values differ by 12%. It is obvious that the integrated counts of  $^6\text{Li}$  1 are larger than ones of  $^6\text{Li}$  2 with or without multiplying material, and the flux perturbation of  $^6\text{Li}$  1 is smaller than that of  $^2\text{Li}$ . But, in the relative measurement, the neutron multiplications measured by the  $^6\text{Li}$  and  $^6\text{Li}$  2 detectors differ by less than 1.6% and are consistent within the range of experimental error. The neutron distribution of  $^6\text{Li}$  1 and  $^6\text{Li}$  2 detectors in the moderator of 46 cm thick with lead 15 cm in thickness is shown in Fig.2.

#### 4.5 Reanalysis of Corrections

For beryllium the measured results are 3%–14% and 1%–7% lower than the calculated ones using ENDF/B-IV and ENDF/B-VI respectively<sup>[6]</sup>. For lead, the measured results are 7% lower than the calculated ones using ENDF/B-IV<sup>[8]</sup>. The conditions of the ANISN calculation were 25 energy groups,  $P_3$  and  $S_{16}$ . It was assumed that the flux and energy distributions of the source neutrons were isotropic and that the source neutron had energy of 13.5 to 14.9 MeV. The low threshold was 0.025 eV.

Dr. D.F. Tian calculated neutron multiplication in Be and Pb using

ANISN code and ENDF/B-VI again. The number of the energy groups is changed to 30 from 25. The low threshold is changed to  $\sim 10^{-4}$  eV from 0.025 eV. Thus the results of experiment and calculation differ by less than 3% for Pb shell of 15 cm thick are listed in Table 2<sup>[8][10]</sup>.

## 5. CONCLUSIONS

The measured results given in this report don't contain the effect of neutron reflection, which will be calculated, from moderator back to the multiplying material.

The corrections were calculated by Dr. D.F. Tian again. The calculated results of L.Y. Liu and D.F. Tian will be analyzed further.

The reproducibility is satisfactory and the previous and recent results of experiment differ by 1.1%

It is demonstrated that the principle of experiment is valid by measuring neutron multiplication with the small polyethylene sphere.

The flux perturbation of enriched  $^6\text{Li}$  glasses has been experimentally studied. It is found that the effect of flux perturbation in the  $^6\text{Li}$  2 is 12% larger than one in the  $^6\text{Li}$  1. But, the experimental results show that the effect of the flux perturbation of the thin  $^6\text{Li}$  glass detector on measurement of multiplication is negligible.

The first stage of studies on systematic errors has ended up. So far, it hasn't been found that the systematic errors having been checked make a significant impact on the measured values of neutron multiplication. However, the studies will be further carried out so that the accuracy of the measured results can be improved.

## ACKNOWLEDGMENTS

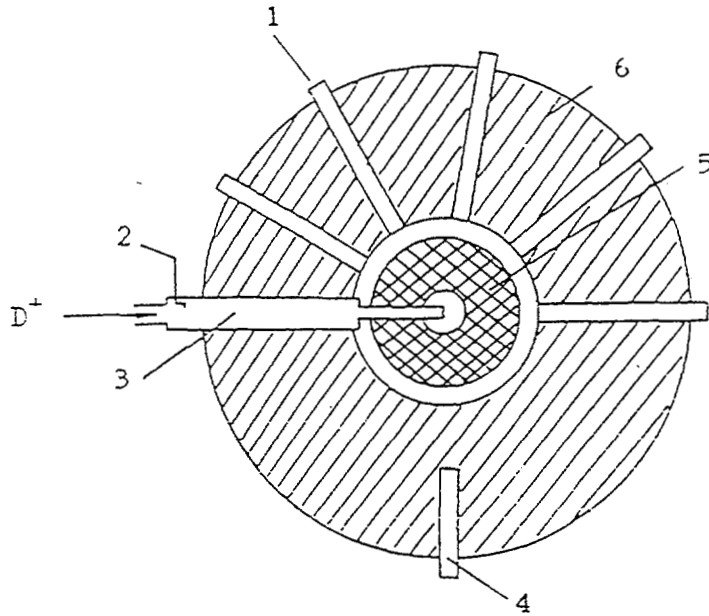
We would like to express our gratitude to Prof. Chengan Liu, Dr. Lianyan Liu and Dr. Dongfeng Tian for their providing the calculation.

This work is supported by the Natural Science Foundation of China and the Science Foundation of CAEP. This work was also supported by International Atomic Energy Agency under the research contracts No. 5828 / RB and 5828 / R1 / RB.

## REFERENCES

- [1] T.K.BASU et al., "Neutron Multiplication Studies in Beryllium for Fusion Reactor Blankets," Nucl. Sci. Eng., 70,309(1979)
- [2] C.WONG et al., "Measurements and Calculations of the Leakage Multiplication from Hollow Beryllium Spheres," Fusion Technol.,8,1165(1985).
- [3] V.A.ZAGRYADSKIJ et al., "Measurement of Neutron Leakage from U, Th and Be Spherical Assemblies with a Central 14 Mev Source," INDC(CCP)-272 / G, IAEA, Vienna, Austria (1987).
- [4] J.R.SMITH and J.J.KING, "Neutron Multiplication in Bulk Beryllium," Fusion Technol., 19,1925 (1991).
- [5] E.T.CHENG, "Review of the Nuclear Data Status and Requirements for fusion Reactor," Proc. Int. Cinf. on Nuclear Data for Sci. Tech., Mito, Japan, May 30-June, 1988.
- [6] W.M.JIANG et al., "Experiment of Neutron Multiplication in Beryllium," China Nuclear Science & Technology Report, CINIC-00687 (1992).
- [7] Y.CHEN, G.CHEN, R. Liu et al., "Experiments of Neutron Multi-

- plication in Beryllium," *Fusion Technol.*, 19,1919(1991).
- [8] Y.CHEN, R.LIU et al., "Measuremetn of Neutron Multiplication in Lead Assembiles," *Fusion Technol.*, 23, 68(1993).
- [9] L.Y.LIU and E.T.CHENG, "Preliminary Abalyses of SWINPC Beryllium Neutron Multiplication Intergral Exoeriments," *Fusion Technol.*, 19,1925(1991).
- [10] C.A.LIU and D.F.TIAN, Beijing Institute of Applied Physics and Computational Mathematics, Private Communication(1993).
- [11] S.YAMAGYCHI, "Thermal Flux Perturbation of Lithium-Glass Scintillator," *Nucl. Instr. and Meth.* A274(1989) 568-572.



1. detector channels; 2. alpha counter; 3. target chamber;  
4. monitor; 5. multiplying material; 6. polyethylene.

**Fig.1 Schematic diagram of polyethylene sphere system**

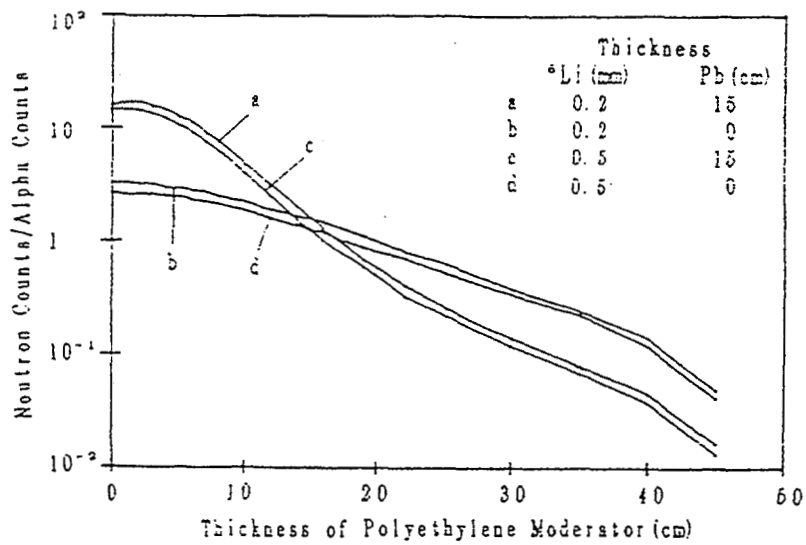
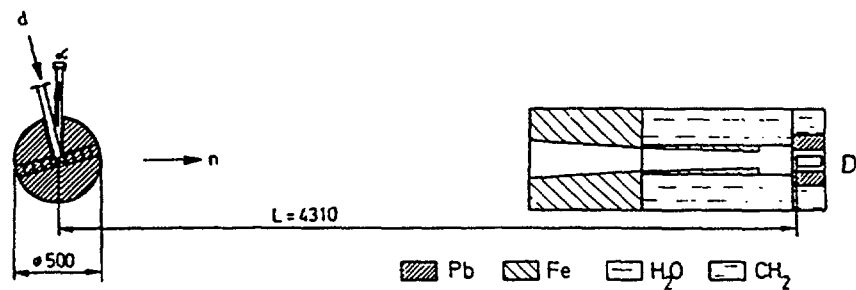


**fig.2 Neutron distribution in polyethylene sphere**

# PRESENTATION OF EXPERIMENTAL BENCHMARK DATA AND THEIR UNCERTAINTIES

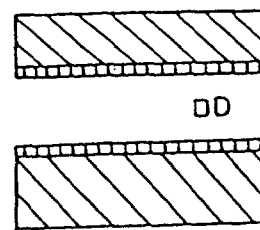
K. Seidel and S. Unholzer

Technische Universität Dresden, Institut für Kern- und Teilchenphysik  
Mommßenstrasse 13, D-01062 Dresden, Germany



Fe  
 Pb  
 $CH_2$

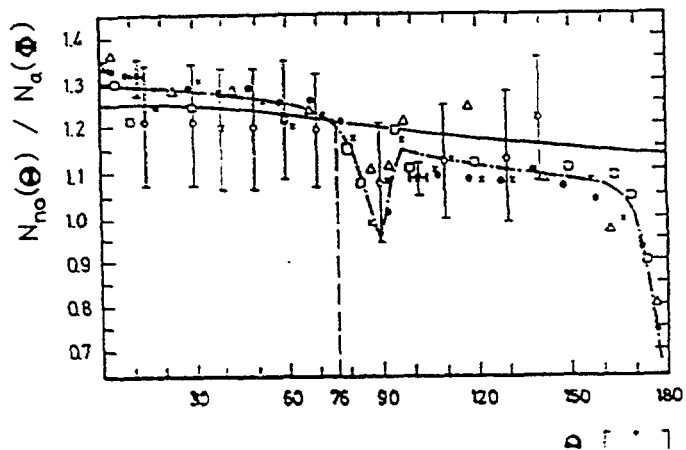
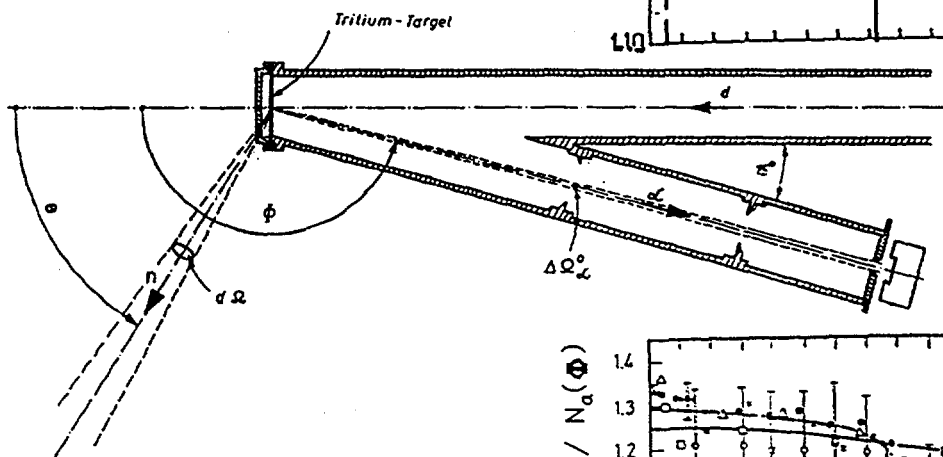
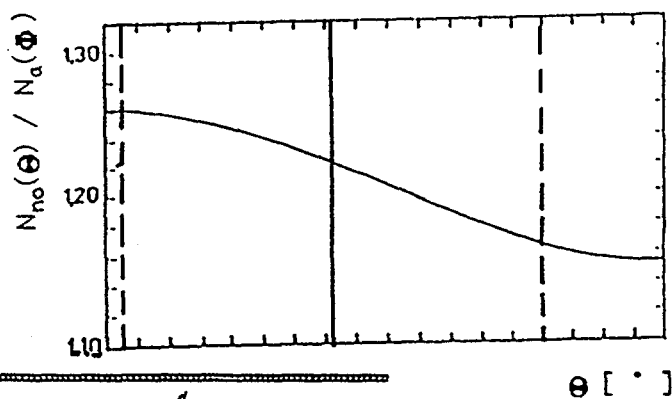
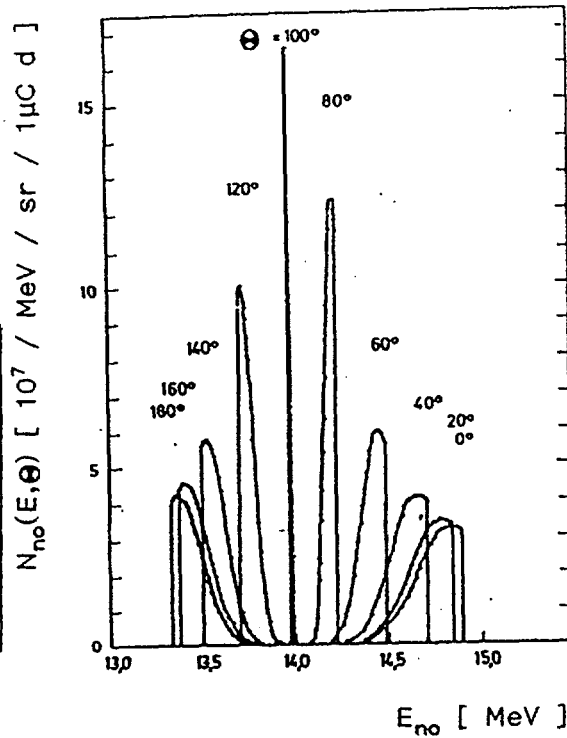
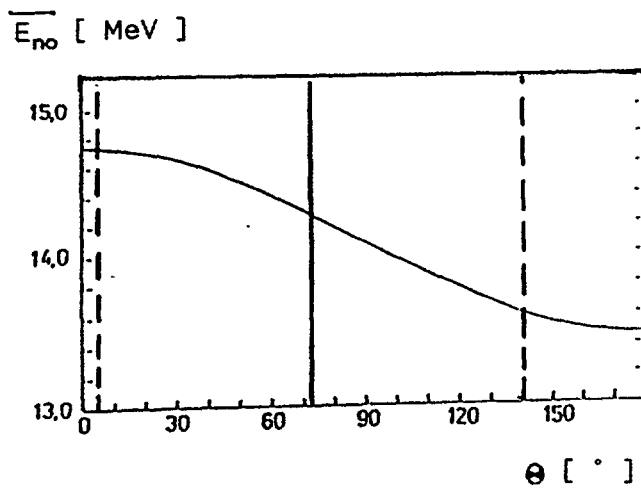
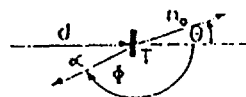
$\phi_n(E)$     $\phi_r(E)$     $\phi_n(t)$



Description of

- \* neutron source
- \* assembly
- \* data normalization
- \* background correction
- \* uncertainties

# Source Description



## Assembly Description

Geometry: drawing, mathematical expressions ( MCNP notation ? )

Composition: mass densities [ g / cm<sup>3</sup> ],  
 atomic densities [ 10<sup>24</sup> / cm<sup>3</sup> ],  
 taking into account small slits as for example between bricks or  
 slabs of the material investigated and other inhomogeneities

## Data Normalization

$\phi_n(E)$  should be normalized to one source neutron started for  $E > E_{thr}$ ,  
 needs normalized response function of the detector.  
 \* \*

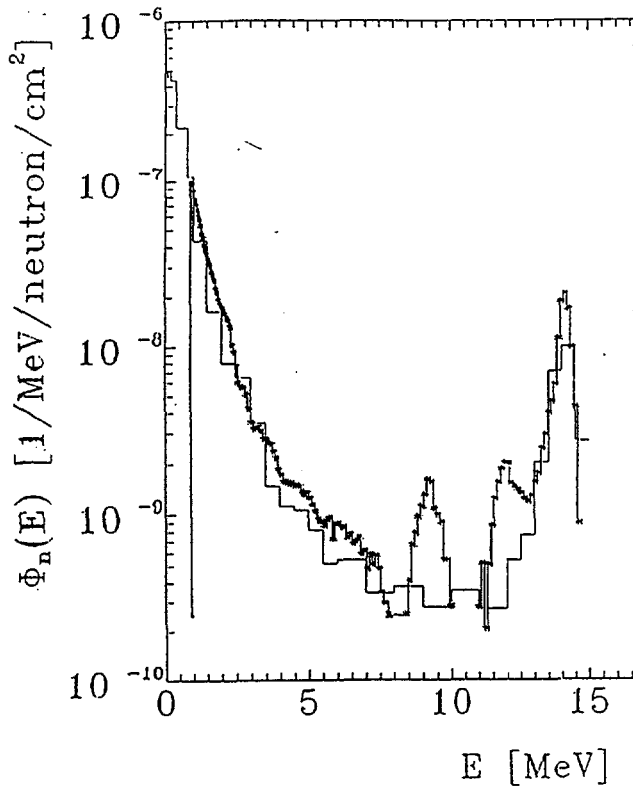
$\phi_r(E)$  normalized to one source neutron,  
 could be presented in energy bin structure, but for dominating  
 peaks also separately, that could be of interest at least for such  
 peaks as the positron annihilation line.  
 \*

$\phi_n(t)$  normalized to one source neutron,  
 needs the presentation of the absolute detector efficiency  $\epsilon(E)$   
 for folding the calculated  $\phi$ .

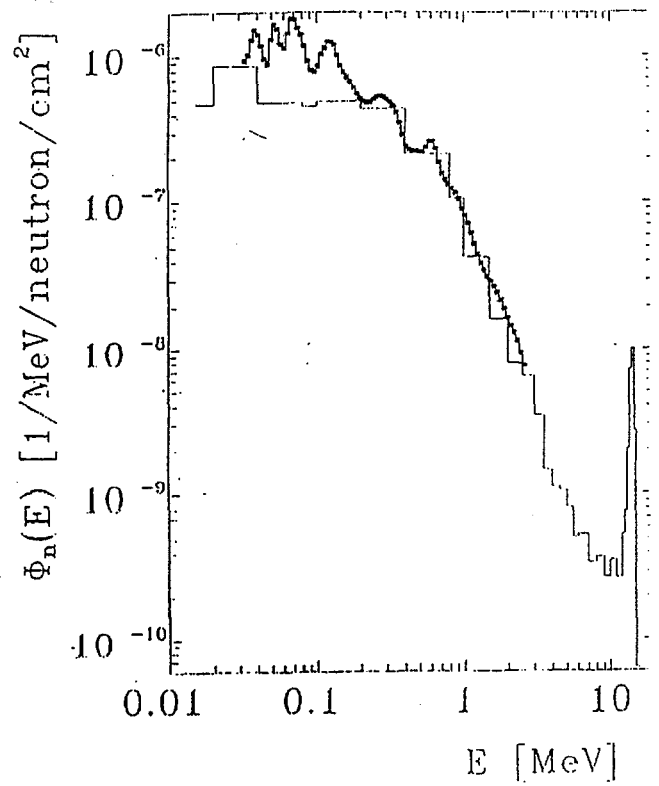
The source monitor constants has to be consistent with source  
 description.

\*

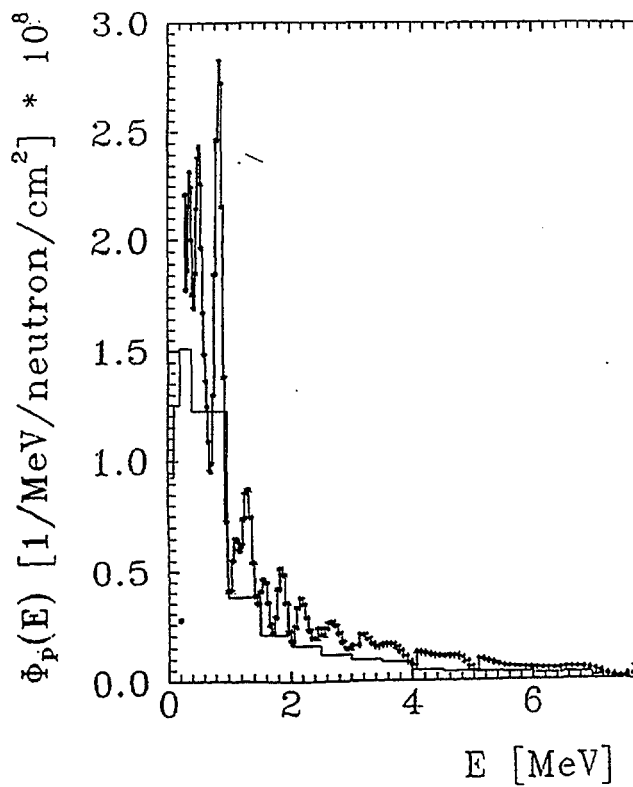
*Fe ( 30 cm ) QD=349cm*  
*b=00 x=00*  
 Neutrons



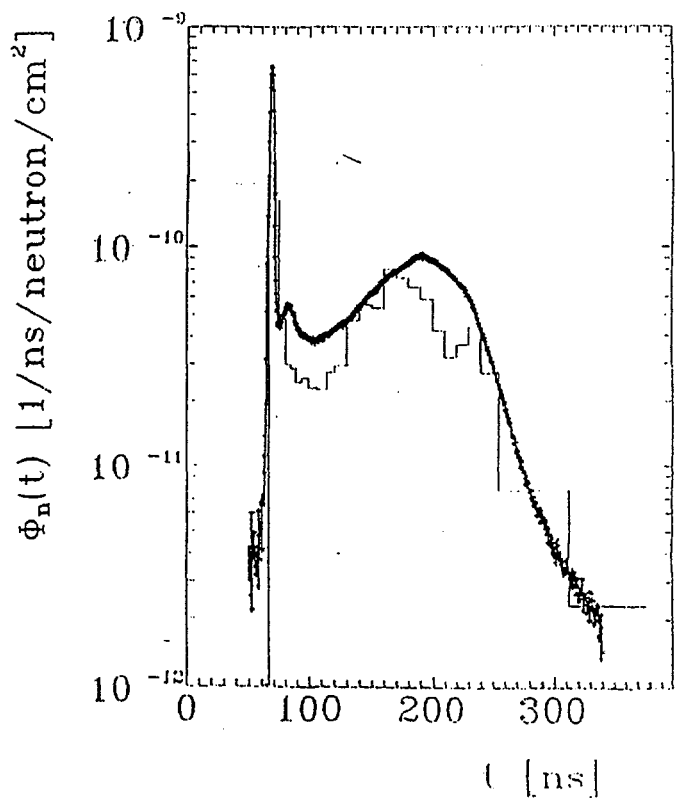
*Fe ( 30 cm ) QD=349cm*  
*b=00 x=00*  
 Neutrons

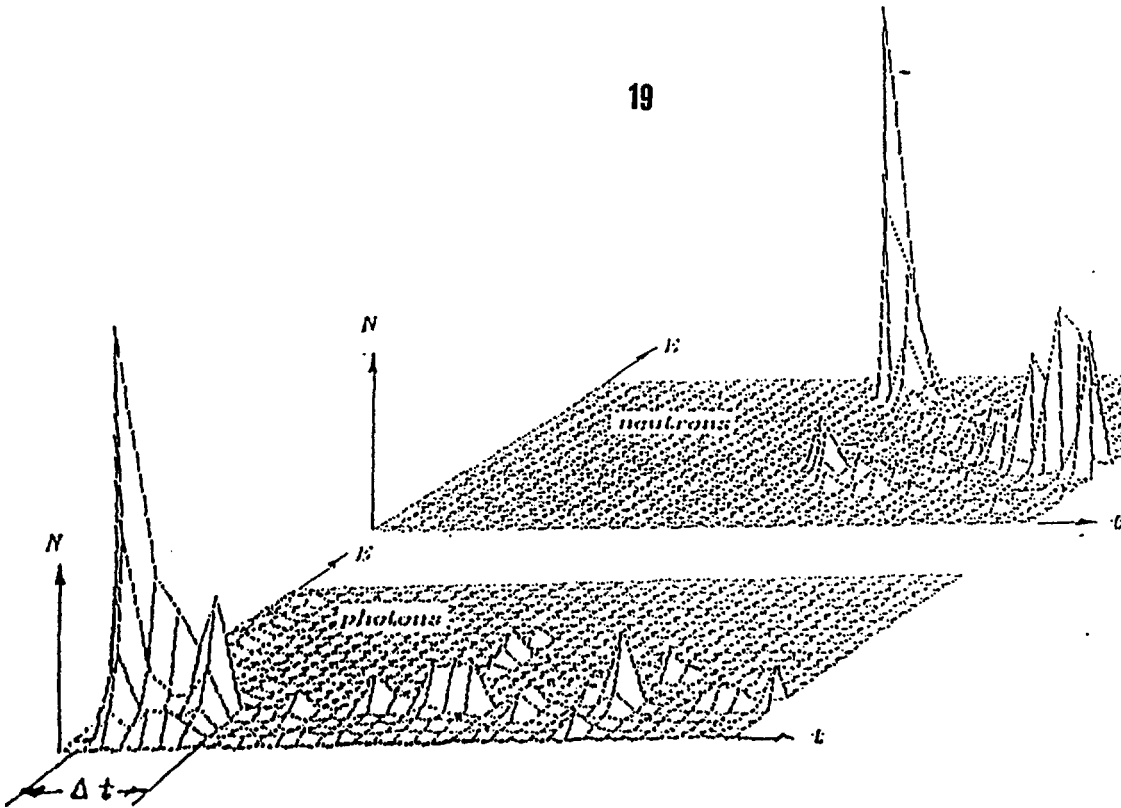


*Fe ( 30 cm ) QD=349cm*  
*b=00 x=00*  
 Photons  
 W3



*Fe ( 30 cm ) QD=349cm*  
*b=00 x=00*  
 Neutrons  
 eff=5529

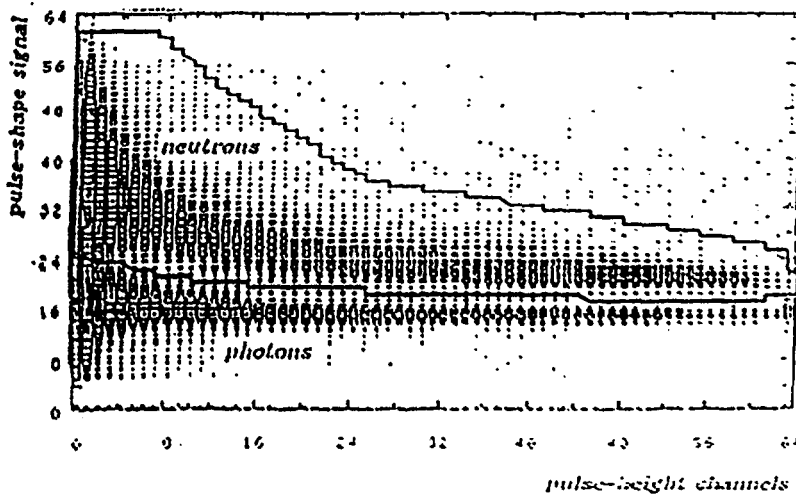




$t$  - time-of-arrival at the detector  
 $E$  - energy derived from the pulse height

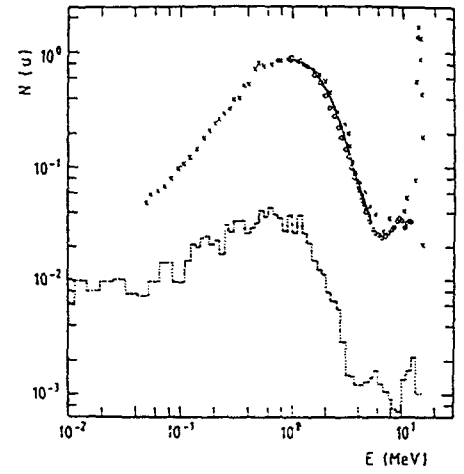
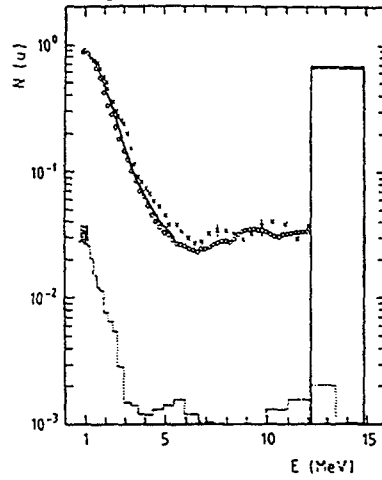
Two-dimensional data acquisition  $N(t,E)$  by operating the neutron generator in pulsed mode allows background and in-scattering reduction to the necessary level.

Detector : NE 213 liquid scintillator with  $n$ - $\gamma$  discrimination

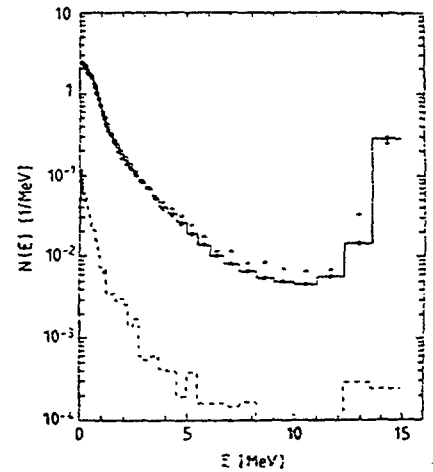
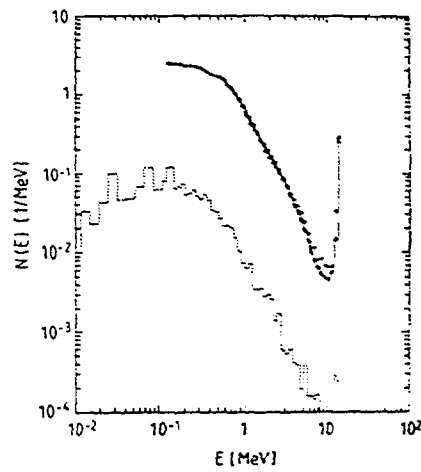


## Background Correction

Pb sphere

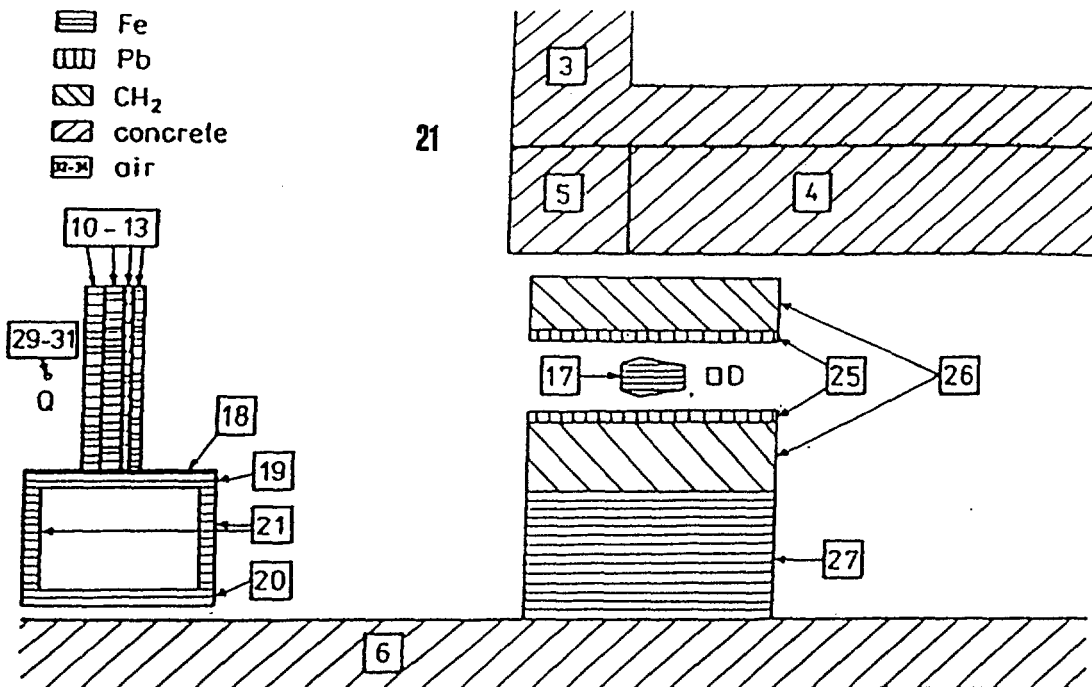


U sphere

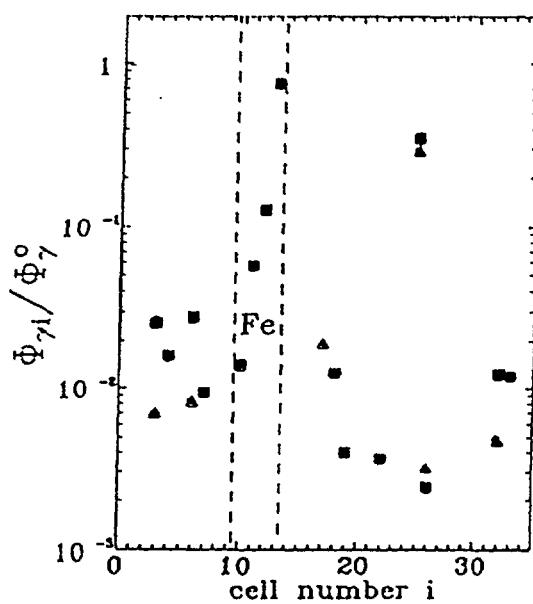
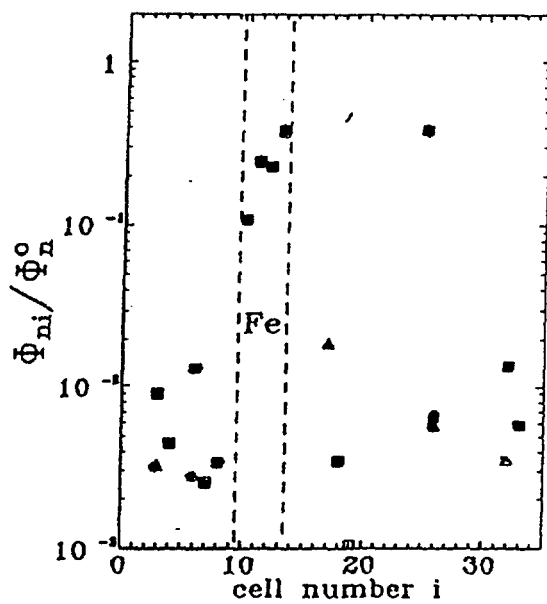


in the order of 1%, not negligible.

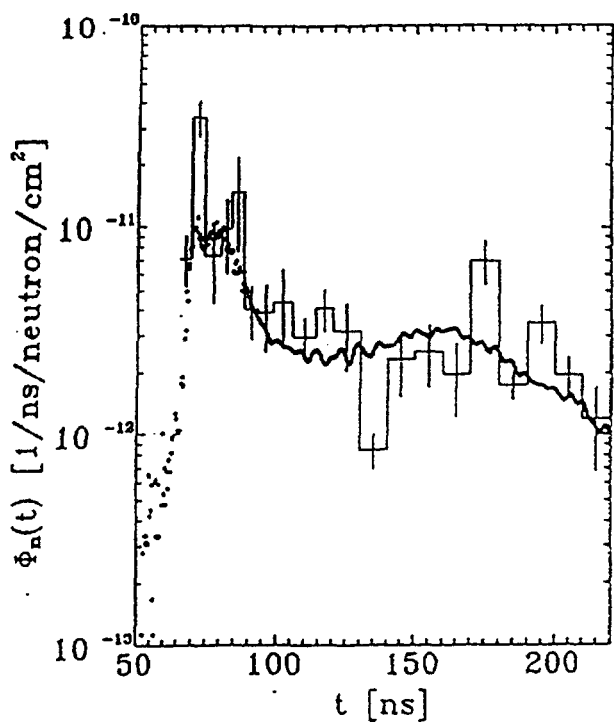
Fe slabs



21



■ without cone (17)  
 ▲ with cone



$$\phi_{exp}^{id.} = \phi_{exp} - (\phi_{calc} - \phi_{calc}^{id.})$$

The file should include both, statistical and systematic uncertainties. They should be separable. The components estimated as contributions to the systematic error should be listed.

## Conclusions

The presentation of experimental benchmark data should contain:

source description an energy distribution that takes into account effectively for the assembly investigated the anisotropy of energy and energy spread, the anisotropy of the source strength, neutron interactions ( down-scattering, absorption,..) in target holder, cooling....,  
a time distribution - if toa spectra are presented - that takes into account the neutron interactions in the target holdering,

assembly description the geometry and the material composition that takes into account inhomogeneities  $\ll$  mean-free-path of the neutrons as effective densities,

data normalized to one source neutron in energy bin structure; peaks of special interest may be separated;  
the normalization constants has to be consistent with the source description;  
for time-of-arrival the energy-dependence of detector efficiency is needed;

background corrected values that may be based on calculations,

uncertainty file, see above.

## MEASUREMENTS OF FUSION NEUTRON MULTIPLICATION IN SPHERICAL BERYLLIUM SHELLS

H. Giese, F. Kappler, R. Tayama<sup>1</sup>, U. von Möllendorff  
Kernforschungszentrum Karlsruhe GmbH  
P.O.B. 3640, 76021 Karlsruhe, Germany  
Fax: +49 7247 82 4874

<sup>1</sup>Permanent address: Hitachi Eng. Co., Hitachi, Japan

A. Alevra, H. Klein  
Physikalisch-Technische Bundesanstalt  
P.O.B. 3345, 38023 Braunschweig, Germany  
Fax: +49 531 592 9292



XA9642729

### Abstract

New results of spherical-shell transmission measurements with 14-MeV neutrons on pure beryllium shells up to 17 cm thick are reported. The spectral flux above 3 MeV was measured using a liquid scintillation detector. At 17 cm thickness, also the total neutron multiplication was measured using a Bonner sphere system. The results agree well with calculations using beryllium nuclear data from the EFF-1 or the ENDF/B-VI library.

### Introduction

Beryllium is one of the materials favored for multiplying neutrons in the blanket of a deuterium-tritium fusion reactor. Such multiplication by a factor of the order of 1.5 is required for tritium breeding self-sufficiency. However, important discrepancies exist among the beryllium nuclear data evaluations of Ref.[1] and Ref.[2], that have been used in the EFF-1 and the ENDF/B-VI libraries respectively. This concerns both the  $\text{Be}(n,2n)$  cross section at energies from threshold to 14.8 MeV, which primarily governs the multiplication, and the secondary energy and angular distributions of neutrons after collisions with beryllium, which govern the transport in the bulk material.

A spherical shell transmission experiment [3] on pure Beryllium is attractive as a "benchmark" in these circumstances. It can be treated in 1-dimensional transport calculations so that many different codes can be used, e.g., codes that utilize double-differential emission cross sections (DDX). The quantity measured by neutron detectors outside the sphere can either be the total fluence, yielding the total leakage multiplication (leakage neutrons per source neutron) or the spectral fluence, yielding partial leakage multiplications (leakage neutrons in specified energy windows per source neutron). Total fluence can be measured with better precision, and the total multiplication is near to the quantity of prac-

tical interest to the blanket designer; however, compensation effects may make the total fluence insensitive to erroneous nuclear data [4, 5]. Spectral fluence measurements, on the other hand, are more complex and less precise but they allow more specific conclusions about nuclear data to be drawn.

Several earlier experiments of either kind have been reported. Those on total leakage multiplication [6 – 10] show controversial results, at least at beryllium thicknesses beyond one mean free path which for 14 MeV neutrons amounts to about 5.5 cm. The earlier experiments on spectral fluence are not fully conclusive because of experimental difficulties [11] or limitation to a rather thin beryllium shell [12].

The Karlsruhe Neutron Transmission Experiment (KANT), performed on a set of spherical beryllium shells up to 17 cm thick, comprises both spectral and total fluence measurements.

## Experiment

### *General*

Details of KANT have been described earlier [13]. The neutron source is a conventional neutron generator employing a deuteron beam and a titanium-tritium target. Spherical beryllium shells of different thicknesses can be mounted so that the target is at their center. A cut of the target chamber is shown in Fig. 1.

In contrast with the former description, the target was at ground potential in all measurements reported here. The neutron pulse parameters were 0.3  $\mu$ s width at 160  $\mu$ s repetition period for the spectrum measurements and 30  $\mu$ s width at 1 ms period for the total fluence measurements. The neutron source strength was measured by registering the  $\alpha$  particles associated with the neutrons produced in the  $T(d,n)^4He$  reaction with a silicon surface barrier detector at  $120^\circ$  on the right of the deuteron beam direction (see Fig. 1). All counting rates were low enough to keep dead-time induced counting losses below about 1%.

### *Neutron spectrometry*

Spectrometry of neutrons emerging from the spherical shell (or from the bare target chamber) is accomplished in the slow range (thermal to 100 keV) by a time-of-flight technique and in the fast range (50 keV to 15 MeV) by unfolding the pulse height spectra from various proton-recoil detectors, namely, several different proportional counter tubes up to about 6 MeV and a liquid scintillation detector for the 3 to 15 MeV range. All detectors are absolutely calibrated in efficiency to yield fluences and thus multiplication values.

As far as spectrometry is concerned, the present paper presents specifically the scintillator results. This detector consists of a standard BA-1 cell of 5 cm height and 5 cm diameter containing NE-213 liquid scintillator. It is coupled via a 5 cm long light guide to an XP2020 photomultiplier. For the separation of neutron and photon induced signals a commercially

available system (Canberra Mod. 2160A) developed by Sperr et al.[14] was employed which is easier to adjust than the zero-crossing system used in former measurements. The resolution parameters of the detector were determined by careful measurements of various  $\gamma$  sources as described by Dietze and Klein[15]. Its neutron response was calculated by the NRESP7 code[16]. The FANTI code[17] is used for spectrum unfolding[18]. Scintillator results are reported below for the beryllium shell thicknesses of 5, 10 and 17 cm. The detector was positioned at  $60^\circ$  on the right of the deuteron beam, i.e. horizontally towards the right in Fig. 1, at a distance of 180 cm from the center.

#### *Total fluence measurement*

In addition to the spectral fluence measurements the total neutron leakage was determined using the PTB Bonner sphere (BS) spectrometer (see Ref.[19] and references cited therein). The BS set denoted "C", used in the present experiment, consists of 11 polyethylene moderators with diameters of 7.6 cm (3") to 38.1 cm (15") and a spherical He-3 proportional counter as central detector for the thermalized neutrons. In addition, the He-3 counter was employed as bare and Cd-covered detector. The complete response matrix required for the unfolding procedure has been determined by adjusting discrete-ordinate calculations to calibration data obtained for thermal neutrons and monoenergetic neutrons beyond 1 keV [19]. The BS measurements were performed at the same emission angle used for the scintillation detector but at a distance of 144.5 cm. The 13 experimental net counting rates were unfolded using the slightly modified PTB version of the SAND-II code[20] and the Monte Carlo simulated spectral fluence as a-priori information. The resulting spectral neutron fluence covers the entire energy range. Since the neutron source was investigated both bare and covered with the Be shell the total multiplication factor can be extracted from the total neutron fluences. At first, however, corrections have to be made to account for the anisotropic neutron emission of either assembly (see "Calculations" section). A more detailed description of the BS measurements will be given elsewhere[21].

#### *Room-return background*

For every single measurement, the background of neutrons scattered from the walls etc. and from the air was measured separately using a cylindrical or approximated-conical shadow shield between the neutron emitter (the target chamber with or without a surrounding beryllium shell) and the detector. All shadow shields consisted of 20 cm of steel on the side towards the emitter, followed by 20 cm of hydrogenous plastic and, in case of a detector sensitive to thermal neutrons, 1 mm of cadmium sheet. They were assembled from cylindrical slabs of various diameters to match the sizes of emitter and detector.

#### Calculations

The calculations used to obtain expected leakage spectra and multiplications for this experiment were described earlier in some detail[4].

### *1-dimensional S(N) calculations*

The 1-dimensional S(N) transport results from the ANTRA-1 code [22] are repeated in Table 1 for comparison. This code can utilize both the EFF-1 and the ENDF/B-VI nuclear data libraries (see Introduction). It does not rely on truncated Legendre expansions to describe angular distributions but uses DDX data in a direct numerical way which is more appropriate for a nucleus like beryllium.

### *3-dimensional Monte-Carlo calculations*

The 3-dimensional Monte-Carlo results were newly calculated [23] using now version 4.2 of the MCNP code. They take into account the slight anisotropy, both in neutron energy and yield, of the source reaction T(d,n). Other deviations from spherical symmetry are caused by the radial channels in the beryllium shells and, more importantly, by the distribution of matter in the target chamber (Fig. 1). As a result, the fluence at the detector differs from the fluence averaged over a concentric spherical surface around the source by an anisotropy factor which depends on the beryllium thickness and on the neutron energy window considered. The factor can be obtained in the MCNP calculations by comparing "point estimator" and "leakage" outputs. Corresponding to the definition of leakage multiplication given above, both the measured fluences and the ones calculated as "point estimators" at the detector have been corrected by the inverse of this factor to make them comparable to "4 $\pi$ " fluences or 1-dimensional calculation results. At the measurement position the anisotropy factor amounted to 1.139 for the bare target chamber and 1.043 for the assembly with the 17 cm thick beryllium shell (for details see Ref. [21]).

The Monte Carlo calculations also show a neutron leakage from the bare target chamber which exceeds the source strength by a factor of 1.062. This is obviously due to neutron multiplication within the chamber, mainly by (n,2n) reactions on copper. Since the leakage multiplication of a beryllium shell is the leakage per *source* neutron, not per neutron entering the beryllium, only the bare-chamber fluence measured with the Bonner sphere system was corrected for the chamber multiplication, so as to obtain the number of source neutrons. The chamber multiplication is contained, therefore, in all leakage multiplication results given below. Leakage multiplication is not an absolute characteristic of a given spherical shell but depends, in every possible definition, to some extent on the particular experimental arrangement.

## **Results**

Fig. 2 shows experimental and MCNP calculated spectra above 0.1 MeV. The experimental points below 3 MeV are the counter tube data published earlier [4]. An expanded plot of the data above 3 MeV for the thickest beryllium sphere is shown in Fig. 3. The discrepancies around 10 MeV may be due to the inadequate calculational treatment and nuclear data used in the MCNP calculation for the inelastic scattering from copper, the main

constituent of the target chamber (Fig. 1). An improvement could likely be obtained with double differential  $\text{Cu}(n,n')$  data taking into account pre-equilibrium neutron emission.

The spectral fluence of leakage neutrons obtained by unfolding the net BS data is shown in Fig. 4. The MCNP result used as a-priori information was only slightly modified by the SAND code to achieve compatibility with the measured data.

Table 1 gives results for the 3-15 MeV leakage energy window at three beryllium shell thicknesses and the total leakage multiplication (thermal-15 MeV) for the 17 cm thick shell. The estimated experimental uncertainties (one standard deviation) are  $\pm 6\%$  for the window (scintillator) data and  $\pm 7\%$  for the total (BS) data. All the calculation/experiment ratios indicate excellent agreement, except the ANTRA-1 results for total leakage. The latter deviation is attributable to the neglect of upscattering at thermal energies in that calculation.

The calculated leakages for the 3-15 MeV window do not show any significant effect of the choice of the beryllium nuclear data set as it was found for the 0.3-3 MeV window [4]. This might be explained, e.g., by mutual compensation of differences in the  $(n,2n)$  and the elastic scattering cross sections. A similar compensation effect between the  $(n,2n)$  cross section and the energy and angular distributions of neutrons emitted from beryllium is believed to explain why even the calculated total leakage multiplications are so close to each other [5].

## Conclusion

Measurements were made of the partial leakage multiplication above 3 MeV from spherical beryllium shells of 5, 10 and 17 cm thickness fed with 14 MeV neutrons, as well as the total leakage multiplication from the 17 cm shell.

Calculations of these partial leakage multiplications using beryllium nuclear data from either the EFF-1 or the ENDF/B-VI library agree well with the measurements and with each other, in spite of the differences existing between those nuclear data evaluations.

The same can be concluded for the total leakage result. In this case a very similar finding was reported by Smith et al. [10].

## Acknowledgements

*The authors express their gratitude to Dr. U. Fischer for discussions and continuous theoretical assistance, to Mr. H. Fries for experimental assistance, to Dr. H.O. Klages for helpful hints and loans of experimental equipment, to Dr. F. Käppeler for a loan of  $\gamma$  calibration sources, and to Prof. G. Kessler for his continued support of this work.*

## References

[1]

P.G. Young and L. Stewart, Report LA-7932-MS (1979)

[2]

S.T. Perkins, E.F. Plechaty and R.J. Howerton, Nucl. Sci. Eng. 90 (1985) 83-98

[3]

H.A. Bethe, J.R. Beyster and R.E. Carter, J. Nucl. Energy 3 (1956) 207-223 and 273-300, 4 (1957) 3-25 and 147-163

[4]

U. von Möllendorff, U. Fischer, H. Fries, H. Giese, F. Kappler, R. Tayama, T. Tsukiyama and E. Wiegner, Fusion Technology 1992 (C. Ferro, M. Gasparotto and H. Knoepfel, eds.), Elsevier 1993, Vol. 2, p. 1537-1541

[5]

U. Fischer and U. von Möllendorff, Fus. Tech. 24 (1993) 229-230

[6]

T.K. Basu et al., Nucl. Sci. Eng. 70 (1979) 309-313; see also V.R. Nargundkar, T.K. Basu and O.P. Joneja, Fus. Tech. 12 (1987) 380-394

[7]

V.A. Zagryadskij, M.I. Krainev, D.V. Markovskij, V.M. Novikov, D.Yu. Chuvilin and G.E. Shatalov, Report INDC(CCP)-272/G, IAEA, Vienna (1987)

[8]

R.S. Hartley, N.E. Hertel and J.W. Davidson, Fus. Eng. Des. 10 (1989) 133-138

[9]

Y. Chen, G. Chen, R. Liu, H. Guo, W. Chen, W. Jiang and J. Shen, Fus. Tech. 19 (1991) 1919-1924

[10]

J.R. Smith, J.J. King, J.W. Davidson and M.E. Battat, Fus. Tech. 23 (1993) 51-67

[11]

C. Wong, E.F. Plechaty, R.W. Bauer, R.C. Haight, L.F. Hansen, R.J. Howerton, T.T. Komoto, J.D. Lee, S.T. Perkins and B.A. Pohl, Fus. Tech. 8 (1985) 1165-1173

[12]

S.P. Simakov, A.A. Androsenko, P.A. Androsenko, B.V. Devkin, S.I. Dubrovina, M.G. Kobozev, A.A. Lychagin, V.A. Talalaev, D.Yu. Chuvilin and V.A. Zagryadskij, Fusion Technology 1992 (C. Ferro, M. Gasparotto and H. Knoepfel, eds.), Elsevier 1993, Vol. 2, p. 1489-1493

[13]

H. Ebi, W. Eyrich, H. Fries, H. Giese, K. Hayashi, F. Kappler, U. von Möllendorff and T. Tsukiyama, *Fus. Eng. Design* 18 (1991) 317-322

[14]

P. Sperr, H. Spieler, M.R. Maier and D. Evers, *Nucl. Inst. Meth.* 116 (1974) 55-59

[15]

G. Dietze and H. Klein, *Nucl. Inst. Meth.* 193 (1982) 549-556

[16]

G. Dietze and H. Klein, Report PTB-ND-22 (1982) and unpublished upgradings

[17]

G. Bulski et al., *Int. Conf. Nuclear Data for Science and Technology*, Antwerp, 6-10 Sept. 1982; see also R. Etzel, Diplomarbeit (unpublished), Univ. Stuttgart (1991)

[18]

R. Tayama, unpublished report (1993)

[19]

A.V. Alevra, M. Cosack, J.B. Hunt, D.J. Thomas and H. Schraube, *Rad. Prot. Dosim.* 40 (1992) 91-102

[20]

W.N. McElroy, S. Berg, T. Crockett and R.G. Hawkins, Report AFWL-TR-67-41, U.S. Air Force Weapons Laboratory (1967)

[21]

A. Alevra et al., KfK report, to appear

[22]

A. Schwenk-Ferrero, Reports KfK-4163 (1986) and KfK-4788 (1990)

[23]

F. Kappler, unpublished report (1993)

**Table 1**  
 Leakage multiplication results and calculation/experiment ratios. B-VI stands for ENDF/B-VI

Beryllium Shell			Leakage Neutrons per Source Neutron							
Thick-ness	Out-side Dia.	Inside Dia.	Energy Range	Exper-iment	Calculation			Calculation/Experiment		
					MCNP	AN-TRA	AN-TRA	MCNP	AN-TRA	AN-TRA
					EFF-1	EFF-1	B-VI	EFF-1	EFF-1	B-VI
5cm	30cm	20cm	3 - 15MeV	0.715	0.710	0.699	0.697	0.99	0.98	0.97
10cm	30cm	10cm	3 - 15MeV	0.582	0.579	0.555	0.552	0.99	0.95	0.95
17cm	44cm	10cm	3 - 15MeV	0.382	0.385	0.395	0.392	1.01	1.03	1.03
			therm. -15MeV	1.65	1.689	1.857	1.793	1.02	1.13	1.09

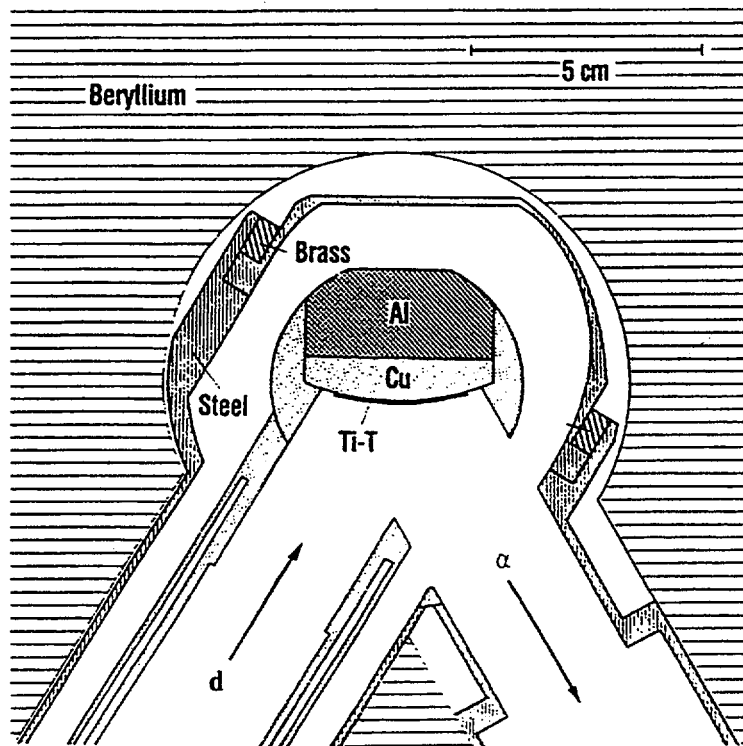


Figure 1  
Horizontal cut through target chamber (MCNP calculational model)

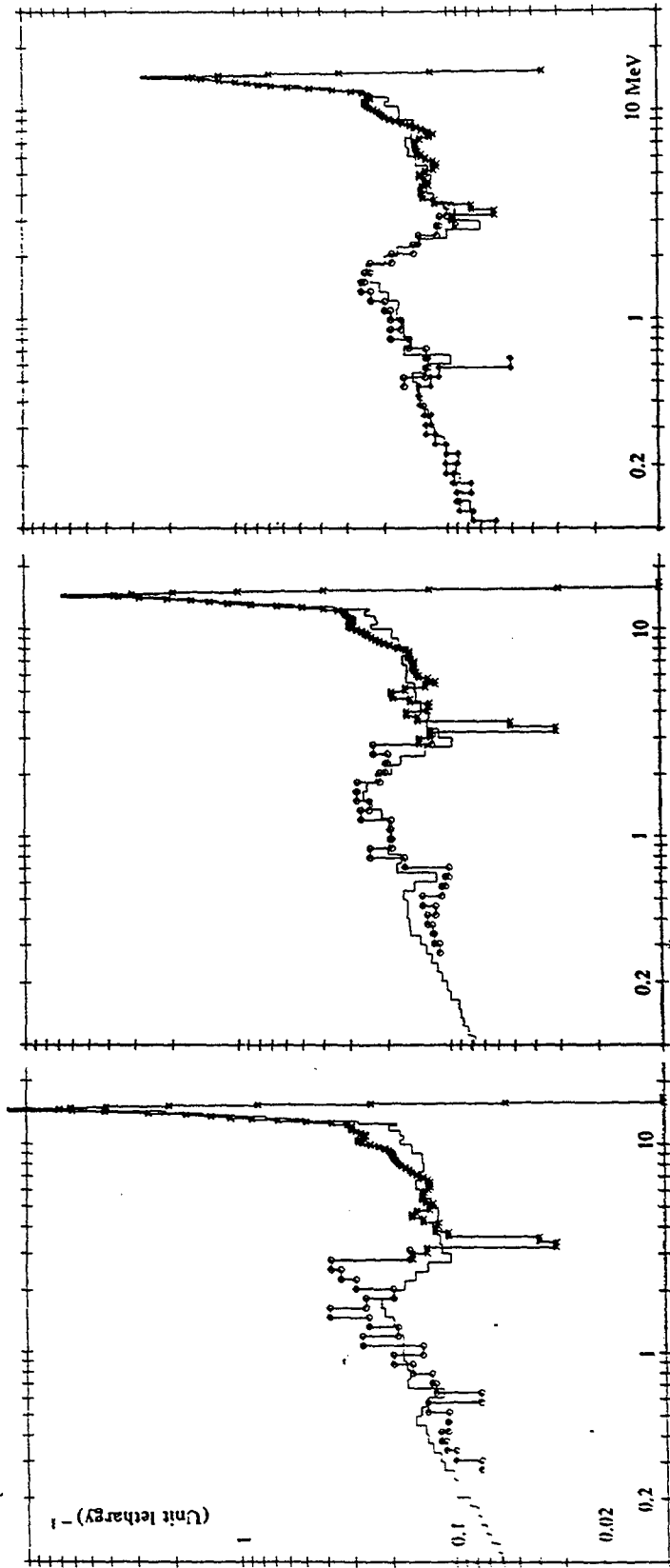


Figure 2  
 Leakage neutron spectra (neutrons per source neutron and unit lethargy) from 5, 10 and 17 cm thick beryllium shells (left to right) in energy range above 0.1 MeV.  
 Line without symbols: MCNP-4.2 calculation  
 Cross symbols: Scintillation detector  
 Other symbols: Proton recoil proportional counters

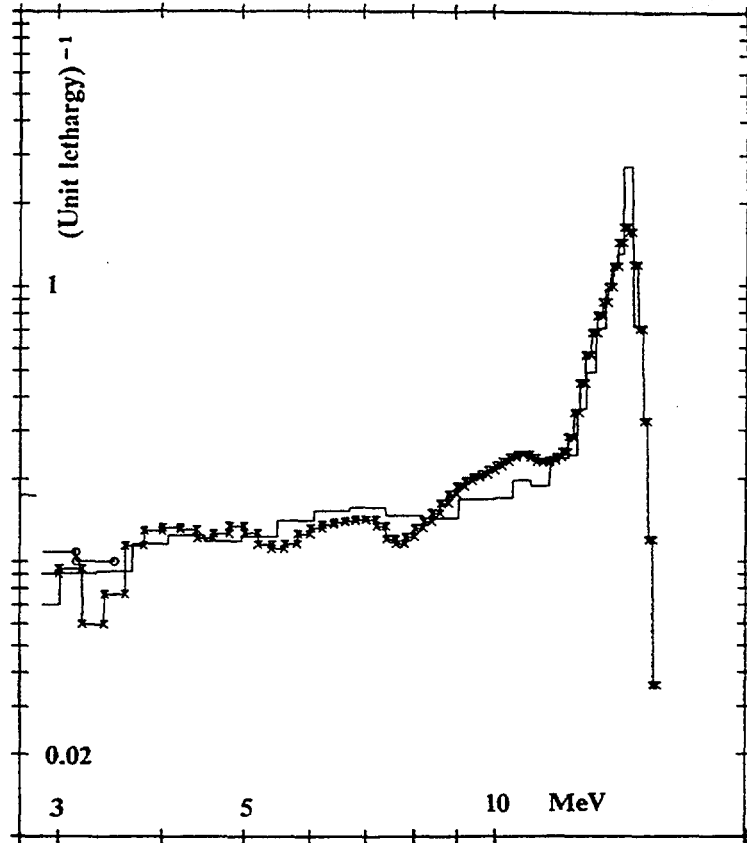


Figure 3

Expanded part of spectrum from 17 cm shell. Unit and symbols as in Fig. 2

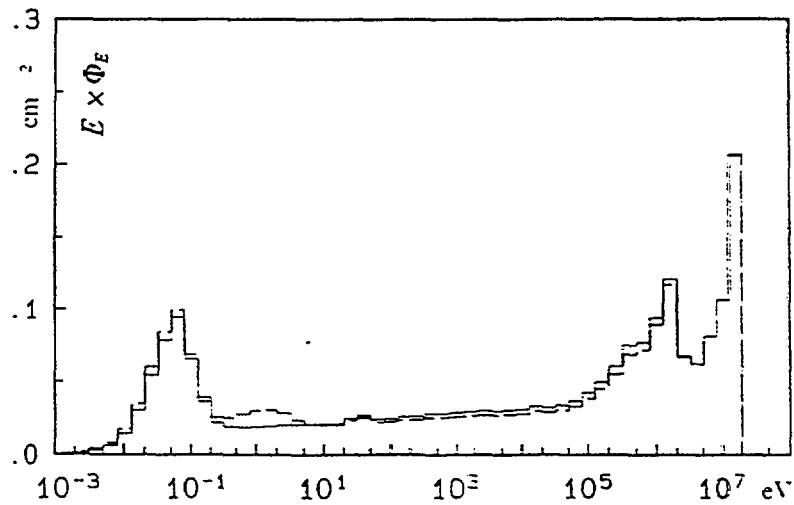


Figure 4

Normalized spectral neutron fluence from the 17 cm thick beryllium shell, presented as lethargy  $E_n \times \Phi_E$  versus neutron energy  $E_n$ , as unfolded from BS data (thick dash-dotted line), using the MCNP calculation (thin line) as a-priori information.

**The Karlsruhe Neutron Transmission Experiment****(KANT):**

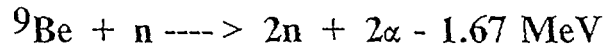
XA9642730

**Spherical Shell Transmission Measurements  
with 14 MeV Neutrons on Beryllium**

**U. von Möllendorff, U. Fischer, H. Giese,  
F. Kappler, R. Tayama<sup>1</sup>, E. Wiegner  
Kernforschungszentrum Karlsruhe GmbH  
P.O.B. 3640, 76021 Karlsruhe, Germany**

**<sup>1</sup>Permanent address: Hitachi Eng. Co., Hitachi, Japan**

**H. Klein, A. Alevra  
Physikalisch-Technische Bundesanstalt  
P.O.B. 3345, 38023 Braunschweig, Germany**



Schwelle  $E_n = 1.85 \text{ MeV}$

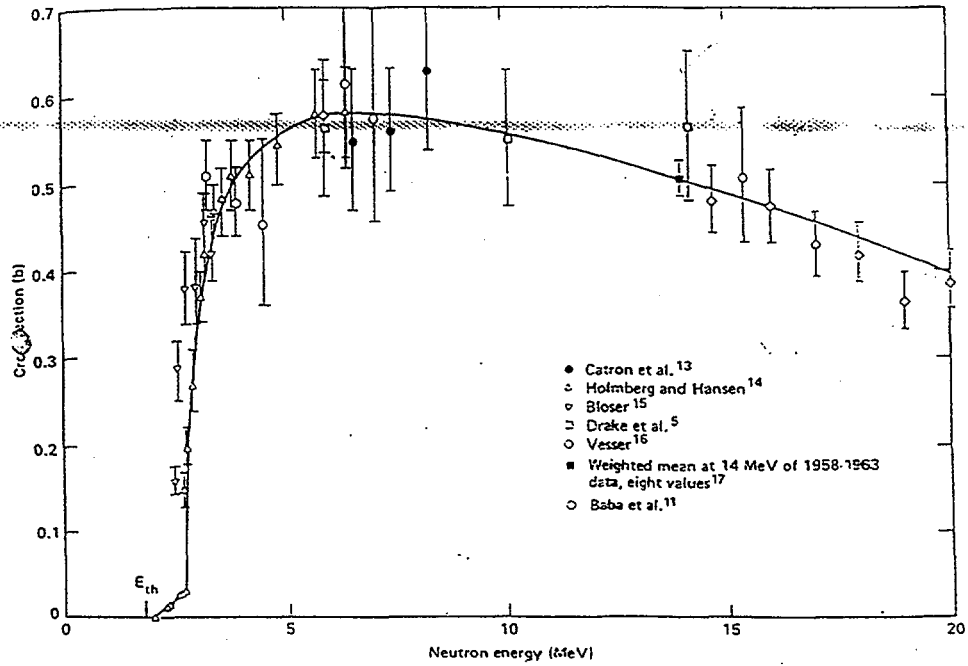
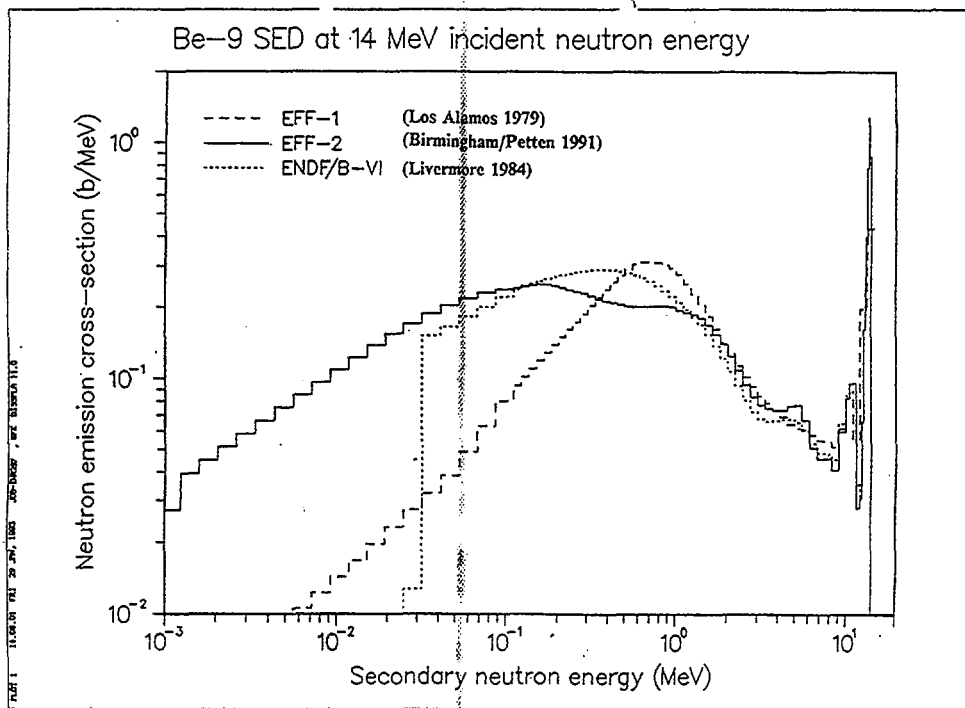


Fig. 1. The  ${}^9\text{Be}(n,2n)2\alpha$  cross section. The line represents the results used in the present work.



# Spherical Shell Transmission Experiment

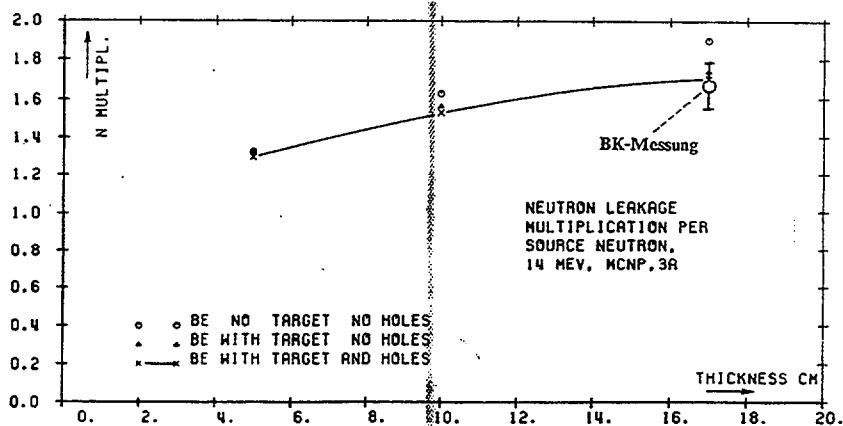
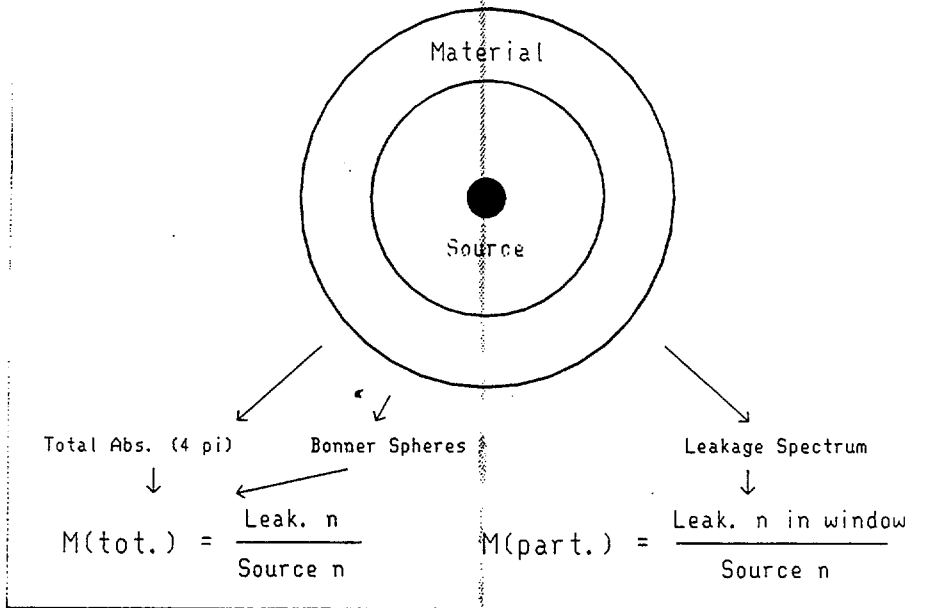


Figure 3 Neutron leakage multiplication in spherical beryllium shells with the inner radius of 5 cm. Effect of the target assembly and of radial holes.

## Neutron generator

- Deuterium ions from pulsed duoplasmatron source, pulse width 0.3 to 30  $\mu$ s
- DC acceleration, maximum voltage  $\approx$  200 kV
- Air cooled Ti- $^3$ H target
- Yield  $\approx$   $10^{11}$  n/s instantaneous,  $10^9$  n/s time averaged

## Spectroscopy of leakage neutrons

### 1. Time-of-flight method: thermal ... 100 keV

- 17 m long evacuated flight tube
- Steel collimators at tube entrance and at detector
- Background measured separately with shadow bar inside evacuated tube
- Detector: Boron-vaseline + NaI scintillators
- Fast multichannel scaling analyser, minimum dwell time 50 ns/channel

### 2. Proton recoil method: 50 keV ... 14 MeV

- Spectrum obtained by unfolding from pulse height distribution
- Wall-scattered background measured separately using shadow cone

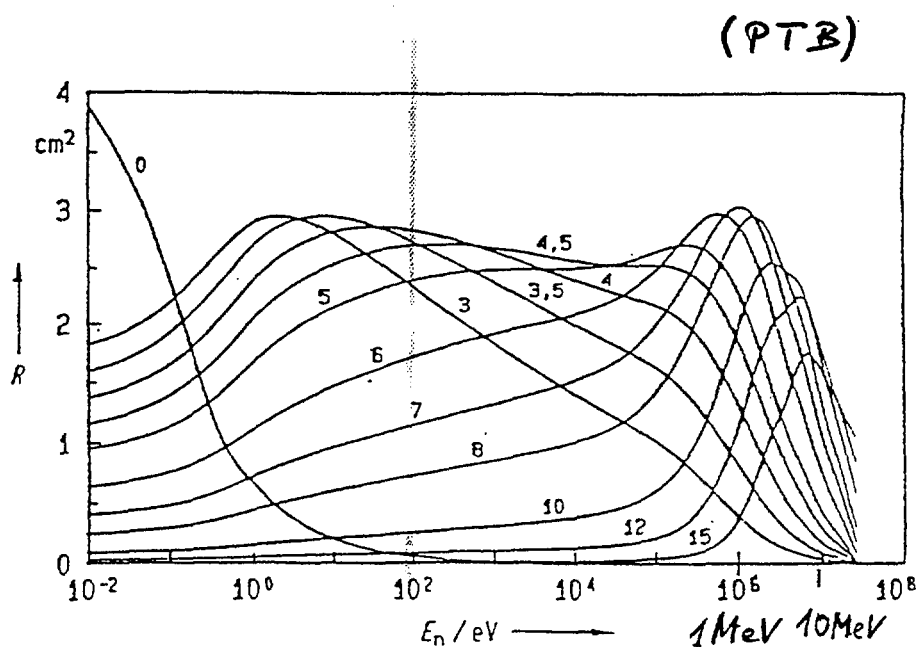


Bild 6 Ansprechvermögen  $R$  der Bonner Kugeln des Satzes 'c' in Abhängigkeit von der Neutronenenergie  $E_n$ . Die Kurven sind für

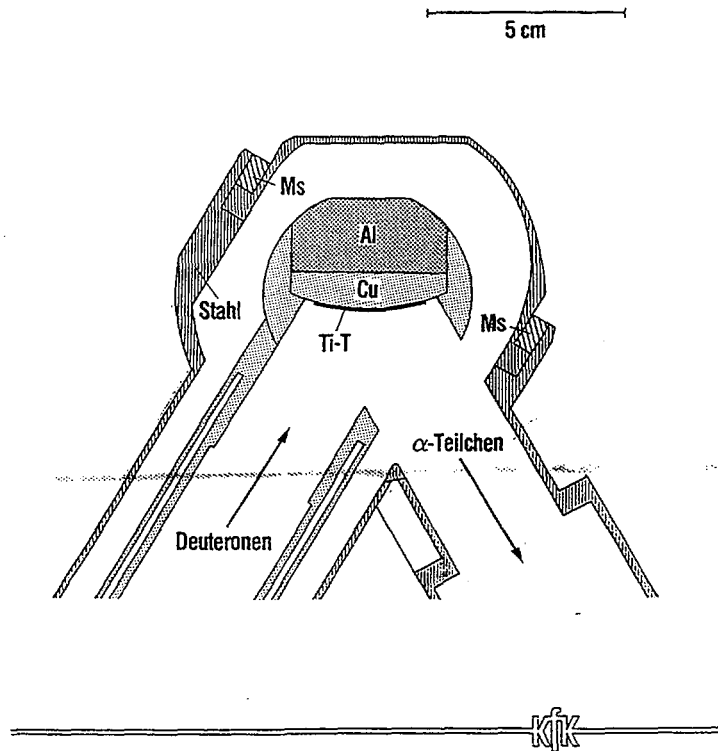


Fig.1  
Horizontal cut through the target chamber  
(MCNP calculational model)

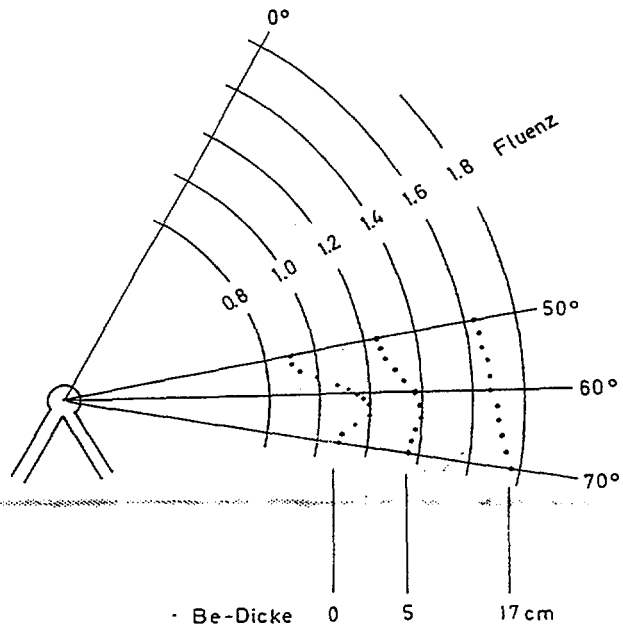
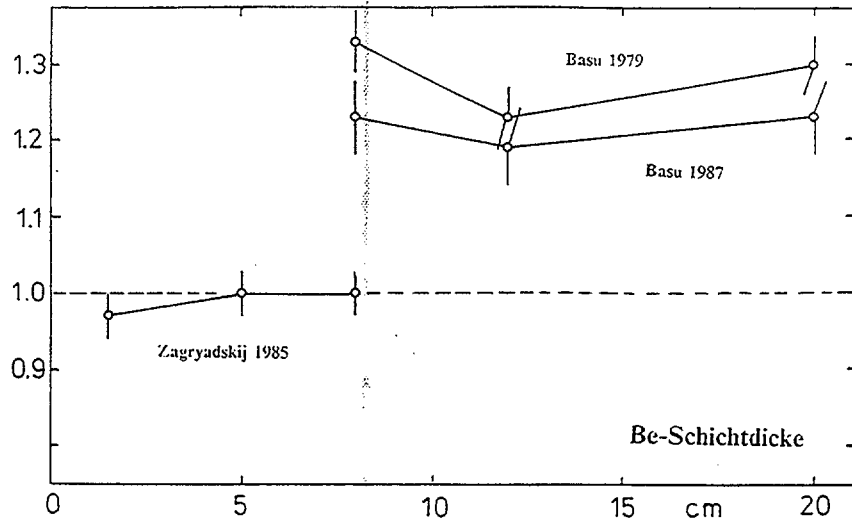


Abb. 15  
Berechnete Neutronenemission als Funktion der Richtung für die  
Beryllium-Schichtdicken 0 cm, 5 cm und 17 cm

Die Fluenz ist berechnet als "point estimator" 1445 mm vom Zentrum in der j  
den Richtung, aber angegeben als Anzahl der Leckneutronen in  $1 \pi$  pro (

C/E Totale Leckagemultiplikation



C/E Totale Leckagemultiplikation

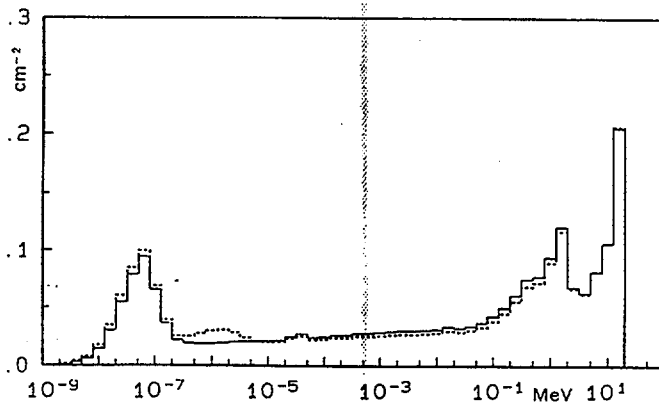
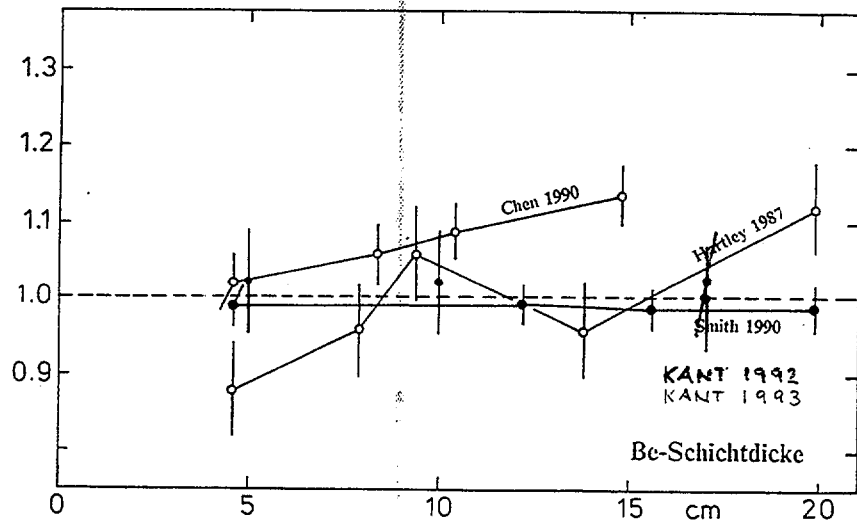


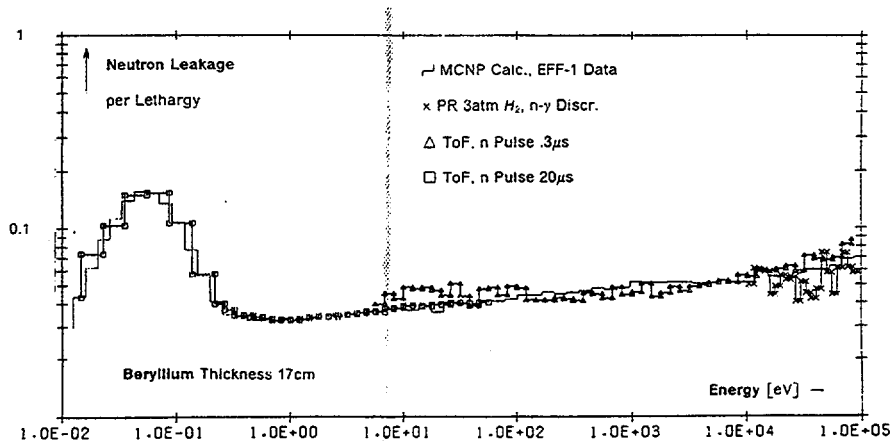
Figure 1

Normalized leakage neutron spectrum from the 17 cm thick beryllium shell, presented as lethargy  $E_n \times \Phi_n$  versus neutron energy  $E_n$ .

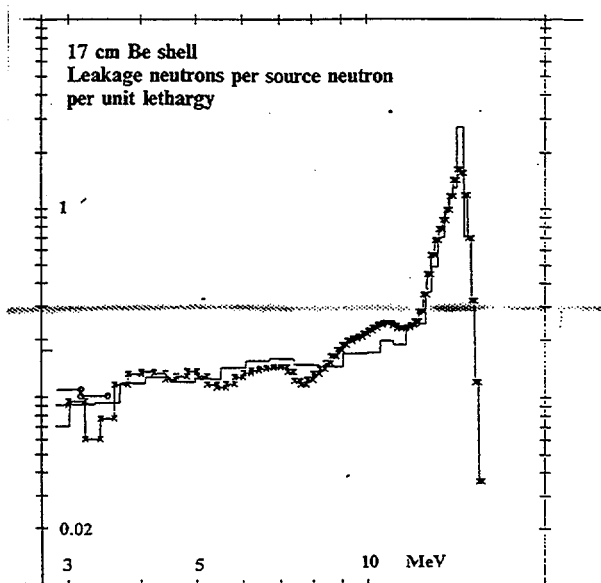
Thick dashed line: experiment, unfolded from Bonner sphere measurement.

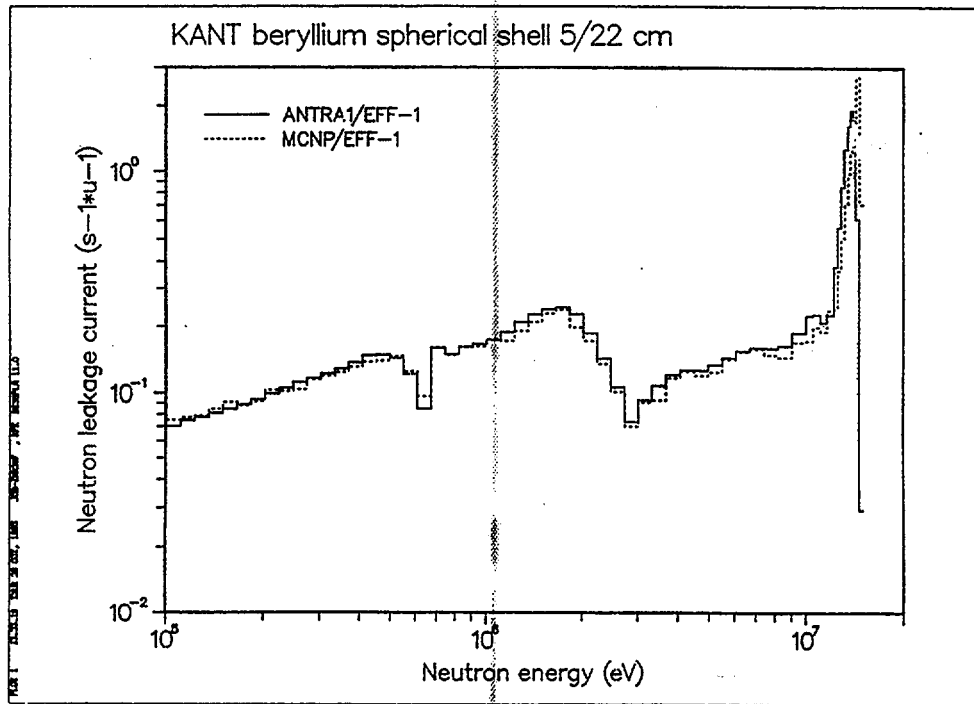
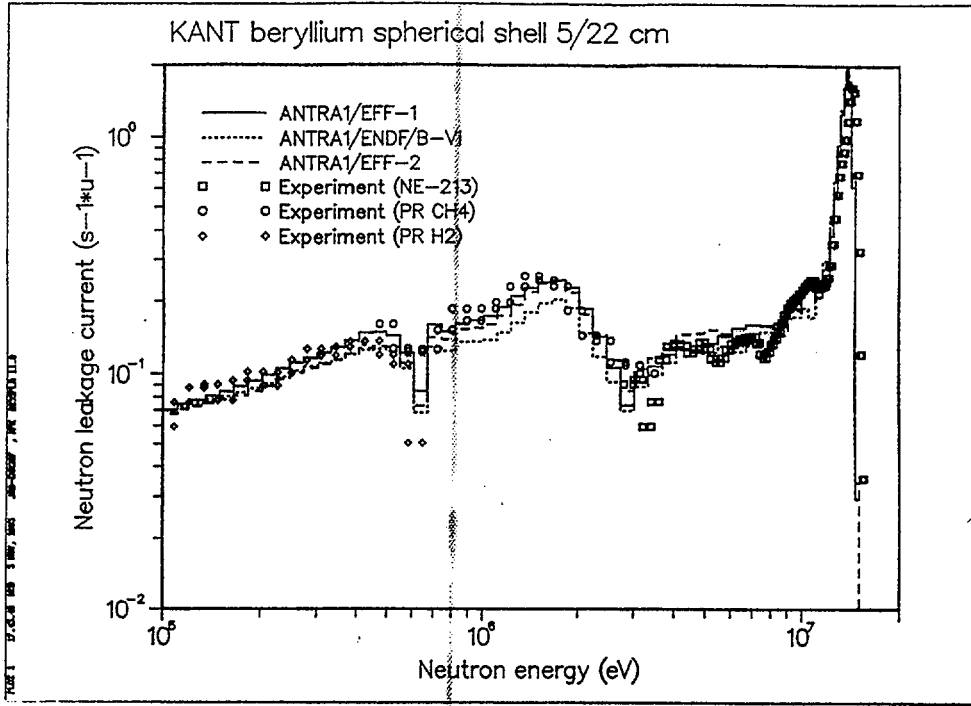
Energy Range	Method	Detector		Special Techniques	Source Pulse	
					Width	Period
2.53mcV - 50eV	Time-of-Flight Spectroscopy (17m flight path)	Boron-Vaseline + NaI scintillators			20-30 $\mu$ s	25ms
10eV - 100keV				Cd - Filter	0.3 $\mu$ s FWHM	4ms
50 - 600keV	Proton Recoil Spectroscopy	Proportional Counter Tubes	5cm diameter 20cm long 3 bar H <sub>2</sub>	n- $\gamma$ Discr.	20-30 $\mu$ s	2ms
0.3 - 2McV			5cm diameter 20cm long 4 bar CH <sub>4</sub>			
0.8 - 6McV		9cm diameter 89cm long 3 bar CH <sub>4</sub>				
3.3 - 15McV		NE-213 Scintillator	5cm diameter 5cm long	n- $\gamma$ Discr.		

Table 1. Survey of KANT Neutron Spectroscopy Methods



Measured and Calculated Neutron Spectra per Source Neutron





		Leakage Neutrons per Source Neutron						
Thick-ness	Energy Range	Exper-iment	Calculation			Calculation/Experiment		
			MCNP	ANTRA		MCNP	ANTRA	
				EFF-1	EFF-1		B-VI	EFF-1
5cm	0.3 - 3MeV	0.435	0.403	0.402	0.364	0.93	0.92	0.84
	3 - 15MeV	0.715	0.710	0.699	0.697	0.99	0.98	0.97
10cm	0.3 - 3MeV	0.410	0.419	0.445	0.387	1.02	1.09	0.94
	3 - 15MeV	0.582	0.579	0.555	0.552	0.99	0.95	0.95
17cm	0.3 - 3MeV	0.385	0.344	0.370	0.307	0.94	1.01	0.84
	3 - 15MeV	0.382	0.385	0.395	0.392	1.01	1.03	1.03
	1meV - 15MeV	1.65	1.689	1.857	1.793	1.02	1.13	1.09

Table 1  
Leakage multiplication results and calculation/experiment ratios (B-VI stands for ENDF/B-VI).  
Experimental uncertainties: ±6% (partial leakage multiplications), ±7% (total leakage multiplication)



BULK SHIELD BENCHMARK EXPERIMENT  
ON STAINLESS STEEL  
AT THE FRASCATI NEUTRON GENERATOR  
NET Subtask NDB2-1  
(ENEA - CEA Collaboration)

P. Batistoni  
M. Angelone, M. Martone, M. Pillon, V. Rado  
ENEA - Fusion Dept. - Neutronics Division  
C.R.E. Frascati  
I-00044 Frascati (Rome) ITALY

Presented at the IAEA Consultant Meeting on  
"Preparation of Fusion Benchmarks in Electronic Format  
for Nuclear Data Validation Studies"  
Dec 13-16, 1993 - IAEA Vienna, Austria

## INTRODUCTION

In the framework of the European Technology Program for NET/ITER, ENEA - Frascati and CEA - Cadarache in collaboration, are performing a bulk shield benchmark experiment, using the 14-MeV Frascati Neutron Generator (FNG)

The purpose of the experiment is to provide accurate and reliable experimental data for the validation of the nuclear database and methods, used in shielding design, through a rigorous analysis of the results.

Integral quantities will be measured and compared with the same calculated quantities using a discrete ordinate (BISTRO) and a Monte Carlo (MCNP) code.

In the case of discrepancy between measured and calculated quantities larger than those expected from data base uncertainty, a sensitivity analysis will be performed to find the cross section responsible for.

## THE FNG FACILITY

The Frascati Neutron Generator FNG produces a nearly isotropic 14-MeV neutron source through the  $T(d,n)\alpha$  fusion reaction. A deuteron beam (up to 3 mA) is accelerated up to 330 KeV and focusses on a fixed tritiated target.

The target contains 10 Ci of tritium adsorbed in a titanium layer deposited in 1-mm thick copper alloy disk of 24 mm in diameter. The target is cooled by a water flow in the 1-mm gap between the copper disk and the 1-mm stainless steel cap.

FNG can produce up to  $5 \times 10^{11}$  n/s, but for the moment it has permission to operate limited at less than 1/3 of its design intensity.

FNG has been expecially designed to perform benchmark experiments to improve nuclear data base. Its main characteristics are a light target to produce a clean spectrum, and a large bunker to reduce the neutron background due to the room return.

## DESCRIPTION OF THE EXPERIMENT

- The experiment consists of the irradiation by 14-MeV neutrons of a stainless steel block (AISI 316), in a configuration allowing for deep penetration measurements of neutron and gamma fluxes.
  
- The block is made by 14 adjacent 5 cm thick plates (1m x 1m) for a total thickness of 70 cm.
  
- The block is located at 5.3 cm from the 14-MeV neutron source, at the center of the FNG bunker hall, at a distance of at least 4 m from walls, the ceiling and the floor.
  
- The block is provided with a central horizontal channel to introduce rods of variable inner diameter for the location of detectors at different penetration depths.
  
- The neutron reaction rates of various detectors (calibrated micro-fission chambers and activation foils of different materials) are measured inside the block at different penetration depths, up to 65 cm.
  
- Gamma fluxes are also measured inside the block using ionization chambers and TLD as gamma detectors.

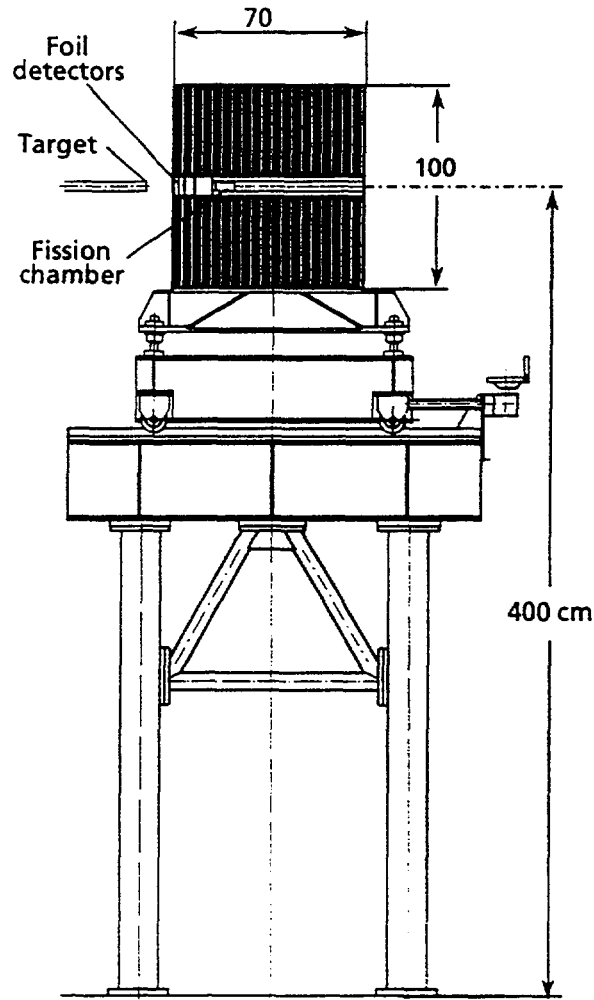


Fig. 1

## NEUTRON MEASUREMENTS INSIDE THE BLOCK

The activation technique has been employed to measure neutron reaction rates at seven different penetration depths inside the block, up to 60 cm.

Eight different activation reactions have been selected with different energy responses (fusion peak range, MeV range and slowing down range).

Micro fission chambers (provided by the CEA team) have also been employed for measurements inside the block. These are  $^{235}\text{U}$ ,  $^{238}\text{U}$ ,  $^{237}\text{Np}$  fission chambers, with a length of 8 cm and an external diameter of 8 mm. The fissile deposit is 2 cm long and the amount of fissile material is known within a few percent uncertainty.

### EXPERIMENTAL ERRORS

- Absolute source intensity	
Associated alpha-particle method	$< \pm 3.0 \%$
- Activation foils	
$\gamma$ -ray detector calibration	$\pm 2.0 \%$
Counting statistics for $z < 55$	$< \pm 5.0 \%$
for $z \geq 55$	$< \pm 16.0 \%$
- Micro fission chambers	
$^{235}\text{U}$ deposit mass	$\pm 2.0 \%$
$^{238}\text{U}$ deposit mass	$\pm 2.0 \%$
$^{237}\text{Np}$ deposit mass	$\pm 5.0 \%$
Counting statistics	$< \pm 3.0 \%$

Selected dosimetry reactions						
Reaction	Half-life	Isotopic abun- nd. (%)	$\gamma$ -ray energy (keV)	$\gamma$ -ray branching (%)	90% response range (MeV)	
$^{27}\text{Al}(n,\alpha)^{24}\text{Na}$	15.02h	100.0	1368.6	100.0	10 - 14	
$^{56}\text{Fe}(n,p)^{56}\text{Mn}$	2.579h	91.72	846.8	98.9	10 - 14	
$^{58}\text{Ni}(n,2n)^{57}\text{Ni}$	1.503d	68.26	1377.6	77.9	14	
$^{58}\text{Ni}(n,p)^{58}\text{Co}$	70.92d	68.26	810.8	99.5	2.9 - 14	
$^{115}\text{In}(n,n')^{115\text{m}}\text{In}$	4.486h	95.7	336.3	45.8	0.8 - 14	
$^{103}\text{Rh}(n,n')^{103\text{m}}\text{Rh}$	56.1m	100.0	20.-22.7	7.66	0.3 - 14	
$^{55}\text{Mn}(n,\gamma)^{56}\text{Mn}$	2.579h	100.0	846.8	98.9	0.00017- 0.06	
$^{197}\text{Au}(n,\gamma)^{198}\text{Au}$	2.694d	100.0	411.8	87.0	0.00015- 0.3	

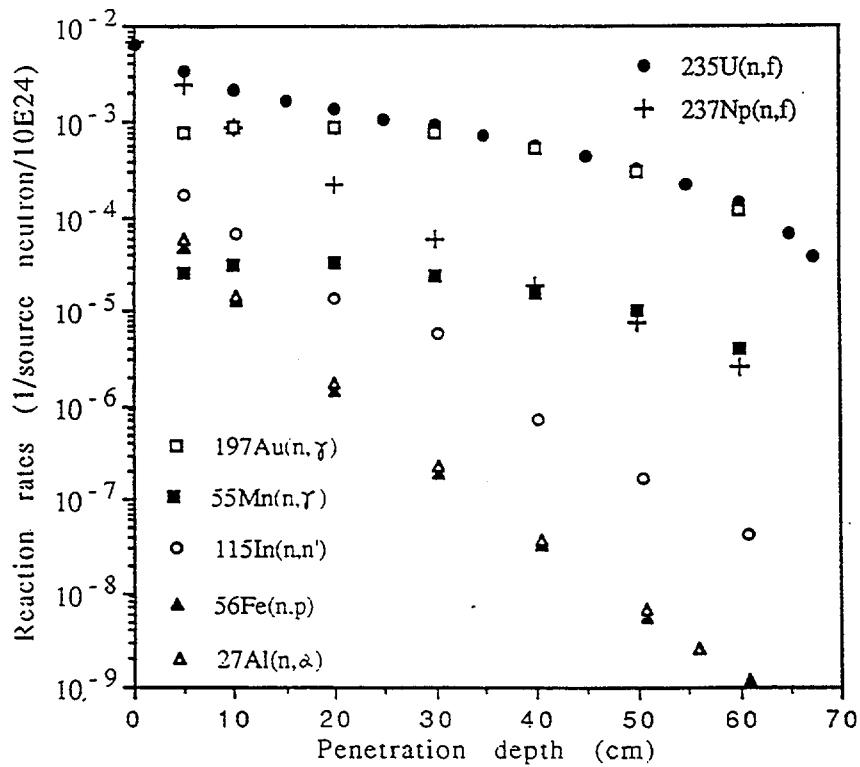


Fig.1

## MCNP CALCULATIONS

The analytical interpretation of the experimental measurements has been carried out by means of the MCNP.4 code. This Monte Carlo code allows for an adequate representation of the experimental features and an accurate treatment of the neutron transport with continuous cross sections.

The transport cross sections have been originated from EFF.1

The energy and angular distributions of the neutron source have been accurately represented, taking into account the reaction kinematics and the energy loss of the deuteron beam in the tritium-titanium target.

A very stressed variance reduction was required to improve the statistical accuracy for the the deep penetration and the slowing down effects.

The representation of the exact activation foil geometry was requested for the low energy detectors (Au and Mn) for which the resonant self absorption effects are quite significant.

The configuration of the micro-fission chambers, as well as the extention and the location of the fissile deposit, has also been described in a dedicated MCNP model.

The room background contribution at the detector positions has been estimated by a separate MCNP model, including the whole experimental environment and the bunker walls. This contribution is negligible at any neutron energy beyond a 7 cm depth inside the block.

For all the calculated responses, the relative standard deviation due to calculation statistics ranges from 1 to 4%.

The activation and fission reaction cross sections were taken from the International Reactor Dosimetry File IRDF-90.

The uncertainties on calculated reaction rates due to the uncertainty on activation cross sections have been calculated from IRDF-90 covariance data and taken into account.

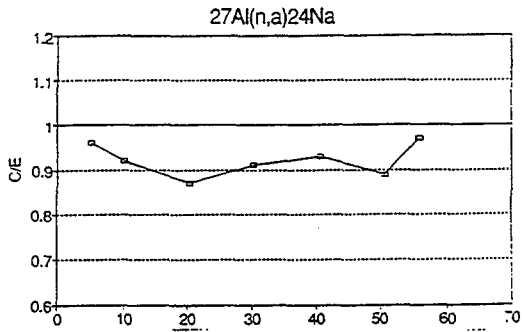
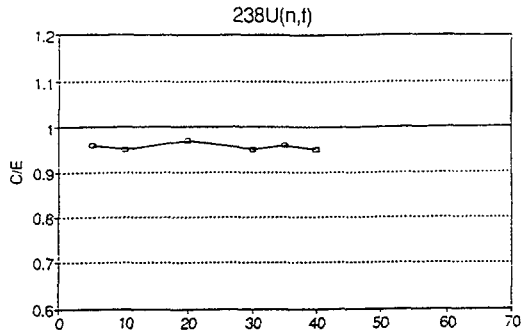
## C/E COMPARISON

The analysis performed with MCNP + EFF1 shows that the C/E ratios of the calculated over the measured reaction rates are generally close to unity.

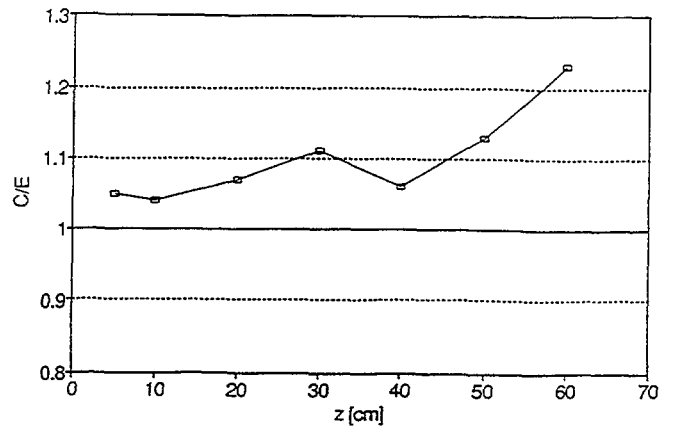
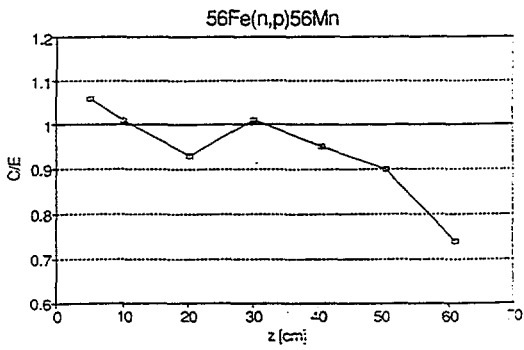
The uncertainties on C/E values, obtained summing quadratically the individual errors on C and on E values, are generally smaller than  $\pm 7\%$ , with the only exception of  $^{55}\text{Mn}(n,\gamma)$  ( $\pm 11\%$  at any position) and for  $^{27}\text{Al}(n,\alpha)$  ( $\pm 10\%$ ) and  $^{56}\text{Fe}(n,p)$  ( $\pm 16\%$ ) measurements for  $z > 55$  cm.

These uncertainties are larger or comparable with the corresponding (C/E-1) differences for detectors sensible to fast neutrons,  $^{27}\text{Al}(n,\alpha)$  and  $^{56}\text{Fe}(n,p)$ , and for detectors sensible to thermal neutrons,  $^{55}\text{Mn}(n,\gamma)$ ,  $^{197}\text{Au}(n,\gamma)$  and  $^{235}\text{U}(n,f)$ .

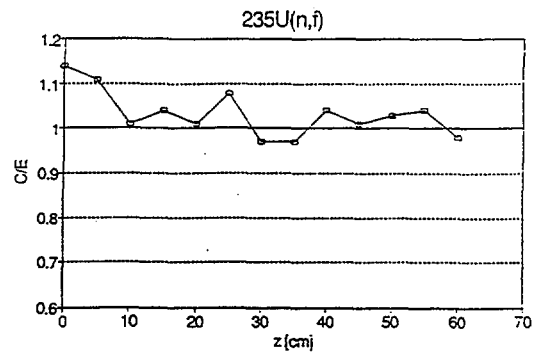
At intermediate neutron energy however, the C/E values for  $^{115}\text{In}(n,n')$  and for  $^{237}\text{Np}(n,f)$  show a trend of increasing departure from unity with increasing penetration depth, the discrepancies being larger than the total errors.



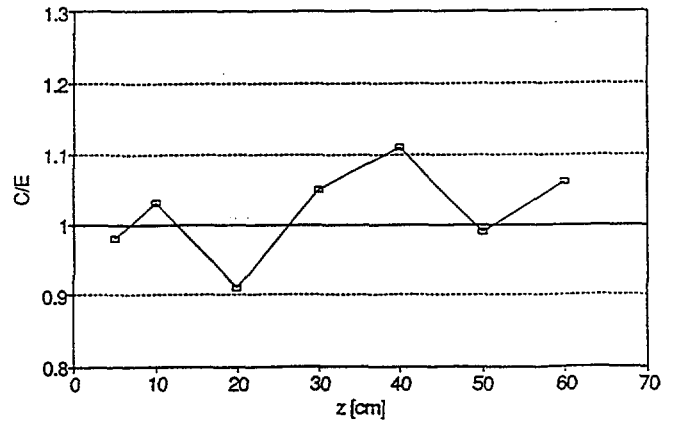
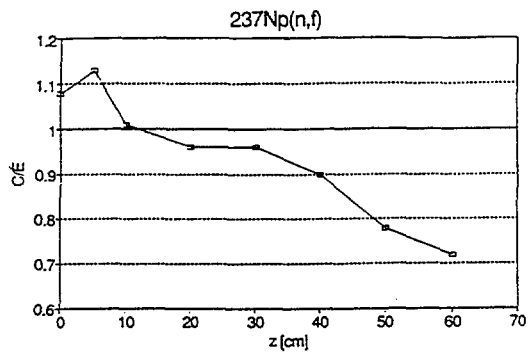
MCNP



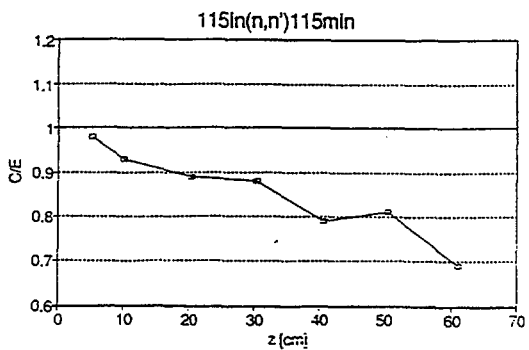
MCNP



MCNP



MCNP



MCNP

## CONCLUSIONS

The ENEA/CEA bulk shield experiment is almost completed. Many neutron and gamma flux measurements have been performed at different penetration depths inside the block up to 65 cm, providing an accurate experimental data base.

More experimental work is in progress to complete activation measurements employing  $^{103}\text{Rh}(n,n')$ ,  $^{58}\text{Ni}(n,2n)$  and  $^{58}\text{Ni}(n,p)$  reactions.

The C/E comparison generally confirms the validity of the EFF.1 library for shielding design calculations.

However, a discrepancy between measured and calculated reaction rates has been found for detectors sensible to  $\sim$ MeV energy neutrons.

This discrepancy may be due to an inadequate treatment of the Fe cross section in the region of the unresolved resonances or to the Fe inelastic cross section.

The analysis of the C/E values is currently in progress by the CEA team by sensitivity and uncertainty analysis.

The numerical analysis will be extended to the new version of the European Fusion File EFF.2 as soon as it will be available.



## **Fusion Integral Experiments at FNS**

**Y. Oyama**

**Japan Atomic Energy Research Institute**

**IAEA Consultants' Meeting  
on  
Preparation of Fusion Benchmarks in Electronic Format  
for Nuclear Data Validation Studies**

**December 13-16, 1993**

**IAEA Headquarters in Vienna, Austria**

## FUSION INTEGRAL EXPERIMENTS

---

### Two Categories of Experiments

1. Clean Benchmark
2. Engineering Benchmark

#### Clean Benchmark

- Nuclear data validation
- Simple geometry
- Simple material Configuration

Measured parameters are related to cross section, e.g., spectrum, reaction rate

But measured parameters are integrated in space, angle, and energy.

Integrated measurement will reduce the uncertainty from differential parameters

## FUSION INTEGRAL EXPERIMENTS (continued)

---

#### Engineering Benchmark

- Validation for nuclear calculation code, modeling
- Fusion reactor environment simulation for geometry and material configuration

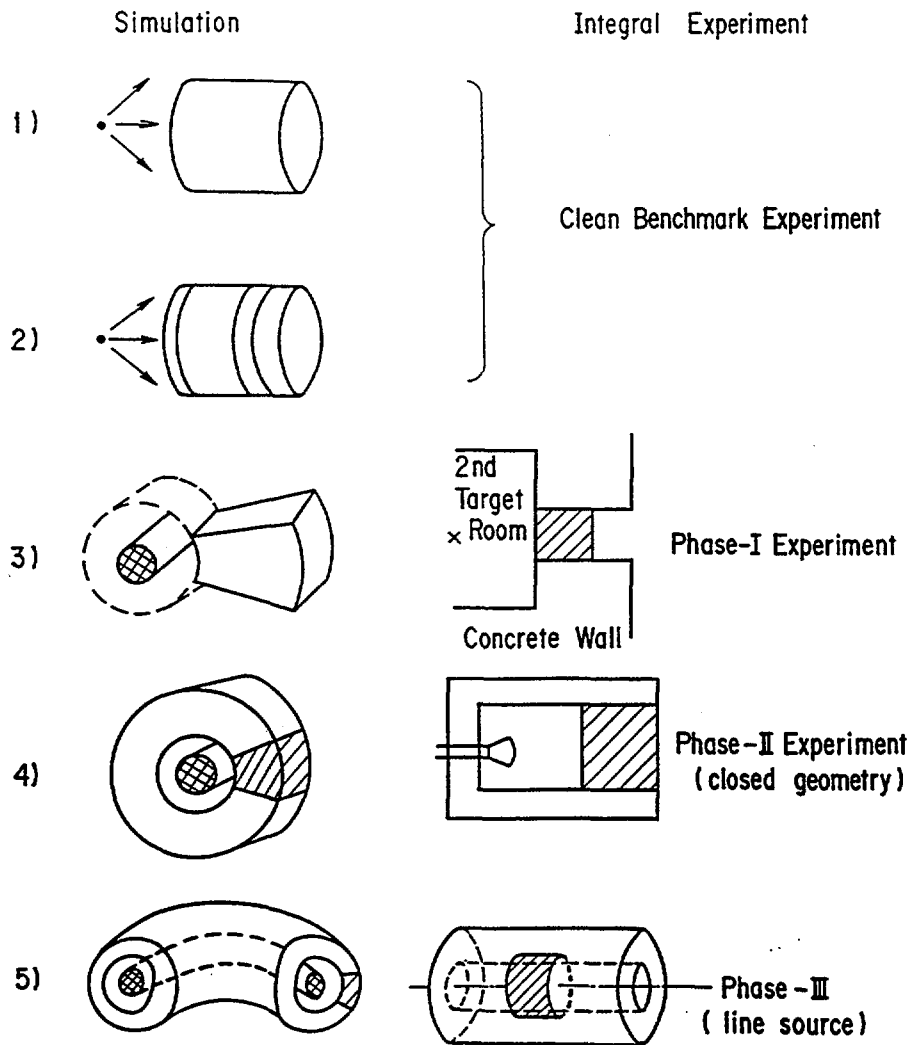
Measured parameters are key quantities in reactor design, e.g.,

- Tritium breeding ratio  
(tritium production rate from both  ${}^6\text{Li}$  and  ${}^7\text{Li}$ )
- Nuclear heating rate, dose rate, damage rate

Measured parameters are also integrated in space, angle and energy, and material

Experiments should include typical complexity for modeling verification

## Stages of Integral Experiment



## CLAEN BENCHMARK EXPERIMENTS at FNS

Before FNS construction with small neutron source of  $\sim 10^{10}$  n/s

FNS completed in 1982

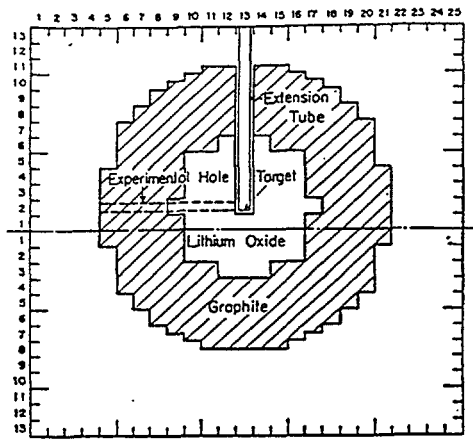
### Sphere Experiments (1974~1979)

- Li, Li-C, Li-U-C, Li<sub>2</sub>O-C Blankets in pseudo-spherical assemblies similar to critical assembly geometry

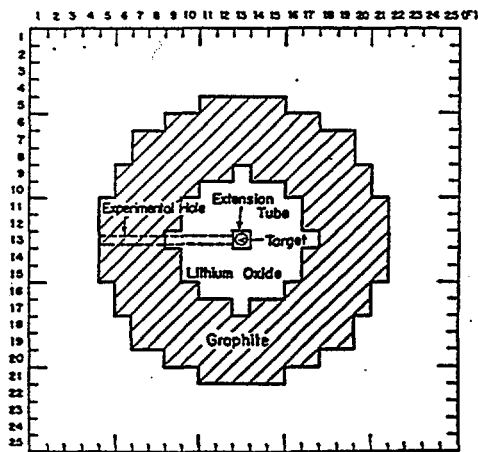
Fission reaction rate measurements

Too much approximation for sphere by blocks

--> Slab geometry



(a) Horizontal section



(b) Vertical section

Fig.2.1 Horizontal and vertical sections across the center of  $\text{Li}_2\text{O-C}$  experimental assembly.

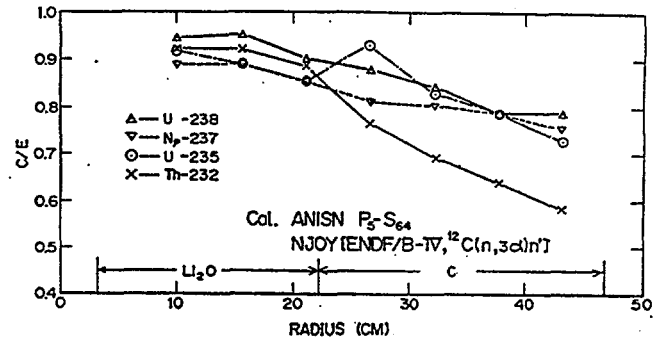


Fig.1.1 Comparison of the calculated and experimental result for  $\text{Li}_2\text{O-C}$  assembly.

## CLAEN BENCHMARK EXPERIMENTS (continued)

After FNS construction with  $10^{11} \sim 10^{12}$  n/s  
and pulse operation with 2 ns

### Slab Experiments (1982~ 1993)

- In-system neutron response

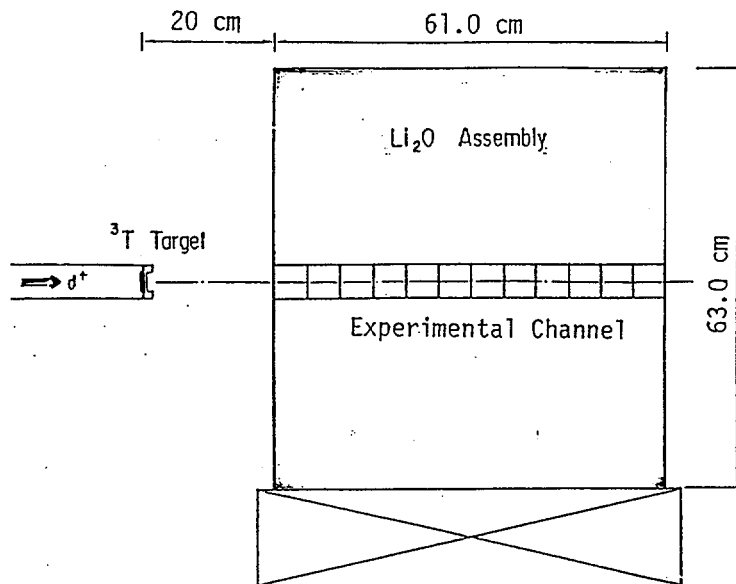
$\text{Li}_2\text{O}$ , C, Be, W, Fe, Cu

Neutron spectrum, Activation reaction rate  
Fission reaction rate

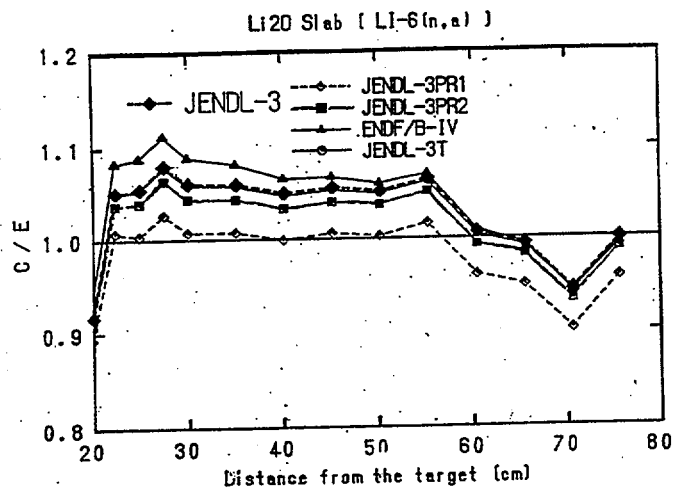
- In-system gamma-ray response (1991~)

$\text{Li}_2\text{O}$ , C, Be, W, Fe, Cu

Gamma-ray spectrum, Gamma-ray heating



Experimental Arrangement



## CLAEN BENCHMARK EXPERIMENTS (continued)

### Slab-TOF Experiment (1983~1990)

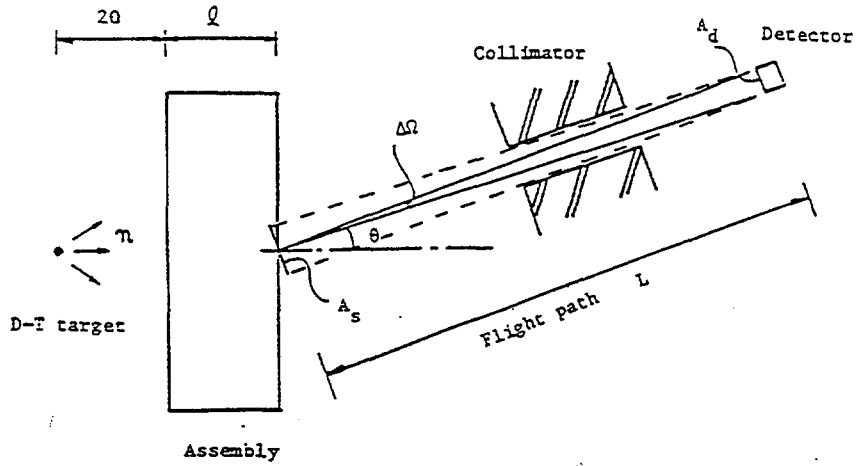
- Angular neutron flux on slab

Li,  $\text{Li}_2\text{O}$ , C, Be, Fe, Pb,  $\text{Lq.N}_2$ ,  $\text{Lq.O}_2$

Relation to DDX,  
Angle-energy integration by neutron transport

Validation for both nuclear data library and code

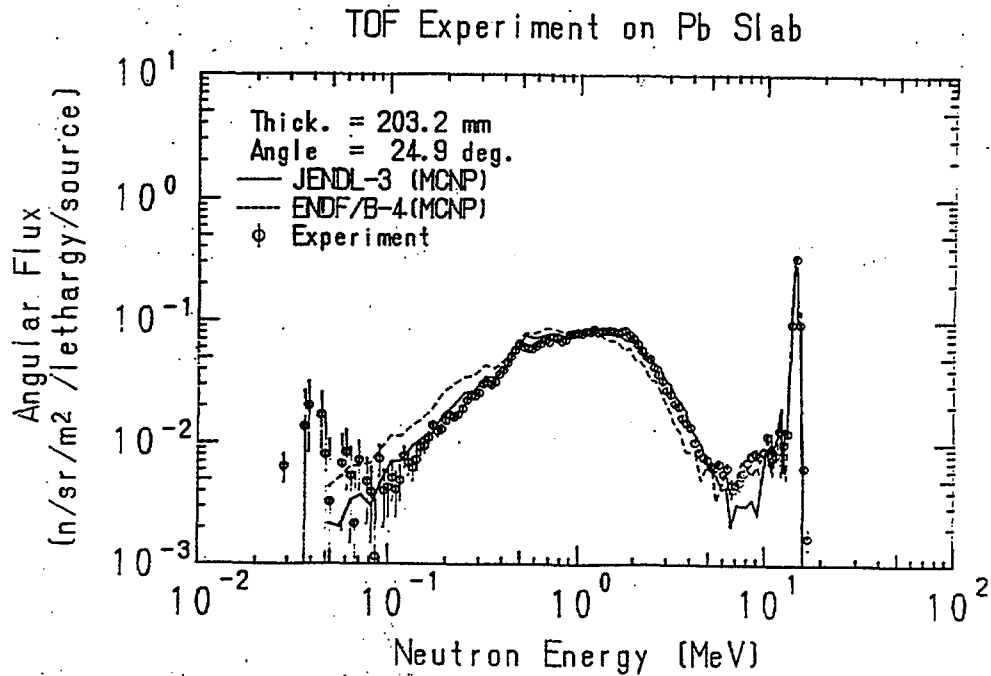
Interconnection from DDX to integral results



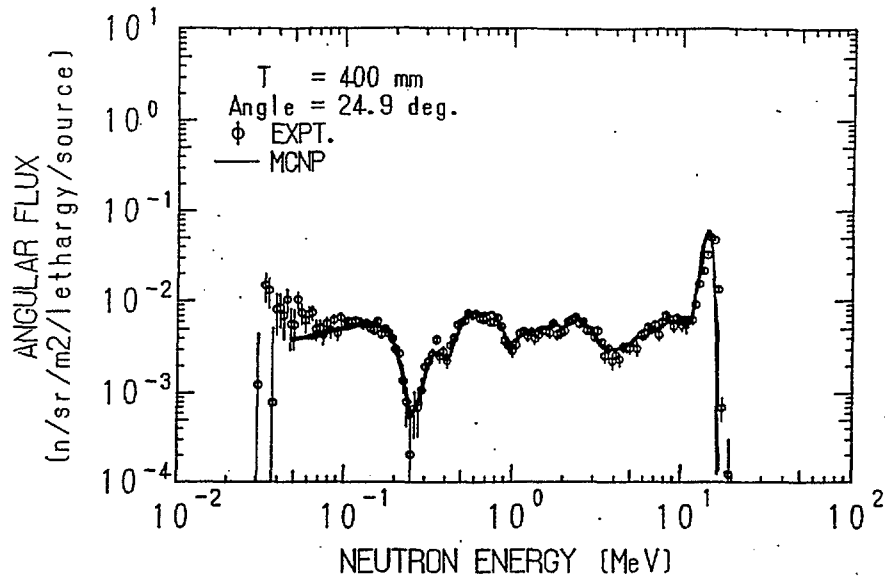
$$\Phi(r=0, z=20+t, \theta, E_n) = \frac{C(E_n)}{\epsilon(E_n) \cdot \Delta\Omega \cdot A_s \cdot S_n \cdot T(E)}$$

[n/sr/cm<sup>2</sup>/unit lethargy/source neutron]

- $C(E_n)$  : counts per unit lethargy for neutrons of energy  $E_n$
- $\epsilon(E_n)$  : detector efficiency for neutrons of energy  $E_n$
- $\Delta\Omega_n$  : solid angle subtended by the detector at a point on surface of assembly ( $\cong A_d/L^2$ )
- $A_s$  : area defined by the collimator on the vertical plane to the central axis at the surface of assembly
- $S_n$  : neutron yield
- $T(E)$  : attenuation by air



## Lithium-Oxide ( JENDL-3 )



## ENGINEERING BENCHMARK EXPERIMENTS at FNS

### JAERI/USDOE Collaboration (1984~1993)

- Engineering oriented experiment to confirm  
Tritium Breeding Issue

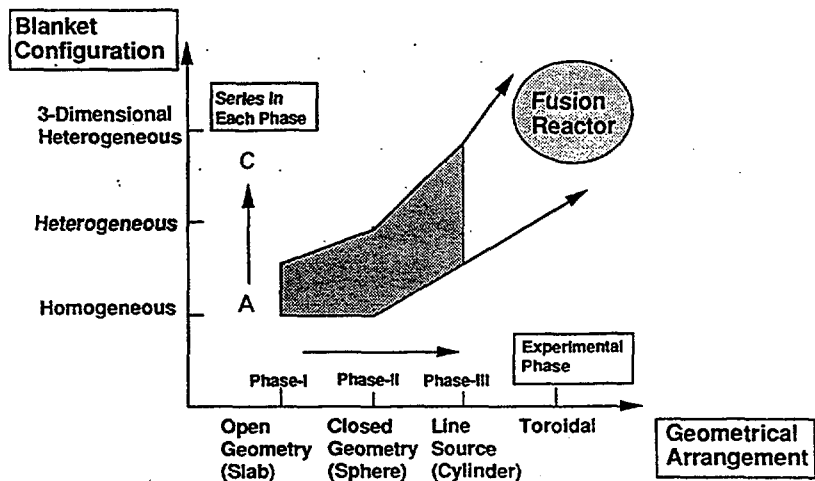
Li<sub>2</sub>O breeding blanket with Be neutron multiplier

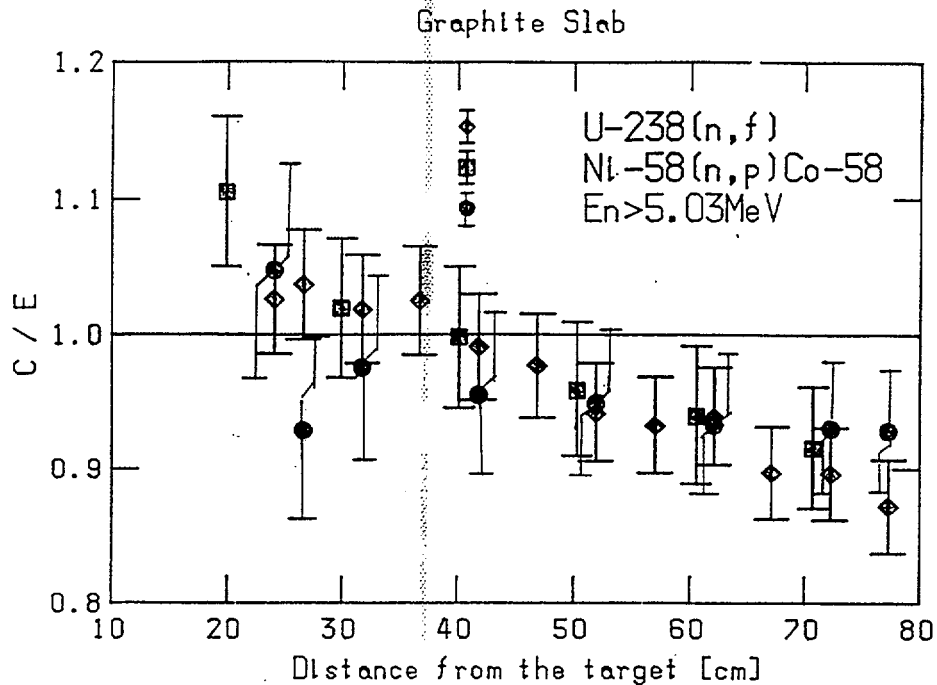
Three stages of fusion reactor simulation  
Slab-like, Sphere-like and Annular blankets  
for toroidal simulation

Tritium production rate measurement

Derivation of safety factor for prediction of design  
calculation from the joint experiments

### Stratage for Simulation of Fusion Reactor





## EXPERIMENTAL DATA HANDLING PRINCIPLE AT FNS

---

### Modeling

- give homogenized densities and region
- point data assumed for measured quantity unless special definition is made
- experimental error or correction includes the error for assumption of point data, e.g., self-shielding, void, averaging
- measurement channel is modeled based on experimental setup

### Data format

- format fits for a plot program, e.g., Kaleida Graph on Machintosh or a plot program on VAX WS
- data are presented so as to correspond to the calculated one, e.g., angular neutron flux, scalar flux, reaction rate, heating rate (erg/g)

## Collection of Experimental Data for Fusion Neutronics Benchmark

## Titles of Experiments and Authors:

1. Tritium Breeding Ratio in Li, Pb-Li, Pb-Li-C, Be-Li, Be-Li-C, Spheres Measured with Pellets and/or LiF TLDs.  
T. Iguchi, M. Nakazawa, J. Cetnar, K. Sugiyama, A. Takahashi and K. Sumita
- ② Measurement of Leakage Spectrum from Beryllium Sphere and Beryllium-Lithium Sphere  
Y. Murakami, K. Yoshioka, K. Yamada, A. Takahashi and K. Sumita
- ③ Gamma-ray Energy Spectra Emitted from Spheres with 14 MeV Neutron Source  
J. Yamamoto, T. Kanaoka, I. Murata, A. Takahashi and K. Sumita
- ④ Numerical Data of Leakage Neutron Spectra from Various Sphere Piles with 14 MeV Neutrons  
C. Ichihara, K. Kobayashi, S. A. Hayashi, I. Kimura, J. Yamamoto and A. Takahashi
5. Angular Neutron Flux Spectra Leaking from Slabs (I)  
Y. Oyama and H. Maekawa
6. Integral Experiment on Graphite Cylindrical Assembly  
H. Maekawa et al.
7. Integral Experiment on Li<sub>2</sub>O Cylindrical Assembly  
H. Maekawa et al.
8. Integral Experiment on Beryllium Cylindrical Assembly  
H. Maekawa et al.

	1	2	3	4	5	6	7	8	9
Title	○	○	○	○	○	○	○		
Authors	○	○	○	○	○	○	○		
Organization	○	○	○	○	○	○	○		
Facility	○	○	○	○	○	○	○		
Date	○	○	○	○	○	○	○		
Measured Quantity	○	○	○	○	○	○	○		
Experimental Method	○	○	○	○	○	△	△		
Neutron Source Characteristics	○	○	○	○	○	○	○		
Material/Geometry/Configuration	○	○	○	○	○	○	○		
Experimental Data with Errors	○	○	○	○	○	○	○		
Error Assessment	○	○	○	○	○	△	△		
References	○	○	○	○	○	○	○		
Description of Data Treatment	○	○	○	○	○	△	△		
Comments and So Forth	×	×	○	×	×	×	×		
Nuclear Data File to be Referred	○	○	○	○	×	×	×		
Example of Analysis	×	○	○	○	△	△	△		

Table 5.1 Dimensions of the slabs.

Material	Geometry	Size	Thickness
Beryllium	Pseudo-Cylinder	Effective Radius: 314 mm	50.8, 152.4 mm
Carbon	"	"	50.6, 202.4, 404.8 mm
Lithium Oxide	"	"	48, 200, 400 mm
Lead	"	"	50.8, 203, 406 mm
Iron	Cylinder	Radius: 500 mm	50, 200, 400, 600 mm

Measuring angles: 0, 12.2, 24.9, 41.8 and 66.8 degree

Table 5.2 Flight path as a function of slab thickness and angle.

Angle	Slab thickness				
	48(50.6,50.8)	152.4	200(202.4)	400(404.8)	600
0	738 cm	728	723	703	683
12.2	---	729	724	704	684
24.9	740	731	726	708	689
41.8	744	736	732	716	700
66.8	753	748	746	736	725

Table 5.3 Chemical composition and atomic densities.

Material	Atomic densities atoms/cm <sup>3</sup>	
Graphite		
C	8.280 x 10 <sup>22</sup>	
Beryllium		
Be	1.215 x 10 <sup>23</sup>	
Lithium Oxide		
<sup>7</sup> Li	5.338 x 10 <sup>22</sup>	(5.371 x 10 <sup>22</sup> )*
<sup>6</sup> Li	4.278 x 10 <sup>21</sup>	(4.304 x 10 <sup>21</sup> )*
O	2.883 x 10 <sup>22</sup>	(2.901 x 10 <sup>22</sup> )*
Fe	1.557 x 10 <sup>21</sup>	(1.098 x 10 <sup>21</sup> )*
Ni	1.837 x 10 <sup>20</sup>	(1.295 x 10 <sup>20</sup> )*
Cr	4.223 x 10 <sup>20</sup>	(2.977 x 10 <sup>20</sup> )*
Mn	3.309 x 10 <sup>19</sup>	(2.333 x 10 <sup>19</sup> )*
Lead		
Pb	3.2874 x 10 <sup>22</sup>	
Iron		
Fe	8.3699 x 10 <sup>22</sup>	
Mn	7.1857 x 10 <sup>20</sup>	
C	7.2906 x 10 <sup>20</sup>	
Si	2.8132 x 10 <sup>19</sup>	
Cr	1.7024 x 10 <sup>19</sup>	
Al	2.7944 x 10 <sup>19</sup>	
Ni	1.1200 x 10 <sup>19</sup>	

\* for 200 and 400 mm-thick slabs

4  
Table 5. Mid energy of measured spectra for lithium oxide experiment.

0.11629E-01	0.12225E-01	0.12852E-01	0.13511E-01	0.14203E-01	0.14932E-01
0.15697E-01	0.16502E-01	0.17348E-01	0.18238E-01	0.19173E-01	0.20156E-01
0.21189E-01	0.22275E-01	0.23418E-01	0.24618E-01	0.25880E-01	0.27207E-01
0.28602E-01	0.30069E-01	0.31610E-01	0.33231E-01	0.34935E-01	0.36726E-01
0.38609E-01	0.40589E-01	0.42670E-01	0.44857E-01	0.47157E-01	0.49575E-01
0.52117E-01	0.54789E-01	0.57598E-01	0.60551E-01	0.63656E-01	0.66919E-01
0.70350E-01	0.73957E-01	0.77749E-01	0.81735E-01	0.85926E-01	0.90332E-01
0.94963E-01	0.99832E-01	0.10495E+00	0.11033E+00	0.11599E+00	0.12193E+00
0.12819E+00	0.13476E+00	0.14167E+00	0.14893E+00	0.15657E+00	0.16459E+00
0.17303E+00	0.18191E+00	0.19123E+00	0.20104E+00	0.21134E+00	0.22218E+00
0.23357E+00	0.24555E+00	0.25814E+00	0.27137E+00	0.28528E+00	0.29991E+00
0.31529E+00	0.33145E+00	0.34845E+00	0.36631E+00	0.38509E+00	0.40484E+00
0.42559E+00	0.44742E+00	0.47035E+00	0.49447E+00	0.51982E+00	0.54647E+00
0.57449E+00	0.60395E+00	0.63491E+00	0.66747E+00	0.70169E+00	0.73766E+00
0.77548E+00	0.81524E+00	0.85704E+00	0.90098E+00	0.94718E+00	0.99574E+00
0.10468E+01	0.11005E+01	0.11569E+01	0.12162E+01	0.12786E+01	0.13441E+01
0.14130E+01	0.14855E+01	0.15616E+01	0.16417E+01	0.17259E+01	0.18144E+01
0.19074E+01	0.20052E+01	0.21080E+01	0.22161E+01	0.23297E+01	0.24491E+01
0.25747E+01	0.27067E+01	0.28455E+01	0.29914E+01	0.31447E+01	0.33060E+01
0.34755E+01	0.36537E+01	0.38410E+01	0.40379E+01	0.42450E+01	0.44626E+01
0.46914E+01	0.49319E+01	0.51848E+01	0.54506E+01	0.57301E+01	0.60239E+01
0.63327E+01	0.66574E+01	0.69988E+01	0.73576E+01	0.77348E+01	0.81314E+01
0.85483E+01	0.89866E+01	0.94473E+01	0.99317E+01	0.10441E+02	0.10976E+02
0.11539E+02	0.12131E+02	0.12753E+02	0.13406E+02	0.14094E+02	0.14816E+02
0.15576E+02	0.16375E+02	0.17214E+02	0.18097E+02	0.19025E+02	0.20000E+02

5  
Table 5. Source neutron spectrum for lithium oxide experiment.

<< Spectrum >>

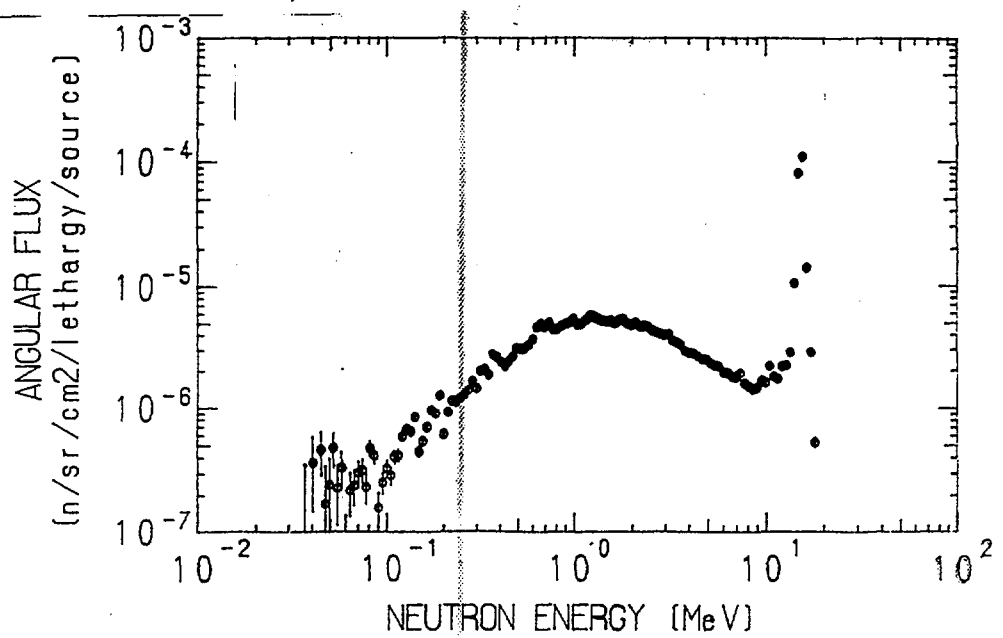
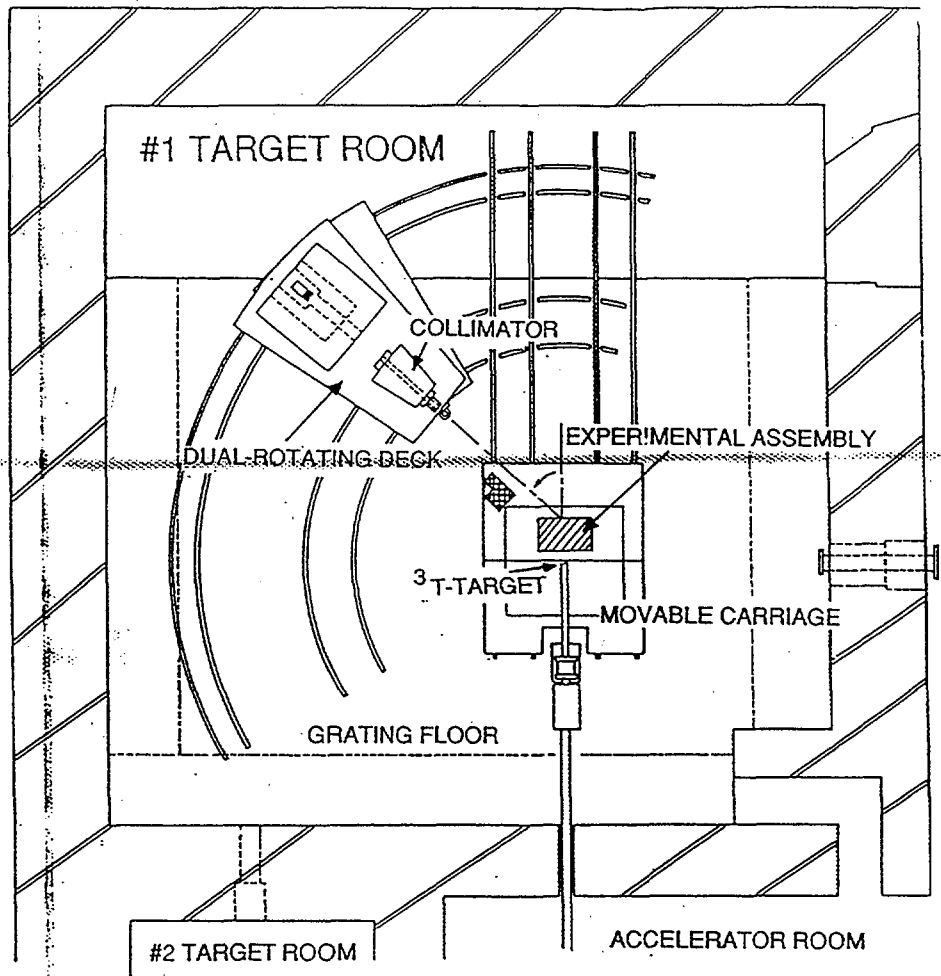
0.00000E+00	0.00000E+00	0.00000E+00	0.00000E+00	0.00000E+00	0.00000E+00
0.00000E+00	0.00000E+00	0.00000E+00	0.00000E+00	0.00000E+00	0.00000E+00
0.00000E+00	0.00000E+00	0.00000E+00	0.00000E+00	0.00000E+00	0.00000E+00
0.00000E+00	0.00000E+00	0.00000E+00	0.38843E-04	-0.23326E-03	-0.40772E-03
-0.38707E-03	-0.22803E-03	-0.22690E-03	-0.43178E-03	-0.33428E-03	-0.10290E-03
-0.19368E-03	-0.15603E-03	-0.24334E-03	-0.12879E-03	-0.11297E-03	-0.84896E-04
0.14694E-04	0.13582E-06	-0.25100E-04	-0.23554E-04	0.13008E-04	0.28749E-04
0.36420E-04	0.24219E-04	0.46619E-04	0.68370E-04	0.52588E-04	0.45198E-04
0.79750E-04	0.13229E-03	0.11647E-03	0.83708E-04	0.10510E-03	0.11641E-03
0.10924E-03	0.15439E-03	0.17258E-03	0.14427E-03	0.19349E-03	0.22872E-03
0.22715E-03	0.27335E-03	0.32231E-03	0.29709E-03	0.31727E-03	0.39820E-03
0.35119E-03	0.47096E-03	0.47510E-03	0.46600E-03	0.48809E-03	0.52999E-03
0.55491E-03	0.55844E-03	0.65924E-03	0.67612E-03	0.72404E-03	0.84729E-03
0.84034E-03	0.90638E-03	0.99356E-03	0.10156E-02	0.10042E-02	0.10911E-02
0.12193E-02	0.11338E-02	0.12103E-02	0.12633E-02	0.13734E-02	0.13767E-02
0.14881E-02	0.15126E-02	0.14865E-02	0.14711E-02	0.15725E-02	0.15354E-02
0.15752E-02	0.15751E-02	0.15728E-02	0.16819E-02	0.14839E-02	0.16390E-02
0.15652E-02	0.16129E-02	0.15268E-02	0.14327E-02	0.14975E-02	0.15326E-02
0.14350E-02	0.16907E-02	0.19937E-02	0.22590E-02	0.28919E-02	0.24352E-02
0.13675E-02	0.12826E-02	0.11295E-02	0.11129E-02	0.11243E-02	0.94764E-03
0.96315E-03	0.10080E-02	0.94194E-03	0.85143E-03	0.85572E-03	0.73651E-03
0.67772E-03	0.64803E-03	0.66015E-03	0.55770E-03	0.49315E-03	0.50626E-03
0.55392E-03	0.58301E-03	0.71392E-03	0.86232E-03	0.10749E-02	0.13009E-02
0.14618E-02	0.26726E-02	0.38429E-02	0.49230E-02	0.42123E-01	0.72069E+00

<< Error >>

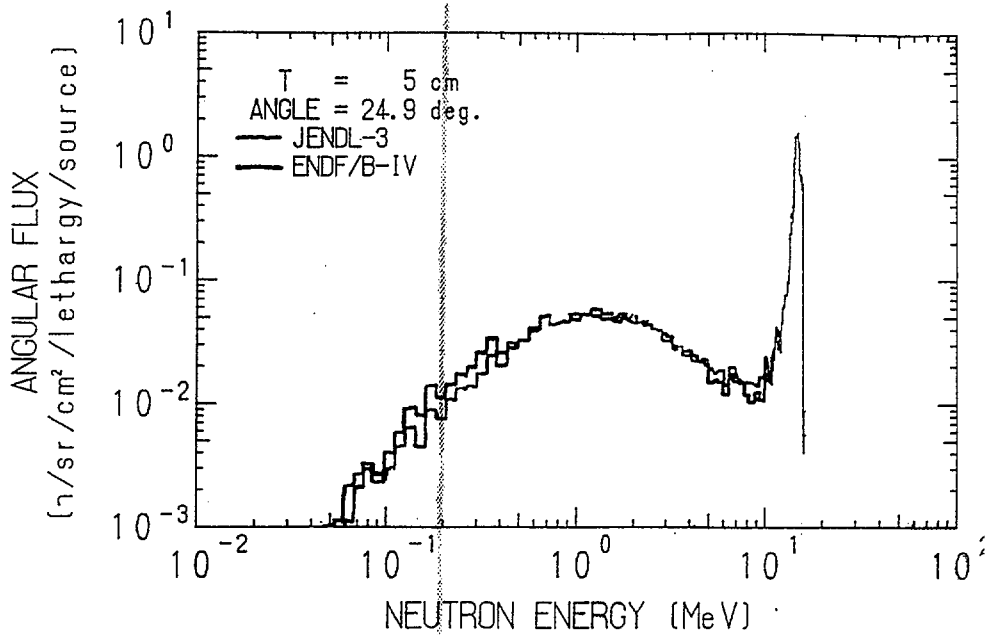
0.75202E+00	0.10665E+00	0.68642E-02	0.18478E-02	0.10033E-02	0.61280E-03
0.10000E+01	0.10000E+01	0.10000E+01	0.10000E+01	0.10000E+01	0.10000E+01
0.10000E+01	0.10000E+01	0.10000E+01	0.10000E+01	0.10000E+01	0.10000E+01
0.10000E+01	0.10000E+01	0.10000E+01	0.10000E+01	0.10000E+01	0.10000E+01
0.10000E+01	0.10000E+01	0.10000E+01	0.65202E+01	0.10844E+01	0.60055E+00
0.53903E+00	0.82295E+00	0.76646E+00	0.35929E+00	0.44942E+00	0.12900E+01
0.59629E+00	0.66016E+00	0.38481E+00	0.59723E+00	0.65474E+00	0.76332E+00
0.39013E+01	0.37272E+03	0.20169E+01	0.20545E+01	0.33264E+01	0.13957E+01
0.10988E+01	0.15605E+01	0.75778E+00	0.48421E+00	0.63129E+00	0.72026E+00
0.38153E+00	0.22786E+00	0.24160E+00	0.33078E+00	0.25070E+00	0.23318E+00
0.24786E+00	0.17150E+00	0.14846E+00	0.18106E+00	0.13468E+00	0.11681E+00
0.11486E+00	0.97837E-01	0.81690E-01	0.94555E-01	0.85082E-01	0.70162E-01



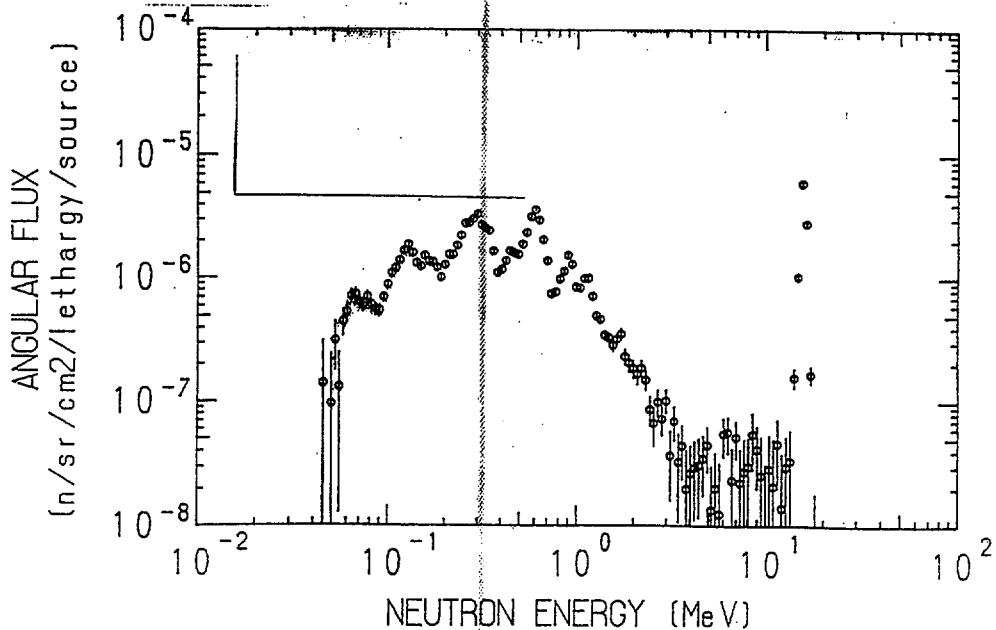
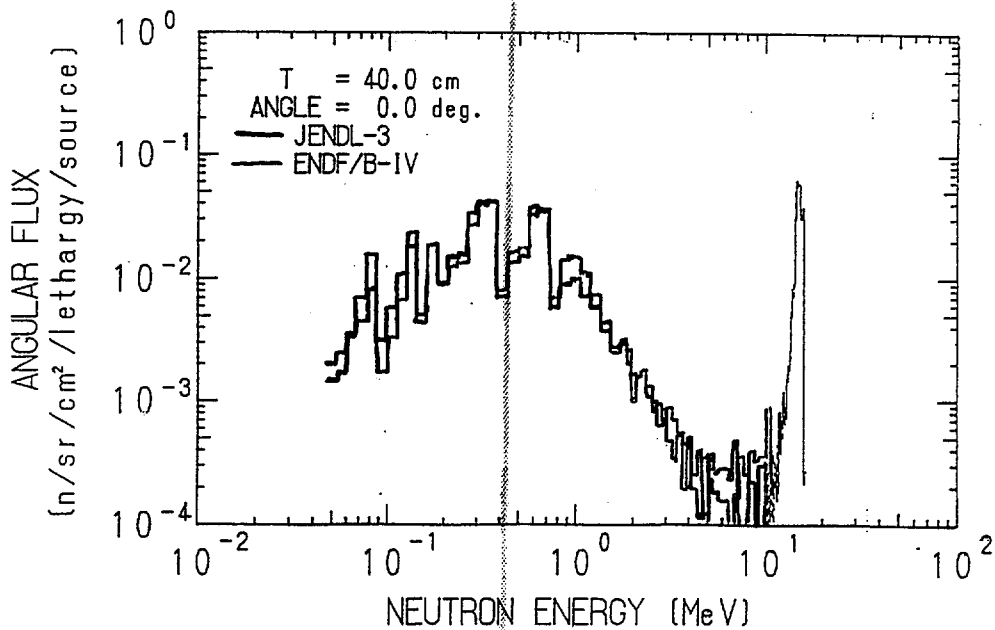
## Experimental Arrangement



Fe, MCNP-CAL.



Fe, MCNP-CAL.



20970

```

C
C          FLUX.RJE ( GRP69.DAT/GRP72.DAT , WEIGHT.DAT )
C
C S=0 ----> R=1      24 TABLES
C S=1 ----> R=AVE.    8 TABLES
C S=2 ----> R=BOTH   32 TABLES
C
C $RJE FLUX ----> QMTOVAX ----> *PLOTTER*
C
C PARAMETER (IGMAX=176, LANGMX=160, IMAX=50)
C -----(( IGMAX IS MAXIMUM OF GROUP NUMBER ))
C -----(( LANGMX IS MAXIMUM OF ANGULAR QUADRATURE ))
C -----(( IMAX IS MAXIMUM OF IM MESH ))
C DIMENSION ENERGY(IGMAX), ELETH(IGMAX), WEIGHT(80),
* W(LANGMX), CUTAFL(IMAX, LANGMX), FL(LANGMX),
* FLX(6, LANGMX, IGMAX), FLUX(6, 10, IGMAX),
* FLMAX(6, 10, IGMAX), FLMIN(6, 10, IGMAX),
* R(IMAX), RFLUX(10, IGMAX), ANGLE(10)
C REMIND 9
C READ(5,500) IGRP, IM, JM, IO3, MM, NFLSV, IOPT, IS
C READ(5,501) RSIZE
C READ(5,502) (ANGLE(M), M=1,8)
C IGRP1=IGRP+1
C READ(5,503) (ENERGY(L), L=1, IGRP1)
C READ(5,504) (WEIGHT(K), K=1,80)
C 500 FORMAT(8I5)
C 501 FORMAT(1H ,F8.2)
C 502 FORMAT(1H ,F8.2)
C 503 FORMAT(6E12.5)
C 504 FORMAT(5E14.7)
C DO 5 KK=1,80
C K=KK*80
C W(K)=WEIGHT(KK)
C 5 CONTINUE
C DO 6 J=1,IM
C *** FOR NON UNIFORM MESH (FE) *****
C RSIZE=20.0
C IM0=20
C DO 6 J=1,IM0
C
C R(J)=RSIZE*(FLOAT(J)-0.5)/FLOAT(IM)
C R(J)=RSIZE*(FLOAT(J)-0.5)/FLOAT(IM0)
C 6 CONTINUE
C
C IDUM=IM*JM+IM*JM*(IO3*(IO3+3))/2+MM*JM
C DO 10 L=1, IGRP
C ELETH(L)=LOG(ENERGY(L)/ENERGY(L+1))
C READ(9) (DUM,I=1, IDUM), ((CUTAFL(J,K), K=1,MM), J=1, IM)
C DO 20 J=1,5
C DO 20 K=81,160
C *** WHEN SOURCE NORMALIZATION IS IN /APAI *****
C FLX(J,K,L)=CUTAFL(J,K)/(4.0*3.14159*ELETH(L))
C *** WHEN SOURCE NORMALIZATION IS IN /SR *****
C FLX(J,K,L)=CUTAFL(J,K)/ELETH(L)
C *****
C 20 CONTINUE
C DO 30 J=1,5
C K1=81
C K2=83
C DO 40 M=1,8
C U=0.
C V=0.
C FLMAX(J,M,L)=-1.
C FLMIN(J,M,L)=1.
C K0=K1+1

```

9 番 = output assign

127	35	125	5	160	9	1	2
50.0							
12.2	24.9	33.9	41.8	49.5	57.5	65.8	81.4
0.16487+08	0.16231+08	0.15980+08	0.15732+08	0.15488+08	0.15248+08	0.15008+08	0.14768+08
0.15012+08	0.14779+08	0.14550+08	0.14324+08	0.14102+08	0.13883+08	0.13668+08	0.13456+08
0.12445+08	0.12252+08	0.12062+08	0.11875+08	0.11691+08	0.11510+08	0.11331+08	0.11156+08
0.10317+08	0.10157+08	1.00000+7	9.51229+6	9.04837+6	8.60708+6	8.18731+6	7.78801+6
6.37628+6	6.06531+6	5.78950+6	5.48812+6	5.22046+6	4.96785+6	4.72367+6	4.49329+6
4.72367+6	4.49329+6	4.06570+6	3.67879+6	3.32871+6	3.16637+6	3.01194+6	2.86505+6
2.36525+6	2.34570+6	2.30686+6	2.23130+6	2.12248+6	2.01897+6	1.92050+6	1.82684+6
1.42274+6	1.35335+6	1.28735+6	1.22456+6	1.16484+6	1.10803+6	1.05259+6	1.00259+6
7.42736+5	7.06512+5	6.72055+5	6.39279+5	6.08101+5	5.78444+5	5.50232+5	5.23397+5
3.68832+5	3.33733+5	3.01974+5	2.98491+5	2.97211+5	2.94518+5	2.87247+5	2.73237+5
2.02419+5	1.92547+5	1.83156+5	1.74224+5	1.65727+5	1.57644+5	1.49956+5	1.42642+5
1.11090+5	9.80366+4	8.65169+4	8.25034+4	7.94987+4	7.69991+4	7.47379+4	7.26522+4
0.9768061E-02							
0.6463375E-02							
0.5038980E-02							
0.3634186E-02							
0.2438095E-02							
0.1438095E-02							
0.08463375E-02							
0.0000000E-02							

<< Explanation of the Input Data >>

- IGRP, IM, JM, IO3, MM, NFLSV, IOPT, IS
- RSIZE
- (ANGLE(M), M=1,8)
- (ENERGY(L), L=1, IGRP1)
- (WEIGHT(K), K=1,80)
- IGRP : Number of Energy Groups
- IM : Number of R-meshes
- JM : Number of Z-meshes
- IO3 : Order of Legendre Polynomial Expansion
- MM : Number of Sq Quadrature Sets
- NFLSV : Device Number for Assignment of the Flux File from DOT
- IOPT : no meanings
- IS : Output Option
- RSIZE : Radius
- ANGLE : Angles
- ENERGY : Energy Boundaries
- WEIGHT : Quadrature Weight

GRT

GRTUNCL \*R-Z;AIR(0)20CM+FE(40.0 CM);P5S16;I04=-6;SIG0-J3; 1990/7/04 \*

0  
18\$  
0 5 2 35 85 125 4 5 129 18  
0 24 24 2 1 30000 10 0 1 0  
18 0 0 16  
2\*\*  
-1.000 0. 0.  
T  
1\*\*  
FO.0  
2\*\*  
4I0.0 79I20.0 60.0  
3\*\*  
0.81500E-03 0.79910E-03 0.90460E-01 0.92590E-01 0.91070E-01 0.16530E+00  
0.18680E+00 0.18360E+00 0.94720E-01 0.26310E-01 0.25950E-01 0.18920E-01  
0.72560E-02 0.71190E-02 0.65930E-02 0.41510E-02 0.40890E-02 0.40278E-02  
0.26560E-02 0.25640E-02 0.25230E-02 0.16460E-02 0.13610E-02 0.13460E-02  
0.95820E-03 0.67030E-03 0.66260E-03 0.56630E-03 0.41800E-03 0.41300E-03  
0.39050E-03 0.30880E-03 0.11980E-02 0.10650E-02 0.95380E-03 0.91730E-03  
0.88890E-03 0.96770E-03 0.99670E-03 0.99730E-03 0.10810E-02 0.11880E-02  
0.12590E-02 0.13490E-02 0.14080E-02 0.14590E-02 0.15120E-02 0.15660E-02  
0.17040E-02 0.18740E-02 0.20330E-02 0.19200E-02 0.19030E-02 0.19410E-02  
0.19630E-02 0.20330E-02 0.20050E-02 0.19750E-02 0.19890E-02 0.120430-02  
0.38090E-02 0.36900E-02 0.36480E-02 0.34680E-02 0.32030E-02 0.29930E-02  
0.26390E-02 0.23220E-02 0.20880E-02 0.18280E-02 0.15350E-02 0.13280E-02  
0.11560E-02 0.89910E-03 0.77690E-03 0.59450E-03 0.53450E-03 0.41980E-03  
0.36900E-03 0.28520E-03 0.25180E-03 0.19930E-03 0.16780E-03 0.95140E-04  
0.37670E-04 0.26720E-04  
FO.0  
4\*\*  
19I0.0 14I20.0 50.0  
5\*\*  
F1.0  
6\*\*  
1.0  
7\*\*  
1.0  
8\$ \$  
35R1 4Q35  
35R2 79Q35  
10\$ \$  
4I3 18  
4I19 24 1Q6  
11\$ \$  
6Z  
6Z 4I1 6  
12\*\*  
6Z  
6Z 6R8.3910-2  
9\$ \$  
-13 -19  
13\*\*  
-0.97753 -0.90676 -0.82999 -0.74536 -0.64979 -0.53748  
-0.39441 -0.14907 1M8  
14\*\*  
F1.0  
T T

DOT

\*\*RZ; AIR(20 CM)+FE(40.0 CM);DZ=0.5 CM;P5S16;I04=6;SIG0-J3;1990/7/04\*

0  
61\$ \$  
0 5 2 35 85 125 4 5 129 18  
2Z 24 0 160 2R1 3Z  
1 10 15 4 6 2 4Z  
2Z 0 0 0 3Z 0 0  
3 3Z 0 5Z  
2 2R1 5Z 0 8  
0  
62\$ \$  
2 3 4 14 15 9 10 11 12 13 8 60000 0 0  
63\*\*  
0.0 1.0-2 9Z 0.0 0.0 0.0 FO.0  
T  
7\*\*  
-0.21082 -0.14907 1M1 -0.42164 -0.39441 -0.14907  
1M2 -0.55777 -0.53748 -0.39441 -0.14907 1M3  
-0.66667 -0.64979 -0.53748 -0.39441 -0.14907 1M4  
-0.76012 -0.74536 -0.64978 -0.53748 -0.39441 -0.14907  
1M5 -0.84327 -0.82999 -0.74536 -0.64979 -0.53748  
-0.39441 -0.14907 1M6 -0.91894 -0.90676 -0.82999  
-0.74536 -0.64979 -0.53748 -0.39441 -0.14907 1M7  
-0.98883 -0.97753 -0.90676 -0.82999 -0.74536 -0.64979  
-0.53748 -0.39441 -0.14907 1M8 1Q80  
3R-0.97753 5R-0.90676 7R-0.82999 9R-0.74536 11R-0.64979 13R-0.53748  
15R-0.39441 17R-0.14907 3R0.97753 5R0.90676 7R0.82999 9R0.74536  
11R0.64979 13R0.53748 15R0.39441 17R0.14907  
T  
6\*\*  
0.0 0.13586-1 1N2 4R0.97681-2  
0.0 0.64738-2 0.50390-2 0.64738-2  
1N4 0.64634-2 0.71124-2 1N2  
1N5 0.64634-2 0.14381-2 0.36342-2  
0.14381-2 0.64634-2 1N6 0.64738-2  
0.71124-2 0.36342-2 1N3 1N7  
0.97681-2 0.50390-2 0.71124-2 0.14381-2  
0.71124-2 0.50390-2 0.97681-2 1N8  
0.13586-1 0.97681-2 0.64738-2 0.64634-2  
1N4 1N8 1Q80  
T  
3\*\*  
FO.0  
T  
1\*\*  
FO.0  
2\*\*  
4I0.0 79I20.0 60.00  
4\*\*  
19I0.0 14I20.0 50.0  
5\*\*  
F1.0  
8\$ \$  
35R1 4Q35  
35R2 79Q35  
10\$ \$  
4I13 18  
4I19 24 1Q6  
11\$ \$  
6Z  
6Z 4I1 6  
12\*\*  
6Z  
6Z 6R8.3910-2  
9\$ \$  
-13 -19  
T T

70



Table 5.3 Error analysis for the reaction-rate measurements.  
The measured data are presented in Table 5.2.

Item	Error [ $\pm$ %]
Counting statistics	0.5 ~ 9
Detector efficiency	<u>2.5</u>
Natural abundance	< 0.2
Foil weight	< 0.1
Sum peak	0.5 (only for $^{24}\text{Na}$ )
Saturation factor	0.3 for $^{57}\text{Ni}$ 0.5 for $^{24}\text{Na}$ 1.0 for $^{115\text{m}}\text{In}$ 2.0 for $^{116\text{m}}\text{In}$
Source neutron yield	<u>3.0</u>
Times for irradiation, Cooling and measuring	$\sim$ negligible
Decay data	< 0.5

Table 3.6.1 Systematic errors of flux

error source	systematic error
1) Source neutron intensity	$\pm 2$ %
2) Efficiency	
$E_n > 200$ keV	<u>&lt; 2</u> %
$80 < E_n < 100$ keV	5-10 %
$50 < E_n < 80$ keV	10-20 %
3) Solid angle	$\ll 1$ %
4) Effective measured area	<u>&lt; <math>\pm 2</math></u> %
5) Air attenuation correction	$\ll 1$ %

*exclude for relative*

XA9642733

73



XA9642733

**BENCHMARK ACTIVITIES IN THE  
RADIATION SHIELDING INFORMATION CENTER**

**J. E. White**

**Oak Ridge National Laboratory**

**IAEA Consultants Meeting  
Preparation of Fusion Benchmarks in Electronic Format  
for Nuclear Data Validation Studies  
December 13-16, 1993  
Vienna, Austria**

## **RSIC HAS A LONG HISTORY AND CONTINUING INTEREST IN RADIATION TRANSPORT BENCHMARKS**

- **Collaboration with the American Nuclear Society ANS-6 Shielding Standards Committee since 1969**
  - **Involvement with the CSEWG Shielding Subcommittee and Shielding Data Testing and Applications Subcommittee since 1967**
  - **Liaison between ANS Mathematics and Computations and Radiation Protection and Shielding Divisions on Benchmarks since 1990**
- 
- **Collaboration with NEADB on Establishing Electronic Database for Shielding Benchmarks since 1991 (Informal discussions on visits by Sartori)**
  - **Collaboration with ORNL Engineering Physics and Mathematics Division Nuclear Analysis and Shielding Section on Development of an Electronic Database (SINBAD) since 1992**
  - **Collaboration on FENDL Project to Include Fusion Benchmarks in the SINBAD Database Form (1993)**

## **RSIC PUBLISHED SHIELDING BENCHMARKS IN SUPPORT OF ANS-6 SHIELDING STANDARDS**

- **ORNL-RSIC-25 (ANS-SD-9) Published in 1969 (for testing computational methods)**
  - Fission spectrum in Infinite Graphite**
  - $C_s^{137}$  in Infinite  $H_2O$**
  - Fission, Fusion in Infinite Air**
  - Co-60 Plane Source on Air/Ground Interface**
  
- **SUPPLEMENT 1 Published in 1970 (Problems, solutions added)**
  - New problem added (1- & 3-GeV Protons in Fe)**
  - New Solution - O5R on Graphite problem**

---

- **SUPPLEMENT 2 Published in 1974 (Problems added)**
  - Neutron, photons Polyethelene slab**
  - Neutron transport in thick sodium**
  
- **Problems described, solution data presented in the report**
  
- **RSIC Packaged Cross Section Data as Part of the Data Library Collection (DLC)**

**RSIC WILL PROVIDE LIAISON BETWEEN  
ANS DIVISIONS FOR FUTURE BENCHMARK  
DEVELOPMENT AND PUBLICATION**

- **ANS Mathematics and Computations (M&C) Division Initiated Collaboration with ANS Radiation Protection and Shielding (RPS) Division on Joint Benchmarks**
  
  - **RSIC will Provide Liaison**
- 
- **RSIC will Publish M&C Benchmark Reports (formerly done by Argonne Code Center)**
  
  - **RSIC will Renew ANS RPS Benchmark Activity**
  
  - **RSIC Goal: To Publish Benchmarks in Database Format and Provide Access in User-Friendly Form**

**RSIC HAS PROMOTED DATA TESTING  
BENCHMARKS THROUGH INVOLVEMENT IN  
THE U.S.A. CSEWG**

- **Shielding Subcommittee Established in 1967 to help assure ENDF/B would Provide Adequate Evaluations for Shielding Calculations (RSIC Chair)**
  
- **Shielding Benchmarks Established by that Subcommittee**
  
- **Shielding Data Testing and Applications Subcommittee Established in CSEWG Reorganization (RSIC Chair)**

---

- **Published Vol. II of CSEWG Benchmark Specifications Book in 1986**
  
- **New Contributions**
  - SB5. Fusion Reactor Shielding Benchmark**
  - SB6. Fusion Reactor Shielding Benchmark II, Duct Streaming Experiment and Analysis**
  
- **SB5 and SB6 will be Used for FENDL Data Testing**

## **RSIC ENCOURAGES INTERNATIONAL COOPERATION IN DEVELOPING A DATA BASE FOR RADIATION TRANSPORT BENCHMARKS**

- **The NEA Initiated Efforts to Develop Database for Shielding Benchmarks (~1991)**
- **NEADB Commissioned AEA Winfrith for Some Preliminary Studies (~1992)**
- **NEA NSC Endorsed the Idea and Promoted Additional Development (June 1993)**
- **ORNL EPMD Nuclear Analysis and Shielding Section Developed Database for Tower Shielding Reactor Experiments using dBASE (Relational Database)**
- **NEADB and RSIC will Exchange Staff Members in FY 1994 to Further Develop the Concept (SINBAD)**
- **FENDL Working Group I on Calculational and Experimental Benchmarks Recommends its Benchmark Data be Submitted to RSIC for Inclusion in SINBAD (Nov. 1993)**

# SINBAD - Shielding Integral Benchmark Archival Database

Hamilton T. Hunter  
D.T. Ingersoll  
R.W. Roussin

## BACKGROUND

Quality assurance requirements for advanced reactor designs have long indicated the need to organize and preserve available experimental and calculational benchmark results. A database needed to facilitate intercomparison and analysis. Some examples of results of interest are,

Integral experiments involving complex geometries,  
~~2D and 3D data analysis used to predict performance~~  
parameters.

Access to needed data without introducing reproduction errors is justification alone.

## SINBAD Data Structure

Experimental Data	-	10 Detector databases, 1 Material/Slab composition, 1 Detector description
Theoretical Data	-	2 Calculational output databases, 1 Code input, 1 Material/Mixture, 1 Mesh
<del>General</del>	<del>-</del>	<del>1 Configuration identification 1 General facility setup, 1 Reference</del>

Total databases with minor support databases = 37.  
Total database search and control subroutines = 55.

## II. COMPILATION OF SHIELDING BENCHMARK SPECIFICATIONS

## SB5. Fusion Reactor Shielding Benchmark

A. Benchmark Name and Type: ORNL Fusion Shielding Benchmark; a Series of Attenuation Experiments and Analyses.

B. System Description: Neutron and photon flux spectra have been measured and calculated for the case of neutrons, produced by D-T reactions, incident on various laminated slab shields composed of stainless steel and borated polyethylene.

C. Model Description: The experimental configuration is three-dimensional but may to a good approximation be reduced to a two-dimensional configuration. The three-dimensional configuration will first be described for the sake of generality and then the two-dimensional configuration used in an ORNL analysis will be discussed.

## 1. Three-Dimensional Configuration

In Fig. 1 a horizontal cut through the room that houses the experiment is given. In this figure and throughout this discussion the z-axis is the axis of the deuteron beam, the x-axis is parallel to the floor and roof, and the y-axis is perpendicular to the floor and the roof. The iron cavity liner around the target serves as a spectrum modifier and makes the neutron spectrum incident on the experimental shield configuration similar to the spectrum incident on the first wall of a fusion reactor. The front of the thermal shield is always located 50 cm behind the detector location. The thermal neutron shield in Fig. 1 is composed of stainless steel 304, is 5.08 cm thick, and has a square cross sectional area, 152.4 cm by 152.4 cm. This stainless steel slab is identical to the stainless steel slabs used as part of the laminated shield configurations described later. In Figs. 2 and 3 other views of the experimental configuration and the experimental room are given. The dimensions given in Figs. 1-3 are

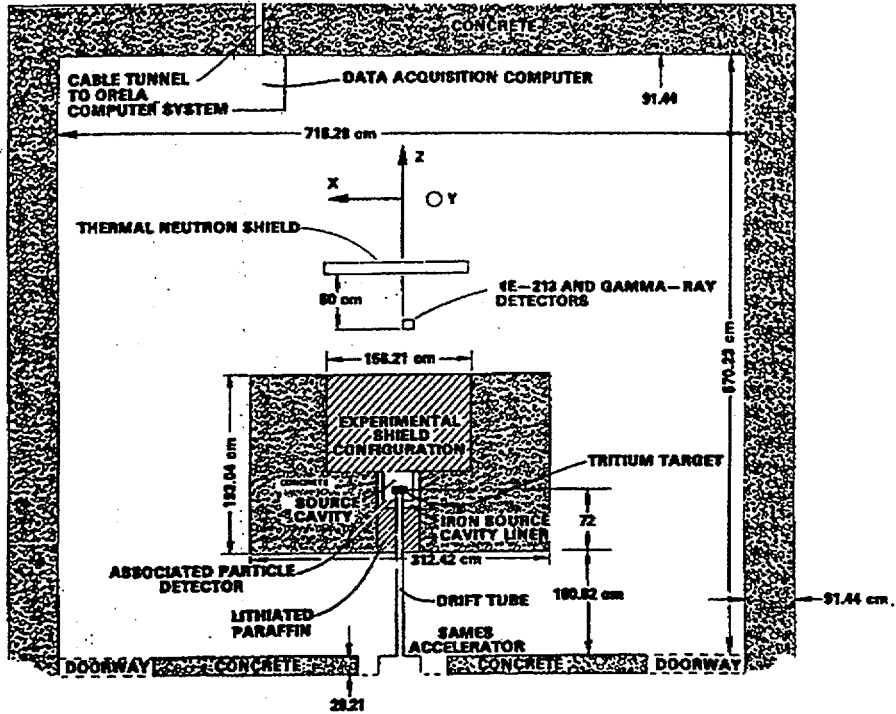
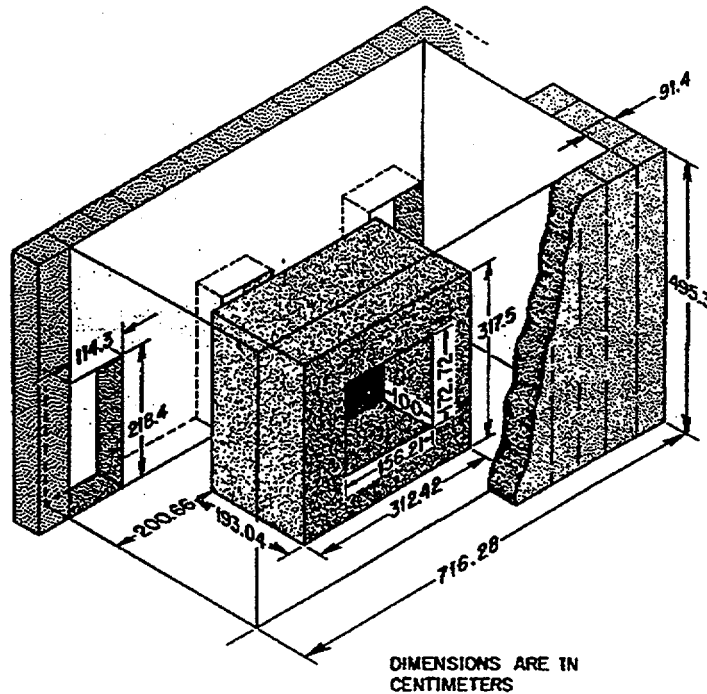


Fig. 1 - Horizontal schematic of experimental enclosure. See Figs. 2 and 3 for additional dimensions. (Drawing not to scale)



DIMENSIONS ARE IN  
CENTIMETERS

Fig. 2 - Three-dimensional view of experimental enclosure. See Figs. 1 and 3 for additional dimensions. (Drawing not to scale)

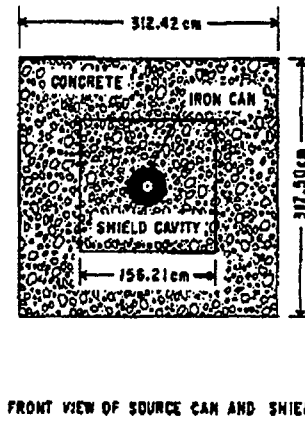
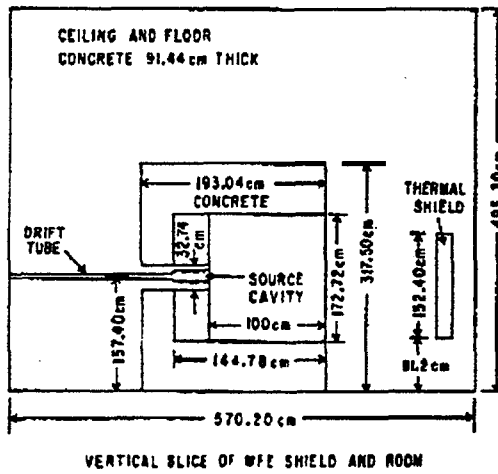
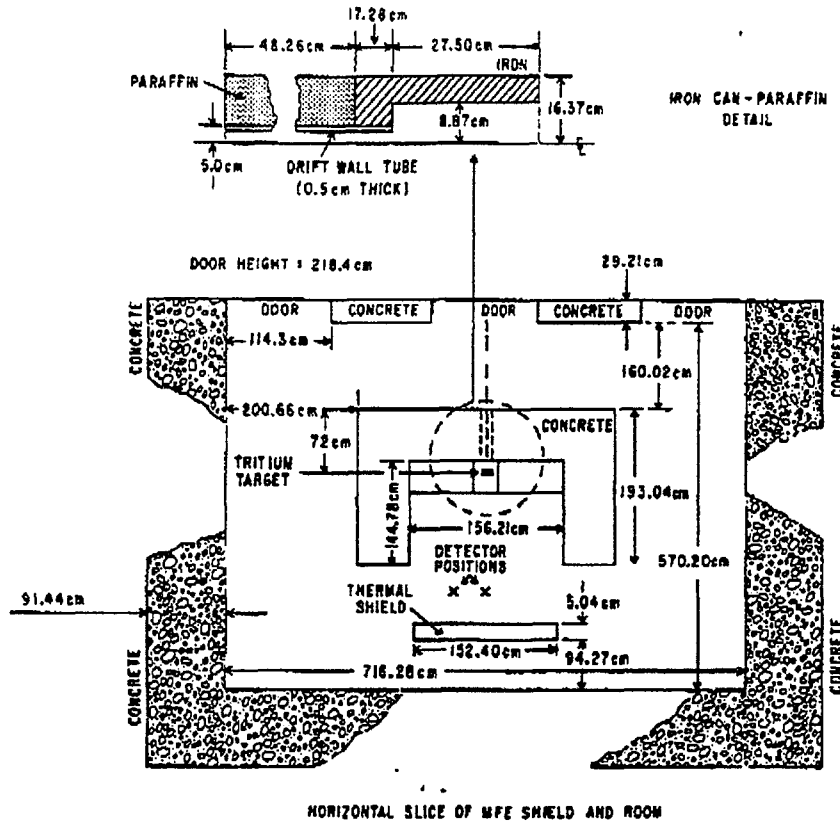


Fig. 3 - Additional schematics of experimental enclosure. See Figs. 1 and 2 for additional dimensions (Drawing not to scale)

sufficient to enable the experiment to be modeled to any desired detail, but the reader who wishes to model the experiment in three dimensions should also see Ref. 1.

## 2. Two-Dimensional Configuration

In Fig. 4 the reduced geometry representation of the experiment that is used to obtain the calculated results presented later is shown. The geometry in Fig. 4 is two-dimensional in that there is cylindrical symmetry about the z-axis. In the two-dimensional model the lithiated-paraffin that is shown in Fig. 1 is not included. In the two-dimensional model the back concrete wall is placed directly against the stainless steel thermal neutron shield. The thermal shield is located 73 cm behind the detector<sup>1</sup> (as shown in Fig. 4). The two-dimensional model dimensions given in Fig. 4 correspond very approximately to the dimensions in Figs. 1-3. In the two-dimensional model the outside boundary of the configuration is to be taken as an albedo surface with a reflection coefficient of .2 for all particle types and energies. This reflection coefficient was determined by matching particle flux contours obtained with the two-dimensional model shown in Fig. 4 with particle flux contours obtained using a two-dimensional representation of the complete experimental room. More detail concerning the determination of this reflection coefficient will be found in Ref. 1. Also shown in Fig. 4 is a typical experimental laminated shield configuration as it is used in the two-dimensional representation of the experiment. In the experiment the experimental slab configuration is always located as shown in Fig. 4, i.e., the front of the experimental slab configuration is always 21.5 cm from the source.

## 3. Material Composition

In Table 1 the number densities of the materials that occur in Figs. 1-4 are given. Also included in this table are the compositions of the material slabs that were used in the various experiments.

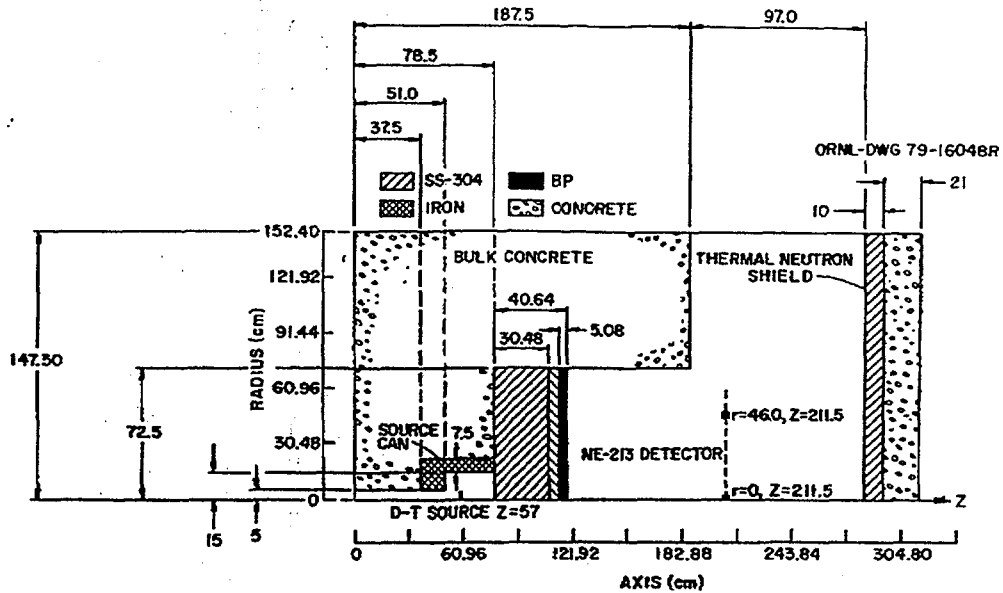


Fig. 4 - Two-dimensional calculational model of the experimental configuration.

Table 1

Composition of Materials Used in the Calculation

Element	Number Density (atom/cm Barn)					
	Concrete	Air	Iron Can	SS-304	BP*	LP**
H	$7.86 \times 10^{-3}$				$7.13 \times 10^{-2}$	$5.926 \times 10^{-2}$
B-10					$4.87 \times 10^{-4}$	
B-11					$1.97 \times 10^{-3}$	
C					$3.41 \times 10^{-2}$	$3.338 \times 10^{-2}$
N		$3.64 \times 10^{-5}$				
O	$4.39 \times 10^{-2}$	$9.74 \times 10^{-6}$			$3.64 \times 10^{-3}$	$1.125 \times 10^{-2}$
Na	$1.05 \times 10^{-3}$					
Mg	$1.40 \times 10^{-4}$					
Al	$2.39 \times 10^{-3}$					
Si	$1.58 \times 10^{-2}$					
K	$6.90 \times 10^{-4}$					
Ca	$2.92 \times 10^{-3}$					
Cr					$1.77 \times 10^{-2}$	
Mn					$1.77 \times 10^{-3}$	
Fe	$3.10 \times 10^{-4}$		$8.48 \times 10^{-2}$		$6.02 \times 10^{-2}$	
Ni					$7.83 \times 10^{-3}$	
Li-6						$5.565 \times 10^{-4}$
Li-7						$6.944 \times 10^{-3}$

\* BP = Borated Polyethylene

\*\* LP = Lithiated Paraffin

#### 4. Method of Calculation

This benchmark may be calculated with  $S_n$  transport methods coupled with special first and last flight corrections. The preferred technique is described in Section E, Calculated Results.

The benchmark may also be calculated in three-dimensions using Monte Carlo technique. Sufficient information has been provided for a three-dimensional calculation, and results can be compared with data in Appendix A. Reference 11 and 12 should be consulted for further details and analysis techniques.

#### D. Experimental Data

The neutron source was obtained by focusing a 250 keV deuteron beam on a cylindrical titanium-tritide (TiT) target<sup>2</sup> having a radius of .64 cm, a thickness of 4 mg/cm<sup>2</sup> and a density of 4.28 g/cm<sup>3</sup>. The neutron source strength was measured by using the associated particle technique. More details concerning the experiment will be found in Ref. 3.

The neutron-gamma-ray detector consisted of 66.1 g of NE-213 liquid scintillator contained in a cylindrical aluminum can having a wall thickness of  $4.32 \times 10^{-2}$  cm. The active volume of the detector was 79 cm<sup>3</sup> (4.66 cm diameter and 4.66 cm height). Neutron and gamma ray events were separated using pulse shape discrimination methods. The neutron and gamma pulse height spectra were unfolded using FERD<sup>4</sup> to produce energy spectra. The neutron response matrix was obtained using the pulsed neutron beam from the Oak Ridge Linear Accelerator and the gamma ray response matrix was generated using gamma ray sources of known energy. The energy resolution of the detector varies as

$$R_N = \sqrt{300 + \frac{800}{E_N}} \quad (1)$$

for neutrons of energy  $E_N$  in MeV, and

$$R_Y = \sqrt{170 + \frac{288}{E_Y}} \quad (2)$$

for gamma rays of energy  $E_Y$  in MeV. The quantities  $R_N$  and  $R_Y$  are full width and half maximum (in percent) of the detector response (assumed Gaussian) to neutrons and gamma rays.

Experimental data have been obtained for the seven configurations outlined in Table 2. For all of the configurations except number one, the neutron flux per unit energy for all energies  $> 850$  keV and the gamma ray flux per unit energy for all energies  $> 750$  keV have been measured at several detector locations. In the case of configuration number one, i.e., the configuration with no laminated slab shield, gamma ray measurements were not made and data were taken only with the detector on the axis of the deuteron beam. The experimental data for all of the configurations are shown in Appendix A.

#### E. Calculated Results

All of the analytical results reported in this benchmark description are based on the two-dimensional configuration shown in Fig. 4 and discussed previously. This configuration was modeled in r-z geometry using 42 radial and 82 axial mesh intervals. The radial and axial boundaries used in the calculations are given in Table 3.

The sequence of radiation transport calculations necessary to obtain the neutron and gamma ray energy spectra is complex and very detailed and is described fully in Refs. 1 and 5, so only the salient features are discussed here.

The neutron source calculation was carried out using a procedure that is described in detail in Ref. 2. Also, additional details concerning the source calculation are given in Ref. 1. The probability that a deuteron of energy  $E_d$  reacts while traveling a distance  $dx$  in a target containing  $N_t$  tritium atoms per  $\text{cm}^3$  is<sup>2</sup>

$$P = N_t \int_0^{E_d} \sigma(E) dE / (dE/dx) \quad (3)$$

where  $\sigma$  is the microscopic cross section for the  $T(D,n)^4\text{He}$  reaction and  $dE/dx$  is the stopping power for deuterons in the target material. If  $\sigma$  is expressed as the angular differential cross section for the reaction, then  $P$  is also the probability for the emission of the neutron into any solid angle. The differential cross section and stopping power used in the calculation reported here are taken from Ref. 2. Equation (3) can be used to determine the neutron emission probabilities for all deuteron energies and for all angles into which the neutron is emitted. The energies of the neutrons are then obtained as a function of  $E_d$  and emission angle using the kinematic equations for a two-body reaction.<sup>1,2</sup> The probabilities for the emission of neutrons into the solid angles defined by the polar angle intervals of 0-40, 40-90, and 90-180 degrees with respect to the axis of the deuteron beam for the case of 250 keV deuterons incident on a  $4 \text{ mg/cm}^2$  thick titanium-tritide target are given as a function of neutron energy in Table 4. The energy intervals correspond to the energy boundaries of the group structure used to describe the multigroup cross sections. The angular interval of 0-40 degrees corresponds to the angle at which neutrons are emitted directly out of the mouth of the source cavity, i.e., the polar angle defined by a ray from the D-T source to the mouth of the cavity is  $\sim 40$  degrees. The 40-90 and 90-180 degree angular intervals correspond to the angles at which neutrons are emitted into the lateral surface and towards the rear of the source cavity, respectively. These angular intervals were selected on the basis of the source cavity geometry.<sup>1</sup> The data in Table 4 serve as the input to the radiation transport codes used to calculate the neutron and gamma ray energy spectra. The average energy of the emitted neutrons for the angular intervals considered may easily be obtained from the probabilities in Table 4.

TABLE 2  
COMPOSITION AND THICKNESS OF STAINLESS STEEL 304  
AND BORATED POLYETHYLENE SLABS

Configuration	Composition						Total Slab Thickness (cm)
	SS-304 <sup>a</sup>	SS-304	BP <sup>b</sup>	SS-304	BP	SS-304	
Slab Thickness (cm)							
1	0						0
2	15.24						15.24
3	30.48						30.48
4	30.48	5.08	5.08				40.64
5	30.48	5.08	5.08	5.08			45.72
6	30.48	5.08	5.08	5.08	5.08		50.80
7	30.48	5.08	5.08	5.08	5.08	5.08	55.88

<sup>a</sup>Stainless steel type 304

<sup>b</sup>Borated polyethylene

All of the  $S_n$  transport calculations used to obtain the data reported here, incorporated a 53-neutron, 21-gamma-ray energy group library obtained by collapsing the 171-neutron, 36-gamma-ray VITAMIN C data library (ENDF/B-IV).<sup>6</sup> The VITAMIN C library was created as a general purpose cross section data set for the analysis of fusion neutronics problems. The fine group library was collapsed using the ANISN<sup>7</sup> code by representing the experimental

TABLE 3  
 THE RADIAL AND AXIAL BOUNDARIES USED  
 IN THE TWO-DIMENSIONAL CALCULATIONS

Radial Boundaries (cm)	Axial Boundaries (cm)	
0.0000		
0.5000	150.000	264.060
1.0000	157.500	265.330
2.0000	165.000	266.600
3.0000	172.500	267.870
4.0000	180.000	269.140
5.0000	187.500	270.410
7.5000	195.000	271.680
10.000	196.500	272.950
12.500	198.000	274.220
15.000	199.500	275.490
17.500	201.000	276.760
20.000	202.500	278.030
22.500	203.500	279.300
25.625	204.500	280.570
28.750	205.500	281.840
31.875	206.500	283.110
35.000	207.500	284.380
38.125	208.500	285.650
41.250	209.500	286.920
44.375	210.500	288.190
47.500	211.500	289.460
50.625	212.500	298.068
53.750	216.500	306.676
56.875	220.500	315.284
60.000	224.500	323.892
63.125	228.500	332.500
66.250	231.040	335.000
69.375	233.580	337.500
72.500	236.120	361.000
75.000	238.660	362.000
79.800	241.200	366.000
84.600	243.740	371.080
89.400	246.280	402.790
94.200	248.820	434.500
99.000	251.360	437.000
101.00	253.900	439.500
114.00	256.440	442.000
127.00	258.980	444.500
140.00	260.250	449.750
142.50	261.250	455.000
145.00	262.790	460.250
147.50		465.500

components in the angular intervals given in Table 4 in spherical geometry and using the neutron energy distribution in that angular interval as the source spectrum. That is, a different cross section collapse calculation was used in the three regions corresponding to the polar angular intervals  $0-40^\circ$ ,  $40-90^\circ$ , and  $90-180^\circ$ . The energy boundaries of the collapsed data library, given in Table 5, were based in part on those used in the DLC-47 library<sup>8</sup>, but expanded at high energies so that the D-T neutron source could be more accurately represented in the transport calculations. The angular dependence of the cross sections for all nuclei was approximated using a  $P_3$  Legendre expansion. The composition of the materials used in the calculations are given in Table 1.

The sequence of radiation transport calculations used to obtain the neutron and gamma ray energy spectra is shown in Fig. 5. The sequence is initiated by performing three separate calculations using the GRTUNCL code<sup>9</sup> to obtain the uncollided neutron and first collisions source distributions at all spatial mesh intervals in the calculational geometry. The GRTUNCL code as used here assumed isotropic neutron emission from a point source. A GRTUNCL calculation was made for each of the angular intervals shown in Table 4 using the incident source spectra shown in Table 4 in each of the angular intervals. To ensure that the contribution to the uncollided neutron flux and first collision sources were due to neutrons emitted in the angular intervals specified in Table 4, black absorbers were interposed in the calculational geometry to confine the source neutrons to these angles. The purpose of the sequence of calculations is to account approximately for the energy-angle dependence of the neutrons from the D-T source.

TABLE 4

PROBABILITY FOR THE EMISSION OF NEUTRONS INTO THE  
SPECIFIED ENERGY AND SOLID ANGLE INTERVALS  
FOR 250 KEV INCIDENT DEUTERONS

Energy Interval (MeV)		Polar Angular Interval		
		0°-40°	40°-90°	90°-180°
14.92	15.68	0.0130		
14.55	14.92	0.0902	0.0697	
14.19	14.55	0.0168	0.2460	
13.80	14.19		0.0750	0.2163
13.50	13.80			0.2088
12.84	13.50			<u>0.0642</u>
		0.1200	0.3907	0.4893

The uncollided flux and first collision source data from each GRTUNCL calculation are combined to form a single source tape which is the input data to the two-dimensional discrete ordinates code DOT.<sup>10</sup> This code calculates the collided flux distributions using the first collision data as a spatially distributed source. These calculations were completed using an S<sub>12</sub> angular quadrature. A final scattering source tape is generated in DOT and is employed to carry out a last-flight transport calculation using the FALSTF code<sup>9</sup> to obtain the neutron and gamma ray flux distributions at each detector from GRTUNCL to yield the total flux at each detector location. These distributions are processed to obtain the neutron and gamma ray energy spectra by smoothing the flux per unit energy in each multigroup energy interval with an energy-dependent Gaussian response function having a width determined by Eq. (1) for neutrons, and Eq. (2) for gamma rays.

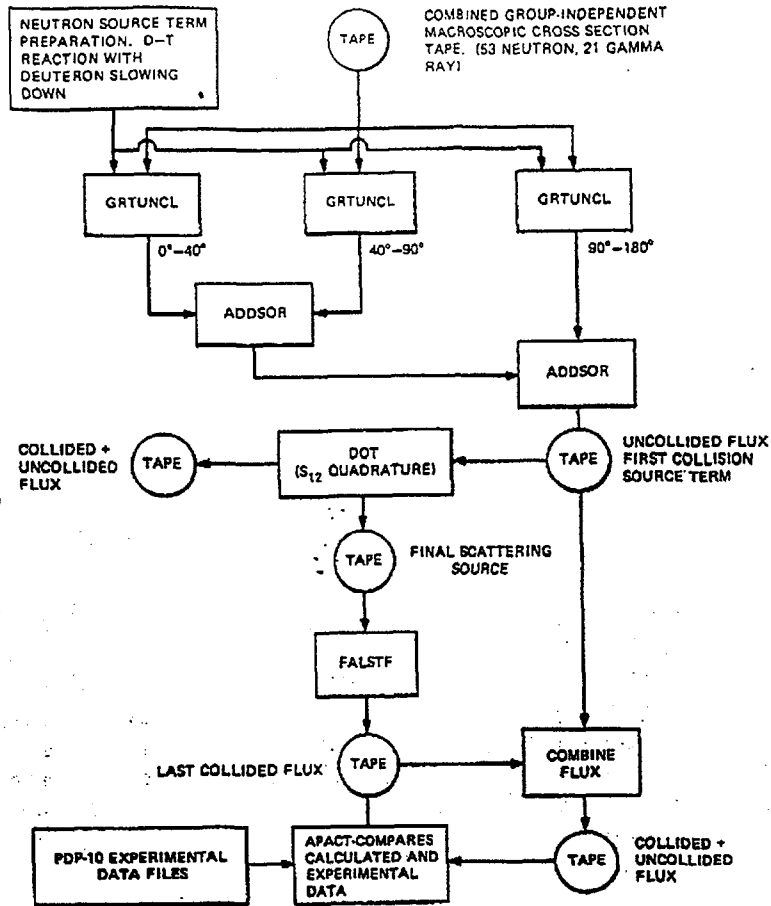


Fig. 5 - Block diagram of  $S_n$  calculational scheme

TABLE 5

53-NEUTRON, 21-GAMMA-RAY ENERGY RADIATION TRANSPORT CROSS SECTION GROUP STRUCTURE

Neutron Group	Upper Energy (eV)	Neutron Group	Upper Energy (eV)	Gamma Ray Group	Upper Energy (MeV)
1	0.17333E + 08	28	0.60810E + 06	54	14.0
2	0.15683E + 08	29	0.49787E + 06	55	12.0
3	0.14918E + 08	30	0.36883E + 06	56	10.0
4	0.14550E + 08	31	0.29850E + 06	57	8.0
5	0.14191E + 08	32	0.29720E + 06	58	7.5
6	0.13840E + 08	33	0.18316E + 06	59	7.0
7	0.13499E + 08	34	0.11109E + 06	60	6.5
8	0.12840E + 08	35	0.67379E + 05	61	6.0
9	0.12214E + 08	36	0.40868E + 05	62	5.5
10	0.11052E + 08	37	0.24788E + 05	63	5.0
11	0.10000E + 08	38	0.23579E + 05	64	4.5
12	0.90484E + 07	39	0.15034E + 05	65	4.0
13	0.81873E + 07	40	0.91188E + 04	66	3.5
14	0.74082E + 07	41	0.55308E + 04	67	3.0
15	0.60653E + 07	42	0.33546E + 04	68	2.5
16	0.49659E + 07	43	0.20347E + 04	69	2.0
17	0.40657E + 07	44	0.12341E + 04	70	1.50
18	0.36788E + 07	45	0.74852E + 03	71	1.0
19	0.27253E + 07	46	0.45400E + 03	72	0.60
20	0.23653E + 07	47	0.27536E + 03	73	0.20
21	0.23069E + 07	48	0.16702E + 03	74	0.10
22	0.22313E + 07	49	0.10130E + 03		0.010
23	0.16530E + 07	50	0.61442E + 02		
24	0.13534E + 07	51	0.37267E + 02		
25	0.86294E + 06	52	0.10677E + 02		
26	0.82085E + 06	53	0.41399E + 00		
27	0.74274E + 06		0.10000E - 04		

The measured and calculated differential neutron energy spectra as a function of SS-304 and BP slab composition and thickness are compared in Fig. 6 when the NE-213 detector is on the axis of symmetry. The neutron source-to-detector distance is 154.5 cm. In Fig. 6, and the comparisons of other data given below, the solid curves are measured spectra and the points are the calculated results. The two solid curves for each configuration represent the 68% confidence interval in the measured spectra obtained from the unfolding procedure that is used to obtain energy spectra from the pulse height data. The spectra are arranged in order of increasing slab thickness from top-to-bottom in the figure and both the measured and calculated data are normalized to one D-T neutron.

The spectra are compared for neutron energies above 850 keV. The calculated and measured spectra are in excellent agreement for all of the configurations except when the slab contains 15.24 cm of SS-304 (configuration 2). In general, the agreement is favorable in the neutron energy range between 850 keV and ~11 MeV. The calculated results are systematically higher than the measured data between ~11 and 12.5 MeV, in good agreement between 12.5 and ~15 MeV, and then the calculated data exhibit a more rapid roll-off at the higher neutron energies. It is not kinematically possible for the incident deuterons (250 keV) to produce neutrons with energies above 15.1 MeV in the D-T reaction. The indication of more energetic neutrons in the spectra is a manifestation of the response of the experimental instrumentation and the difference in the roll-off at neutron energies above ~15 MeV can be attributed to the Gaussian response function being convoluted with neutron energy bins (pulse height channels and multigroup energy intervals) that differ between measured and calculated data.

The measured and calculated differential neutron energy spectra as a function of SS-304 and BP slab composition and thickness when the detector is off the axis of symmetry are compared in Fig. 7. The NE-213 detector was positioned at a distance of 46.0 cm normal to the deuteron beam - tritium

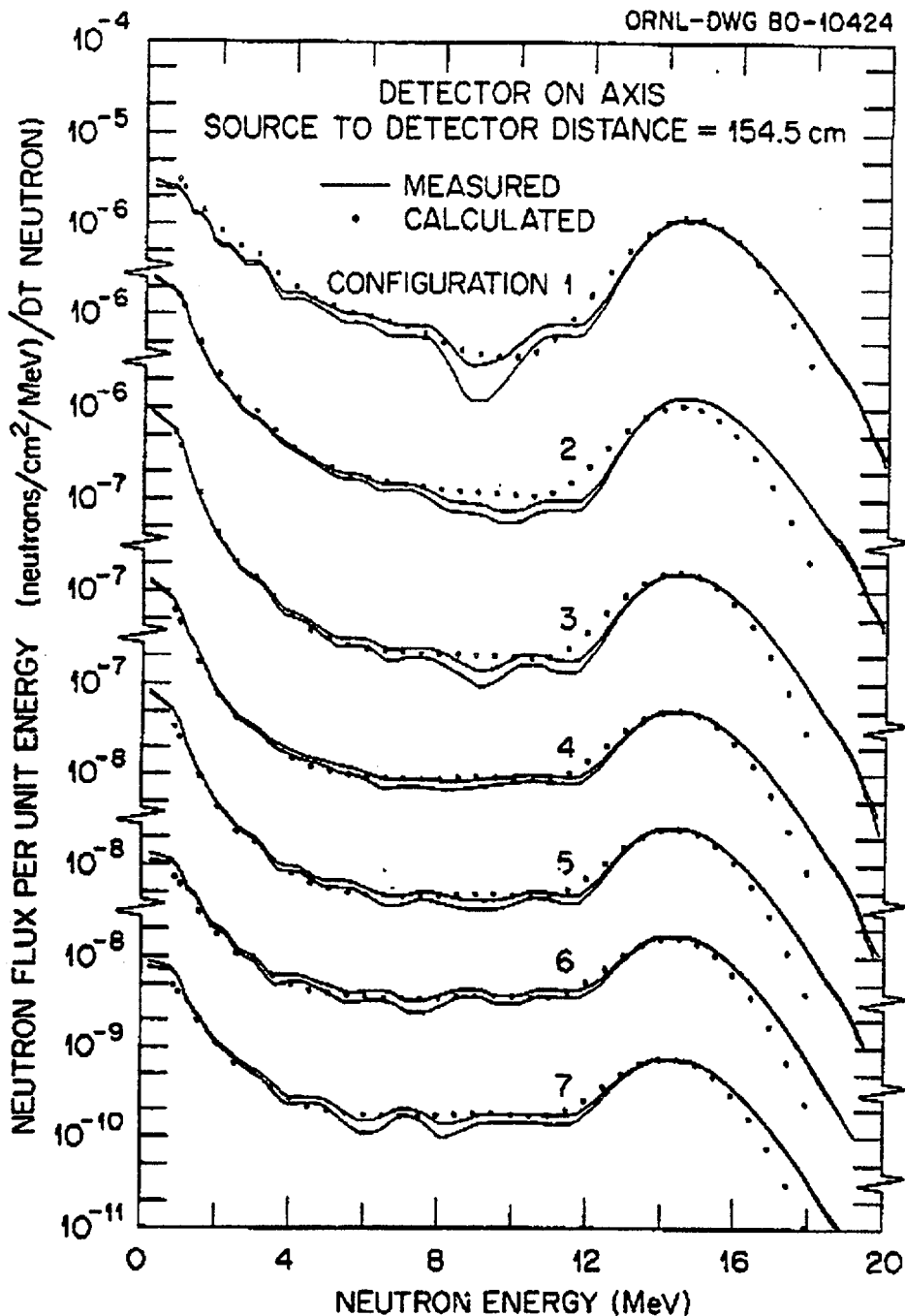


Fig. 6 - Neutron flux per unit energy vs. energy for various slab configurations, (See Table 2) when the detector position is on the axis of the deuteron beam.

target axis for all of the slab configurations except for that comprised of 30.48 cm of SS-304 (configuration 3). For this measurement, the detector was located at a distance of 100 cm from the beam axis. A series of measurements of neutron spectra in the plane perpendicular to the deuteron beam axis revealed that the neutron yield was symmetric about the axis. Consequently, the incorporation of the two-dimensional representation of the experimental apparatus and the detector location in the r-z geometry of the calculational model can be correlated with the actual detector location in the cartesian coordinate system of the experiment.

The comparisons in Fig. 7 are similar to those in Fig. 6 except for configuration 3 where the detector location is 100 cm off axis. For this case, the disagreement may be due to the fact that the albedo surface at the boundary of the reduced geometry is not satisfactory when the detector is too close to the surface.

The differential gamma ray energy spectra for the cases with the detector is on and off the axis of symmetry as a function of SS-304 and BP slab thickness and composition are compared in Figs. 8 and 9. The measured and calculated spectra are compared for gamma rays having energies above 750 keV. The measured and calculated data are in good agreement for gamma rays with energies to  $\sim 8$  MeV. The calculation reproduces the measurements in magnitude but because of the rather coarse energy group structure, the various peaks in the measured differential distributions are not reproduced. The important point to note in these comparisons is that the gamma rays that contribute to these spectra are due, in part, to the reactions of low energy neutrons ( $< 850$  keV) with the slab materials. Thus, even though the neutron spectra are not measured below 850 keV the gamma ray comparisons in Figs. 8 and 9 are some indication that the calculated neutron spectra below 850 keV are reasonably reliable.

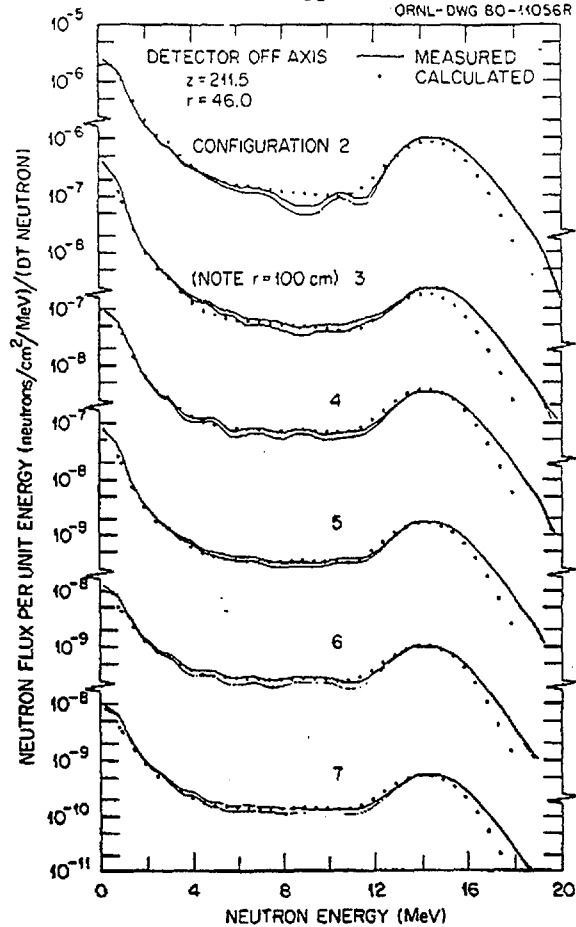


Fig. 7 - Neutron flux per unit energy vs. energy for various slab configurations (See Table 2) when the detector position is not on the axis of the deuteron beam.

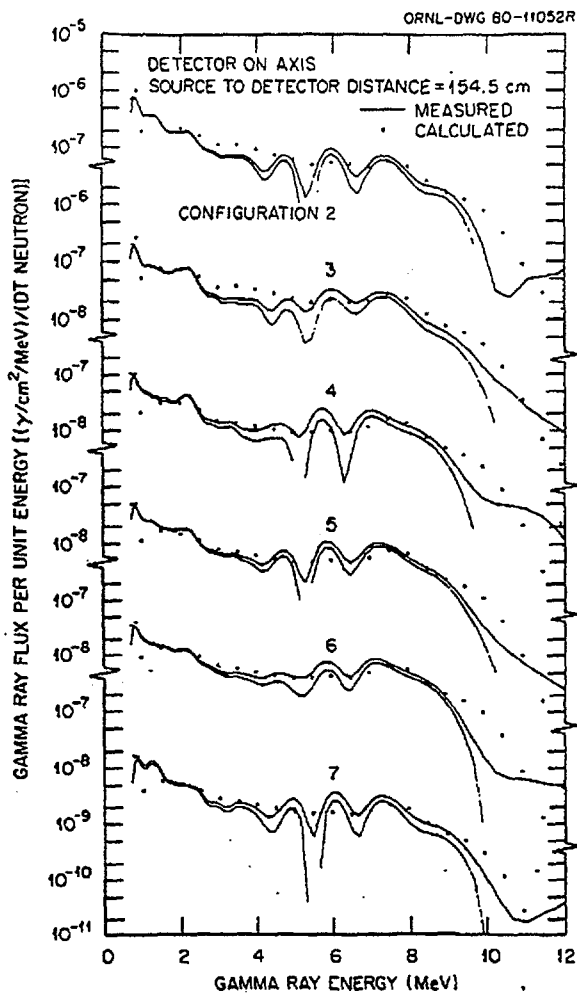


Fig. 8 - Gamma ray flux per unit energy vs. energy for various slab configurations when the detector is on the axis of the deuteron beam.

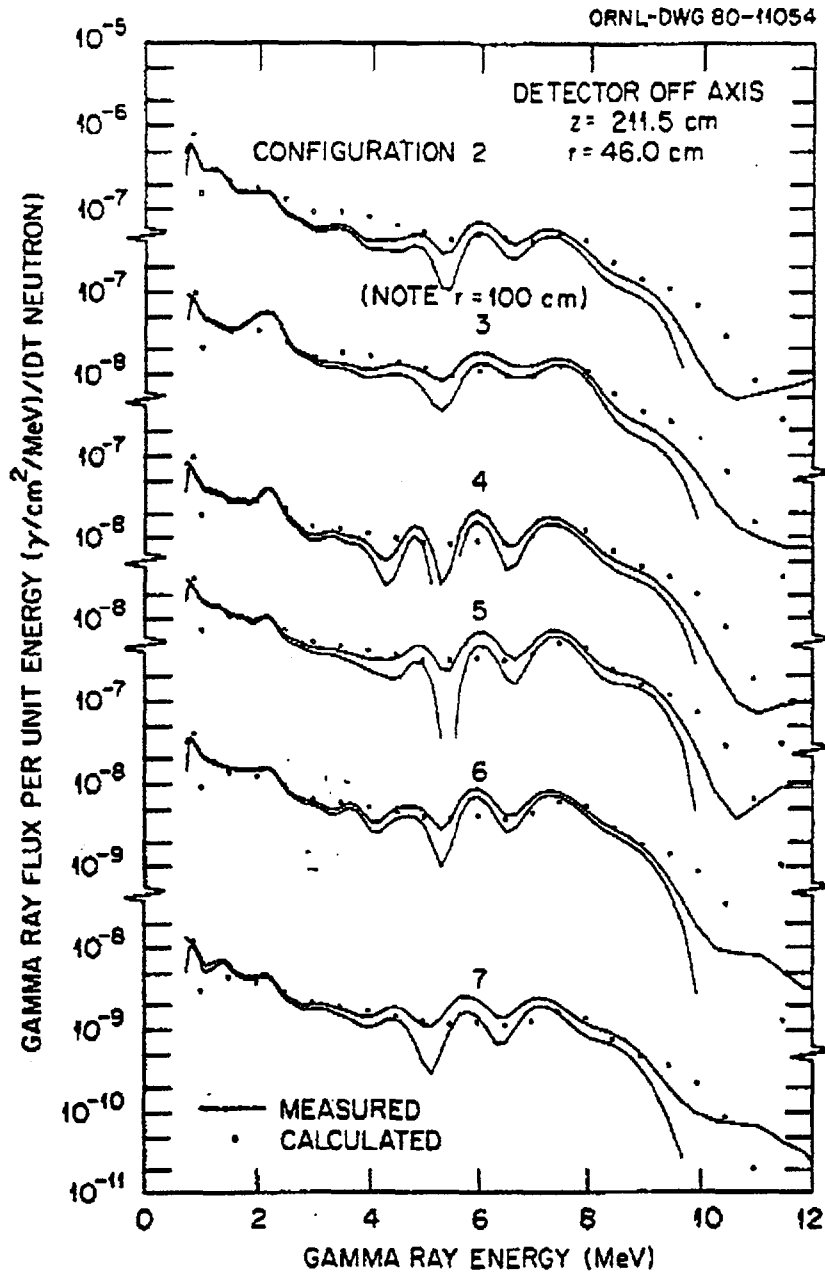


Fig. 9 - Gamma ray flux per unit energy vs. energy for various lab configurations when the detector is not on the axis of the deuteron beam.

F. References

1. R. T. Santoro et al., "Calculational Procedures for the Analysis of Integral Experiments for Fusion Reactor Design," ORNL/TM-7094, Oak Ridge National Laboratory (1981).
2. T. R. Fewell, "Absolute Determination of 14-MeV Neutron Yields," SC-RR-67-346, Sandia Laboratories (1967).
3. G. T. Chapman, G. L. Morgan, J. W. McConnell, "The ORNL Integral Experiments to Provide Data for Evaluating the MFE Shielding Concept. Part I: Attenuation Measurements," ORNL/TM-7356, Oak Ridge National Laboratory; see also, "Integral Experiments for Fusion Reactor Design: Experimentation," G. T. Chapman and G. L. Morgan to be published in the Proceedings of the International Conference on Nuclear Cross Sections for Technology, Knoxville, TN, October 22-26, 1979.
4. W. R. Burrus and V. V. Verbinski, "Fast-Neutron Spectroscopy with Thick Organic Scintillators," Nucl. Instrum. Methods 67, 181 (1969).
5. R. T. Santoro et al., "Calculation of Neutron and Gamma Ray Energy Spectra for Fusion Reactor Shielding Design: Comparison with Experiment," Nucl. Sc. Eng. 78, 259 (1981); see also "Integral Experiments for Fusion Reactor Design: Analysis," R. T. Santoro et al., Proceedings of the International Conference on Nuclear Cross Sections for Technology, Knoxville, TN, Oct. 22-26, 1979.
6. ORNL/RSIC-37, Radiation Shielding Information Center, Oak Ridge National Laboratory (1975) available as DLC/4-1-Vitamin C.

7. W. W. Engle, Jr., "A User's Manual for ANISN, a One-Dimensional Discrete Ordinates Code with Anisotropic Scattering," K-1693, Oak Ridge National Laboratory (1967).
8. "BUGLE, Coupled 45 Neutron, 16 Gamma Ray, P<sub>3</sub>, Cross Sections" for Studies by the ANS 6.1.2 Shielding Standards Working Group on Multigroup Cross Sections, DLC/47, Radiation Shielding Information Center, Oak Ridge National Laboratory (1977).
9. R. A. Lillie, R. G. Alsmiller, Jr. and J. T. Mihalcz, "Design Calculations for a 14-MeV Neutron Collimator," Nucl. Technol. 43, 373 (1979).
10. W. A. Rhoades and F. R. Mynatt, "The DOT III Two-Dimensional Discrete Ordinates Transport Code," ORNL/TM-4280, Oak Ridge National Laboratory (1979).
11. E. Schmidt and P. F. Rose, "Monte Carlo Calculations of a Fusion Reactor Shielding Experiment," Nucl. Sci. Eng. 84, 300 (1983).
12. R. T. Santoro and J. M. Barnes, "Monte Carlo Calculations of Neutron and Gamma-Ray Energy Spectra for Fusion Reactor Shield Design: Comparison with Experiment," ORNL/TM-8707 (1983)

## II. COMPILATION OF SHIELDING BENCHMARK SPECIFICATIONS

## SB6. Fusion Reactor Shielding Benchmark II

A. Benchmark Name and Type: Fusion Reactor Shielding Benchmark II: Duct Streaming Experiments and Analyses.

B. System Description: Neutron and photon flux spectra have been measured and calculated for the case of neutrons produced by D-T reactions streaming through a cylindrical iron duct surrounded by concrete. Measurements and calculations have also been obtained when the iron duct is partially filled by a laminated stainless steel and borated polyethylene shadow bar.

C. Model Description: The experimental configuration is three-dimensional but may to a good approximation be reduced to a two-dimensional configuration. The three-dimensional configuration will first be described and then the two-dimensional configuration used in the ORNL analysis will be discussed. Both the three-dimensional configuration and the approximate two-dimensional configuration are similar to those used in the benchmark SB5.<sup>1</sup>

## 1. Three-Dimensional Configuration

In Fig. 1 a horizontal cut through the room that houses the experiment is given. In this figure and throughout this discussion the z-axis is the axis of the deuteron beam, the x-axis is parallel to the floor and roof, and the y-axis is perpendicular to the floor and the roof. The iron cavity liner around the target serves as a spectrum modifier and makes the neutron spectrum incident on the experimental shield configuration similar to the spectrum incident on the first wall of a fusion reactor. The thermal neutron shield in Figure 1 is composed of stainless steel 304, is 5.08 cm thick, and has a square cross sectional area, 152.4 cm by 152.4 cm. In Figs. 2 and 3 other views of the experimental enclosure and the experimental room are given.

In the present series of experiments the spatial region labeled "the experimental shield configuration", Fig. 1 was filled by a concrete block with a cylindrical iron duct at its center. The concrete block has a height of 172.72 cm, a width of 156.2 cm and a length of 78.0 cm. The iron duct has an inside diameter of 30.0 cm, a thickness of 7.50 cm. The iron duct forms an extension of the source can. The duct extends 85.0 cm from the tritium target (neutron source) and the length-to-diameter (L/D) ratio of the duct is 2.83. The L/D ratio is measured from the tritium target to the mouth of the duct.

The dimensions given in Figs. 1-3 and above are sufficient to enable the experiment to be modeled to any desired detail, but the reader who wishes to model the experiment in three dimensions should also see Ref. 2. The positions of the detectors in Figs. 1 and 3 are only illustrative. The detector positions at which experimental data are available, are completely defined in Section D.

## 2. Two-Dimensional Configuration

In Fig. 4 the reduced geometry representation of the experiment that is used to obtain the calculated results presented later is shown. In some cases the iron duct was partially filled by a cylindrical shadow. In Fig. 5 the reduced geometry of the experiment is shown with the shadow bar in place. Also, in Fig. 5, the dimensions and composition of the shadow bar are shown. The end of the shadow bar closest to the source is at  $z = 77.0$  cm.

The geometry in Figs. 4 and 5 is two-dimensional in that there is cylindrical symmetry about the  $z$  axis. The concrete block around the duct has a radius of 72.5 cm. In the two-dimensional model the lithiated paraffin that is shown in Fig. 1 is not included. Also in the two-dimensional model the back concrete wall is placed directly against the stainless steel thermal shield.

In the two-dimensional model the radial boundary of the configuration is taken as an albedo surface with a reflection coefficient of 0.2 for all particle types and all energies. This reflection coefficient was determined by matching particle flux contours obtained with the two-dimensional



FIGURE 3

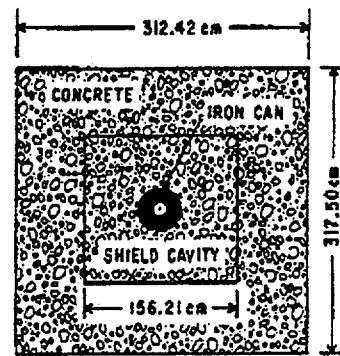
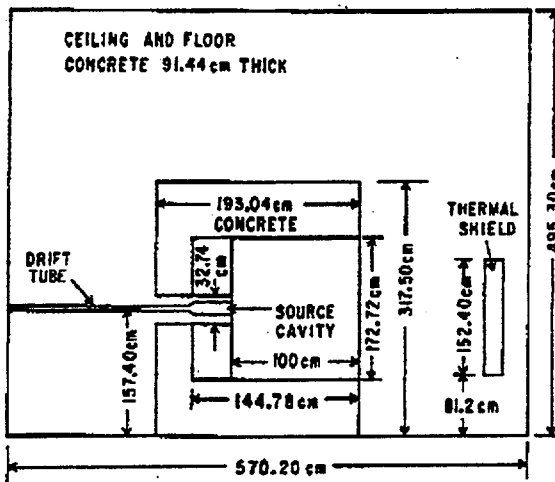
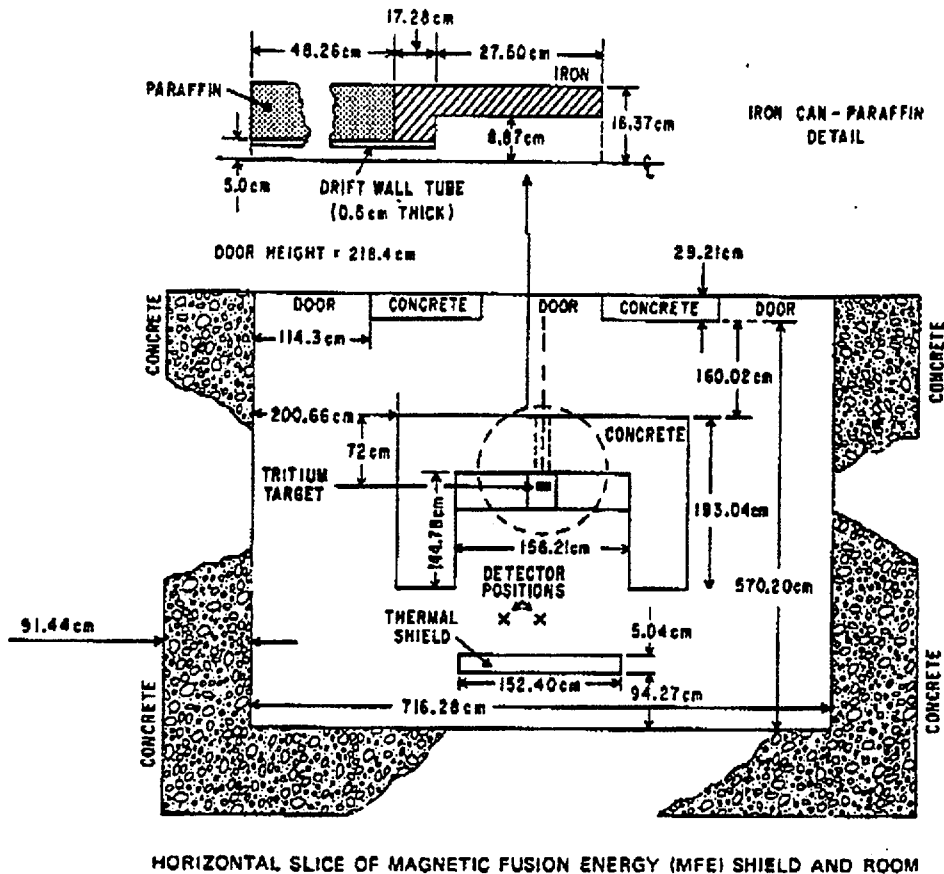


Fig. 3. Additional schematics of experimental enclosure. See Figs. 1 and 2 for additional dimensions. [Drawing not to scale]

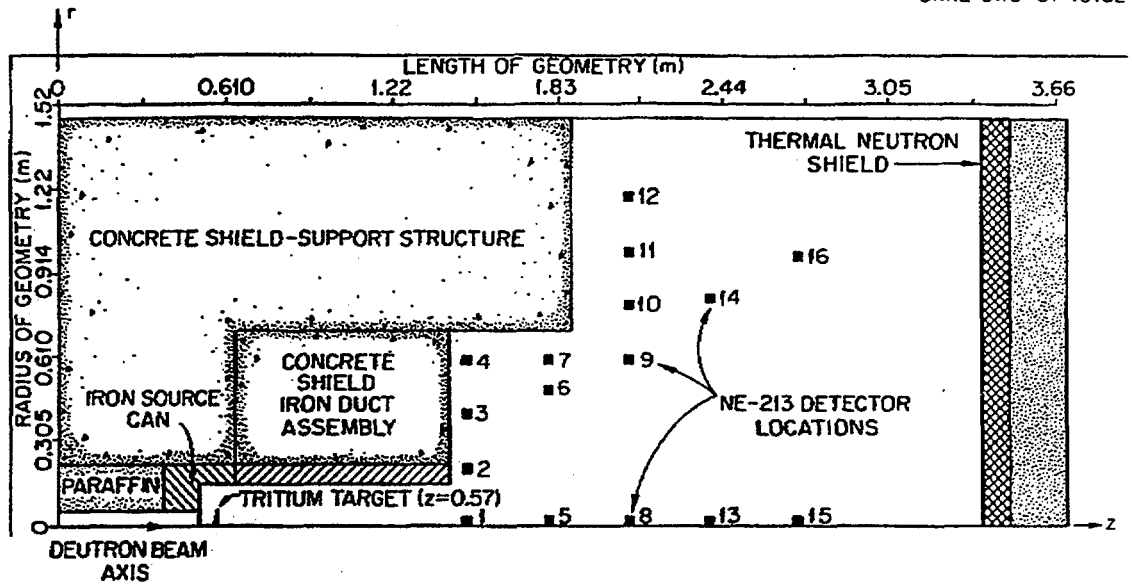


Fig. 4. Two-dimensional model of the experimental configuration. The model is cylindrically symmetric about the deuteron beam axis.

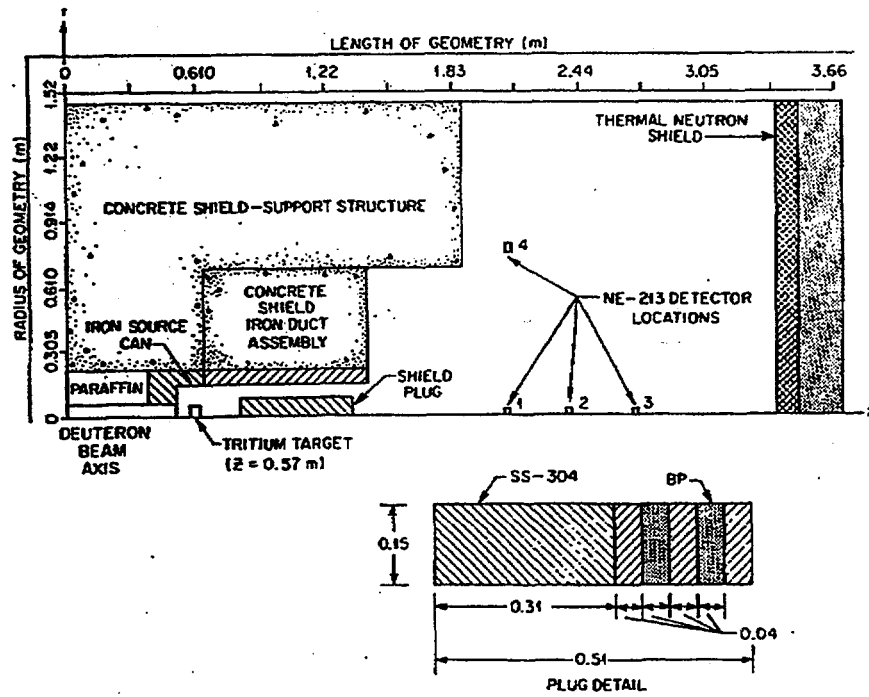


Fig. 5. Two-dimensional model of the experimental configuration with the shield plug, i.e., shadow bar, in place.

representation of the complete experimental room. More details concerning the determination of this reflection coefficient will be found in Ref. 2.

### 3. Material Composition

In Table 1 the number densities of the materials that occur in Figs. 1-5 are given. These are the number densities that were used in carrying out all of the calculation.

### 4. Method of Calculation

With the two-dimensional model the benchmark may be calculated with either discrete ordinates or Monte Carlo methods. In the case of discrete ordinates methods, however, satisfactory results are not obtained until corrections obtained using Monte Carlo methods are applied. The calculational procedures are described and the results obtained are presented in Section E, Analytical Results and Comparisons with Experimental Data.

The benchmark may also be calculated using a three-dimensional model and Monte Carlo techniques, but such calculations have not yet been performed.

D. Experimental Data: The neutron source was obtained by focusing a 250 keV deuteron beam on a cylindrical titanium-tritide (TiT) target having a radius of 0.64 cm, a thickness of 4 mg/cm<sup>3</sup> and a density of 4.28 g/cm<sup>3</sup>. The neutron source strength was measured by using the associated particle technique.

The neutron-gamma-ray detector consisted of 66.1 g of NE-213 liquid scintillator contained in a cylindrical aluminum can having a wall thickness of  $4.32 \times 10^{-2}$  cm. The active volume of the detector was 79 cm<sup>3</sup> (4.66 cm diameter and 4.66 cm height). Neutron and gamma-ray events were separated using pulse shape discrimination methods. The neutron and gamma pulse height spectra were unfolded using FERD<sup>4</sup> to produce energy spectra. The neutron response matrix was obtained using the pulsed neutron beam from the Oak Ridge Electron Linear Accelerator and the gamma-ray response matrix was generated using gamma-ray sources of known energy. The energy resolution of the

detector varies as

$$R_N = \sqrt{300 + \frac{800}{E_N}} \quad (1)$$

for neutrons of energy  $E_N$  in MeV, and

$$R_\gamma = \sqrt{130 + \frac{288}{E_\gamma}} \quad (2)$$

for gamma rays of energy  $E_\gamma$  in MeV. The quantities  $R_N$  and  $R_\gamma$  are the full width at half maximum (in percent) of the detector response (assumed Gaussian) to neutrons and gamma rays.

Experimental data have been obtained at 16 detector locations when the shadow bar was not present and at 4 detector locations when the shadow bar was present. In the experiment, the detector position was specified in a right-handed coordinate system with the z axis corresponding to the deuteron beam axis and the x axis parallel to the experimental room floor. The coordinates of the detector positions at which experimental data are available are given in Table 2. The origin of z coordinates is as shown in Figs. 4 and 5. In this coordinate system the target is at  $z = 0.57\text{m}$  so the source to detector distance is obtained by subtracting 0.57m from the z coordinate of the detector given in Table 2. The detector positions are shown in Figs. 4 and 5. In the two dimensional models the radial coordinates of the detector are given by  $\sqrt{x^2+y^2}$ .

At each detector location the neutron flux per unit energy for all energies  $>850$  keV and the gamma-ray flux per unit energy for all energies  $>750$  keV have been measured. The experimental data at each detector location are given in Appendix A. As part of the data unfolding process, a confidence interval with a width of two standard deviations is obtained so the data presented are in all cases the upper and lower limits of this confidence interval.

Table 1. Composition of Materials Used in the Calculation

Element	Number Density (atom/cm Barn)					
	Concrete	Air	Iron	SS-304	BP*	LP**
H	$7.86 \times 10^{-3}$				$7.13 \times 10^{-2}$	$5.926 \times 10^{-2}$
B-10					$4.87 \times 10^{-4}$	
B-11					$1.97 \times 10^{-3}$	
C					$3.41 \times 10^{-2}$	$3.338 \times 10^{-2}$
N		$3.64 \times 10^{-5}$				
O	$4.39 \times 10^{-2}$	$9.74 \times 10^{-6}$			$3.64 \times 10^{-3}$	$1.125 \times 10^{-2}$
Na	$1.05 \times 10^{-3}$					
Mg	$1.40 \times 10^{-4}$					
Al	$2.39 \times 10^{-3}$					
Si	$1.58 \times 10^{-2}$					
K	$6.90 \times 10^{-4}$					
Ca	$2.92 \times 10^{-3}$					
Cr				$1.77 \times 10^{-2}$		
Mn				$1.77 \times 10^{-3}$		
Fe	$3.10 \times 10^{-4}$		$8.48 \times 10^{-2}$	$6.02 \times 10^{-2}$		
Ni				$7.83 \times 10^{-3}$		
Li-6						$5.565 \times 10^{-4}$
Li-7						$6.944 \times 10^{-3}$

\*BP = Borated Polyethylene

\*\*LP = Lithiated Paraffin

E. Analytical Results and Comparisons with Experimental Data: All of the analytical results reported in this benchmark description are based on the two-dimensional configurations shown in Figs. 4 and 5.

In the three subsections below, analytical results obtained using discrete ordinates methods, discrete ordinates plus Monte Carlo methods, and Monte Carlo methods are presented and compared with the experimental data. Only representative comparisons are presented here but comparisons with all of the data are given in Refs. 5, 6, and 7.

#### 1. Discrete Ordinates Transport Methods

The sequence of radiation transport calculations used to obtain neutron and gamma-ray spectra by discrete ordinates methods is complex and has been described in detail elsewhere so only a very brief description will be given here.<sup>1,2,5,6,7</sup>

The configuration in Fig. 4 was modeled in r-z geometry using 62 radial and 87 axial mesh intervals. The radial and axial boundaries used in the calculations are given in Table 3. The energy-angle dependence of the neutrons from the D-T source was taken into account in the calculations by the methods described in Refs. 1, 2, 5, 6, and 7. The cross section data used are based on ENDF/B-IV, are the same as those used in Ref. 1, and are available from the Radiation Shielding Information Center of the Oak Ridge National Laboratory.<sup>8</sup> The group boundaries are shown in Table 4. The calculations were carried out using the DOT<sup>9</sup> code in conjunction with the first and last flight codes GRTUNCL<sup>10</sup> and FALSTF<sup>11</sup>. In the calculations, a  $S_{12}$  angular quadrature and a  $P_3$  Legendre expansion were used. A flux convergence criterion of  $10^{-4}$  was used and the flux was calculated using weighted differences. Here, as in Ref. 1, the radial boundary of the two-dimensional configuration was taken to be an albedo surface for both neutron and gamma rays, with a reflection coefficient of 0.20 at all energies. The manner in which this reflection coefficient was derived is described in Ref. 2.

In Fig. 6 the calculated and experimental neutron fluxes per unit

Table 2. Detector Coordinates

Detector Number	Detector Coordinates (m)		
	x	y	z
1	0.00	0.00	1.51
2	0.19	0.00	1.51
3	0.39	0.00	1.51
4	0.59	0.00	1.51
5	0.00	0.00	1.78
6	0.47	0.00	1.78
7	0.59	0.00	1.78
8	0.00	0.00	2.08
9	0.59	0.00	2.08
10	0.79	0.00	2.08
11	0.98	0.00	2.08
12	1.19	0.00	2.08
13	0.00	0.00	2.38
14	0.81	0.00	2.38
15	0.00	0.00	2.70
16	0.98	0.00	2.70
1	0.00	0.00	2.08
2	0.00	0.00	2.38
3	0.00	0.00	2.70
4	0.79	0.00	2.08

\*Figs. 4 and 5 show a two-dimensional model of the experimental configuration, so in Figs. 4 and 5 the radial position,  $r$ , of the detector is given by  $\sqrt{x^2+y^2}$ .

Table 3. The Radial and Axial Boundaries Used in the Two-Dimensional Model of the Experiment

Radial Boundaries (cm)		Axial Boundaries <sup>a</sup> (cm)	
0	6.0000E 01	1.5000E 02	2.9498E 02
5.0000E-01	6.1000E 01	1.5750E 02	2.9798E 02
1.0000E 00	6.4000E 01	1.6500E 02	2.9898E 02
2.0000E 00	6.7000E 01	1.7250E 02	2.9998E 02
3.0000E 00	7.0000E 01	1.8000E 02	3.0348E 02
4.0000E 00	7.3000E 01	1.8750E 02	3.0698E 02
5.0000E 00	7.6000E 01	1.9500E 02	3.1048E 02
7.5000E 00	7.9000E 01	1.9650E 02	3.1398E 02
1.0000E 01	8.0000E 01	1.9800E 02	3.1748E 02
1.2500E 01	8.1000E 01	1.9950E 02	3.2098E 02
1.5000E 01	8.3833E 01	2.0100E 02	3.2448E 02
1.6333E 01	8.6667E 01	2.0250E 02	3.2798E 02
1.7667E 01	8.9500E 01	2.0350E 02	3.2898E 02
1.9000E 01	9.2333E 01	2.0450E 02	3.2998E 02
2.0397E 01	9.5167E 01	2.0550E 02	3.3249E 02
2.1795E 01	9.8000E 01	2.0650E 02	3.3499E 02
2.4197E 01	9.9500E 01	2.0750E 02	3.3750E 02
2.6598E 01	1.0100E 02	2.0850E 02	3.5798E 02
2.9000E 01	1.0400E 02	2.0950E 02	3.5898E 02
3.0000E 01	1.0700E 02	2.1050E 02	3.5998E 02
3.1000E 01	1.1000E 02	2.1150E 02	3.6931E 02
3.3667E 01	1.1300E 02	2.1250E 02	3.7865E 02
3.6333E 01	1.1600E 02	2.1400E 02	3.8798E 02
3.9000E 01	1.1900E 02	2.1407E 02	3.8898E 02
4.0000E 01	1.2000E 02	2.1650E 02	3.8998E 02
4.1000E 01	1.2100E 02	2.2053E 02	3.9998E 02
4.4000E 01	1.2700E 02	2.2455E 02	4.0998E 02
4.7000E 01	1.4000E 02	2.2858E 02	4.1998E 02
5.0000E 01	1.4250E 02	2.3261E 02	4.2098E 02
5.3000E 01	1.4500E 02	2.3663E 02	4.2198E 02
5.6000E 01	1.4750E 02	2.4066E 02	4.3307E 02
5.9080E 01		2.4469E 02	4.4415E 02
		2.4871E 02	4.5524E 02
		2.5274E 02	4.6633E 02
		2.5677E 02	4.7741E 02
		2.6079E 02	4.8850E 02
		2.6482E 02	4.9100E 02
		2.6885E 02	4.9350E 02
		2.7287E 02	4.9600E 02
		2.7690E 02	4.9850E 02
		2.8093E 02	5.0375E 02
		2.8495E 02	5.0900E 02
		2.8898E 02	5.1426E 02
		2.9198E 02	5.1950E 02

<sup>a</sup>These axial boundaries have an origin of coordinates that is different from that shown in Figs. 4 and 5. To express the axial boundaries in the coordinate system with the origin of coordinates as shown in Figs. 4 and 5, the value 150 cm must be subtracted from the values given in the table.

Table 4. <sup>53</sup>-Neutron, 21-Gamma-Ray Energy Radiation  
Transport Cross Section Group Structure

Neutron Group	Upper Energy (eV)	Neutron Group	Upper Energy (eV)	Gamma Ray Group	Upper Energy (MeV)
1	0.17333E + 08	28	0.60810E + 06	1	14.0
2	0.15683E + 08	29	0.49787E + 06	2	12.0
3	0.14918E + 08	30	0.36883E + 06	3	10.0
4	0.14550E + 08	31	0.29850E + 06	4	8.0
5	0.14191E + 08	32	0.29720E + 06	5	7.5
6	0.13840E + 08	33	0.18316E + 06	6	7.0
7	0.13499E + 08	34	0.11109E + 06	7	6.5
8	0.12840E + 08	35	0.67379E + 05	8	6.0
9	0.12214E + 08	36	0.40868E + 05	9	5.5
10	0.11052E + 08	37	0.24788E + 05	10	5.0
11	0.10000E + 08	38	0.23579E + 05	11	4.5
12	0.90484E + 07	39	0.15034E + 05	12	4.0
13	0.81873E + 07	40	0.91188E + 04	13	3.5
14	0.74082E + 07	41	0.55308E + 04	14	3.0
15	0.60653E + 07	42	0.33546E + 04	15	2.5
16	0.49659E + 07	43	0.20347E + 04	16	2.0
17	0.40657E + 07	44	0.12341E + 04	17	1.5
18	0.36788E + 07	45	0.74852E + 03	18	1.0
19	0.27253E + 07	46	0.45400E + 03	19	0.60
20	0.23653E + 07	47	0.27536E + 03	20	0.20
21	0.23069E + 07	48	0.16702E + 03	21	0.10
22	0.22313E + 07	49	0.10130E + 03		0.01
23	0.16530E + 07	50	0.61442E + 02		
24	0.13534E + 07	51	0.37267E + 02		
25	0.86294E + 06	52	0.10677E + 02		
26	0.82085E + 06	53	0.41399E + 00		
27	0.74274E + 06		0.10000E - 04		

energy are shown for detectors 1 to 4 in Fig. 4, i.e., at  $z = 1.51\text{m}$  and  $r = 0.0, 0.19, 0.39, \text{ and } 0.59\text{m}$ . The solid curves are the measured spectra and the points show the calculated results. The two solid curves for each detector location represent the 68% confidence interval, i.e., plus and minus one standard deviation, in the measured spectra that is introduced by the unfolding procedure used to obtain the neutron spectra from the pulse-height distributions. The calculated data have been smoothed by convoluting the neutron flux per unit energy in each multigroup interval with an energy-dependent Gaussian response function having a width given by Eq. (1). The calculated and measured spectra are absolutely normalized to a source strength of one D-T neutron. For purposes of displaying the data, some of the spectra have been multiplied by  $10^{-n}$ ,  $n=1, 2, \text{ etc.}$  The actual magnitude of these spectra are restored by multiplying by the appropriate factor of  $10^n$ .

Inspection of Fig. 6 reveals that the calculated and measured spectra are generally in good agreement in the neutron energy range between 850 keV and  $\sim 10$  MeV. The neutrons that contribute to the spectra in this energy range result from inelastic reactions of the source and secondary neutrons in the experimental apparatus or are those which have undergone multiple collisions in transit from the source to the detector.

At neutron energies above  $\sim 10$  MeV, the agreement among the calculated and measured differential neutron energy spectra is less favorable and the agreement varies significantly as a function of detector location. The neutrons that contribute to the spectra in this energy range are either uncollided neutrons emanating directly from the source (particularly for the on-axis detectors) or are those that reach the detector as the result of a single scattering from the experimental apparatus, particularly the iron duct. These single scattered neutrons arise from both elastic and inelastic reactions which at energies above  $\sim 10$  MeV have angular distributions that are very forward peaked. When these angular distributions are represented by a  $P_3$  Legendre expansion, the angular dependence of the scattering probabilities are not adequately described. As a result, the neutron flux at the detector may be either over- or under-estimated depending upon the angle at which the neutron scatters in transit from the source to the detector. This phenomenon

is evident in the calculated spectra at the off-axis detector locations shown in Fig. 4.

In order to assess the impact of single scattering on the neutron energy spectra, the discrete ordinates calculations were carried out using a  $P_7$  Legendre polynomial expansion to represent the neutron scattering cross sections. Although some improvement was noted in the agreement between the calculated and measured spectra, it became apparent that satisfactory comparisons required an even higher order of expansion to account for the single scattered neutron contribution to the high energy neutron flux. Results obtained when the single scattering contribution to the neutron flux is calculated using Monte Carlo methods are presented in the next subsection of this benchmark specification.

The calculated differential gamma-ray spectra are compared with the measured spectra in Fig. 7 for the same four detectors considered in Fig. 6. Similar comparisons for the other detector locations in Fig. 4 are given in Ref. 5. These spectra are compared for gamma rays having energies above 750 keV. The calculated data were obtained by convoluting the gamma-ray flux per unit energy in each multigroup energy interval with an energy-dependent Gaussian response function having a width given by Eq. (2). All of the calculated data were obtained using the discrete ordinates transport methods. Gamma rays produced from inelastic and neutron capture reactions have nearly isotropic angular distributions and are well represented in the discrete ordinates transport calculations by a  $P_3$  Legendre polynomial expansion. The calculation generally reproduces the measurements in magnitude but because of the rather coarse energy group structure, the various peaks in the measured differential distributions are not reproduced.

## 2. Discrete Ordinates Plus Monte Carlo Transport Methods

To determine if the discrepancies shown in Fig. 6 are due to an inadequate calculation of the single scattering contribution to the neutron flux, a procedure was developed that allows the single scattering contribution to be calculated by Monte Carlo methods. This procedure is described in

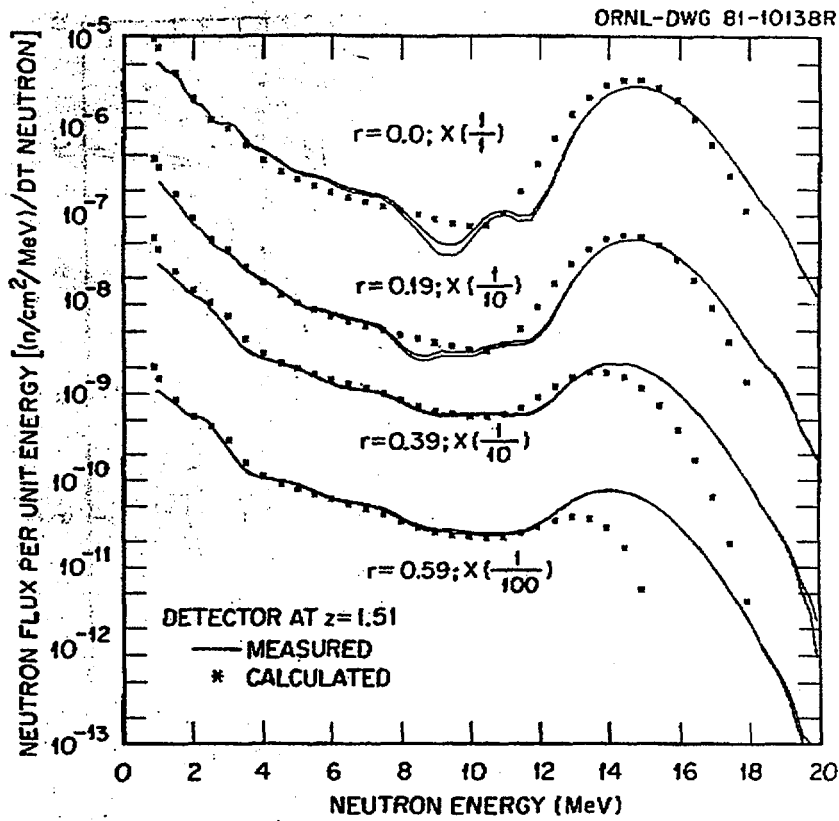


Fig. 6. Neutron flux per unit energy versus neutron energy for the detectors at  $z = 1.51$  m;  $r = 0.0, 0.19, 0.39,$  and  $0.59$  m. The calculated data were obtained using discrete ordinates radiation transport methods.

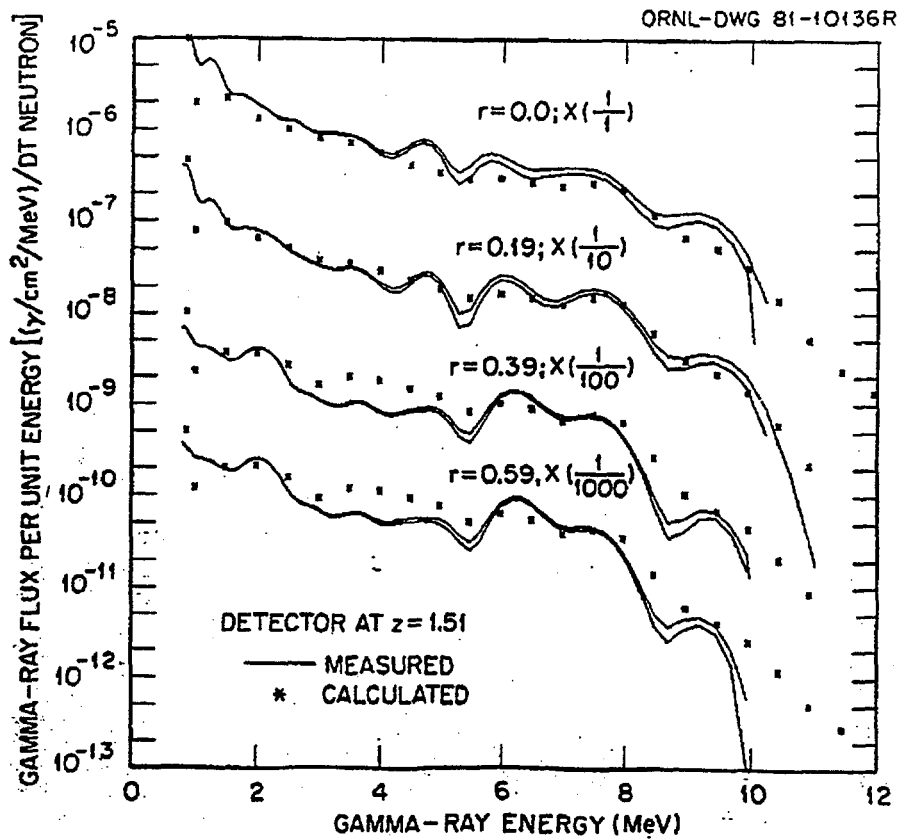


Fig. 7. Gamma-ray flux per unit energy versus gamma-ray energy for the detectors at  $z = 1.51$  m;  $r = 0.0, 0.19, 0.39,$  and  $0.59$  m. The calculated data were obtained using discrete ordinates radiation transport methods.

detail in Ref. 5 so only a brief discussion will be given here. Basically, for neutron energies  $>10$  MeV, the first collision contribution to the neutron flux per unit energy as obtained by discrete ordinates methods using the  $P_3$  Legendre expansion is removed, i.e., subtracted, from the total neutron flux per unit energy and a Monte Carlo estimate of this first collision contribution is used. The Monte Carlo estimate is obtained using a Monte Carlo code that samples directly from the angular distributions that are included in the ENDF/B-IV file. In the work reported here, the recently developed Monte Carlo code PX MORSE<sup>12</sup> was used to estimate the single scattering contribution, but any other continuous energy-angle Monte Carlo code could be used.

In Fig. 8 the calculated and experimental neutron flux per unit energy are compared for the same detector locations that were considered in Fig. 6; i.e., the experimental data in Fig. 8 are the same as those in Fig. 6.

As in Fig. 6, the solid curves show the measured spectra and the points are the calculated data. In Fig. 8, two sets of calculated points are given for some detector locations at neutron energies above  $\sim 10$  MeV. These points indicate the upper and lower bounds on the calculated spectra due to the statistical variation in the estimated single scattered neutron scalar flux introduced by the Monte Carlo calculations. The band defined by these points represents plus or minus one standard deviation in the calculated data.

Comparison of these data with those shown in Fig. 6 reveal that significant improvement at the higher energies has been achieved among the calculated and experimental spectra when the calculated data are obtained using the improved treatment of neutron single scattering.

Consider the cases where the detector is on the axis of the duct, i.e.,  $r = 0.0$ . The agreement between the calculated and measured neutron spectra is favorable above  $\sim 10$  MeV. In the neutron energy range between  $\sim 11$  and  $\sim 13$  MeV, the calculated data are higher than the measured data, but the difference between the calculated and measured data is reduced compared to the same spectra shown in Fig. 6.

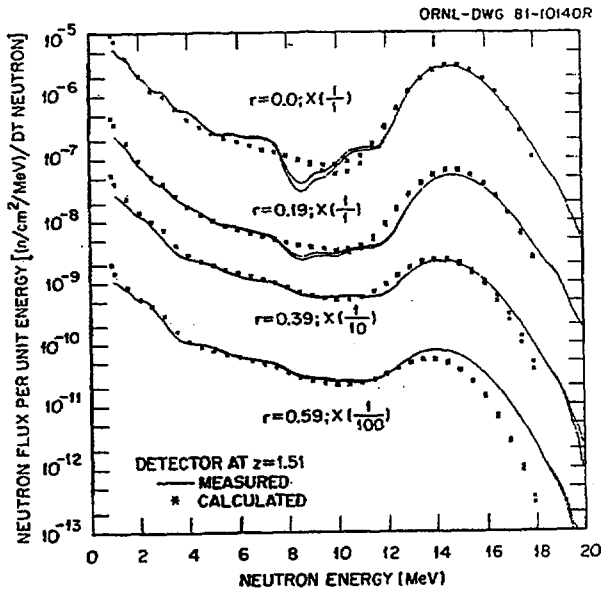


Fig. 8. Neutron flux per unit energy versus neutron energy for the detectors at  $z = 1.51$  m;  $r = 0.0, 0.19, 0.39,$  and  $0.59$  m. The calculated data were obtained using a combination of discrete ordinates and Monte Carlo radiation transport methods.

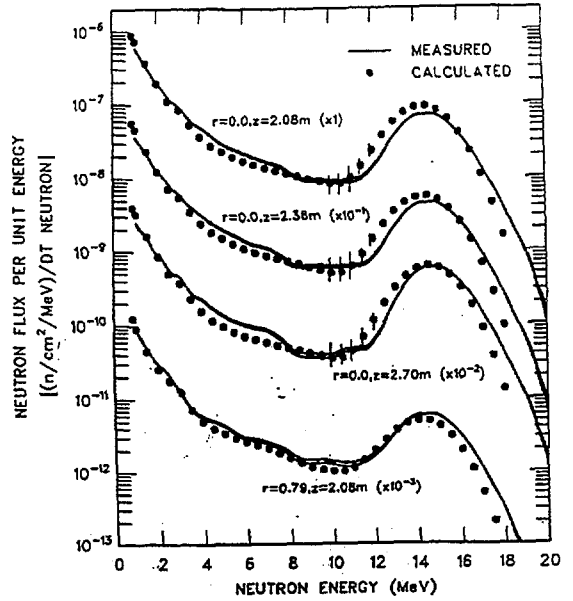


Fig. 9. Neutron flux per unit energy versus neutron energy for the detectors at  $r = 0.0$  m, and  $z = 2.08, 2.38,$  and  $2.70$  m and at  $r = 0.79$  m,  $z = 2.08$  m. The results in this figure are for the case when the shadow bar (see Fig. 5) is in place. The calculations were carried out using a combination of discrete ordinates and Monte Carlo transport methods.

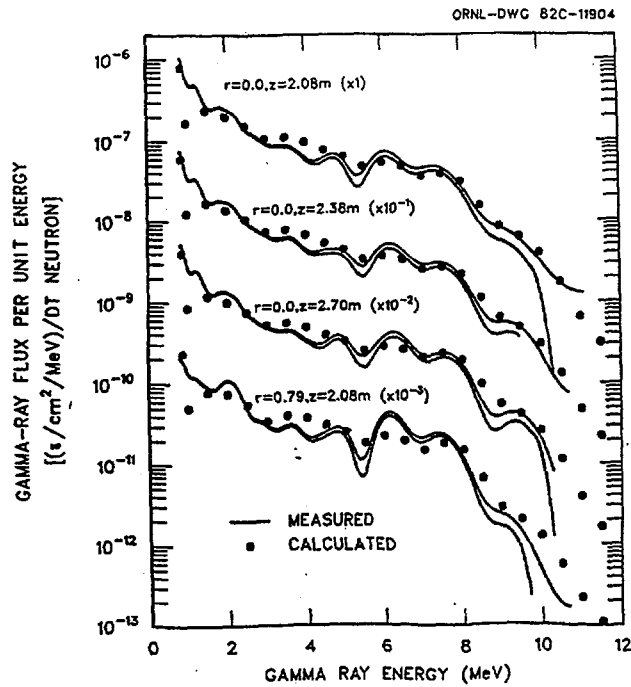


Fig. 10. Gamma-ray flux per unit energy versus gamma-ray energy for the detectors at  $r = 0.0$  m and  $z = 2.08, 2.38,$  and  $2.70$  m and  $r = 0.79$  m and  $z = 2.08$  m. The calculations were carried out using discrete ordinates radiation transport methods.

Calculated results obtained are compared with the data measured when the shadow bar was in place (see Fig. 5) in Figs. 9 and 10. The calculated neutron results were obtained using a combination of discrete ordinates and Monte Carlo methods as explained above and the calculated gamma-ray results were obtained using only discrete ordinates methods. The degree of agreement between the calculated and measured neutron spectra in Fig. 9 is similar to that shown in Fig. 8. Similarly, the degree of agreement between the calculated and experimental gamma ray data in Fig. 10 is comparable to that shown in Fig. 7.

### 3. Monte Carlo Transport Methods

In this subsection, calculated results obtained using entirely Monte Carlo methods are presented and compared with the experimental data. The geometry used in the calculations is that shown in Fig. 4. Computational results obtained using Monte Carlo methods for the configuration in Fig. 5, i.e., the configuration with the shadow bar in place, have not been made.

The calculations were carried out with the code MCNP.<sup>13</sup> MCNP is a general purpose, continuous-energy, generalized geometry, time-dependent coupled neutron-photon Monte Carlo transport code. Pointwise cross section data are treated in considerable detail in energy grids that are tailored for each isotope in the cross section data libraries. The angular distributions for elastic and inelastic scattering are also described on a fine grid of incident neutron energies and linear interpolation methods are used to obtain the angular distribution of the scattered neutrons vs. incoming neutron energy. The angular distributions of the outgoing particles are then sampled in a continuous fashion. In these calculations, however, the reflection coefficient of 0.2 for neutrons and gamma rays at the radial boundary of the two-dimensional configuration (see Fig. 2) was not included; i.e., particles were allowed to escape from these boundaries without reflection. Much more detail concerning the code will be found in Ref. 13.

The energy-angle distribution of the source neutrons was taken into account in the same manner as that described previously. The calculations

were carried out using cross section data based on ENDF/B-V and are those available at the National Magnetic Fusion Energy Computing Center for use with MCNP. More details concerning the calculational procedure will be found in Ref. 7.

The Monte Carlo fluxes were binned into energy intervals having the same widths as those used in the calculations in Refs. 1, 5, 6, and 7 and the smoothing of the MCNP results with the detector response was carried out in the same manner as in these references. The error bars on the MCNP results correspond to one standard deviation. When no error bars are shown, they are smaller than the plotted points. The error bars were obtained by separately smoothing the upper and lower bounds of the fluxes determined from the statistical variation in the fluxes in each energy bin.

In Fig. 11 the calculated and experimental neutron fluxes per unit energy per source neutron for detector locations 8, 9, and 11 in Fig. 4 are shown. The corresponding gamma-ray fluxes at detectors 8 and 9 are shown in Fig. 12.

Examination of Figs. 11 and 12 shows that the spectra calculated with MCNP are generally in good agreement with the experimental data.

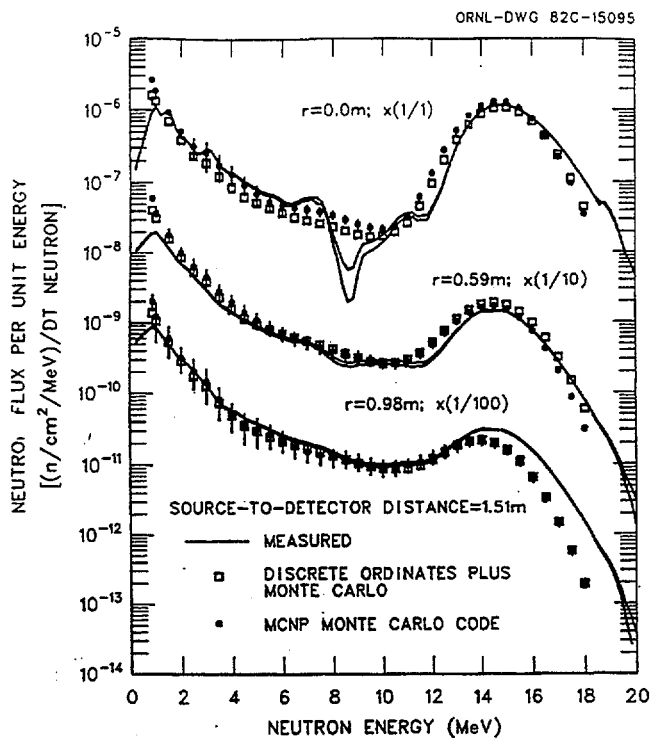


Fig. 11 Neutron flux per unit energy versus neutron energy for a source-to-detector distance of 1.51 m and radial distances of 0.0, 0.59, and 0.98 m from the axis. The target is at  $z = -0.57$  so the  $z$  position of the detector in the coordinate system of Fig. 4 is 2.08 m.

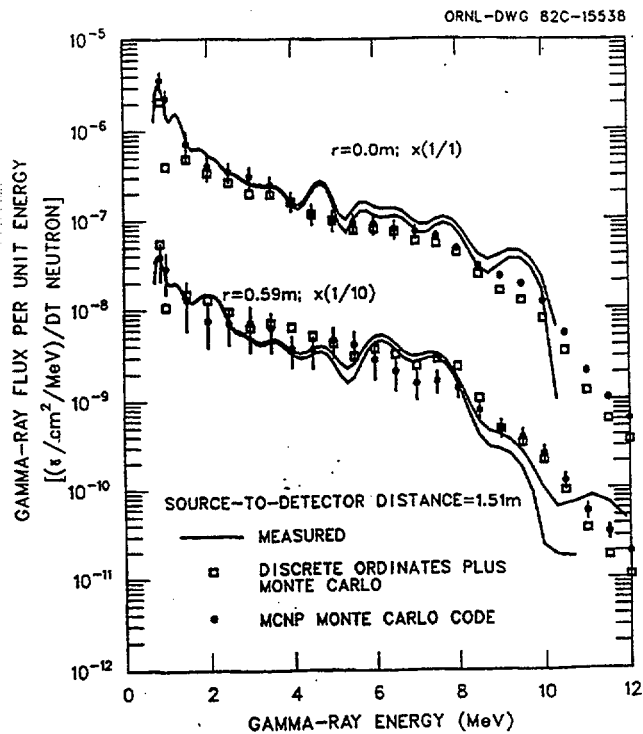


Fig. 12 Gamma-ray flux per unit energy versus gamma-ray energy for a source-to-detector distance of 1.51 m and radial distances of 0.0 and 0.59 m from the axis. The target is at  $z = -0.57$  so the  $z$  position of the detector in the coordinate system of Fig. 4 is 2.08 m.

## REFERENCES

1. Cross Section Evaluation Working Group Benchmark Specifications, Benchmark SB5, "Fusion Reactor Shielding Benchmark", BNL-19302, Vol. II, Brookhaven National Laboratory (1983).
2. R. T. Santoro et al., "Calculational Procedures for the Analysis of Integral Experiments for Fusion Reactor Design", ORNL/TM-5777, Oak Ridge National Laboratory (1981).
3. T. R. Fewell, "Absolute Determination of 14-MeV Neutron Yields", SC-RR-67-346, Sandia Laboratories (1967).
4. W. R. Burrus and V.V. Verbinski, "Fast-Neutron Spectroscopy With Thick Organic Scintillators", Nucl. Inst. Methods 67, 181 (1969).
5. R. T. Santoro et al., "Calculated Neutron and Gamma-Ray Energy Spectra From 14-MeV Neutrons Streaming Through an Iron Duct: Comparison with Experiment", Nucl. Sci. Eng. 80, 586 (1982).
6. R. T. Santoro et al., "Comparison of Measured and Calculated Neutron and Gamma-Ray Energy Spectra Behind an In-Line Shielded Duct", J. of Fusion Energy 2, 6 (1982).
7. R. T. Santoro et al., "Streaming of 14-MeV Neutrons Through an Iron Duct - Comparison of Measured Neutron and Gamma-Ray Energy Spectra with Results Calculated Using the Monte Carlo MCNP Code", Nucl. Sci. Eng. 84, 260 (1983).
8. ORNL/RSIC-37 Radiation Shielding Information Center, Oak Ridge National Laboratory (1975), available as DLC/41-VITAMIN C.

## REFERENCES (cont'd)

9. W. A. Rhoades and F. R. Mynatt, "The DOT III Two-Dimensional Discrete Ordinates Radiation Transport Code", ORNL/TM-4280, Oak Ridge National Laboratory (1979).
10. R. A. Lillie, R. G. Alsmiller, Jr., and J. T. Mihalcz, "Design Calculations for a 14-MeV Neutron Collimator", Nucl. Technol. 43, 373 (1979).
11. "FALSTF, Informal Notes", CCC-351, Radiation Shielding Information Center, Oak Ridge National Laboratory (1979).
12. M. M. Wadell, Jr., "EXMORSE, A Continuous Energy Monte Carlo Code", Ph.D. Thesis, University of Tennessee (1981).
13. "MCNP - A General Purpose Monte Carlo Code for Neutron and Photon Transport", LA-7396-M (Rev.) Los Alamos National Laboratory, Los Alamos Monte Carlo Group (1981).

**NEXT PAGE(S)  
left BLANK**

The talk presented at IAEA Consultants Meeting on "Preparation of fusion benchmarks in electronic format for nuclear data validation studies" (13-16 December 1993, IAEA, Vienna)

REVIEW OF EXPERIMENTS AND SPECIFICATIONS  
ON NEUTRON LEAKAGE SPECTRA FROM SPHERICAL SHELLS.

S. P. Simakov



XA9642734

Institute of Physics and Power Engineering  
249020 Obninsk, The Russian Federation

Abstract. The main goals of present work are review of publications and compilation of specifications and numerical data on neutron leakage spectra from spherical assembles with T(d,n) or Cf neutron sources in the center. Tables of main experimental parameters, needed for the transport calculations, are presented, as well as analysis of actual experimental factors that cause the deviations from "clean" spherical configuration. The whole numerical information is available for less than 50% of reviewed experiments. These data could be used for intercomparison of experimental data measured in different laboratories and for evaluated data libraries testing.

Introduction

Integral experiments, that simulate the parts of nuclear engineering units, are considered to be suitable for testing of the calculations methods and evaluated data files in more simplified and convenient experimental conditions [1,2]. In the large variety of integral experiments there are ones in which materials under investigation have the shape of spherical shell, and point source of radiation is located in the center (so called clean benchmarks). Due to spherical symmetry (one dimensional geometry), the task is simple for computer simulating that make it possible to systematically examine mainly the validity of evaluated nuclear data libraries both of general interest and processed especially for transport calculations.

In the present work the experiments with T(d,n) and Cf sources, that give monoenergetic 14MeV and continues energy distributed neutrons, are reviewed and compiled. Such experiments are highly important, since these sources have spectral characteristics close

to neutron spectra in fusion or fission reactors. For example, the compilation of benchmarks specifications to validate the FENDL database was indicated as an urgent need at recent Meetings held by IAEA at JAERI, Japan (November 1993) and Chengdu, China (November 1990).

In the previous review [2] the experiments, performed before 1982, are scanned. During last decade many new measurements have been made. Moreover, it seems to be the first time when, besides literature review, the attempt to collect numerical data of original experiments is done. It is obvious that only whole and accurate information is sufficient for intercomparison of different experiments and for evaluated data files testing. This goal assumed receiving numerical specifications about neutron source, size and chemical composition of spheres, and other parameters of experiment that could influenced on comparison of experimental and calculated results.

The first attempt of such compilation was made by author this year and was published in [3]. The present work contains the updated version of compilation, enriched by new recently received data, and analyses of problem how to approximate actual 3 dimensional geometry and measuring methods by simple calculating model.

#### Review of research centers, contributed to this problems

The neutron leakage measurements have been performed in several laboratories in USA, Japan and Europe in the framework of national or international programs. To give the common filling about the total number of experiments, the laboratories, sources type and number of spheres are listed in Table 1. It shows that many experiments is made in a few research centers and it could be used as a database for evaluated data validation.

The details of these experiments are listed in Tables 2-5 and are discussed in paragraphs below.

Table 1. Scope of neutron leakage spectra measurements.

Country	Laboratory	Source	Numb. of Spheres
CSFR	Institute of Radiation Dosimetry, Prague (IRD)	T(d,n)	5
Germany	Technical University, Dresden (TUD)	T(d,n)	2
	Zentralinst. fur Kernforschung, Rossendorf (ROS)	Cf	2
	Kernforschungszentrum, Karlsruhe (KFK)	T(d,n)	3
Japan	Osaka University, Osaka (OSA)	T(d,n)	22
	Tohoku University, Tokyo (TOH)	T(d,n)	1
USA	Livermore National Laboratory (LRL)	T(d,n)	33
	University of Illinois (UI)	T(d,n)	1
	University of Illinois (UI)	Cf	3
	Los Alamos Scientific Laboratory (LAS)	T(d,n)	1
USSR	Inst. of Phys. and Power Eng., Obninsk (FEI)	T(d,n)	19
	Inst. of Phys. and Power Eng., Obninsk (FEI)	Cf	20
	Inst. of Technic. Phys., Chelyabinsk (ITF)	T(d,n)	16
	Kiev State University, Kiev (KGU)	T(d,n)	4
----- Total		T(d,n)+Cf	132

#### Neutron Sources

T(d,n). Neutrons from these reaction are usually generated on electrostatic accelerator (neutron generators) by bombarding the solid tritium targets with deuterons accelerated to energy 100-400keV. Energy and yield are the functions of emission angle, deuteron energy, tritium concentration in the target and other factors. To illustrate the typical anistropy of T(d,n) source, the neutron energy E and relative yield Y versus emission angle  $\theta$  and deuteron energy  $E_d$  for thick TiT target (target thickness more then deuteron stopping range) could be analytically expressed:

$$\begin{aligned}
 E(E_d, \theta) &= E_0(E_d) + E_1(E_d)\cos(\theta) + E_2(E_d)\cos^2(\theta) \\
 Y(E_d, \theta) &= Y_0(E_d) + Y_1(E_d)\cos(\theta) + Y_2(E_d)\cos^2(\theta)
 \end{aligned}
 \tag{1}$$

The parameters of this expressions are determined experimentally for thin target chamber at different deuteron energies [29]. For example at  $E_d=250\text{keV}$ , formulas (1) give the angular anistropy  $Y(0^\circ)/Y(180^\circ) = 11\%$ , and energy variation  $E(0^\circ)-E(180^\circ) = 1.5\text{MeV}$ , that means that T(d,n) reaction is actually spherically nonsymmetric neutron source. Moreover, besides this the neutron yield is influenced by neutron interaction with materials of target assembly and other factors. Hence for correct comparison with transport calculations, the energy-angular distribution of

source neutrons have to be measured or calculated. Such information is available from some experiments, from others - angular-energy distributions of source neutrons should be modeled by Monte-Carlo calculations or at least taken in the simplest form like (1).

$^{252}\text{Cf}$ . The prompt neutron fission spectrum of this isotope is adopted as standard one [30]. The uncertainty is estimated at level 1.2-10% over neutron energy range 0.01-20MeV. In benchmark experiments  $^{252}\text{Cf}$  source is usually packed in thin and small ampoule, so the corrections for attenuation and scattering is small compare to other experimental uncertainties.

In the work [33] the method of time of flight neutron spectroscopy of leaking neutrons with fast ionization chamber is proposed. In that case thin wall (0.35mm) ionizing chamber with  $\emptyset 10\text{mm}$  active Cf layer (intensity of  $10^5$ - $10^6$  neutrons/sec) was used. The fast pulses from the fission chamber give the stop pulses for TOF spectroscopy and total number of the fission events or source neutron yield. The advantage of this method is that measuring of neutron leakage spectra (with sphere) and detector efficiency (fission chamber without shell) are performed in similar experimental conditions, that decrease systematic errors.

#### Spherical assemblies

The reviewed measurements were performed for wide range of materials. These materials are listed in first column of Tables 2-5 in increasing atomic mass number order and materials studies cover main structural and fissile elements. The next columns are sphere outer (R) and inner (r) radii; wall thickness ( $t=R-r$ ) expressed in centimeters and in mean free path of 14MeV or 2.1MeV (in the case of  $^{252}\text{Cf}$  source) neutrons. It is seen from the Tables, that shell thicknesses cover range from 0.2 to 6 of mean free path.

In the experiments with 14MeV neutrons the spheres had a duct (entrance hole) for input beam tube and target chamber. In the experiments with  $^{252}\text{Cf}$  ampoule this duct is usually filled by the same materials. The radius of entrance hole is indicated in column 5. Some shells has more complicated duct shape. For example, the hole in Livermore Laboratory spheres has a cone shape with angle  $8^\circ$ , this is why radius in this case is indicated approximately;

whereas the KFK beryllium shells have two radial channels [19].

The chemical composition and main nucleus concentrations are listed in 6 and 7 columns. These values were taken from original works or from handbook [31], in the case of absent this information, and marked with asterisk. Some spheres were packed outside and/or inside in special containers - its material and thickness are listed in the next column. For example, the note SS-0.47 Cu-0.2 means that outer surface of the sphere was covered by 0.47cm thick stainless steel and inner - 0.2cm copper.

The specification listed in this paragraph are necessary as input parameters for model calculations. Regrettably, there are published experiments, for which some important parameters are not available from publications scanned.

#### Measurement techniques and leakage spectra

The majority of the measurements have been accomplished by time of flight technique (TOF), the other part - by pulse recoiled spectrometry method (PRS). The advantage of TOF method is a higher achievable accuracy, since the time response function of organic scintillator detector has simple Gaussian form, while pulse height response to monoenergetic neutrons is a step like function. Thus, in PRS method one should unfold measured spectrum to obtain energy one, the later procedure introduce additionally uncertainty at least of 10-15%.

The neutron leakage spectra were measured mainly by organic (NE213 liquid, stilbene crystal) or lithium glass scintillation detectors and gas proportional counters. These detectors cover the neutron energy range from thermal to 15MeV (the measured interval is indicated in column 12 for every experiment).

For comparison with transport calculations the distance  $L$  between sphere center and detector is rather important factor. Studies [2] show that at  $L \geq 3R$  the shell may be approximated by a point source of radiation, the measured leakage spectrum (current) is equal the neutron flux at detector spot. In the case of measuring with  $T(d,n)$  source the angle  $\theta$  between sphere-detector axis and deuteron beam is important as well, since due to source anisotropy the outgoing neutron flux have to be angular dependent.

The numerical data on leakage spectra were obtained either from publications or from private communications with authors of original measurements. The data collected in this way upto today are marked with cross in the last column of Tables 2-5. The data of [32] is not indicated in Table 4, since leakage spectra are presented as a time of flight distribution and direct comparison with transport calculation will be complicated.

Formats of numerical data, provided by authors, are slightly different. There are often three of them.

- (1) Leakage energy spectrum (current) with identification of mean or left and right energy of bins:

$LE(E)$  [1/MeV]  $\equiv$  number of neutrons/MeV/one source neutron

- (2) Leakage lethargy spectrum (current):

$LL(E) \equiv$  number of neutrons/ $\ln(E_r/E_l)$ /one source neutron

where  $E_l$  and  $E_r$  are left and right edges of energy intervals

- (2a) In the case of identification of the edges of bins, this spectrum could be converted to energy one using:

$$LE(E) = LL(E) * \ln(E_r/E_l) / (E_r - E_l) \quad (2)$$

- (2b) If only mean bin energies  $E_m$  are present in the file, then it could be done by the next way:

$$LE(E) = LL(E) / E_m \quad (3)$$

Formulas (2)-(3) was used for transformation lethargy spectrum to energy one and back. The same procedure was done with absolute errors array.

For illustration of data collection, the neutron leakage spectra from aluminium shell with  $T(d,n)$  source are shown in the Fig.1. The Al shell of the same size was measured by TOF technique in IPPE (Obninsk) and KGU (Kiev), but by PRS method in IRD (Prague). Fig.1 shows that data disagree each other. Comparison with transport calculation and the energy dependence of Al total cross section results in that IPPE data are more realistic with point of spectrum shape and absolute values.

### Conclusions and Acknowledgements

Up today literature review and the attempt to collect numerical data on neutron leakage spectra measured for spherical assemblies with T(d,n) and  $^{252}\text{Cf}$  sources are made. The present experience discovered the difficulties in searching all necessary numerical specifications about particular experiment in published materials. This forced us to communicate with authors of the original measurements, but this procedure was not always successful as well. As a result, by the end of 1993, the data for less than 50% of published experiments are available for this compilation. On this occasion the author of present compilation would like express his sincere acknowledgments to authors who have sent the numerical data on request.

The author hopes that results of this review and compilation will help to researchers, involved in this problem, to exchange experimental data, compare the experimental results each other and, as a final goal, validate the evaluated data libraries and transport codes.

### Addendum.

In the previous part of this talk the parameters and specifications, that easily could be determined from publications, are compiled and discussed. But besides them, there are specific parameters related to particular measuring technique and experiment. They often are not specified in published materials, but have to be taken into account during the comparison between the experimental and calculated results. There is other problem as well: some transport codes use one-dimensional (spherical) approximation, thus they output could be compared only with the results of ideal spherical benchmark experiment. In practice, however, there are factors that break this symmetry and could brings other perturbation:

- angular anisotropy of source neutrons and energy distortion by target assembly;
- the hole(s) (radial channel) in the shell assembly for input the neutron source;
- time of flight neutron spectrometry with bulk samples.

Therefore before the comparison with one dimensional transport calculations, the experimental data have to be corrected for these factors.

In this Addendum we would like to demonstrate these particular specifications and non-spherical correction procedures, using our own experience in the neutron leakage spectroscopy [20].

Angular distribution of source neutrons. For correct comparison with transport calculations the real angular distribution and energy spectrum of the source neutrons have to be known, since the target chamber could affect on simple energy-angular distribution of neutrons produced in  $T(d,n)$  reaction (1). Historically, in our researches we used two target designs. In the first one (Fig.2a) the  $\varnothing 28\text{mm}$  TiT target on 1mm thick Cu-backing was sealed with help of copper nut. Angular distribution of 14MeV neutrons, measured by Al foils activation and time of flight (TOF) technique, is shown in Fig.3. The experimental points and calculation of exponential attenuation (solid curve) indicate that at angles close to  $90^\circ$  the copper backing and nut attenuate neutron flux by 20% in comparison with prediction for infinitely thin target assembly (1), that corresponds 4% reduction of neutron yield in the whole solid angle. To reduce this effect, we became use in the latter experiments the  $\varnothing 11\text{mm}$  TiT target, hold by the thin (wall thickness 0.5mm) aluminium cone (Fig.2b). The evaluated angular distribution of 14MeV neutrons is shown by dashed curve in the Fig.3. In this case the attenuation of total number of  $T(d,n)$  neutrons is less then 2.5%.

Energy distribution of source neutrons. The neutrons inelastically scattered by the target materials have to affect on energy distribution of source spectrum. This is illustrated in the Fig.5, where the spectra of source neutrons measured with our target assemblies (Fig.2) are shown. The measurements have been performed by time of flight technique in two experimental geometries: short (3.8m) and long (6.8m) flight paths, schematically drawn in Fig.4. The both spectra have asymmetric 14MeV peak of different FWHM and broad energy distribution with maximum near 1MeV.

The FWHM of the 14MeV peak is directly connected with time  $\Delta t$  and spatial  $\Delta L$  resolutions and flight path  $L$  of the spectrometer as well as with intrinsic energy uncertainty  $\Delta E$  of the source. In our

case, given the values  $\Delta t=3.5\text{ns}$ ,  $\Delta L=5.0\text{cm}$ ,  $\Delta E=0.5\text{MeV}$ , the time resolution contribute the dominant part to the visible energy resolution at  $0^\circ$  angle:

$$\Delta E = E \sqrt{(2\Delta t/t^2)^2 + (2\Delta L/L)^2 + (\Delta E/E)^2} = \begin{cases} 1.5\text{MeV}, L=3.8\text{m} \\ 1.0\text{MeV}, L=6.8\text{m} \end{cases} \quad (4)$$

The asymmetric left (low energy) tail of 14MeV peak results from neutron interaction with collimator walls in the detector shielding. This is confirmed by comparatively analysis of geometries: at short flight path source neutrons are collimated by paraffin channel, whereas at 6.8m location - by the iron cone and the hole in the concrete wall; in the first case inelastic scattering on light nuclei (hydrogen, carbon) results in relatively large low energy tail of 14MeV peak.

The wide energy bump at energies less than 5MeV corresponds the neutrons inelastically scattered by target itself and chamber (main constituent - copper): the shape of this part of spectra coincides with the energy distribution of secondary neutrons from  $\text{Cu}(n, xn)$  reaction at 14MeV [34] (solid histogram in Fig.5). The ratio of integral under the spectrum in 0-5MeV interval to the total square depends only on target assembly:  $\approx 4\%$  for assembly shown in Fig.2a, and 2% - Fig.2b.

The channel in the spherical assembly had usually 5-6.2cm diameter that correspond the removed material about 2-2.5% of total shell weight. The correction have to be the same order but could be energy depended, thus we introduce correction function as a ratio of leakage spectra calculated for shells without and with channel:  $C_1(E)=L(E)/L_c(E)$ .

In the time of flight method the neutron energy is strictly connected with the distance between sample and detector and flight time only for the infinitely small sample. In benchmark experiments the size of assembly is not negligibly small: ratio of sphere radius to flight path is about 3% that could result in some correction. To evaluate this correction one should simulate the time of flight benchmark experiment and data reduction procedure: geometry of experiment, neutron detector efficiency and the real travel time, that neutron spent on the way source-sphere-detector. The evaluated correction function then could be determined as

$C_2(E) = L(E)/L_T(E)$ , where  $L_T(E)$  - leakage energy spectrum calculated from modeling the time of flight measuring technique.

Since the yield of source neutrons has angular anisotropy the spectra of neutrons leaking from the outer surface of shell have to be angular dependent as well. The Tables 2-5 show that leakage spectra usually have been measured at one or several angles in the forward semisphere. It means that measured spectrum  $L(E, \Theta)$  at definite angle  $\Theta$  should be corrected:  $C_3(E) = L(E)/L(E, \Theta)$ , where  $L(E)$  leakage averaged over the whole solid angle  $4\pi$ .

The total correction function is  $C(E) = C_1(E) \times C_2(E) \times C_3(E)$  and leakage spectrum, corrected for non spherical effect, could be obtained:  $L_{true}(E) = L_{raw}(E) \times C(E)$ . For illustration  $C(E)$  and its components are shown in Fig.6 for Bi shell and T(d,n) source. It was calculated by Monte-Carlo code BRAND [35], the results was published in [20]. Figure shows that corrections are energy dependent functions and have the values up to 6-10% for shell thickness of 1.4mfp, that close to the experimental uncertainty.

Thus, for correct comparison with one-dimensional transport calculations the following factors and procedures have to be taken into account:

Factor	Recommendation how may be taken into account
<u>Modeling of source flux entering the inner surface of the shell</u>	
Source angular distr.	To measure (calculate) angular distribution from real target chamber, in the case of thin target expression like (1) could be used.
Source energy distr.	"14MeV" peak mean energy is a function of angle (1), target chamber scattering (if not negligible) have to be measured or calculated.
<u>Modeling of real shell configuration</u>	
Shell hole(s)	Correction by simulation 3-dim. geometry ( $C_1$ )
<u>Modeling of detection of flux leaking from outer shell surface</u>	
One angle det.	Correction for angular anisotropy of leaking flux ( $C_3$ )
Energy resol.	To fold the calculated leaking spectrum with measured detector and collimator response functions
TOF method	Correction by simulation TOF experiment ( $C_2$ )

## References

1. J.J. Schmidt. Acta Physica Hungrica. 1991, v.69, p.269.  
FENDL-2 and associated benchmark calculations. Report INDC(NDS)-260, Vienna, 1992  
E.T.Cheng, D.L.Smith. Proc.of Int.Conf on "Nuclear Data for Science and Technology, (13-17 May 1991, Julich, FRG), p.273
2. И.Г.Горячев, Ю.И.Колесатов и др. Интегральные эксперименты в проблеме переноса ионизирующих излучений. М., Энергоатомиздат, 1985
3. Симаков С.П. Вопросы атомной науки и техники. Серия Ядерные константы, 1993, вып.1, с.43; Report INDC/p(93)-49, Vienna, 1993.
4. M.L.Stels, J.D.Anderson e.a. Nucl.Sci. and Eng., 1971, v.46, p.53
5. L.F.Hansen, J.D.Anderson e.a. Nucl.Sc. and Eng., 1970, v.40, p.262
6. G.S.Sidhu, W.E.Farley e.a. Nucl.Sci. and Eng., 1977, v.63, p.48
7. L.F.Hansen, C.Wong e.a. Nucl.Sci. and Eng., 1976, v.60, p.27
8. L.F.Hansen, J.D.Anderson e.a. Nucl.Sci. and Eng., 1969, v.35, p.227
9. L.F.Hansen. Preprint UCRL-97188, Livermore, 1987
10. L.F.Hansen, J.D.Anderson e.a. Nucl.Sci. and Eng., 1973, v.51, p.278
11. R.H.Johnson, J.J.Dorning e.a. Proc of Conf.on Nucl Cross Sections and Technology. NBS Special publication 425, v.1, p.169  
N.E.Hertel, R.H.Johnson e.a. Fusion Technology, 1986, v.9, p.345
12. L.F.Hansen, H.M.Blann e.a. Nucl.Sci. and Engin., 1986, v.92, p.382  
L.F.Hansen, C.Wong e.a. Nucl.Sci. and Engin., 1979, v.72, p.35
13. C.E.Ragan, G.F.Auchampaugh e.a. Nucl.Sci. and Eng., 1976, v.6, p.33
14. A.Takahashi. Proc.Intern.Conf. Santa Fe, 1985, p.59  
Y.Yanagi, A.Takahashi. OKTAVIAN Report A-84-02, Osaka, 1984
15. C.Ichihara e.a. Proc.Intern.Conference on Nuclear Data for Science and Tech. (Mito, 1988), p.  
C.Ichihara e.a. Report JAERI-M91-062, 1991, p.255  
C.Ichihara, S.Hayashi e.a. Report JAERI-M88-065, 1988, p.263  
C.Ichihara e.a. Proc.of Int.Conf on "Nuclear Data for Science and Technology, (13-17 May 1991 Julich, FRG), p.223
16. K.Sugiyama e.a. Oktavian Report C-86-02, Osaka, 1986
17. T.Kasahara, H.Hashikura e.a. OKTAVIAN Report A-84-04, Osaka, 1984
18. S.Iwasaki, N.Odano e.a. Proc.Intern.Conf.on Nuclear Data for Science and Techn.(Mito, 1988), p.229
19. U.von Mollendorff, U.Fischer e.a. Fusion Technology 1992, (C.Ferro, M.Gasparotto and H.Knoepfel, eds.), Elsevier 1993, v.2, p.1537  
H.Giese, F.Kappler, R.Tayama, U.von Moelledorff e.a. Proc. of ECENES-conference, Japan, September 1993 (to be appear)
20. S.P.Simakov, A.A.Androsenko e.a. Fusion Technology 1992, (C.Ferro, M.Gasparotto and H.Knoepfel, eds.), Elsevier 1993, v.2, p.1489  
С.П.Симаков, А.А.Андросенко и др. Вопросы атомн. науки и техники. Сер.Ядерные константы. 1992, вып.3-4, с.93; Там же, 1992, вып.1, с.48; Там же, 1990, вып.2, с.5  
S.P.Simakov, A.A.Androsenko e.a. Report INDC(CCP)-351, Vienna, 1993  
A.A.Androsenko e.a. Kernenergie, 1988, v.10, p.422  
А.А.Андросенко и др. Нейтронная физика, М., 1988, т.3, с.194
21. Д.Л.Бродер, Д.И.Готлиб и др. Нейтронная физика. М., 1984, ч.4, с.223  
В.Е.Leshchenko, Yu.N.Onishchuk e.a. Proc.of Int.Conf on "Nuclear Data for Science and Technology, (13-17 May 1991, Julich), p.445
22. J.Pulpan, M.Kralik e.a. Fusion Eng. and Design, 1993, v.23, p.57  
А.А.Борисов, В.А.Загрядский и др. Препринт ИАЭ-4990/8, Москва 1989
23. D.Albert, W.Hansen e.a. Report ZFK-562, Dresden, 1985  
T.Elfruth, D.Seeliger e.a. Kerntechnik, 1987, v.49, p.121  
T.Elfruth, T.Nehl e.a. Kerntechnik, 1990, v.55, p.156

24. Л. А. Трыков, Ю. И. Колеватов и др. Вопросы дозиметрии и защиты от излучения. Вып. 18, М., Атомиздат, 1979, с. 93
25. Л. А. Трыков, Ю. И. Колеватов и др. Препринт ФЗИ-1096, Обнинск, 1980
26. Л. А. Трыков, Ю. И. Колеватов и др. Вопросы атомн. науки и техн. Серия Ядерные констаты, 1990, вып. 1, с. 166
27. О. А. Баранов, В. В. Коробейников и др. Вопросы атомн. науки и техн. Серия Ядерные констаты, 1990, вып. 1, с. 28
28. Л. А. Трыков, Ю. И. Колеватов и др. Препринт ФЗИ-943, Обнинск, 1979  
Л. А. Трыков, Ю. И. Колеватов и др. Препринт ФЗИ-1730, Обнинск, 1985
29. J. Csikai e. a. Report IAEA-TECDOC-410, Vienna, 1987, p. 296
30. W. Mannhart. Report IAEA-TECDOC-410, Vienna, 1987, p. 158
31. О. Ф. Немец, Ю. В. Гофман. Справочник по ядерной физике. "Наукова думка". Киев, 1975
32. А. И. Сауков, Б. И. Суханов и др. Вопросы атомн. науки и техн. Серия Ядерные констаты, 1991, вып. 4, с. 3  
А. Р. Vasilyev, Ya. Z. Kandiev e. a. Proc. of Int. Conf on "Nuclear Data for Science and Technology, (13-17 May 1991 · Julich), p. 217
33. С. П. Симаков и др. Препринт ZFK-646, с. 111, Дрезден, 1988
34. A. Pavlik and H. Vonach. Physics Data, n<sup>o</sup> 13-4, Fachinformationszentrum Karlsruhe, 1988
35. А. А. Андросенко, П. А. Андросенко. Вопросы атомной науки и техники Серия: Физика и техника ядерных реакторов, 1985, вып. 7, с. 33

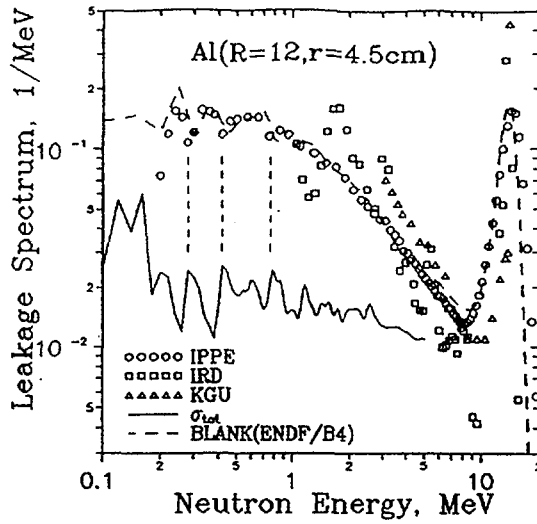


Fig. 1. Intercomparison of different experiments data (IPPE [20], IRD [22] and KGU [21]) for Al shell.

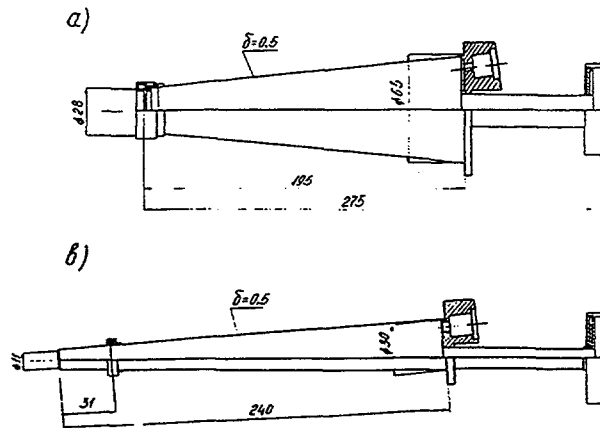


Fig. 2. Two arrangements of solid tritium target, used in shell neutron spectroscopy experiments in [20].

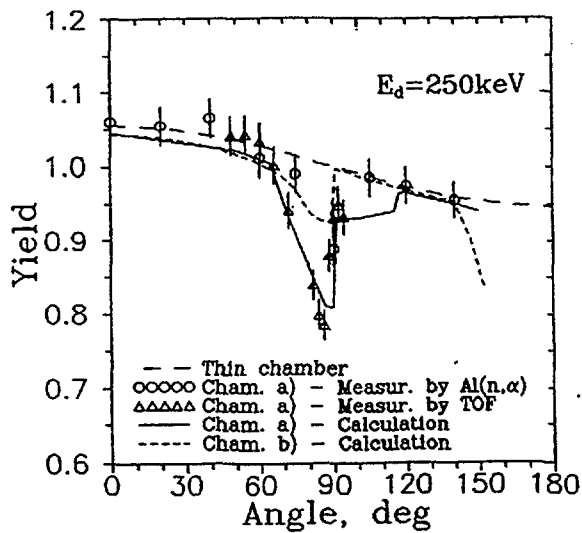


Fig. 3. Angular distribution of T(d,n)-source neutrons for target chamber design shown in Fig. 2 a) and b).

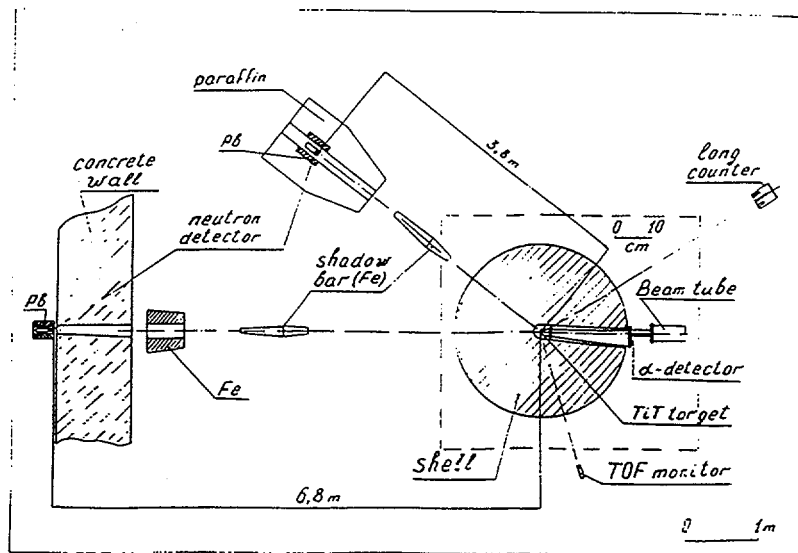


Fig. 4. Arrangement of time of flight spectrometer, used in shell neutron spectroscopy experiments in [20].

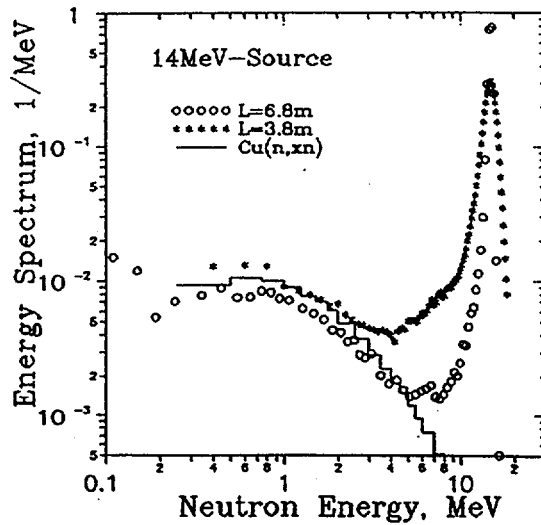


Fig. 5. Energy distribution of T(d,n)-source neutrons for two experimental set-up shown in Fig. 4.

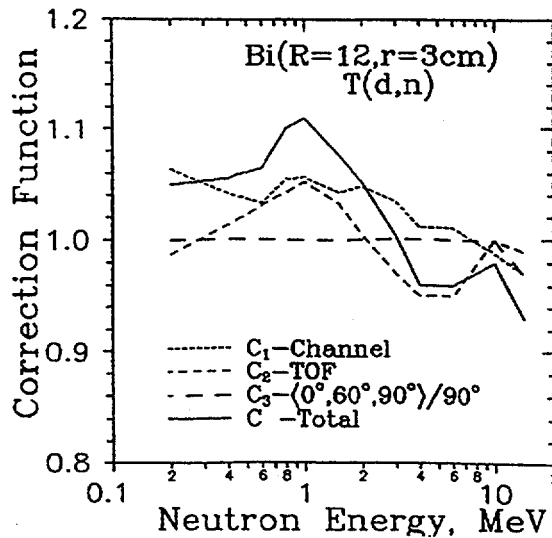


Fig. 6. Corrections for non-spherical effects [20].

Table 2. Neutron Leakage Spectra for spheres with T(d,n) source, measured in USA Laboratories.

Material	Radii		Wall, cm	t=R-r	Duct r, cm	Chem. Compos.	Concentr. $10^{23} \text{ cm}^{-3}$	Vessel (cm)		Detector $\theta, \text{ deg}$	$E_1$ - $E_2$ Mev	Met-Lab. Ref.	Numer. Data
	2	3						outer	inner				
H <sub>2</sub> O	10.48	~0.8	~9.7(1.0)	~1.8	H		0.669*	SS-0.05	SS-0.05	27	7.5	TOF LRL	[4]
	19.05	~0.8	~18.3(1.8)	~2.4	O		0.334*	SS-0.20	SS-0.20				
N	10.5	~0.8	~9.7(0.6)	~1.8	N			SS-0.03	SS-0.03	27	7.6 $10^{-4}$	TOF LRL	[5]
	55.9	~0.8	~55.1(3.0)	~5.0				SS-0.25	SS-0.25				
	163.95	129.8	~34.12(1.8)					SS-0.47	Cu-0.53	26, 125	9.6	TOF LRL	[6]
C	4.19	~0.8	~3.4(0.5)	~1.3	C		0.939			30, 120	7-10	2-15 TOF LRL	[7, 8]
	10.16	~0.8	~9.4(1.3)	~1.4			0.892						
	20.96	~0.8	~20.2(2.9)	~1.8			0.926						
O	10.5	~0.8	~9.7(0.7)	~1.8	O					30, 120	7-10	2-15 TOF LRL	[5, 7]
Al	8.94	~0.8	~8.1(0.9)	~1.4	Al		0.603*			30, 120	7-10	2-15 TOF LRL	[7, 9]
			(1.6) ~										
			(2.6) ~										
Si	10.16	~0.8	~9.3(0.9)	~1.4	Si		0.519*			30, 120	7-10	2-15 TOF LRL	[9]
			(1.2) ~										
Ti		~0.8	(2.2) ~		Ti		0.566*			30, 120	7-10	2-15 TOF LRL	[7]
			(3.5) ~										
Fe	4.46	~0.8	~3.7(0.9)	~1.3	Fe(98.5%)		0.834*			30, 120	7-10	.01-15 TOF LRL	[10, 7]
	13.41	~0.8	~12.6(2.9)	~1.6	Mn(0.5%)		0.004*						
	22.30	~0.8	~21.5(4.8)	~1.9									
Fe	36.0	7.5	28.5(6.4)	4.25	Fe		0.847*			90	2	1-15 PRS IU	[11]
Cu	4.0	~0.8	~3.9(1.0)	~1.3	Cu		0.842*			30, 120	7-10	TOF LRL	[9]
Ho	4.60	~0.8	~3.8(0.8)	~1.3	Ho		0.320*			26	10	1-15 TOF LRL	[12]
Ta	3.40	~0.8	~2.6(1.0)	~1.2	Ta		0.553*			26	10	1-15 TOF LRL	[12]
	10.20	~0.8	~9.4(3.0)	~1.4									
W	10.36	~0.8	~9.6(2.2)	~1.4	W		0.632*			30, 120	7-10	1-15 TOF LRL	[9]
Au	6.21	~0.8	~5.4(1.9)	~1.3	Au		0.589*			26	10	1-15 TOF LRL	[12]
Pb	5.60	~0.8	~4.8(1.0)	~1.3	Pb		0.330*			26	10	1-15 TOF LRL	[12]
	5.76	~0.8	~5.0(1.0)	~1.3	Th(100%)		0.298*			30, 120	7-10	TOF LRL	[12]
<sup>235</sup> U	3.145	~0.8	~2.3(0.7)	~1.2	<sup>235</sup> U(93.2%)		0.432			26, 120	10	1-15 TOF LRL	[12]
	5.925	~0.8	~5.1(1.5)		<sup>238</sup> U(6.8%)		0.030						
<sup>238</sup> U	7.996	2.233	5.773(1.5)	Com1	<sup>238</sup> U(93.5%)		0.432	Cd(0.076)		0	39	0.2-15 TOF LAS	[13] +
					<sup>235</sup> U(6.5%)		0.030						
<sup>238</sup> U	3.64	~0.8	~2.8(0.8)	~1.2	<sup>238</sup> U(99.0%)		0.470			30, 120	7-10	1-15 TOF LRL	[12]
					C(1%)								
<sup>239</sup> Pu	3.50	~0.8	~2.7(0.7)	~1.2	<sup>239</sup> Pu(93.7%)								
	5.36	~0.8	~4.6(1.3)	~1.3	<sup>240</sup> Pu(5.90%)					26, 120	7-10	1-15 TOF LRL	[12]
					<sup>241</sup> Pu(0.41%)								

Comment 1. The entrance hole configuration see in original work [13].



Table 4. Neutron Leakage Spectra for spheres with T(d,n) source, measured in Europe Laboratories.

Material	Radii		Wall, t=R-r cm(t/mfp)	Duct r, cm	Chem. Compos.	Concentr. $10^{23} \text{ cm}^{-3}$	Vessel (cm)		Detector		$E_1 - E_2$ MeV	Method	Lab.	Ref.	Numer. Data	
	R, cm	r, cm					outer	inner	$\theta$ , deg	L, m						
1	2	3	4	5	6	7	8	9	10	11	12	13	14	15	16	
Be	15.0	10.0	5.0(0.9)	Com1	Be	1.229*					$10^{-8}$	0.1	TOF	KFK [19]		
	15.0	5.0	10.0(1.8)										.05-6		PRS	
	22.0	5.0	17.0(3.1)								60	1.8	3-15		PRS	
Be	11.0	6.0	5.0(0.9)	2.5	Be(99.4%)	1.236			0, 30, 60	3.8	0.4-15	TOF	FEI [20]	+		
	5.7	2.5	3.2(0.6)	1.5							8	7.1			0.1-15	TOF
	6.9	2.5	4.4(0.8)	1.5							8	7.1			0.1-15	TOF
	9.7	2.5	7.2(1.3)	1.5							8	7.1			0.1-15	TOF
	12.8	2.5	10.3(1.9)	1.5							8	7.1			0.1-15	TOF
	15.25	2.5	12.8(2.3)	1.5							8	7.1			0.1-15	TOF
	17.35	2.5	14.9(2.7)	1.5							8	7.1			0.1-15	TOF
	22.3	2.5	19.8(3.6)	2.0							8	7.1			0.1-15	TOF
Be	11.0	6.0	5.0(0.9)	2.5	Be(99.4%)	1.236			0	10	6-15	TOF	KGU [21]			
Be	11.0	6.0	5.0(0.9)	2.5	Be(99.4%)	1.236			0	2.8	1-15	PRS	IRD [22]	+		
Al	12.0	4.5	7.5(0.6)	3.1	Al(99%) Si(0.3%) Fe(0.3%) Ti(0.3%)	0.5966			0, 40, 75	3.8	0.2-15	TOF	FEI [20]	+		
Al	12.0	4.5	7.5(0.6)	3.1	Al(99%)	0.5966			0	10	6-15	TOF	KGU [21]	+		
Al	20.0	10.0	10.0(0.8)	≈1.5	Al	0.603			0, 90	0.6	3-15	PRS	KGU [21]	+		
Al	12.0	4.5	7.5(0.6)	3.1	Al	0.5966				3.0	1-15	PRS	IRD [22]	+		
Ti	16.25	15.0	1.25(0.2)	3.1	Ti	0.566			0, 40, 75	3.8	0.2-15	TOF	FEI [20]	+		
Fe	12.0	4.5	7.5(1.7)	3.1	Fe	0.8374				3.0	1-15	PRS	IRD [22]	+		
Fe	12.0	4.5	7.5(1.7)	3.1	Fe(99%) Mn(0.45%) Cr(0.3%) C(0.15%)	0.8374			0, 40, 75	3.8	0.2-15	TOF	FEI [20]	+		
Ni	12.0	4.5	7.5(1.7)	3.1	Ni	0.9016			0, 40, 75	3.8	0.2-15	TOF	FEI [20]	+		
Ni	12.0	4.5	7.5(1.7)	3.1	Ni	0.9016				3.0	1-15	PRS	IRD [22]	+		
PbLi	20.0	6.0	14.0(2.2)	2.5	Pb(83%) Li(17%)	0.276 0.0565	SS-0.1		40	3.8	0.2-15	TOF	FEI [20]	+		

Table 4. (continued).

Material	Radii		Wall, t=R-r	Duct	Chem. Compos.	Concentr. $10^{23} \text{ cm}^{-3}$	Vessel(cm)		Detector		$E_1-E_2$ MeV	Met-hod	Lab.	Ref.	Numer. Data
	R, cm	r, cm	cm(t/mfp)	r, cm			outer	inner	$\theta$ , deg	L, m					
1	2	3	4	5	6	7	8	9	10	11	12	13	14	15	16
Pb	12.0	4.5	7.5(1.7)	2.5	Pb	0.330			0,30,60	3.8	0.2-15	TOF	FEI	[20]	+
Pb	12.0	4.5	7.5(1.7)	2.5	Pb	0.330				3.0	1-15	PRS	IRD	[22]	+
Pb	25.0	2.5	22.5(4.1)		Pb	0.330*			90	4.3	0.1-15	TOF	TUD	[23]	+
Bi	12.0	3.0	9.0(1.4)	2.5	Bi	0.282			0,60,95	3.8	0.4-15	TOF	FEI	[20]	+
U	16.0	10.0	6.0(1.7)		$^{238}\text{U}$ (99.6%) $^{235}\text{U}$ (0.4%)	0.471* 0.002*			90	4.5	0.1-15	TOF	TUD	[24]	+
U	12.0	4.0	8.0(2.2)	2.5	$^{238}\text{U}$ (99.6%) $^{235}\text{U}$ (0.4%)	0.4760 0.0019			0,60,95	3.8	0.4-15	TOF	FEI	[20]	+
U	14.0	5.0	9.0(2.5)	$\approx 1.5$	$^{238}\text{U}$ (99.6%) $^{235}\text{U}$ (0.4%)	0.471 0.0019			0,90	1.0	0.6-15	PRS	KGU	[21]	+
Th	13.0	3.0	10.0(1.7)	2.5	Th	0.293	Al-0.15		0,60,95	3.8	0.4-15	TOF	FEI	[20]	+

Comment 1. Shell has two ducts [19]: 1. entrance hole for deuteron beam of 3cm radius,  
2. hole for associated  $\alpha$ -particle detector of 2.5cm radius at  $120^\circ$  to deuteron beam.

Table 5. Neutron Leakage Spectra for spheres with  $^{252}\text{Cf}$  source.

Material	Radii		Wall, t=R-r cm(t/mfp)	Duct r, cm	Chem. Compos.	Concentr. $10^{23}\text{cm}^{-3}$	Vessel(cm)		Detector		$E_1-E_2$ MeV	Met- hod	Lab.	Ref.	Numer. Data
	R, cm	r, cm					outer	inner	$\theta$ , deg	L, m					
1	2	3	4	5	6	7	8	9	10	11	12	13	14	15	16
$\text{H}_2\text{O}$	25.0				H	0.669*				0.8	0.6-15	PRS	FEI	[26]	+
	35.0				O	0.334*									
Be	11.0				Be	1.229*				2.0	1-14	PRS	UI	[11]	
$\text{CH}_2$	23.0				H C					2.0	1-14	PRS	UI	[11]	
$\text{CH}_2$	30.0				H C					1.5	0.01-14	PRS	FEI	[2, 24]	+
	25.0 50.0				Na	0.254*	Al-0.4			1.5	0.01-14	PRS	FEI	[2, 25]	+
Cr	35.0				Cr	0.801*					0.01-14	PRS	FEI	[26]	+
Cr	7.89	1.6	6.29(1.5)		Cr(99.8%)	0.5119	Cu-0.11	Cu-0.15		0.23	0.04-10	PRS	ROS	[27]	
Fe	10.0	1.0	9.0(2.6)		Fe					0.6-	0.01-14	PRS	FEI	[2, 28]	+
	15.0	1.0	14.0(4.0)							-1.0					
	25.0	1.0	24.0(6.9)												
	20.0	1.0	19.0(5.5)												
	30.0	1.0	29.0(8.4)												
35.0	1.0	34.0(9.8)													
Fe	12.0	4.5	7.5(1.7)	3.1	Fe	0.8374				3.8	0.2-14	TOF	FEI	[20]	+
Ni	8.5	1.5	7.0(2.2)		Ni(99.5%)					0.23	0.04-10	PRS	ROS	[27]	
Nb	12.7	0.09	9.61(2.5)		Nb(99.05%) Zr(0.95%)					2.0	1-14	PRS	UI	[11]	
PbLi	20.0	6.0	14.0(2.2)	2.5	Pb Li	0.276 0.0565	SS-			3.8	0.2-14	TOF	FEI	[20]	+
	20.0 30.0	1.0 1.1	19.0(3.0) 28.9(4.5)		Pb		SS-0.15			0.9	0.02-14	PRS	FEI	[2]	+
Bi	12.0	3.0	9.0(1.4)	2.5	Bi	0.282				3.8	0.4-14	TOF	FEI	[20]	+
U	12.0	4.0	8.0(2.8)	2.5	$^{238}\text{U}$ (99.6%) $^{235}\text{U}$ (0.4%)	0.4760 0.0019				3.8	0.4-14	TOF	FEI	[20]	+
	11.0	1.0	10.0(3.5)		$^{238}\text{U}$ (99.6%) $^{235}\text{U}$ (0.4%)	0.4760 0.0019					0.01-14	PRS	FEI	[26]	+
Th	13.0	3.0	10.0(2.1)	2.5	Th	0.293	Al-0.15			3.8	0.4-14	TOF	FEI	[20]	+

NEXT PAGE(S)  
left BLANK



**BENCHMARK EXPERIMENTS AND ANALYSIS  
WITH HYBRID REACTOR BLANKET MOCK-UPS**

V.V. AFANASIEV, A.G. BELEVITIN, V.V. KHROMOV  
V.L. ROMODANOV, Yu.M. VERZILOV,  
Moscow Engineering Physics Institute, Moscow, USSR

D.V. MARKOVSKIJ, G.E. SHATALOV  
Kurchatov Institute of Atomic Energy, Moscow, USSR

This report summarizes the experimental researches made with the mock-ups, imitating the blanket compositions of hybrid reactor with uranium and lead multipliers of neutrons, and intended for verifying of neutron transport codes. The experimental installation, measured values, experimental results and comparison with 3-D calculations by the BLANK code are described.

## 1. Introduction

Validation of the blanket neutron physics characteristics is one of the important questions in the fusion reactor design studies. It is known [1] that the requirements to the accuracy of predicting the key neutron blanket functionals are rather strict. However, it is rather difficult to achieve the necessary accuracy at the fusion reactor design stage. One of the reasons for it is the nature of neutron interaction with materials at the energies about 14 MeV, which is much more complicated than that in a fission reactor. For the most spread concept of a D-T reactor it is manifested, first of all, in a strong anisotropy in the elastic scattering and in the presence of various channels of inelastic interactions that requires rather high approximations and perfect files of evaluated data for calculations. The complicated geometry of the fusion reactor with the toroidal neutron source distributed in the transversal plasma cross-section in a complex law is another circumstance of no less importance. Its imitation in an

experimental mock-up would require as a matter of fact the construction of the reactor similar to the designed one. Thus at the fusion reactor design stage the validation of its design parameters comes to validation of the neutron codes and data in calculations of the integral benchmark experiments with a 14 MeV neutron source and to determining the safety factors values for certain design parameters based on the results of comparison.

A given paper starts the experimental and calculational neutronics studies of the blanket mock-ups having a complicated structure, made in cooperation of the Kurchatov IAE and the Moscow Engineering Physics Institute in the frame of the National Experimental Fusion Reactor Design (OTR) [2,3]. The experiments are intended for verification of the BLANK code developed at the Kurchatov IAE and other codes in calculations of the key neutronics models corresponding to the key fusion reactor blanket concepts.

Experimental studies were done to order of the Kurchatov IAE. A general guidance of the work and calculational analysis were provided by specialists of IAE. All the experimental researches and necessary methods development were carried out by specialists of the "Neutron generator" laboratory of Moscow Engineering Physics Institute.

A given study represents the benchmark experiments and analysis with the mock-ups imitating concepts of an external and internal blankets of hybrid reactor with neutron multiplication in uranium and lead layers.

## 2. Experimental technique

### 2.1. "Neutron generator" laboratory

The laboratory is intended for the researches in fission and fusion reactors area. It is located in two isolated premises: experimental hall and a control room. A neutron generator and the experimental facility which can be moved along the rails respective to the neutron generator target are located in the hall. The hall is 4.5m high, its main dimensions and the equipment layout are given in Fig. 1.

The D-T neutron generator used as a neutron source has the

following main operational characteristics :

- deuteron acceleration potential, 150 kV;
- neutron yield:  $\sim 5 \cdot 10^{10}$  n/s;
- TiT-target, 45 mm in diameter;
- pulsed and continuous operating modes;
- high frequency deuteron ion source;
- absolute count of neutrons with the error  $\sim 2.7$  % (at one sigma).

## 2.2. Ion beam line and target assembly

A target assembly and a radiometer of  $\alpha$ -particles emerging in a D-T reaction are installed in the ion beam line made of stainless steel, 2 mm thick. A titanium-tritium target upon a copper backing, 1.5 mm thick, cooled with the water layer, 1.5 mm thick, is limited with a brass layer, 0.5 mm thick. The radiometer of  $\alpha$ -particles includes two independent registering channels consisting of a limiting diaphragm, collimating set of  $\alpha$ -particles, scintillation crystal CsJ(Tl), 0.3 mm thick, and a photoelectron multiplier. The registering devices differ by the diameters of diaphragms chosen from the conditions for avoiding the overloading of electronic instrumentation during the operation of the generator and for providing of sufficient count statistics in calibration of the absolute generator yield. The ion beam line and the target assembly are shown in Fig. 2 and 3.

## 2.3. Absolute neutron count system

The registration channel for  $\alpha$ -particles emerging in the reaction  $T(d,n)_2^4\text{He}$  includes a pulse height analyzer based on the CAMAC standards and controlled with the computer MERA-60. In order to take account of neutron yield changes in time, the time of detector irradiations was split into a preset number of time intervals depending on the irradiated isotope half life. A spectrum of  $\alpha$ -particles corresponding to the reaction  $T(d,n)_2^4\text{He}$  was singled out in each time interval. The results of  $\alpha$ -particle spectra processing were transferred to the screen of a display and to a magnetic dick of the computer for further utilization in

calculations of absolute activation rates of the detectors irradiated in the mock-up. During irradiation of the detectors a histogram showing the time behavior of neutron yield and all the absolute parameters of  $\alpha$ -particle spectrum is built-up upon the display.

#### 2.4. Absolute calibration of neutron yield

To avoid the errors related with the measurements of the radiometer geometry and with the crystal efficiency the calibration of  $\alpha$ -radiometer was done with the standard  $\alpha$ -particle sources based on  $^{238}\text{Pu}$ , placed instead of a Ti-T target in the neutron generator. It was shown in special experiments that the variation of the efficiency of the whole system because of the difference in energy of calibrating source  $\alpha$ -particles  $\sim 5.5$  MeV and the energy of  $\alpha$ -particles in  $\text{T(d,n)} \text{}^4_2\text{He}$  about 3.3 MeV is not more than 1.5 %. The neutron yield calibration and the scaling coefficient of efficiencies for the registering devices with various diaphragms were confirmed each time before a new experimental run. The registration of  $\alpha$ -particles was performed at the angle  $174^\circ$  respective to the deuteron beam direction. The anisotropy coefficient of  $\alpha$ -particles calculated taking account of deuteron velocities and their energy loss in an active neutron-producing layer of the target was adopted to be equal to  $1.20 \pm 0.02$ .

#### 2.5. Measurement of absolute reaction rates

The activities of irradiated detectors were measured simultaneously with eight  $\gamma$ -spectrometers based on the NaI(Tl) crystal. All the paths were relatively and absolutely calibrated. The registered  $\gamma$ -spectra were transferred to the CM-4 computer on-line with the MERA-60 computer, where the information about the absolute neutron flux registered during the detector irradiation was stored for the coded processing. The coded processing of detector activities with due regard for a variation in the absolute neutron yield during the experiment, detector parameters and other experimental conditions, allowed one to obtain the absolute reaction rates normalized to one nucleus of the detector and to one

neutron born in the source. The structural diagram of the system is given in Fig. 4.

#### 2.6. Measurement of spectral characteristics

Activation detectors and track ones, sometimes, were used to measure the neutron spectral characteristics in the blanket mock-ups. A long run of experiments was performed with the threshold detectors. The dimensions of detectors were chosen from the conditions of small neutron field perturbations in places of their location. The detectors with a high percent content of the main isotope were used. This allowed one to increase the accuracy of measurements by reduction in the background level and some reactions of interference that is especially important, when the neutron flux intensity in place of measurement was small. The main nuclear physics and geometry characteristics of the threshold detectors, 18 mm in diameter, are given in Table 4.1. The calculated self absorption coefficients for the measured  $\gamma$ -lines were within the range (1-5) %.

#### 2.7. Measurement of tritium production rates

The tritium production rate in lithium-containing zones of the mock-ups was determined from the reactions  ${}^6\text{Li}(n,\alpha){}^3\text{H}$  and  ${}^7\text{Li}(n,n'\alpha){}^3\text{H}$ . As a result of the blanket mock-up irradiation a certain amount of tritium sufficient for obtaining an information about its production rate distribution in axial and radial channels of the mock-up was accumulated. Besides, the nuclear reaction rates  ${}^{35}\text{Cl}(n,\alpha){}^{32}\text{P}$  and  ${}^{31}\text{P}(n,\gamma){}^{32}\text{P}$  were measured which simulated the process of tritium production with the isotopes  ${}^7\text{Li}$  and  ${}^6\text{Li}$ , respectively. The main parameters of blanket mock-up irradiation are given in Table 2.7.1.

##### 2.7.1. Measurement of tritium activity

Lithium carbonate  $\text{Li}_2\text{CO}_3$  was chosen as a material for a lithium-containing detector. The irradiated detector was dissolved in the mixture of acetic and hydrochloric acids in the volumetric

ratio 1:2. After complete dissolving of the detector the produced solution was frozen and the facility was evacuated up to the pressure of 120 Pa. Then the bottle with the solution was heated in a water bath, and a tritium-containing phase was condensed in the measuring bottle cooled with liquid nitrogen. After termination of condensation a dioxane scintillator was added to the tritium-containing phase, and the tritium activity was measured with the "Mark-III" system 80 minutes later, after the exposure. The efficiency of tritium registration was determined by the internal standard method.

Table 2.7.1 The main parameters of blanket mock-up irradiation in the tritium production measurements.

Parameter Type of model	Irradiation time, h	Neutron fluence, neutrons	Average neutron yield, n/s
Hybrid mock-up, uranium multiplier	72	$(5.7 \pm 0.15) \cdot 10^{15}$	$2.2 \cdot 10^{10}$
"Pure" mock-up, lead multiplier	81	$(9.36 \pm 0.25) \cdot 10^{15}$	$3.2 \cdot 10^{10}$

2.7.2.  $^6\text{Li}$  and  $^7\text{Li}$  contributions into the tritium production rate.

Lithium carbonate detectors with two different  $^6\text{Li}$  concentrations were used in the experiments. In the detectors of the first type the  $^6\text{Li}$  concentration corresponded to the concentration of this isotope in the mock-up detector holders. In the detectors of the second type  $^6\text{Li}$  was present as an impurity. Utilization of such a detector set allows one to reduce the thermal neutron field perturbation in the mock-up to a minimum. Assuming the tritium production rate in the detector volume to be constant

one can derive a set of equations including the activities of tritium  $\beta$ -decay (produced in the detectors of various types) and thus separate the contributions into the tritium production rate by various isotopes. The comparison between the tritium production rate in the reactions  ${}^7\text{Li}(n,n'\alpha){}^3\text{H}$  and in the corresponding simulating reaction  ${}^{35}\text{Cl}(n,\alpha){}^{32}\text{P}$  shows that their ratio in all the lithium-containing zones is practically constant. This gives an opportunity to use such an experimentally found ratio for separation of contributions into the tritium production by  ${}^6\text{Li}$  and  ${}^7\text{Li}$  isotopes, when the measurements are done in a condition of a neutron flux deficit. Such a technique was used in measurement within radial channels of the mock-up. The measurement of simulating reaction product activity  ${}^{32}\text{P}$  was done with the Cherenkov counter. A liquid medium with the irradiated detector dissolved in it was used as a counter radiator. The measurements were done at the "Mark-III" set up with two photo multipliers operating in the coincidence mode.

### 2.7.3. Characteristics of detectors and technology of their fabrication.

The detectors for lithium production were done as lithium carbonate pellets packed with aluminum foil, 0.02 mm thick. The pellets were formed by pressing the powder of  $\text{Li}_2\text{CO}_3$  with a hydraulic press under  $\sim 10^8$  Pa. The main characteristics of the detectors used in the experiment are given in Table 2.7.2.

Table 2.7.2 Characteristics of lithium carbonate detectors.

Place of detector	Type of detector	Concentration of isotope, nuclei/g		Diameter of detector, mm	Thickness of detector, mm
		${}^6\text{Li}$	${}^7\text{Li}$		
Axial channel	1	$(8.60 \pm 0.09) 10^{18}$	$(1.63 \pm 0.02) 10^{22}$	30.0	1.30
	2	$(3.79 \pm 0.04) 10^{20}$	$(1.59 \pm 0.02) 10^{22}$		
Radial channel	1	$(8.60 \pm 0.09) 10^{18}$	$(1.63 \pm 0.02) 10^{22}$	19.4	1.34
	2	$(3.79 \pm 0.04) 10^{20}$	$(1.59 \pm 0.02) 10^{22}$		

Detectors in the simulating reactions are the pellets pressed out of the corresponding powders. Their main characteristics are given in Table 2.7.3.

Table 2.7.3 Characteristics of simulating detectors.

Simulating reaction	Detector material	Concentration of target nuclei in the detector, nuclei/gram
$^{31}\text{P}(n,\gamma)^{32}\text{P}$	$\text{Zn}_2\text{P}_2\text{O}_7$	$(3.95\pm 0.02)\cdot 10^{21}$
$^{35}\text{Cl}(n,\alpha)^{32}\text{P}$	$\text{NH}_4\text{Cl}$	$(8.50\pm 0.04)\cdot 10^{21}$

In the measurements within an axial channel of the mock-up the detectors were 30 mm and 19.4 mm in diameter, being 1.3 mm and 3.1 mm thick, respectively. The detectors 19.4 mm in diameter and 3.1 mm thick were used in radial channels. The materials for the detector-radiator pair in the simulating reactions and some their characteristics are given in Table 2.7.4.

Table 2.7.4. Characteristics of the detector-radiator pair.

Reaction	Detector			Radiator material	Registration efficiency
	Material	Range of weight variance, g	Density g/cc		
$^{31}\text{P}(n,\gamma)^{32}\text{P}$	$\text{Zn}_2\text{P}_2\text{O}_7$	1-3	2.61	20 % solution of $\text{H}_2\text{SO}_4$	$43.0\pm 1.3$
$^{35}\text{Cl}(n,\alpha)^{32}\text{P}$	$\text{NH}_4\text{Cl}$	1-5	1.42	$\text{H}_2\text{O}$	$53.0\pm 2.$

## 2.8. Measurements in the uranium zone

### 2.8.1. Track detectors

Fission reactions in a hybrid reactor blanket having an

uranium multiplier of neutrons are the key neutronics functionals from the viewpoint of neutron multiplication. Track detector having a high spatial resolution and not requiring the use of fission fragment yield parameters - not always well known with a sufficient accuracy in the neutron fields the spectra of which are also insufficiently known - were used for their measurements. The registration was done in the  $4\pi$ -geometry in order to adapt the track technique of measuring the fission reaction produced by fast neutron in the presence of fragment spread anisotropy. For this purpose, the measurements were twice repeated with different orientation of a fissile layer in space at each point of the mock-up. Then, these results were averaged. The mica muscovite - its chemical formula is  $KAl_3Si_3O_{10}(OH)$  - was used as a register of fragments, on its surface rhomboid tracks, 10-15  $\mu$  in size, are formed after irradiation by fission fragments and after etching by 48 % hydrofluoric acid at a room temperature for 4-6 hours. In the experiments the fission reaction rates for isotopes  $^{233}\text{U}$ ,  $^{235}\text{U}$ ,  $^{238}\text{U}$ ,  $^{232}\text{Th}$ ,  $^{237}\text{Np}$ , were measured. The isotopes  $^{233}\text{U}$ ,  $^{235}\text{U}$ ,  $^{232}\text{Th}$ , were put on the radiators, 18 mm in diameter, 0.1 mm thick, as thin layers. They have the size of a fissile spot, 10 mm in diameter. The isotopes  $^{238}\text{U}$ ,  $^{237}\text{Np}$  were also put as thin layers on the radiators, 10 mm in diameter, 0.3 mm thick, having a fissile spot diameter equal 8 mm. The material for the radiator backing is aluminum.

#### 2.8.2. Measurements of the reactions $^{238}\text{U}(n,\gamma)$ and $^{238}\text{U}(n,2n)$

These reactions are related with the production of  $^{239}\text{Pu}$  and neutron multiplication in the blankets with uranium. Both reactions were measured by the activation method with the Ge(Li) semiconducting detector, DGDK-63-V type, with the resolution ~4 KeV in the  $\gamma$ -energy range ~(200-300) KeV. The line 277.6 KeV of  $^{239}\text{Np}$  was used to measure the  $^{238}\text{U}(n,\gamma)$  reaction rate. The  $^{238}\text{U}(n,2n)$  reaction rate was measured with the  $\gamma$ -line 208 KeV of  $^{237}\text{U}$ . The contribution of the background  $\gamma$ -lines with energies 209.8 KeV and 205.3 KeV from the isotopes  $^{237}\text{Np}$  and  $^{235}\text{U}$  was also taken into account in this case. The detector assemblies, 100  $\mu$  thick each, of five foils, 15 mm in diameter, made of natural uranium were packed

into aluminum foil, 50  $\mu$  thick. The experimentally measured self-absorption coefficients of  $\gamma$ -quanta with the energies 208.0 KeV and 277.6 KeV were  $1.60 \pm 0.02$  and  $1.44 \pm 0.02$ , respectively.

### 3. Mock-ups geometry and composition

The blanket mock-ups are stratified systems including the first wall material, neutron multiplier, tritium production zone, neutron moderator, some shielding elements. The structural diagram of the mock-up with a uranium breeder is given in Fig. 5. The transversal size of each layer was  $800 \times 1000 \text{ mm}^2$ , their materials and thicknesses are given in Table 3.1. The second blanket mock-up had the same structure and dimensions but uranium was replaced by lead, in a layer 100 mm thick.

Blanket mock-ups had the special bracing set with which they were fastened to a duralumin plate, 10 mm thick. The plate on which the mock-ups were placed was put onto the platform capable to move along the railway track and thus to fix the chosen distance from

Table 3.1 Transversal dimension of blanket mock-ups with uranium and lead neutron multipliers.

Function	Material	Thickness, mm
First wall	Stainless steel	10.
Multiplier	Uranium/Lead	50./100.
First lithium zone	LiAl alloy	60.
Moderator	Plexiglas	21.
Second lithium zone	LiAl alloy	140.
Moderator	Plexiglas	19.
Third lithium zone	LiAl alloy	40.
Moderator	Plexiglas	25.
Shielding	Stainless steel	101.
materials	Plexiglas	33.
	Stainless steel	20.

the blanket surface to the neutron source. The accuracy of fixing the position was  $\pm 1$  mm. The uranium multiplier of neutrons was assembled of the blocks,  $500 \times 500 \times 50$  mm in size; the lead one, of the blocks  $100 \times 100 \times 50$  mm in size with the density 11.2 g/cc. The origin of the detector coordinates in the axial channel was at the central point of a mock-up surface facing the neutron source; the origin of coordinates in the radial channels was at the cross-point of the axial channel with the direction of radial channels, perpendicular to it. The origin of coordinates in the blanket mock-up with uranium multiplier for the first radial channel and for the second one, where activation measurements were performed, corresponded to the axial channel coordinates 37 mm and 198 mm. In the blanket mock-up with lead multiplier the origin of coordinates in radial channel corresponded to the coordinate of an axial channel 148 mm. The tritium production was measured in the four radial channels the origin of coordinates of which corresponded to the coordinates of an axial channel equal 80, 201, 269 and 320 mm in the blanket mock-up with uranium and 130, 251, 319, 370 mm in the mock-up with lead multiplier. The plate on which the mock-up were assembled was located at the distance of 1 m from a concrete floor of the experimental hall. In Fig. 6 and 7 one can see the detector holders in axial and radial channels of the mock-up.

A neutron-producing layer in the tritium target was at the distance  $151 \pm 1$  mm from the front surface of the blanket.

In Tables 3.2 and 3.3 the material composition of both mock-ups are given. The LiAl alloy was used as a lithium-containing material, its density averaged over the whole volume of lithium-containing zones is given in Table 3.2. The density of plexiglas was measured in a separate experiment. The lithium-containing zones were assembled of blocks,  $200 \times 200$  mm<sup>2</sup> in transversal size, 20 mm and 40 mm thick. The content of natural lithium in the blocks was varied from 3.8 % to 5.4 % by weight. The composition and the number of layers in the zones are given in Table 3.4, where average lithium concentrations in each zone are given. The layout of blocks in the layers is given in Fig. 8.

The average lithium concentration in three zones was 4.82 %. The detector holders for tritium production measurement were made of LiAl-alloy with the concentration of lithium equal to 4.40 %.

Table 3.2 Nuclear physics characteristics of the materials used in the blanket mock-ups.

Material	Density, g/cc	Nuclear density, 1/cc
Uranium	18.9	$^{238}\text{U} - 4.76 \cdot 10^{22}$ $^{235}\text{U} - 1.91 \cdot 10^{20}$
Plexiglas ( $\text{CH}_2=\text{C}(\text{CH}_3)-\text{COOH}_3$ )	1.18±0.01	H - $5.68 \cdot 10^{22}$ O - $3.55 \cdot 10^{22}$ C - $1.42 \cdot 10^{22}$
LiAl alloy	2.31±0.02	$^6\text{Li} - 7.22 \cdot 10^{20}$ $^7\text{Li} - 8.94 \cdot 10^{21}$ Al - $4.90 \cdot 10^{22}$
Stainless steel	7.95	C - $4.79 \cdot 10^{20}$ Cr - $1.66 \cdot 10^{22}$ Ni - $8.15 \cdot 10^{21}$ Ti - $9.99 \cdot 10^{20}$ Fe - $6.09 \cdot 10^{22}$

Table 3.3 Lead neutron multiplier composition.

Element	Pb	Sb	Sn	Cu	Bi	As	Fe
Contents, %	96.5-98.0	2.0-3.5	0.2	0.1	0.05	0.03	0.01

Table 3.4 Structure of lithium-containing zones.

Zone number	1	2	3
Zone thickness, mm	60.	140.	40.
Number of layers consisting of blocks having the size in mm	200x200x20 1	1	2
	200x200x40 1	3	-
Average concentration of lithium, % by weight	4.48	5.10	4.40

#### 4. Experimental results

The following spatial distributions of neutron functionals in axial and radial channels of the mock-ups were measured:

- threshold reaction rates;
- fission and capture rates and the neutron multiplication characteristics in the uranium zone;
- tritium production rates in direct and simulating reactions in lithium-containing zones.

All the neutron functionals measured in a given study are normalized to one detector nucleus and to one neutron produced in a tritium layer of the target.

In Table 4.1 the results of reaction rate measurements for various detectors at the distance  $151 \pm 1$  mm from a neutron-producing target layer are given. They can be used for testing the

Table 4.1 Activation rates measured at a distance 151 mm from the tritium-containing layer of the target and nuclear characteristics of the threshold detectors.

Reaction	$^{115}\text{In}(n,n)^{114\text{m}}\text{In}$	$^{204}\text{Pb}(n,n)^{204\text{m}}\text{Pb}$	$^{64}\text{Zn}(n,p)^{64}\text{Cu}$
Activation rate, $10^{28}$ /atom/source	0.298 (10)	0.242 (9)	0.544 (20)
$T_{1/2}$	4.486 h	66.9 m	12.7 h
$\gamma$ -line, KeV	336.	899.	511.
Yield, %	47.	91.2	37.
Abundance, %	99.98	99.2	96.5
Detector thickness, mm	0.90	47.8	99.4
Interfering reaction	$^{115}\text{In}(n,\gamma)^{114\text{m}}\text{In}$	$^{207}\text{Pb}(n,p)^{207}\text{Tl}$ $^{208}\text{Pb}(n,p)^{208}\text{Tl}$	$^{64}\text{Zn}(n,2n)^{63}\text{Zn}$ $^{64}\text{Zn}(n,\gamma)^{65}\text{Zn}$
$T_{1/2}$	54.2 m	4.77 m	38.1 m
Interfering $\gamma$ -line, KeV	417.0	3.07 m	244.1 d
		879.6	511.
		860.4	511.

Reaction	$^{27}\text{Al}(n,p)^{27}\text{Mg}$	$^{56}\text{Fe}(n,p)^{56}\text{Mn}$	$^{107}\text{Ag}(n,2n)^{106}\text{Ag}$
Activation rate, $10^{28}$ /atom/source	0.248 (9)	0.391 (14)	2.64 (9)
$T_{1/2}$	9.46 m	2.57 h	23.96 m
$\gamma$ -line, KeV	844.	847.	511. 512.
Yield, %	71.5	99.	17.9 126.
Abundance, %	100.	99.7	98.8
Detector thickness, mm	0.95	0.94	0.53
Interfering reaction	-	-	$^{107}\text{Ag}(n,2n)^{108}\text{Ag}$ $^{107}\text{Ag}(n,2n)^{106m}\text{Ag}$
$T_{1/2}$	-	-	2.41 m 8.41 d
Interfering $\gamma$ -line, KeV	-	-	511. 511.8

Reaction	$^{65}\text{Cu}(n,2n)^{64}\text{Cu}$	$^{63}\text{Cu}(n,2n)^{62}\text{Cu}$	$^{64}\text{Zn}(n,2n)^{63}\text{Zn}$
Activation rate, $10^{28}$ /atom/source	3.34 (12)	1.91 (7)	0.602 (20)
$T_{1/2}$	12.71 h	9.74 m	38.1 m
$\gamma$ -line, KeV	511.	511.	511.
Yield, %	37.	196.	185.6
Abundance, %	99.2	99.7	99.4
Detector thickness, mm	0.46	0.43	0.33
Interfering reaction	-	$^{63}\text{Cu}(n,\gamma)^{64m}\text{Cu}$	$^{64}\text{Zn}(n,p)^{64}\text{Cu}$ $^{64}\text{Zn}(n,\gamma)^{65m}\text{Zn}$
$T_{1/2}$	-	12.71 h	12.71 h 244.1 d
Interfere $\gamma$ -line, KeV	-	511.	511.

correctnesses of taking account of the target unit effect and normalization to one neutron from the source with due regard for its anisotropy.

In Table 4.2 the results of  $^{63}\text{Cu}(n,2n)$  reaction rate measurement upon the front wall of the mock-up are given. Using them, one can test the spatial and energy source neutron distribution representation, since this reaction has the energy threshold  $E_{\text{th}} \sim 12.6$  MeV and there is a very small amount of backscattered neutrons from the mock-up in the range  $E > E_{\text{th}}$ .

Eight activation detectors were simultaneously irradiated in each mock-up. In the uranium channel not more than four detectors were irradiated simultaneously. The measured activation rates are given in Tables 4.3-4.5.

In the measurement of tritium production rates two types of detectors (see Table 2.7.2) were used. At each point of the mock-up, where the measurements were performed, two detectors of

Table 4.2  $^{63}\text{Cu}(n,2n)^{62}\text{Cu}$  activation rate on the front surface of blanket with uranium multiplier,  $10^{28}$ /atom/source.

Detector coordinate, mm	Activation rate	
	Relative	Absolute
0.	1.	1.95 (7)
35.	0.90 (1)	1.75 (6)
75.	0.75 (6)	1.46 (5)
100.	0.661 (6)	1.29 (4)
120.	0.567 (8)	1.10 (4)
140.	0.517 (5)	1.01 (3)
170.	0.389 (8)	0.76 (3)
200.	0.337 (9)	0.66 (3)
220.	0.277 (5)	0.54 (2)
240.	0.254 (5)	0.50 (2)
260.	0.221 (4)	0.43 (1)
300.	0.173 (2)	0.337 (11)
360.	0.132 (4)	0.258 (13)
400.	0.090 (3)	0.176 (8)
450.	0.074 (2)	0.144 (6)

Table 4.3 Absolute reaction rates in axial channel of the blanket with uranium multiplier ( $10^{28}$ /atom/source).

Detector coordinate, mm	$^{115}\text{In}(n,n')$	$^{204}\text{Pb}(n,n')$	$^{64}\text{Zn}(n,p)$	$^{27}\text{Al}(n,p)$
0.	0.76(3)	0.278(10)	0.67(2)	0.252(8)
10.	0.88(4)	0.258(9)	0.60(2)	0.212(7)
35.	0.86(3)	0.178(6)	0.407(13)	0.126(4)
61.	0.58(2)	0.115(4)	0.250(9)	0.076(3)
91.	0.387(15)	0.081(3)	0.169(6)	0.052(2)
120.	0.264(11)	0.056(2)	0.116(5)	0.0345(10)
142.	0.183(6)	0.047(2)	0.094(4)	0.0265(8)
192.	0.127(5)	0.029(1)	0.054(2)	0.0169(6)
232.	0.086(3)	0.0192(7)	0.0356(12)	0.0107(3)
281.	0.0486(19)	0.0131(13)	0.0213(7)	0.0064(2)
301.	0.0374(18)	0.0094(4)	0.0177(6)	0.0051(1)
321.	0.0311(16)	0.0080(4)	0.0143(9)	0.0042(1)
340.	0.0242(23)	0.0063(3)	0.0116(5)	0.0035(1)
366.	0.0175(7)	0.0056(3)	0.0095(5)	0.0028(1)

Detector coordinate, mm	$^{56}\text{Fe}(n,p)$	$^{107}\text{Ag}(n,2n)$	$^{65}\text{Cu}(n,2n)$	$^{63}\text{Cu}(n,2n)$	$^{64}\text{Zn}(n,2n)$
0.	0.393(14)	2.71(10)	3.43(10)	1.95(7)	0.621(15)
10.	0.329(13)	2.25(9)	2.67(7)	1.59(5)	0.474(13)
35.	0.182(6)	1.22(5)	1.48(4)	0.86(3)	0.259(7)
61.	0.105(4)	0.71(3)	0.84(2)	0.484(17)	0.142(4)
91.	0.071(3)	0.466(18)	0.549(15)	0.304(10)	0.092(3)
120.	0.047(2)	0.305(12)	0.382(10)	0.192(7)	0.0611(16)
142.	0.0359(14)	0.237(10)	0.285(8)	0.141(5)	0.0441(12)
192.	0.0211(7)	0.130(6)	0.156(4)	0.082(3)	0.0232(7)
232.	0.0133(5)	0.085(3)	0.100(3)	0.0511(17)	0.0142(4)
281.	0.0074(3)	0.0495(19)	0.0574(17)	0.0284(10)	0.0081(3)
301.	0.0060(2)	0.0391(14)	0.0462(23)	0.0223(9)	0.0063(2)
321.	0.0049(2)	0.0331(15)	0.0380(11)	0.0183(8)	0.00494(15)
340.	0.0038(2)	0.0243(9)	0.0303(9)	0.0130(5)	0.00404(16)
366.	0.0027(4)	0.0216(16)	0.0233(12)	0.0107(10)	0.00306(10)

the same type connected with each other were put at the same time. The first respective to the neutron source detector had a greater  ${}^6\text{Li}$ -isotope concentration. The coordinates of the point of tritium

Table 4.4 Absolute reaction rates in the first radial channel of the blanket mock-up with uranium multiplier ( $10^{28}$ /atom/source).

Detector coordinate, mm	${}^{115}\text{In}(n,n')$	${}^{64}\text{Zn}(n,p)$	${}^{27}\text{Al}(n,p)$
30.	0.85(4)	0.360(12)	0.118(4)
130.	0.57(3)	0.244(9)	0.084(5)
190.	0.387(18)	0.169(6)	0.057(3)
230.	0.294(14)	0.123(5)	0.0400(16)
290.	0.181(9)	0.077(4)	0.0226(23)
330.	0.130(7)	0.058(3)	0.0188(18)
390.	0.066(5)	0.038(3)	0.0108(8)

Detector coordinate, mm	${}^{56}\text{Fe}(n,p)$	${}^{107}\text{Ag}(n,2n)$	${}^{63}\text{Cu}(n,2n)$	${}^{64}\text{Zn}(n,2n)$
30.	0.163(6)	1.06(7)	0.77(3)	0.240(7)
130.	0.115(4)	0.70(3)	0.473(17)	0.139(4)
190.	0.077(3)	0.49(4)	0.301(13)	0.091(3)
230.	0.056(2)	0.341(12)	0.214(10)	0.063(2)
290.	0.0325(13)	0.199(7)	0.127(5)	0.035(1)
330.	0.0270(16)	0.171(6)	0.102(4)	0.0280(9)
390.	0.0171(10)	0.112(5)	0.066(2)	0.0168(7)

Table 4.5 Absolute reaction rates in the second radial channel of the blanket mock-up with uranium multiplier ( $10^{28}$ /atom/source).

Detector coordinate, mm	$^{115}\text{In}(n,n')$	$^{204}\text{Pb}(n,n')$	$^{64}\text{Zn}(n,p)$	$^{27}\text{Al}(n,p)$
45.	0.112(5)	0.0249(9)	0.0453(17)	0.0145(5)
125.	0.089(4)	0.0211(9)	0.0349(15)	0.0118(4)
165.	0.078(3)	0.0178(8)	0.0310(14)	0.0098(3)
230.	0.058(3)	0.0135(5)	0.0226(10)	0.0073(3)
270.	0.048(2)	0.0108(5)	0.0171(9)	0.0055(2)
310.	0.035(2)	0.0087(4)	-	0.00424(17)
350.	0.0256(13)	0.0067(3)	-	0.00347(14)

Detector coordinate, mm	$^{56}\text{Fe}(n,p)$	$^{107}\text{Ag}(n,2n)$	$^{63}\text{Cu}(n,2n)$	$^{64}\text{Zn}(n,2n)$
45.	0.0195(7)	0.117(4)	0.073(3)	0.0202(5)
125.	0.0148(5)	0.091(3)	0.056(2)	0.0154(5)
165.	0.0124(5)	0.074(3)	0.0459(17)	0.0118(3)
230.	0.0092(4)	0.0528(18)	0.0321(12)	0.0082(3)
270.	0.0072(3)	0.0424(16)	0.0256(10)	0.0061(2)
310.	0.0056(2)	0.0324(13)	0.0187(7)	0.0047(2)
350.	0.00422(17)	0.0264(10)	0.0152(6)	0.0033(3)

production measurement were fixed at the line of connection between the detectors of various types. About 100 detectors were simultaneously irradiated in the mock-up. This allowed one to eliminate the renormalization of the results of separate irradiations. Experimental results are given in Fig. 9-14 and in Tables 4.6, 4.7.

Table 4.6 Tritium production rates in axial channel of the blanket mock-up with uranium multiplier,  $10^{28}$ /Li atom/source.

Lithium zone	Detector coordinate, mm	$T_6$	$T_7$
1	60	19.5 (18)	0.313 (18)
	90	26.2 (16)	0.237 (13)
	105	39.4 (24)	0.199 (11)
	120	75.8 (42)	0.174 (10)
2	141	83.8 (41)	0.135 (8)
	151	42.4 (21)	0.116 (8)
	161	24.9 (13)	0.103 (8)
	171	20.0 (10)	0.088 (6)
	191	13.6 (7)	0.074 (6)
	211	10.6 (7)	0.064 (5)
	231	10.3 (7)	0.054 (4)
	251	12.9 (8)	0.042 (4)
	271	22.5 (13)	0.034 (4)
	281	39.3 (22)	0.031 (9)
3	300	50.7 (27)	0.025 (2)
	310	32.9 (18)	0.023 (2)
	320	27.9 (16)	0.021 (2)
	330	34.0 (19)	0.019 (2)
	340	57.7 (28)	0.017 (2)
	365	74.2 (35)	0.013 (2)

Table 4.7 Tritium production rates in radial channels of the blanket mock-up with uranium multiplier,  $10^{28}/\text{Li atom/source}$ .

	Detector coordinate, mm	Radial channels			
		1	2	3	4
$T_6$	45.	20.6 (14)	10.9 (8)	20.3 (14)	26.3 (18)
	85.	17.7 (12)	9.4 (7)	21.2 (15)	23.1 (16)
	125.	16.4 (12)	7.6 (6)	16.1 (12)	21.2. (16)
	165.	13.1 (10)	7.0 (5)	13.0 (10)	18.3 (14)
	230.	10.8 (8)	3.4 (3)	12.3 (9)	13.1 (10)
	270.	7.5 (6)	3.6 (3)	9.8 (7)	11.6 (9)
	310.	6.1 (5)	2.9 (2)	8.1 (6)	8.9 (7)
	350.	4.9 (4)	1.6 (2)	6.0 (5)	5.8 (5)
$T_7$	45.	0.233 (15)	0.0636 (40)	0.0318 (20)	0.0192 (12)
	85.	0.206 (13)	0.0584 (38)	0.0288 (18)	0.0178 (12)
	125.	0.170 (11)	0.0521 (32)	0.0261 (17)	0.0159 (10)
	165.	0.138 (9)	0.0446 (29)	0.0237 (15)	0.0144 (9)
	230.	0.0912 (62)	0.0340 (22)	0.0178 (12)	0.0113 (7)
	270.	0.0667 (45)	0.0271 (16)	0.0152 (10)	0.0096 (7)
	310.	0.0481 (34)	0.0212 (14)	0.0120 (8)	0.0080 (6)
	350.	0.0343 (23)	0.0161 (10)	0.0096 (7)	0.0066 (6)

The distributions of the fission rates for different fission isotopes and of the  $^{238}\text{U}(n,2n)$  and  $^{238}\text{U}(n,\gamma)$  reaction rates at the central axis of the uranium zone are shown in Table 4.8.

The distributions of the activation rates of simulating reactions  $^{31}\text{P}(n,\gamma)^{32}\text{P}$  and  $^{35}\text{Cl}(n,\alpha)^{32}\text{P}$  in axial and radial channels are given in Tables 4.9, 4.10.

Experimental results for the mock-up with lead multiplier are given in Tables 4.11-4.16.

Table 4.8 Fission and multiplication rates at the axis of uranium zone of the blanket mock-up with uranium multiplier,  $10^{27}$ /atom/source.

Reaction	Positions in axial channel			
	1	2	3	4
$^{233}\text{U}(n, f)$	3.79(24)	3.64(24)	3.91(24)	4.10(25)
$^{235}\text{U}(n, f)$	1.99(7)	2.14(17)	2.13(18)	2.30(18)
$^{238}\text{U}(n, \gamma)$	0.133(5)	0.144(5)	0.165(6)	0.173(6)
$^{238}\text{U}(n, 2n)$	0.196(9)	0.156(9)	0.156(8)	0.134(7)
$^{232}\text{Th}(n, f)$	0.155(12)	0.145(12)	0.136(9)	0.119(9)
$^{237}\text{Np}(n, f)$	1.56(9)	1.46(8)	1.45(8)	1.17(7)
$^{238}\text{U}(n, f)$	0.490(41)	0.458(38)	0.407(34)	0.352(31)
Coordinate, mm	11.	16.	24.	34.

Reaction	Positions in axial channel		
	5	6	7
$^{233}\text{U}(n, f)$	4.07(25)	4.35(25)	4.30(25)
$^{235}\text{U}(n, f)$	2.42(18)	2.34(18)	2.53(19)
$^{238}\text{U}(n, \gamma)$	0.183(6)	0.182(6)	0.337(11)
$^{238}\text{U}(n, 2n)$	0.123(7)	0.119(6)	0.080(6)
$^{232}\text{Th}(n, f)$	0.086(7)	0.080(7)	0.075(6)
$^{237}\text{Np}(n, f)$	1.14(7)	1.08(6)	0.82(5)
$^{238}\text{U}(n, f)$	0.283(25)	0.272(25)	0.194(21)
Coordinate, mm	41.	46.	60.

Table 4.9 Activation rates of simulating reactions in axial channel of blanket with uranium multiplier,  $10^{30}$ /atom/source.

Detector coordinate, mm	$^{31}\text{P}(n,\gamma)^{32}\text{P}$	$^{35}\text{Cl}(n,\alpha)^{32}\text{P}$
60.	1.36 (6)	16.0 (6)
90.	1.43 (6)	10.9 (5)
120.	2.66 (12)	7.79 (35)
141.	2.58 (12)	5.98 (27)
171.	0.82 (4)	4.34 (20)
191.	0.61 (3)	3.61 (17)
211.	0.47 (3)	2.96 (14)
231.	0.44 (3)	2.40 (11)
251.	0.50 (3)	1.96 (9)
281.	1.19 (6)	1.46 (7)
300.	1.36 (7)	1.18 (6)
320.	0.66 (3)	0.98 (5)
340.	1.56 (7)	0.78 (4)
365.	2.24 (9)	0.63 (3)

Table 4.10  $^{35}\text{Cl}(n,\alpha)^{32}\text{P}$  activation rate in radial channels of the blanket mock-up with uranium multiplier,  $10^{30}$ /atom/source.

Detector coordinate, mm	Radial channels			
	1	2	3	4
45.	10.8 (4)	2.95 (13)	1.46 (7)	0.89 (4)
85.	9.57 (40)	2.72 (12)	1.34 (6)	0.83 (4)
125.	7.89 (34)	2.43 (11)	1.21 (6)	0.73 (4)
165.	6.38 (27)	2.08 (10)	1.10 (5)	0.67 (3)
230.	4.55 (20)	1.58 (8)	0.83 (4)	0.53 (3)
270.	3.09 (14)	1.26 (6)	0.70 (4)	0.45 (2)
310.	2.24 (10)	0.99 (5)	0.56 (3)	0.37 (2)
350.	1.60 (8)	0.75 (4)	0.45 (2)	0.30 (2)

Table 4.11 Activation rates in axial channel of the blanket mock-up with lead multiplier ( $10^{28}$ /atom/source).

Detector coordinate, mm	$^{115}\text{In}(n,n')$	$^{204}\text{Pb}(n,n')$	$^{64}\text{Zn}(n,p)$	$^{27}\text{Al}(n,p)$	
0.	0.702(18)	0.285(8)	0.617(18)	0.253(7)	
11.	0.813(21)	0.241(7)	0.508(15)	0.203(6)	
41.	0.716(18)	0.160(5)	0.318(10)	0.120(4)	
76.	0.546(14)	0.097(3)	0.188(6)	0.066(2)	
111.	0.356(9)	0.063(2)	0.118(4)	0.041(1)	
141.	0.257(7)	0.047(2)	0.085(3)	0.0289(9)	
170.	0.172(5)	0.0348(10)	0.062(2)	0.0206(6)	
192.	0.122(3)	0.0299(10)	0.049(2)	0.0164(7)	
242.	0.086(2)	0.0179(8)	0.0330(11)	0.0104(4)	
282.	0.057(2)	0.0134(4)	0.0231(9)	0.0069(3)	
331.	0.0331(9)	0.0082(3)	0.0137(8)	0.0045(2)	
351.	0.0242(7)	0.0065(3)	0.0119(7)	0.0035(2)	
371.	0.0212(6)	0.0062(3)	0.0106(6)	0.0030(2)	
390.	0.0159(5)	0.0048(2)	0.0092(7)	0.0027(1)	
416	0.0116(5)	0.0042(2)	0.0070(6)	0.0018(1)	
Detector coordinate, mm	$^{56}\text{Fe}(n,p)$	$^{107}\text{Ag}(n,2n)$	$^{65}\text{Cu}(n,2n)$	$^{63}\text{Cu}(n,2n)$	$^{64}\text{Zn}(n,2n)$
0.	0.400(10)	2.71(8)	3.36(9)	1.88(5)	0.615(16)
11.	0.310(8)	2.09(6)	2.62(7)	1.46(4)	0.469(12)
41.	0.176(5)	1.16(4)	1.42(4)	0.80(2)	0.260(7)
76.	0.094(3)	0.63(2)	0.77(2)	0.42(1)	0.136(4)
111.	0.056(2)	0.355(12)	0.440(12)	0.239(7)	0.076(2)
141.	0.039(1)	0.250(9)	0.313(9)	0.165(5)	0.051(1)
170.	0.0280(8)	0.174(6)	0.215(6)	0.117(3)	0.034(1)
192.	0.0219(7)	0.136(8)	0.164	0.083(2)	0.0250(9)
242.	0.0129(4)	0.077(3)	0.101(3)	0.047(1)	0.0138(3)
282.	0.0085(3)	0.050(2)	0.0630(18)	0.0298(9)	0.0086(3)
331.	0.0052(2)	0.0306(11)	0.0360(13)	0.0175(5)	0.0046(2)
351.	0.0042(2)	0.0236(9)	0.0282(10)	0.0137(4)	0.0036(2)
371.	0.0035(2)	0.0207(8)	0.0250(10)	0.0113(3)	0.0031(1)
390.	0.0029(1)	0.0165(7)	0.0192(9)	0.0094(3)	0.0024(1)
416	0.0020(1)	0.0131(5)	0.0147(9)	0.0070(30)	0.0018(2)

Table 4.12  $^{35}\text{Cl}(n,\alpha)^{32}\text{P}$  activation rate in radial channels of the blanket mock-up with lead multiplier,  $10^{30}$ /atom/source.

Detector coordinate, mm	Radial channels			
	1	2	3	4
45.	7.69 (34)	2.42 (12)	1.29 (6)	0.75 (4)
85.	7.17 (34)	2.33 (11)	1.24 (6)	0.73 (4)
125.	6.38 (31)	2.18 (10)	1.16 (6)	0.67 (4)
165.	5.43 (27)	1.89 (9)	1.02 (6)	0.61 (4)
230.	3.87 (19)	1.51 (8)	0.83 (5)	0.51 (3)
270.	2.94 (14)	1.27 (6)	0.67 (4)	0.44 (3)
310.	2.24 (11)	1.05 (6)	0.59 (4)	0.37 (3)
350.	1.63 (8)	0.85 (5)	0.49 (3)	0.31 (3)

Table 4.13 Activation rates of simulating reactions in axial channel of the blanket mock-up with lead multiplier,  $10^{30}$ /atom/source.

Detector coordinate, mm	$^{31}\text{P}(n,\gamma)^{32}\text{P}$	$^{35}\text{C}(n,\alpha)^{32}\text{P}$
	110.	0.42 (2)
140.	0.44 (2)	6.13 (28)
170.	0.96 (5)	4.62 (21)
191.	0.93 (5)	3.58 (17)
221.	0.32 (2)	2.80 (13)
241.	0.22 (1)	2.27 (10)
261.	0.19 (1)	1.94 (9)
281.	0.16 (1)	1.53 (7)
301.	0.21 (1)	1.31 (6)
331.	0.44 (2)	0.96 (5)
350.	0.47 (2)	0.83 (4)
370.	0.22 (1)	0.69 (3)
390.	0.67 (3)	0.57 (3)
415.	0.92 (5)	0.46 (2)

Table 4.14 Activation rates in the second radial channel  
of the blanket mock-up with lead multiplier  
( $10^{28}$ /atom/source).

Detector coordinate, mm	$^{115}\text{In}(n,n')$	$^{204}\text{Pb}(n,n')$	$^{64}\text{Zn}(n,p)$	$^{27}\text{Al}(n,p)$
45.	0.222(6)	0.0419(14)	0.076(3)	0.0256(9)
85.	0.197(5)	0.0413(14)	0.068(2)	0.0214(8)
125.	0.178(5)	0.0351(12)	0.062(2)	0.0188(7)
165.	0.151(4)	0.0302(11)	0.0522(18)	0.0155(6)
230.	0.116(3)	0.0231(12)	0.0380(14)	0.0121(5)
310.	0.0688(19)	0.0140(7)	0.0250(12)	0.0077(4)
350.	0.0491(17)	0.0115(7)	0.0168(14)	0.0051(2)
Detector coordinate, mm	$^{56}\text{Fe}(n,p)$	$^{107}\text{Ba}(n,2n)$	$^{63}\text{Cu}(n,2n)$	$^{64}\text{Zn}(n,2n)$
45.	0.0350(9)	0.210(7)	0.137(5)	0.0429(12)
85.	0.0311(9)	0.184(7)	0.118(3)	0.0373(14)
125.	0.0271(8)	0.157(6)	0.103(4)	0.0315(9)
165.	0.0222(6)	0.124(4)	0.083(3)	0.0262(8)
230.	0.0164(5)	0.096(3)	0.060(2)	0.0189(6)
310.	0.0124(5)	0.057(2)	0.0351(12)	0.0099(4)
350.	0.0071(5)	0.0426(18)	0.0248(8)	0.0069(3)

Table 4.15 Tritium production rates in axial channel of the blanket with lead multiplier,  $10^{28}$ /Li atom/source.

Lithium zone	Detector coordinate, mm	T <sub>6</sub>	T <sub>7</sub>
1	110.	10.9 (8)	0.160 (10)
	140.	14.9 (8)	0.126 (8)
	155.	22.2 (13)	0.116 (7)
	170.	36.1 (23)	0.094 (6)
2	191.	40.5 (22)	0.076 (5)
	201.	20.6 (12)	-
	211.	12.5 (3)	-
	221.	9.8 (6)	0.059 (4)
	241.	6.8 (5)	0.048 (3)
	261.	5.5 (4)	0.040 (3)
	281.	5.4 (4)	0.033 (3)
	301.	7.2 (5)	0.028 (2)
	321.	12.8 (8)	-
	331	21.6 (12)	0.020 (2)
3	350.	25.2 (13)	0.018 (2)
	360.	17.5 (10)	-
	370.	15.8 (8)	0.015 (1)
	380.	16.9 (9)	-
	390.	31.2 (17)	0.012 (2)
	415.	41.2 (22)	0.010 (2)

Table 4.16 Tritium production rates in radial channel of the blanket with lead multiplier,  $10^{28}$ /Li atom/source.

	Detector coordinate, mm	Radial channel			
		1	2	3	4
T <sub>6</sub>	45.	11.4 (8)	5.4 (4)	11.6 (8)	14.0 (8)
	85.	9.6 (7)	4.5 (3)	10.5 (7)	11.7 (7)
	125.	8.7 (7)	3.9 (3)	8.7 (7)	11.2 (7)
	165.	7.5 (6)	3.3 (3)	8.0 (6)	9.3 (7)
	230.	5.2 (4)	2.1 (2)	6.5 (5)	6.6 (5)
	270.	3.9 (3)	1.8 (2)	5.5 (4)	5.6 (4)
	310.	3.2 (3)	1.4 (2)	4.3 (3)	4.8 (4)
	350.	2.7 (3)	1.0 (2)	3.1 (3)	2.9 (3)
T <sub>7</sub>	45.	0.155 (8)	0.0485 (28)	0.0260 (16)	0.0150 (10)
	85.	0.144 (8)	0.0469 (28)	0.0250 (15)	0.0147 (10)
	125.	0.128 (7)	0.0439 (26)	0.0232 (14)	0.0136 (9)
	165.	0.109 (6)	0.0379 (24)	0.0205 (14)	0.0123 (8)
	230.	0.0777 (51)	0.0302 (19)	0.0166 (11)	0.0102 (7)
	270.	0.0588 (42)	0.0255 (16)	0.0135 (9)	0.0089 (6)
	310.	0.0449 (31)	0.0209 (14)	0.0118 (8)	0.0075 (6)
	350.	0.0329 (21)	0.0170 (12)	0.0098 (7)	0.0061 (5)

### 5. The main sources of experimental errors

In determination of absolute neutron yield and fluence it has been assumed that the most components of their errors have a systematic nature. Part of them were calculated as mean-square ones in the results from a series of experiments; another part, from estimating of the maximal deviations in the values, when it was practically impossible to arrange a series of measurements, and the error could not be precisely calculated. The main sources of errors in absolute neutron yields and fluences are given in Table 5.1.

The calculation of a mean-square error in absolute neutron yield and fluence shows that they are at the level 2,7 % in the

confidential range equal 0.68. The calculated mean-square error in the absolute  $\gamma$ -activity of detectors, the main sources of which are shown in Table 5.2, is at the level  $\sim$  (2-3) %. The error which emerges in the measurement of relative activities with a multichannel system for measuring of the nuclear reactions rates includes the statistic error in relative normalization of spectrometric tracts, the error due to background reaction effect and is within the range  $\sim$  (2-3) %. Taking account of all the error sources and their components, the error in the measurement of absolute normalized nuclear reaction rates is estimated as (5-7) %.

The procedure of measuring the tritium production is rather complicated and can introduce the errors in the final result of an experiment. Therefore the parameters of the procedure were standardized in order to exclude the possibilities of error emergence during the procedure. The sequence of manipulations in the treatment of detectors and the parameters of processes taking place in that case were determined. The control over the complete transition of tritium from the detector into a tritium-bearing phase was realized with a lithium carbonate detector irradiated within a standard thermal neutron flux.

In all the experiments the procedure of the detector treatment remained later unchanged that excluded an opportunity to increase the experimental error. As a result of tritium  $\beta$ -decay activity treatment with due regard for errors emerging in separation of contributions into the tritium production by its various isotopes, the normalized rates of tritium production were obtained with the error  $\sim$  (8-10) %.

The reaction rates measured in the uranium zone can be divided into two groups by the method of their determination: fission rates (method of solid-state track detectors) and  $^{238}\text{U}(n,\gamma)$ ,  $^{238}\text{U}(n,2n)$  reaction rates (gamma-spectrometric method).

The error in the fission rate measurements includes the errors in determination of a neutron fluence (see Table 5.1), number of isotope nuclei upon the track radiators and in the track technique of registering fission fragments. The number of nuclei was measured by two independent methods: by activity of fissile isotopes and with the thermal neutron flux standard, i.e. with the certified thermal column of the reactor. The error sources and their

components are given in Tables 5.3-5.5.

The sources and the error components in the gamma-spectrometric method of reaction rate measurements -  $^{238}\text{U}(n,\gamma)$  and  $^{238}\text{U}(n,2n)$  - are given in Table 5.2 and estimated within the range (4-7) %.

Table 5.1 Error sources in the absolute value of neutron yield.

Error sources	Value and type of error	
	Systematic, %	Maximal deviation, %
1. Parameters of interaction between a deuteron beam and a tritium layer of the target	-	2.0
2. Presence of the ions $\text{D}_2^+$ and $\text{D}_3^+$ in the deuteron beam	-	0.3
3. Inhomogeneity in tritium density upon the target.	-	1.0
4. Scattering of neutrons upon the structural target materials.	-	0.5
5. Setting of a potential accelerating deuterons.	-	0.5
6. Presence of $\alpha$ -particles from the reaction $^3\text{He}(d,p)^4\text{He}$	-	0.6
7. Presence of neutrons from the reaction $^2\text{H}(d,n)^3\text{He}$	-	0.5
8. Determination of $\alpha$ -particle count rate in calibration of the $\alpha$ -radiometer.	1.0	-
9. Yield of $\alpha$ -particles from a calibrated source.	0.7	-
10. Relative rate of $\alpha$ -particle registration in two channels of the $\alpha$ -radiometer.	1.0	-
11. Pointedness form of a neutron source.	-	0.7
12. Treatment of $\alpha$ -particle spectrum.	0.5	-
13. Errors in the system of absolute $\alpha$ -particle count.	0.3	-

Table 5.2 Error sources in the measurements of the absolute  $\gamma$ -activity of irradiated defectors.

Error sources	Value and type of error	
	Systematic, %	Maximal deviation, %
1. Model for calculations of a photopeak area	-	1.5
2. Calculation of a photopeak area	1.0 - 2.5	-
3. Absolute efficiency of a unit detecting $\alpha$ -activity of the detectors	-	0.8 - 1.5
4. Coefficient of $\gamma$ -quanta self-absorption	-	0.5
5. Cascade summation of $\gamma$ -quanta	-	0.5
6. Effect of background reactions	-	1.0
7. $\gamma$ -quanta yield per decay	-	0.3
8. Half-life period of an isotope	-	0.1

Table 5.3 Error sources in the measurement of nuclei number by  $\gamma$ - and  $\alpha$ -activities of fissile radiators.

Error sources	Statistical, %	Systematic, %
1. Activity of standard $\alpha$ -sources	-	0.7
2. Activity of standard $\gamma$ -sources	-	0.5 - 1.0
3. Calibration of $\alpha$ -spectrometer, $\gamma$ -spectrometer	-	1.0 1.5
4. Yield per decay of $\alpha$ -particles, $\gamma$ -quanta	-	0.5 0.8
5. Number of registered events	0.4 - 1.5	
6. Cascade summation of $\gamma$ -quanta	-	0.5
7. Taking account of the background	-	0.8
8. Half - life period	-	0.1

Table 5.4 Error sources in the measurement of nuclei number with the thermal neutron flux density standard.

Error sources	Statistical, %	Systematic, %
1. Thermal neutron flux standard	-	0.7
2. Flux monitoring	-	1.5
3. Track technique for registering fission fragments	-	2.1
4. Isotope fission cross section	-	0.5

Table 5.5 Error sources in the track technique of fission fragments registration.

Error sources	Statistical, %	Systematic, %
1. Number of tracks	1.0 - 2.5	-
2. Visual technique for the track counting	-	1.5
3. Efficiency of registering the fragments with muscovite	-	1.0
4. Deviation from the $4\pi$ - geometry	-	1.5

## 6. Neutron transport calculations

### 6.1. Transport code

Measured values were calculated by the BLANK code [3] in a 3-dimensional rectangular geometry by the Monte-Carlo method. In 0.1-15.2 MeV energy range the working 18-group constants, prepared from the ENDF/B-4 and ENDL-83 evaluated data, were used with a new version of the collision module FORTUN-88 [4]. Below 0.1 MeV 13-group  $P_1$ -constants [5] with corrections on a resonance self-shielding and neutron temperature in the thermal group were used. The neutron temperatures in zones were determined by the MCU code [6] in calculation with a uniform fission source. Geometry of

calculational model was close to the experimental one. The neutron source target was presented as an uniform disk with a homogenized layer of water and brass, isotropically emitting neutrons with energy linearly depending on  $\mu$  in 13.45-14.75 MeV energy range. Neutron flux was calculated by the track length and the local estimator methods. The details of the calculational model description are given in the Appendix.

## 6.2. Main results of calculations

### 6.2.1. The blanket mock-up with uranium multiplier

Some experimental results in comparison with calculations are shown in Fig. 15-19. Fig. 15 shows agreement of tritium production calculation with experiment in general. The discrepancy in  $T_6$  ~20 % corresponds only to the internal parts of lithium-containing zones. The same effect can be noticed below in calculation of experiment with lead multiplier and can be explained by inadequate moderation by Al in the volume of the zones (as it was mentioned above, below 0.1 MeV 13-group  $P_1$ -neutron data were used). Agreement of  $T_7$  distributions in axial and radial channels in Fig. 15, 16 is quit good. Activation rates in axial channel and radial channel R2 show in Fig. 17 and 18 good agreement with experiment except, may be, ~10 % overestimation of  $^{64}\text{Zn}(n,p)^{64}\text{Cu}$  activation rate, that could be explained by inadequate cross sections, taken from the Lapenas library [2]. In Fig. 19 some reaction rates in uranium zone are shown. The discrepancies ~10 % in calculation of  $^{238}\text{U}(n,f)$  and  $^{238}\text{U}(n,\gamma)$  reaction rates are close to the experimental errors (7-8 %).

### 6.2.2. The blanket mock-up with lead multiplier

Experimental results in comparison with calculations are shown in Fig. 20-22. Fig. 20 shows that the calculation underestimates  $^{115}\text{In}(n,n')$  and  $^{64}\text{Zn}(n,p)$  reaction rates in the first layers of the assembly. That can be explained by underestimation of multiplication in lead. Tritium production rates in lithium-containing zones of the assembly are shown in Fig. 21. There is a good

agreement for  $T_7$  rate in all zones, for  $T_6$  in the first lithium containing zone and in the areas of the following zones near the moderator. In internal parts of these zones calculation overestimates the absorption in  ${}^6\text{Li}$  by ~20 %.. The same effect takes place in calculation of the blanket mock-up with uranium multiplier, as it was mention above.

## 7. Conclusion

Comparison of experimental results with calculations by the BLANK code with ENDF/B-IV neutron data shows agreement within ~10%, close to the errors, for the most measured values, including  $T_7$  and  $T_6$  production rates in lithium-containing zones, distributions of activation rates in channels and reaction rates in uranium. For understanding of ~20 % of  $T_6$  discrepancy in the depth of LiAl zones additional studies are necessary.

Underestimation in the calculation of  ${}^{115}\text{In}(n,n')$  reaction rate in lead zone ones more confirms the underestimation by the neutron data of multiplication in lead, bombarded with 14 MeV neutrons.

## References

1. Cheng E.T. Nuclear data requirements for fusion reactor transport calculations and testing of ENDF/B-V and VI libraries. IAEA AGM, Gaussig (GDR), December 1-5, 1986.
2. Antipenkov A.B., et al. The blanket of the Experimental Fusion Reactor. Report on the IV-th USSR Conference on the Engineering Problems of Fusion (Leningrad, January 19-21, 1988), in Russian.
3. Markovskij D.V. Experimental Fusion Reactor. Main parameters and the state of neutronics. Report on a seminar of country-members of the Council for Mutual Economic Assistance. Varna (Bulgaria), May 4-8, 1987 (in Russian).
4. Marin S.V., Markovskij D.V., Shatalov G.E. Preprint IAEh-2382, Moscow 1977.
5. Markovskij D.V., Borisov A.A. Preprint IAEh-4774, Moscow 1989.
6. Shatalov G.E. DENSTY - the code for calculation of macroscopic cross sections, in: Vopr. atomn. Nauki Tekhn., Ser. "Physics and Techn. of Nucl. React", 8(21., 1981, P.39-41. (in Russian).
7. Liman G.F., Maiorov L.V., Yudkevitch M.S. The Code Package MCU for Radiation Transport in Nuclear Calculations, in: Vopr. atomn. Nauki Tekhn.", Ser. "Phys. and Tekhn. of Nucl. React.", 1985, 7, P. 27-31 (in Russian).

Appendix. 3-D calculational model scheme

Z, cm		Material zones		Material
"U"	"Pb"			
67.0	72.0	3	3	SS
65.0	70.0	6	6	PM
61.7	66.7	3	3	SS
51.6	56.6	6	6	PM
49.1	54.1	7	8	LiAl
47.1	52.1	7	5	LiAl
45.1	50.1	6	6	PM
43.2	48.2	7	8	LiAl
41.2	46.2	7	9	LiAl
37.2	42.2	7	7	LiAl
33.2	38.2	7	10	LiAl
29.2	34.2	6	6	PM
27.1	32.1	8	8	LiAl
25.1	30.1	7	7	LiAl
21.1	26.1	4	4	U / Pb
16.1	16.1	3	3	SS
15.1	15.1	2	2	Void
0.35	0.35	1	1	Target
0.0				

\*\*\*\*\*  
 Neutron source R=1. →  
 Axial channel R=1.8 →

x=50. X,Y  
 y=40. (cm)

## Material zones characteristics

Zone	Material	Nuclear densities
1	Target	H - $2.87 \cdot 10^{22}$
		Cu - $4.70 \cdot 10^{22}$
		O - $1.44 \cdot 10^{22}$
2	Void	O - $5.40 \cdot 10^{19}$
3	Stainless steel 12X18H10T	C - $4.79 \cdot 10^{20}$
		Cr - $1.66 \cdot 10^{22}$
		Ni - $8.15 \cdot 10^{21}$
		Ti - $9.99 \cdot 10^{20}$
		Fe - $6.09 \cdot 10^{22}$
4	Uranium	$^{238}\text{U}$ - $4.76 \cdot 10^{22}$
		$^{235}\text{U}$ - $1.91 \cdot 10^{20}$
	Lead	Pb - $3.16 \cdot 10^{22}$
5	LiAl alloy	$^6\text{Li}$ - $6.45 \cdot 10^{20}$
		$^7\text{Li}$ - $7.95 \cdot 10^{21}$
		Al - $4.93 \cdot 10^{22}$
6	Polimetil- metacrilat	H - $5.68 \cdot 10^{22}$
		C - $3.55 \cdot 10^{22}$
		O - $1.42 \cdot 10^{22}$
7	LiAl alloy	$^6\text{Li}$ - $6.61 \cdot 10^{20}$
		$^7\text{Li}$ - $8.16 \cdot 10^{21}$
		Al - $4.92 \cdot 10^{22}$
8	LiAl alloy	$^6\text{Li}$ - $6.76 \cdot 10^{20}$
		$^7\text{Li}$ - $8.34 \cdot 10^{21}$
		Al - $4.92 \cdot 10^{22}$
9	LiAl alloy	$^6\text{Li}$ - $7.66 \cdot 10^{20}$
		$^7\text{Li}$ - $9.45 \cdot 10^{21}$
		Al - $4.89 \cdot 10^{22}$
10	LiAl alloy	$^6\text{Li}$ - $7.81 \cdot 10^{20}$
		$^7\text{Li}$ - $9.64 \cdot 10^{21}$
		Al - $4.88 \cdot 10^{22}$

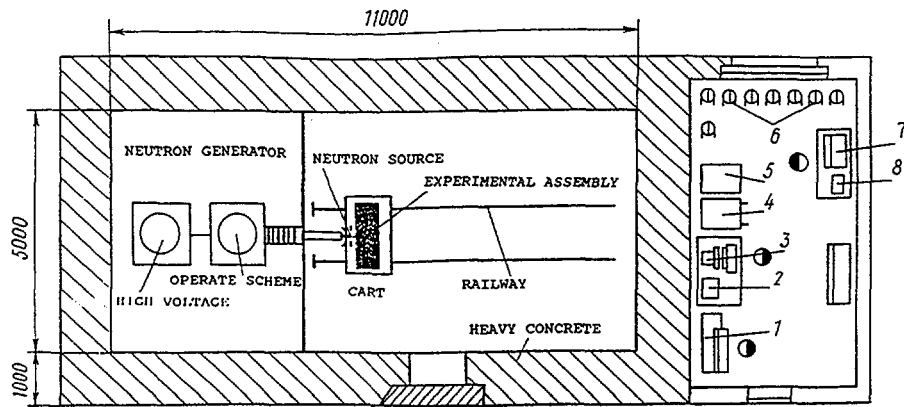


Fig. 1. Laboratory "Neutron Generator".

- 1 - neutron generator panel, 2 - graphic terminal, 3 - terminal
- 4 - computer MERA-60, 5 - CAMAC apparatus, 6 - spectrometer,
- 7 - pulse (amplitude) analyser LP-4900, 8 - tape recorder TDC-3000.

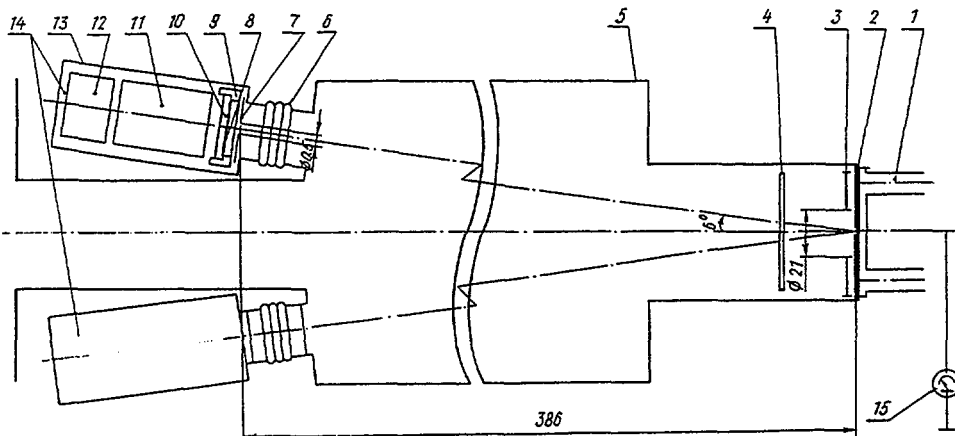


Fig. 2.  $\alpha$ -radiometer design.

- 1 - water cooling system, 2 - titanium-tritium target, 3 - diaphragm,
- 4 - dunatronic ring, 5 - body of the ion conduit, 6 - bellow,
- 7 - diaphragm, 8 - CsI(Tl)-crystal, 9 - mandrel, 10 - backing,
- 11 - photoelectron multiplier, FEU-60 Type, 12 - voltage divider and emitter follower, 13 - body, 14 - registering devices,
- 15 - microammeter.

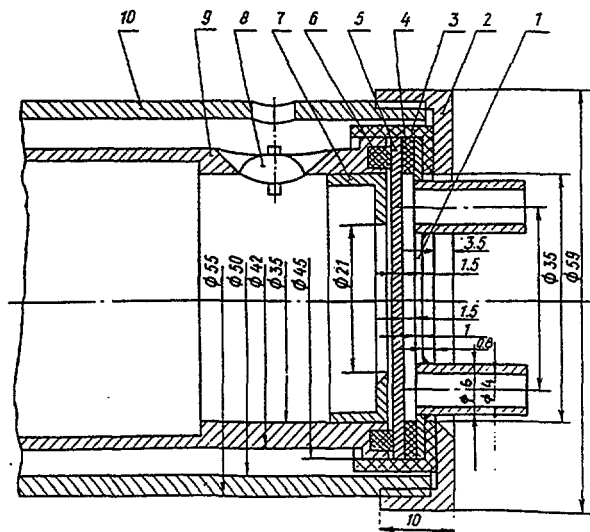


Fig. 3. Target device design.

- 1 - plug (brass), 2 - coupling nut (brass), 3 - insulator (teflon),
- 4 - gasket (rubber), 5 - titanium-tritium target (copper),
- 6 - vacuum gasket (rubber), 7 - ion manifold (steel 12N18H10T),
- 10 - jacket (duralumin).

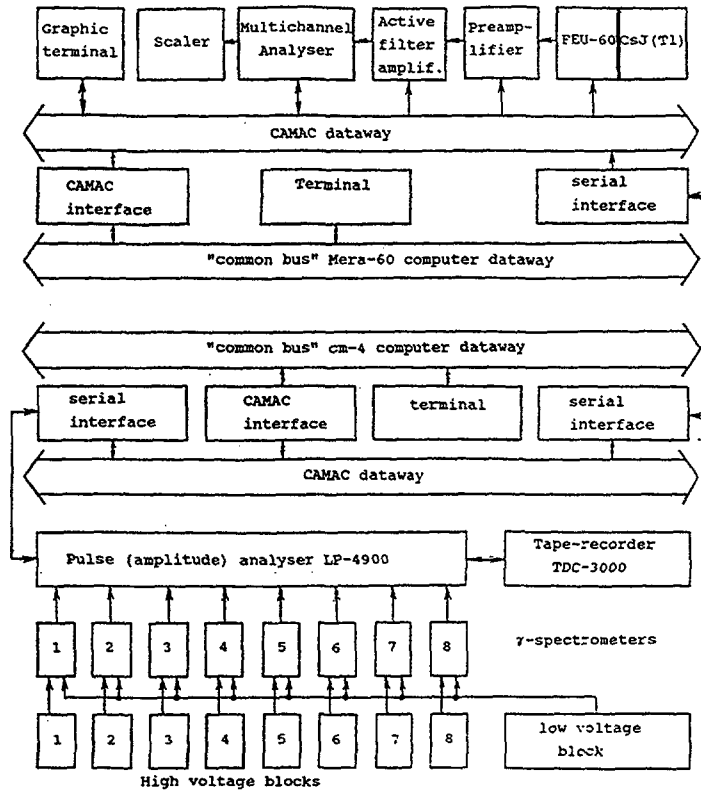


Fig. 4. Structural scheme of system for nuclear reaction rates measurements.

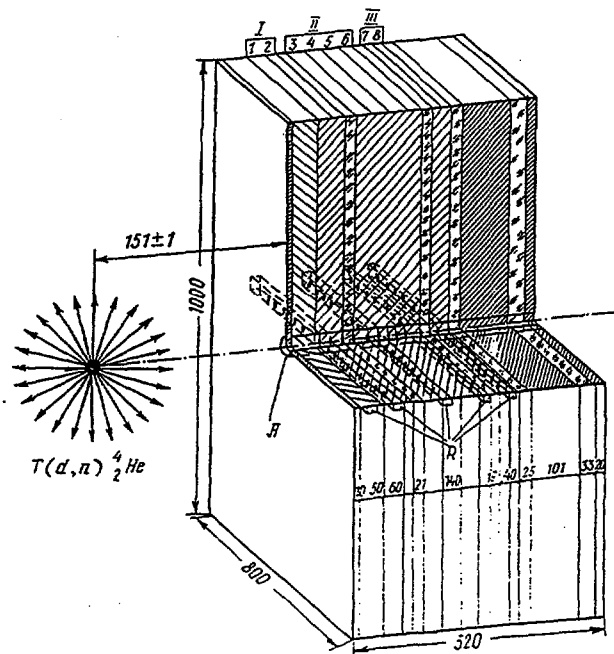


Fig.5. Structural sketch of hybrid blanket mock-up.

Structure of the composition:

- steel 12X18H10T, - metallic uranium, - LiAl-alloy,
- polymethylmetacrylate.

Channels for measurements: A - axial, R - radial, I,II,III- numbers of lithium-containing zones, 1, 2, 3 - numbers of layers.

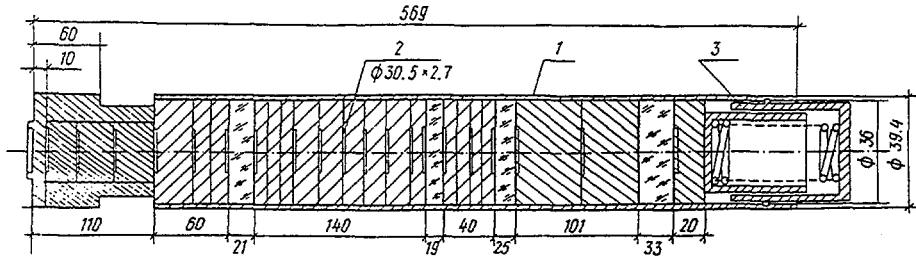


Fig. 6. Detector holder design in the axial channel of the "pure" blanket mock-up.

Composition of the structure:

- steel 12X18H10T, - lead, - LiAl-alloy.
- polymethylmetacrylate, - duralumin.

1-jacket, 2-cavities for detector location, 3-embracing device.

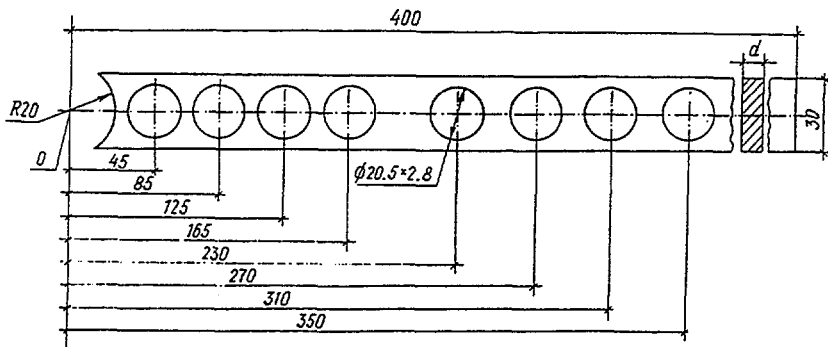


Fig. 7. Detector holder design for a radial channel.

O - is the axial channel axis. Holder thickness  $d=20$  mm for the blocks  $200/200/40$  mm<sup>3</sup>,  $d=12$ mm for the blocks  $200 \times 200 \times 20$  mm<sup>3</sup>.

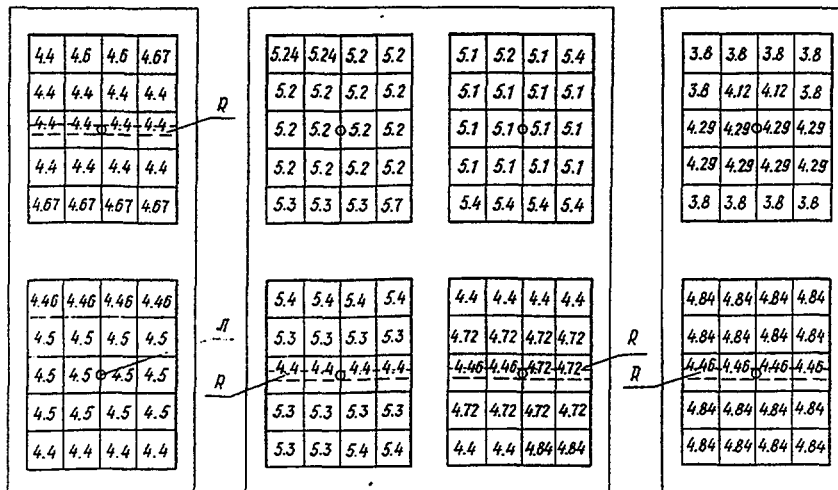


Fig. 8. Map of LiAl-alloy blocks disposition in the zones of tritium production (numbers indicate the Li content in % by weight).

Channels of measurements: A - axial, R - radial.

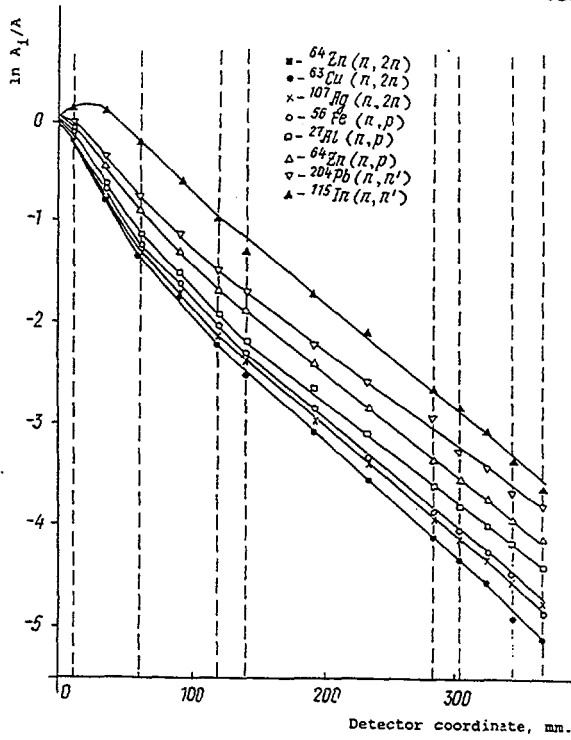


Fig. 9. Relative activation rate distributions in the axial channel of the blanket mock-up with uranium.

A - activation rate on the front mock-up surface,  
 $A_1$  - activation rate of same detector inside the mock-up.

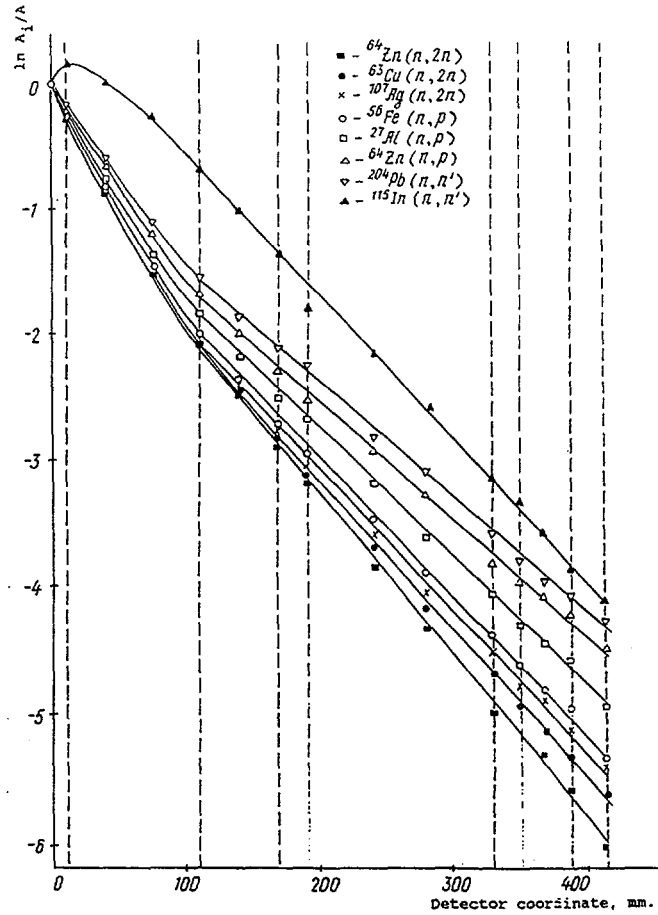


Fig. 10. Relative activation rate distributions in the axial channel of the blanket mock-up with lead.

A - activation rate on the front mock-up surface,  
 $A_1$  - activation rate of same detector inside the mock-up.

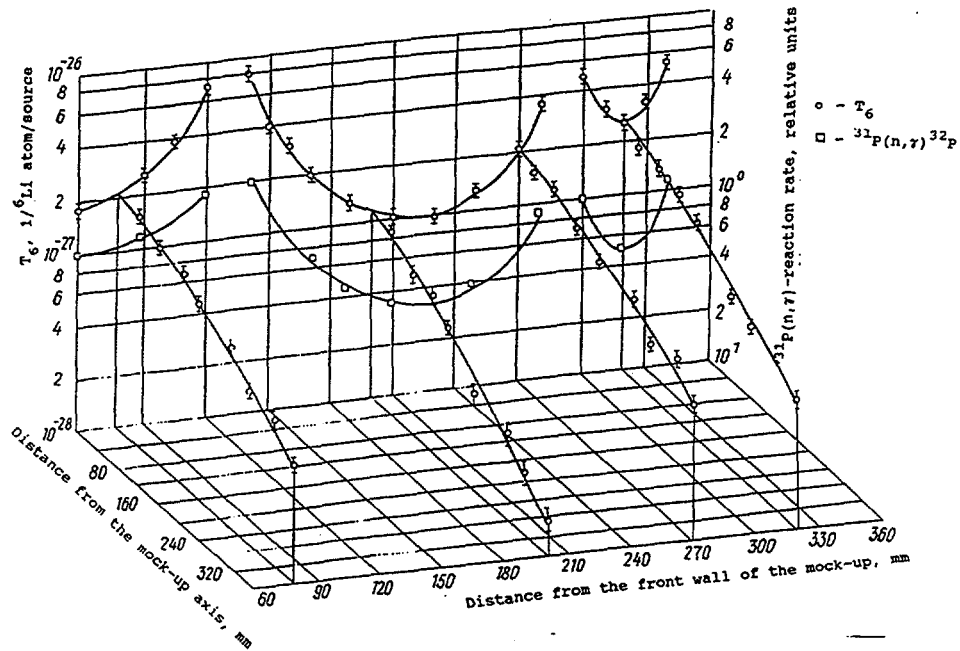


Fig. 11.  $T_6$  distribution in the hybrid blanket mock-up.

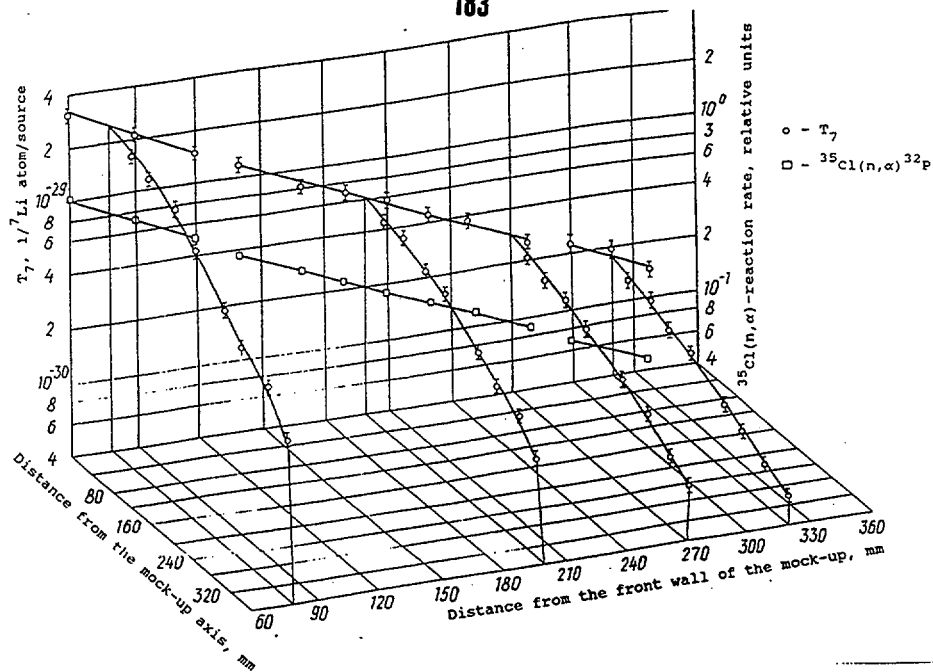


Fig. 12.  $T_7$  distribution in the hybrid blanket mock-up.

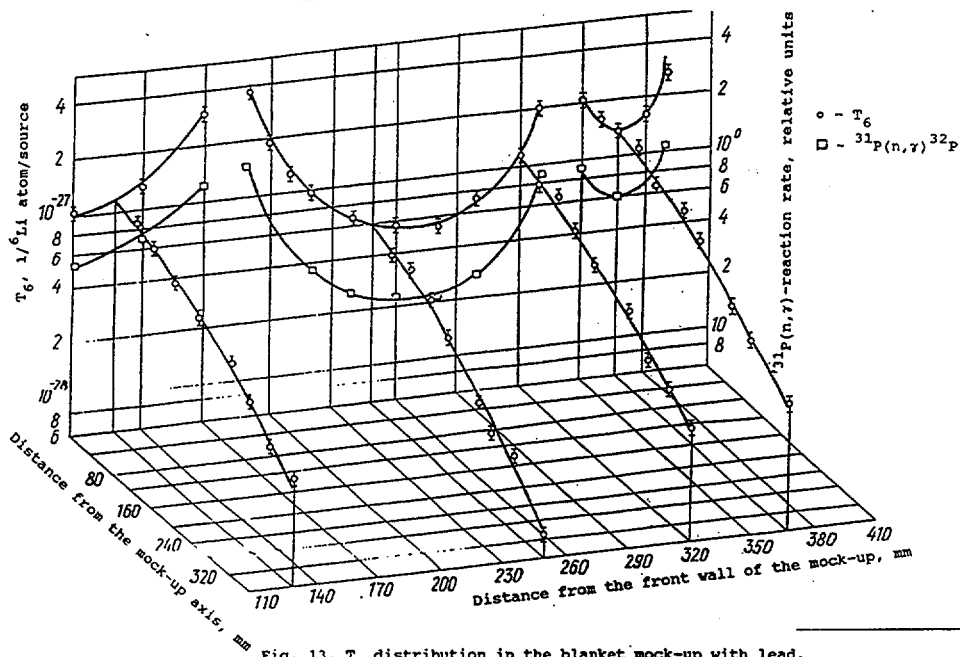


Fig. 13.  $T_6$  distribution in the blanket mock-up with lead.

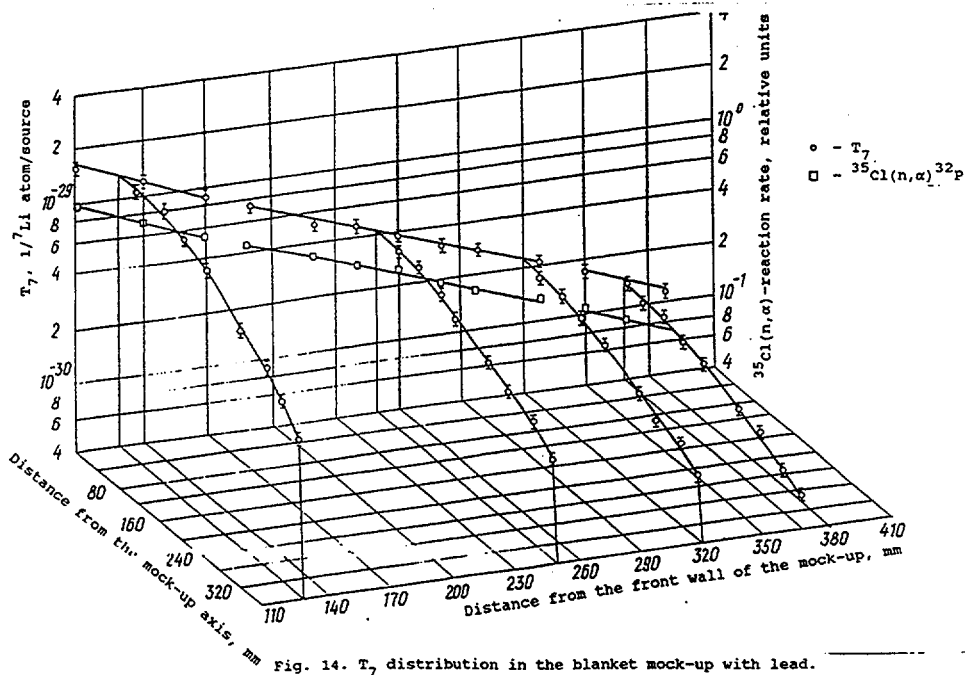


Fig. 14.  $T_7$  distribution in the blanket mock-up with lead.

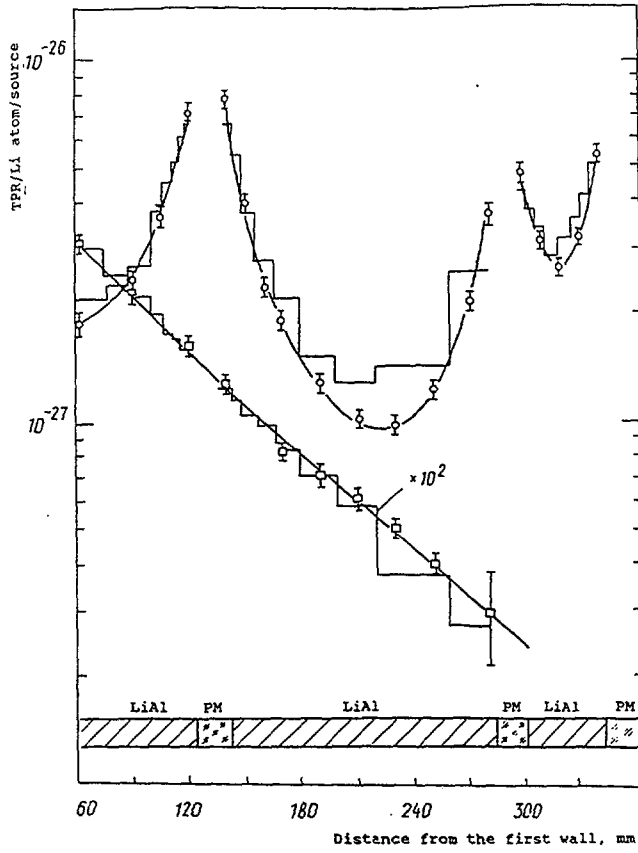


Fig. 15. Tritium production rates in axial channel of the hybrid mock-up.

○ -  $T_6$ , □ -  $T_7$ .

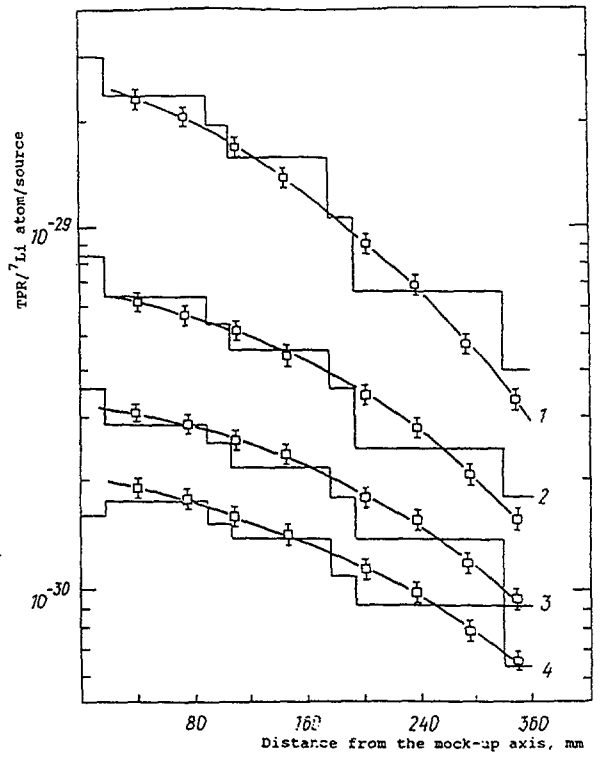


Fig. 16.  $T_7$  distribution in radial channels 1-4 of the hybrid mock-up.

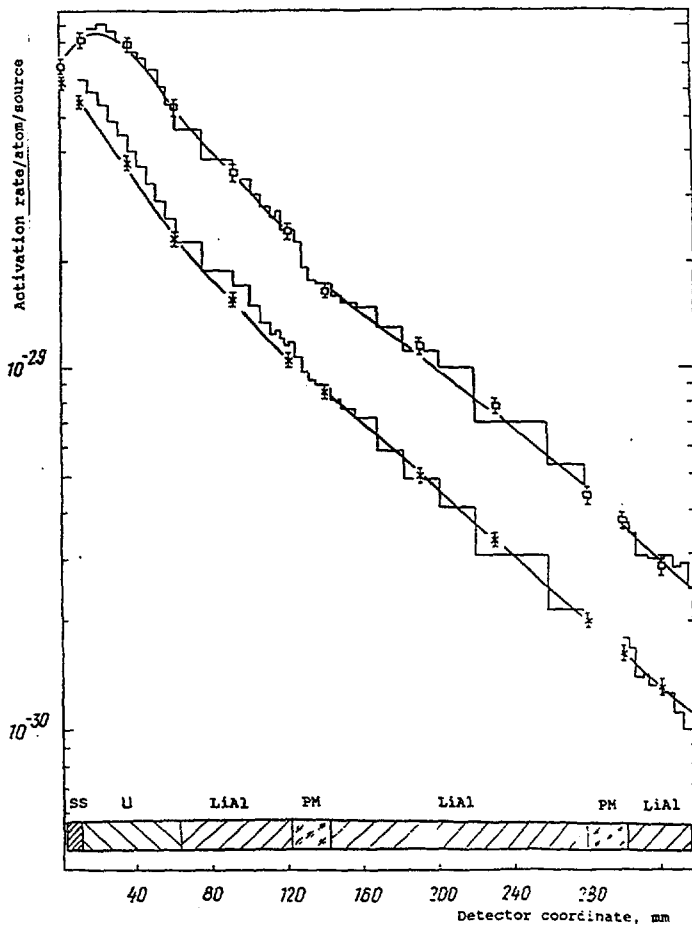


Fig. 17. Activation rates in axial channel of the hybrid mock-up. □ -  $^{115}\text{In}(n,n')$ , Δ -  $^{63}\text{Cu}(n,2n)$ , ○ -  $^{27}\text{Al}(n,p)$ , × -  $^{64}\text{Zn}(n,p)$

□ -  $^{115}\text{In}(n,n')$ , × -  $^{63}\text{Cu}(n,2n)$

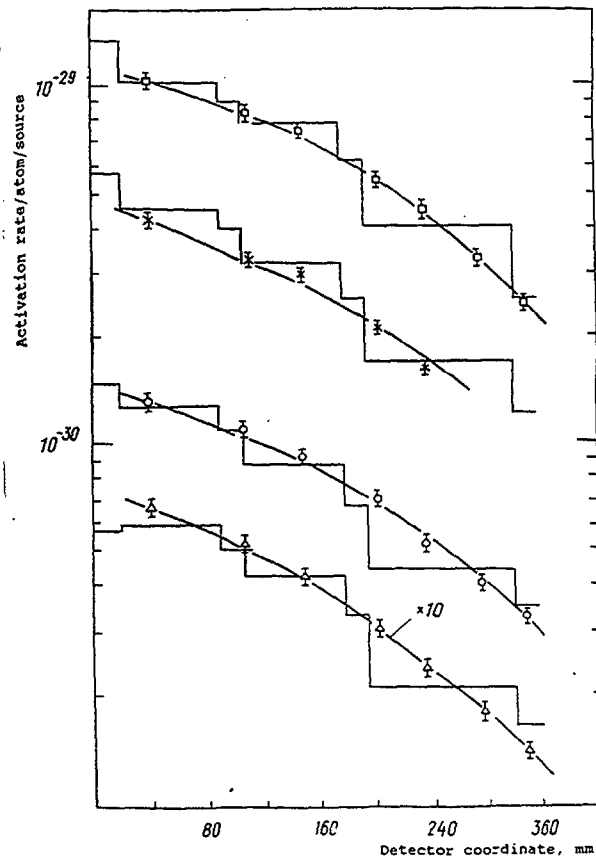


Fig. 18. Activation rates in radial channel of the hybrid mock-up.

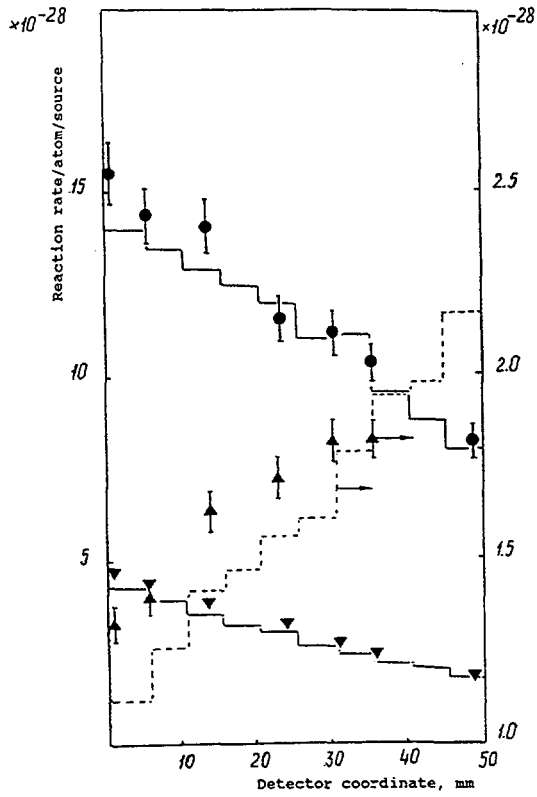


Fig. 19. Reaction rates in uranium in axial channel of the hybrid mock-up.

▼ -  $^{238}\text{U}(n,f)$ , ▲ -  $^{238}\text{U}(n,\gamma)$ , ● -  $^{237}\text{Np}(n,f)$

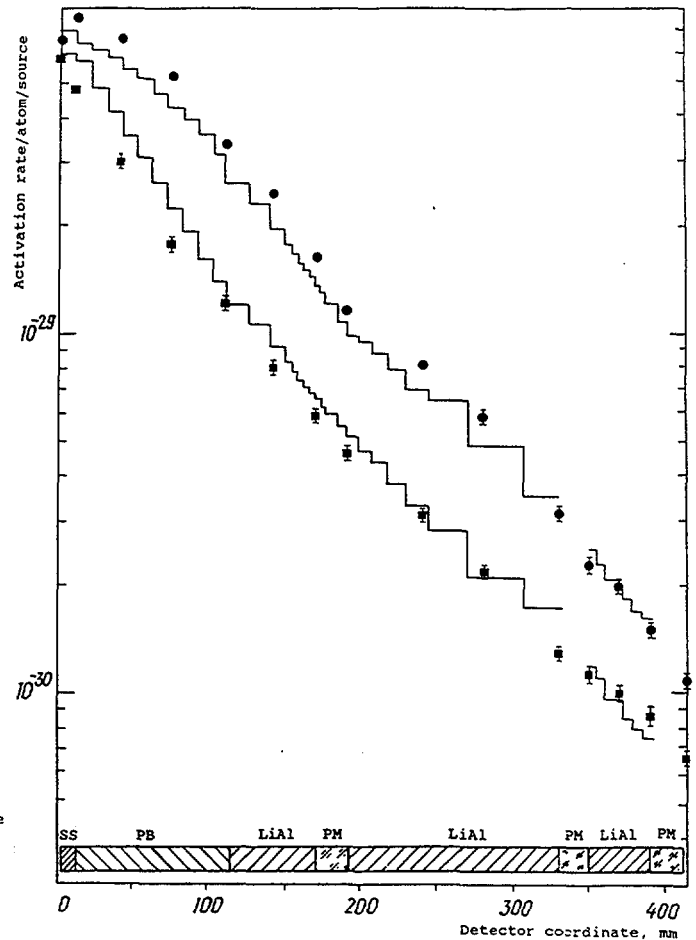


Fig. 20. Activation rates in axial channel of the lead mock-up.

● -  $^{115}\text{In}(n,n')$ ,  $^{115\text{m}}\text{In}$ , ■ -  $^{64}\text{Zn}(n,p)$ ,  $^{64}\text{Cu}$

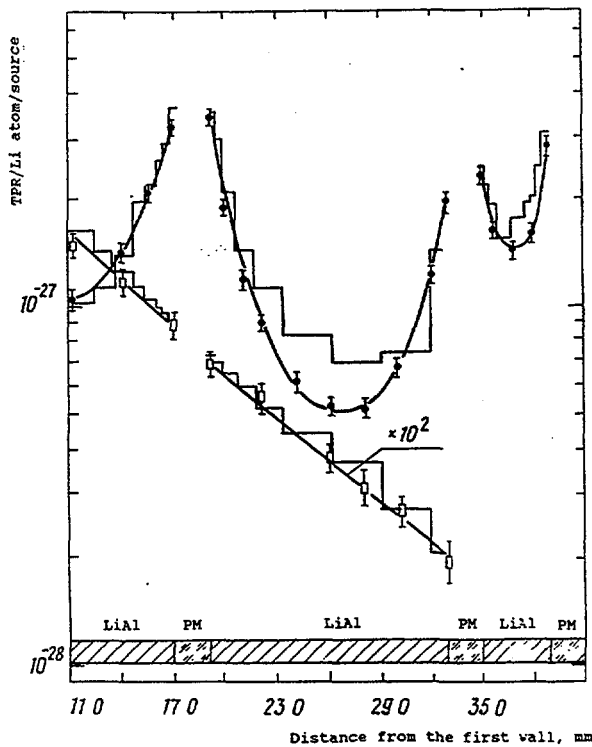


Fig. 21. Tritium production rates in axial channel of the lead mock-up.

● -  $\text{T}_6$ , □ -  $\text{T}_7$

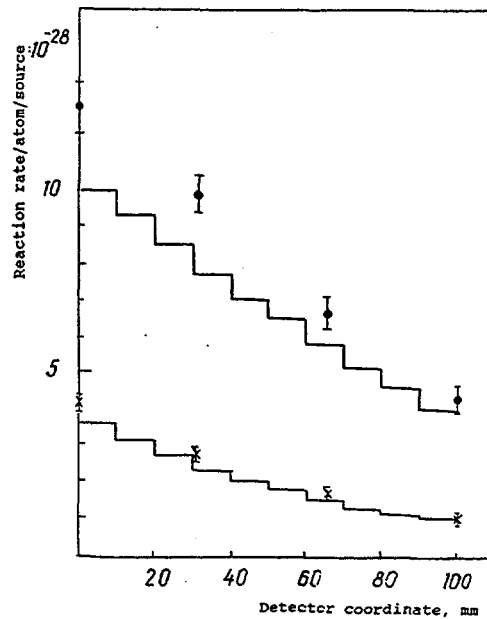


Fig. 22. Reaction rates in lead zone in axial channel of the lead mock-up.

● -  $^{238}\text{U}(n,f)$ , x -  $^{237}\text{Np}(n,f)$

**NEXT PAGE(S)  
left BLANK**

Numerical Data of Leakage Neutron Spectra from Various Sphere Piles with 14 MeV Neutrons



XA9642736

Chihiro ICHIHARA, Katsuhei KOBAYASHI  
Research Reactor Institute, Kyoto University  
Noda, Sennan-gun, Osaka 590-04, Japan

Shu A. HAYASHI  
Institute for Atomic Energy, Rikkyo University  
2-5-1 Nagasaka, Yokosuka, Kanagawa 240-01, Japan

Itsuro KIMURA  
Department of Nuclear engineering, Faculty of Engineering,  
Kyoto University,  
Yoshida-honmachi, Sakyo-ku, Kyoto 606, Japan

Junji YAMAMOTO, Akito TAKAHASHI  
Department of Nuclear Engineering, Faculty of Engineering,  
Osaka University  
2-1, Yamada-oka, Suita, Osaka 565, Japan

#### I Period for the Measurement

From 1984 to 1988

#### II Measured Quantities

The leakage current spectrum from the outer surface of the sphere pile with 14 MeV neutrons normalized per source neutron was measured for each sample. See Ref-1 and -2.

#### III Experimental method

The experiment was performed with the time-of-flight (TOF) technique using the intense 14 MeV neutron source facility OKTAVIAN<sup>3)</sup> at Osaka University. A tritium neutron producing target was placed at the center of the pile. A cylindrical liquid organic scintillator NE-218 (12.7 cm-diam × 5.1 cm-long) was used as a neutron detector, which was located about 11 m from the tritium target, and 55° with respect to the deuteron beam axis. A pre-collimator made of polyethylene-iron multi-layers was set between the pile and the detector in order to reduce the background neutrons. The aperture size of this collimator was determined so that the whole surface of the piles facing the detector could be viewed. The experimental arrangement is given in Fig.1.

#### IV Sample piles

Sample piles were made by filling spherical vessels with sample powder or flakes. Four different types of vessels were used, as the followings.

##### 1) 61 cm diameter shell (Type-I)

This type of vessels are used for the LiF, Mn, Cu, Zr and Mo piles. These are made of stainless steel (JIS SUS-304) for LiF and Zr pile, and Soft steel (JIS SS-41) for the Mn, Cu and Mo piles. Inner diameter, wall thickness of the vessels, are 60 cm and 0.5 cm, respectively. A reentrant hole for a beam duct is equipped, the diameter of which is 5.1 cm up to the center of the vessel as shown in Fig.2.

##### 2) 40 cm diameter vessel (Type-II)

This stainless steel (JIS SUS-304) vessels are used for the TEFLON, Al, Ti, Cr, Co, As, Se and W piles. This is equipped with a 20 cm diameter void at its center and a 11 cm diameter reentrant hole for the target beam duct. The thickness is 0.2 cm everywhere (Fig.3).

3) 60 cm diameter vessel (Type-III)

This is made of 0.5 cm thick stainless steel (JIS SUS-304) and is used only for silicon pile. This vessel has a void and a re-entrant hole of same size as the 40 cm vessel (Fig.4).

4) 28 cm diameter vessel (Type-IV)

This is made of 0.3 cm thick stainless steel (JIS SUS-304) and is used for Nb pile only. Similar reentrant hole is equipped as the type-I vessel (Fig.5).

## V File list

The following table (Table-1) shows the diameters, sample weight, apparent densities, sample thickness in units of centimeters and mean free paths for 14 MeV neutrons.

Table-1 Characteristic parameters of the sample piles

Pile	Diam.(cm)	Sample Weight (kg)	Apparent density ( $\text{g/cm}^3$ )	Thickness	
				cm	MFPs
LiF	61	198.0	1.79	27.5	3.5
TEFLON	40	34.7	1.30	9.8	0.7
Al	40	32.8	1.22	9.8	0.5
Si	60	138.05	1.29	20.0	1.1
Ti	40	41.20	1.54	9.8	0.5
Cr	40	99.7	3.72	9.8	0.7
Mn	61	480.0	4.37	27.5	3.4
Co	40	52.0	1.94	9.8	0.5
Cu	61	675.0	6.23	27.5	4.7
As	40	82.9	3.09	9.8	0.8
Se	40	61.4	2.29	9.8	0.6
Zr	61	311.9	2.84	27.5	2.0
Nb	28	47.7	4.39	11.2	1.1
Mo	61	236.0	2.15	27.5	1.5
W	40	118.6	4.43	9.8	0.8

## VI Neutron Source Characteristics

The pulsed beam line of OKTAVIAN was used. Neutrons were produced by bombarding a 370 GBq tritium target with 250 keV deuteron beam. The energy spectrum of the neutron source is measured by using the same detection system as the each leakage spectrum measurement. The spatial distribution of the emitted neutrons were measured for each target assembly. The theoretical calculations were performed assuming the isotropical neutron source distribution.

The neutron source spectra are given in Table-2 to -6.

## VII Data Processing

The detector efficiency was determined by combining, 1) the Monte Carlo calculation, 2) the measured efficiency derived from the TOF measurement of  $^{252}\text{Cf}$  spontaneous fission spectrum and the Watt's spectrum, and 3) the measured efficiency from the leakage spectrum from a graphite sphere, 30 cm in diameter with the similar detection system.

To monitor the absolute number of the spectrum per source neutron, a cylindrical niobium foil was set in front of the tritium target and irradiated during the TOF experiment. From the  $\gamma$ -ray intensity of the induced activity,  $^{92\text{m}}\text{Nb}$  and the integrated counts of the source neutron spectrum, the absolute neutron leakage spectrum can be obtained. The formulation of this procedure is stated elsewhere<sup>4)</sup>.

## VIII Experimental errors

The experimental errors include only statistical deviation ( $1\sigma$ ) in the measurement of neutrons. The relative error to measure the niobium activation foils is less than 1 % (0.4 to 1 %), which is not included here.

## IX Calculations

The theoretical calculations were performed using MCNP<sup>5)</sup>, which is a three-dimensional continuous energy Monte Carlo transport code. The continuous libraries for MCNP were FSXLIB-J3<sup>6)</sup> derived from 2JENDL-3<sup>7)</sup>. In addition to this JENDL-3 based library, BMCCS, and ENDL-85 attached with MCNP code were also used for the reference.

In all these calculations, neutron room returns, scattered neutrons from the collimator, *etc.* are not taken into account.

An example of the input data for the MCNP calculation are given in the following (Table-7).

**X Numerical data****1. Lithium Fluoride Pile****1-1 Pile**

Sample: Lithium Fluoride powder, 198 kg

## Chemical Composition

LiF	98.07 %	F	1.83 %
Fe	0.005 %	HF	0.02 %
H <sub>2</sub> O	0.008 %	Li <sub>2</sub> SiF <sub>6</sub>	0.04 %
( <sup>6</sup> Li: 7.463 ± 0.038 %)			

Container: 61 cm stainless steel vessel (Type-I)

Apparent density: 1.79 g/cm<sup>3</sup>

Sample thickness: 3.5 mean free paths for 14 MeV neutrons

**1-2 Date of experiment**

Jul.9, 1987

**1-3 Neutron Source spectrum**

Neutron energy spectrum is given in the Table-2.

**1-4 Experimental data**

Numerical data are given in Table-8. Measured spectrum and the calculated ones with MCNP code are shown in the Fig.6. The MCNP calculations were performed with FSXLIB-J3 and BMCCS. BMCCS library adopted LASL-subset for lithium and ENDF/B-IV for fluorine.

**2. TEFLON (Polytetrafluoroethylene)****2-1 Pile**

Sample: TEFLON ( Polytetrafluoroethylene; (CF<sub>2</sub>)<sub>n</sub> ) pellets 2 mm in diameter and 2 mm long  
34.7 kg

## Chemical composition

CF <sub>2</sub>	> 99.9%
Cl	0.087 %

Container: 40 cm diameter stainless steel vessel (Type -II)

Apparent density: 1.30 g/cm<sup>3</sup>

Sample thickness: 0.7 mean free paths for 14 MeV neutrons

**2-2 Date of the expedient**

Mar. 12, 1987

**2-3 Neutron source spectrum**

Neutron source spectrum is given in the Table-3.

**2-4 Experimental data**

Numerical data are given in Table-9. Measured spectrum and the calculated ones with MCNP code are shown in the Fig.7. The MCNP calculations were performed with FSXLIB-J3 and BMCCS. BMCCS library adopted LASL-subset for carbon and ENDF/B-IV for fluorine.

### 3. Aluminum

#### 3-1 Pile

Sample: Aluminum metal powder (grain size: 80 % between 0.2 and 1.0 mm), 32.8 kg

#### Chemical composition

Al	> 99.7 %	Si	< 0.15 %
Fe	< 0.20 %	Cu	< 0.01 %

Container: 40 cm stainless steel vessel (Type-II)

Apparent density: 1.22 g/cm<sup>3</sup>

Sample thickness: 0.5 mean free paths for 14 MeV neutrons

#### 3-2 Date of experiment

Dec. 22, 1988

#### 3-3 Neutron Source spectrum

Neutron source spectrum is given in the Table-4.

#### 3-4 Experimental data

Numerical data are given in Table-10. Measured spectrum and the calculated ones with MCNP code are shown in the Fig.8. The MCNP calculations were performed with FSXLIB-J3 and BMCCS. BMCCS library adopted ENDF/B-IV for aluminum.

### 4. Silicon

#### 4-1 Pile

Sample: Silicon granular (purity 99.9 %), 138.05 kg

Container: 60 cm stainless steel vessel (Type-III)

Apparent density: 1.29 g/cm<sup>3</sup>

Sample thickness: 1.1 mean free paths for 14 MeV neutrons

#### 4-2 Date of experiment

Mar. 13, 1987

#### 4-3 Neutron source spectrum

Neutron source spectrum is given in the Table-3.

#### 4-4 Experimental data

Numerical data are given in Table-11. Measured spectrum and the calculated ones with MCNP code are shown in the Fig.9. The MCNP calculations were performed with FSXLIB-J3 and BMCCS. BMCCS library adopted ENDF/B-III for silicon.

### 5. Titanium

#### 5-1 Pile

Sample: Titanium metal powder (10-20 mesh), 41.2 kg

#### Chemical composition

Ti	> 99.4 %	Mg	0.029 %
Fe	0.084 %	N	0.002 %
Si	< 0.01 %	C	0.006 %
Cl	0.084 %	H	< 0.003 %
Mn	0.002 %	O	0.061 %

Container: 40 cm stainless steel vessel (Type-II)  
 Apparent density: 1.54 g/cm<sup>3</sup>  
 Sample thickness: 0.5 mean free paths for 14 MeV neutrons

#### 5-2 Date of experiment

Aug. 31, 1988

#### 5-3 Neutron source spectrum

Neutron source spectrum id given in the Table-5.

#### 5-4 Experimental data

Numerical data are given in Table-12. Measured spectrum and the calculated ones with MCNP code are shown in the Fig.10. The MCNP calculations were performed with FSXLIB-J3 and BMCCS. BMCCS library adopted ENDF/B-IV for titanium.

### 6. Chromium

#### 6-1 Pile

Sample: Chromium metal powder, 99.7 kg

##### Chemical composition

Cr	> 99.78 %	Fe	0.16 %
C	0.021 %	Si	0.007 %

Container: 40 cm stainless steel vessel (Type-II)  
 Apparent density: 3.72 g/cm<sup>3</sup>  
 Sample thickness: 0.7 mean free paths for 14 MeV neutrons

#### 6-2 Date of experiment

Aug. 21, 1986

#### 6-3 Neutron source spectrum

Neutron source spectrum is given in the Table-6.

#### 6-4 Experimental data

Numerical data are given in Table-13. Measured spectrum and the calculated ones with MCNP code are shown in the Fig.11. The MCNP calculations were performed with FSXLIB-J3 and BMCCS. BMCCS library adopted ENDF/B-IV for chromium.

### 7. Manganese

#### 7-1 Pile

Sample: Manganese metal powder, 490.5 kg

##### Chemical composition

Mn	99.95 %	C	0.005 %
Si	0.002 %	P	0.0001 %
S	0.022 %	Fe	0.020 %

Container: 61 cm steel vessel  
 Apparent density: 4.37 g/cm<sup>3</sup>  
 Sample thickness: 3.4 mean free paths for 14 MeV neutrons

#### 7-2 Date of experiment

Jul. 8, 1987

### 7-3 Neutron source spectrum

Neutron source spectrum is given in the Table-2.

### 7-4 Experimental data

Numerical data are given in Table-14. Measured spectrum and the calculated ones with MCNP code are shown in the Fig.12. The MCNP calculations were performed with FSXLIB-J3 and BMCCS. BMCCS library adopted ENDF/B-IV for manganese.

## 8. Cobalt

### 8-1 Pile

Sample: Cobalt metal powder (300 mesh), 52.0 kg

#### Chemical composition

Co	> 99.50 %	Zn	0.003 %
Ni	0.15 %	Si	0.04 %
Fe	0.12 %	Ca	0.03 %
Mn	0.02 %	S	0.008%
Cu	0.01 %	C	0.03 %
Pb	0.002%		

Container: 40 cm stainless steel vessel

Apparent density: 1.94 g/cm<sup>3</sup>

Sample thickness: 0.5 mean free paths for 14 MeV neutrons

### 8-2 Date of experiment

Mar. 12, 1987

### 8-3 Neutron source spectrum

Neutron source spectrum is given in the Table-3.

### 8-4 Experimental data

Numerical data are given in Table-15. Measured spectrum and the calculated ones with MCNP code are shown in the Fig.13. The MCNP calculations were performed with FSXLIB-J3 and ENDL-85, the 85 version of the ENDL<sub>85</sub>.

## 9 Copper

### 9-1 Pile

Sample: Copper metal powder (100 mesh), 675.0 kg

#### Chemical composition

Cu	99.993 %	S	10 ppm
As	0.6 ppm	Pb	0.3 ppm
Sb	0.2 ppm	Fe	2 ppm
Bi	< 0.1 ppm		

Container: 61 cm normal steel vessel (Type-I)

Apparent density: 6.23 g/cm<sup>3</sup>

Sample thickness: 4.7 mean free paths for 14 MeV neutrons

### 9-2 Date of experiment

Jul. 8, 1987

**9-3 Neutron source spectrum**

Neutron source spectrum is given in the Table-2.

**9-4 Experimental data**

Numerical data are given in Table-16. Measured spectrum and the calculated ones with MCNP code are shown in the Fig.14. The MCNP calculations were performed with FSXLIB-J3 and BMCCS. BMCCS library adopted ENDF/B-IV for copper.

**10 Arsenic****10-1 Pile**

Sample: Arsenic metal powder, 82.9 kg

## Chemical composition

As	> 99.999 %	Fe	0.3 %
Mg	< 0.01 %	Cu	< 0.01 %
Si	< 0.05 %		

Container: 40 cm stainless steel vessel (Type-II)

Apparent density: 3.09 g/cm<sup>3</sup>

Sample thickness: 0.8 mean free paths for 14 MeV neutrons

**10-2 Date of experiment**

Sep. 1, 1988

**10-3 Neutron source spectrum**

Neutron source spectrum is given in the Table-5.

**10-4 Experimental data**

Numerical data are given in Table-17. Measured spectrum and the calculated ones with MCNP code are shown in the Fig.15. The MCNP calculations were performed with ENDL-85 library for arsenic.

**11 Selenium****11-1 Pile**

Sample: Selenium powder, 61.4 kg

## Chemical composition

Se	> 99.9 %		
Te	45 ppm	Na	15 ppm
SiO <sub>2</sub>	16 ppm	S	6 ppm
Hg	4 ppm	Fe	3 ppm

Container: 40 cm stainless steel vessel (Type-II)

Apparent density: 2.29 g/cm<sup>3</sup>

Sample thickness: 0.6 mean free paths for 14 MeV neutrons

**11-2 Date of experiment**

Sep. 2, 1988

**11-3 Neutron source spectrum**

Neutron source spectrum is given in the Table-5.

**11-4 Experimental data**

Numerical data are given in Table-18. Measured spectrum and the calculated ones with MCNP code are shown in the Fig.16. The calculation was not conducted because no nuclear data have been available for the MCNP calculation.

**12 Zirconium****12-1 Pile**

Sample: Zirconium metal flakes, 311.9 kg  
 Container: 61 cm stainless steel vessel (Type-I)  
 Apparent density: 2.84 g/cm<sup>3</sup>  
 Sample thickness: 2.0 mean free paths for 14 MeV neutrons

**12-2 Date of experiment**

Sep. 2, 1988

**12-3 Neutron source spectrum**

Neutron source spectrum is given in the Table-5.

**12-4 Experimental data**

Numerical data are given in Table-19. Measured spectrum and the calculated ones with MCNP code are shown in the Fig.17. The MCNP calculations were performed with FSXLIB-J3 and ENDL-85 for zirconium.

**13 Niobium****13-1 Pile**

Sample: Niobium metal powder (60-200 mesh), 47.7 kg

**Chemical composition**

Nb	> 99.8 %	Ta	0.1 %
O	0.07 %	W	< 0.01 %
H	0.002 %	Zr	< 0.01 %

Container: 28 cm stainless steel vessel (Type-IV)

Apparent density: 4.39 g/cm<sup>3</sup>

Sample thickness: 1.1 mean free paths for 14 MeV neutrons

**13-2 Date of experiment**

Aug. 21, 1986

**13-3 Neutron source spectrum**

Neutron source spectrum is given in the Table-6.

**13-4 Experimental data**

Numerical data are given in Table-20. Measured spectrum and the calculated ones with MCNP code are shown in the Fig.18. The MCNP calculations were performed with FSXLIB-J3 and BMCCS. BMCCS adopted ENDL-76 evaluation, 1976 version of ENDL for niobium.

**14 Molybdenum****14-1 Pile**

Sample: Molybdenum metal powder (4.2 $\mu$ m), 236.0 kg

Chemical composition

Mo	> 99.9 %
Fe	0.003 %
H <sup>2</sup> O	< 0.03 %

Container: 61 cm stainless steel vessel (Type-I)

Apparent density: 2.15 g/cm<sup>3</sup>

Sample thickness: 1.5 mean free paths for 14 MeV neutrons

**14-2 Date of experiment**

Jul. 9, 1987

**14-3 Neutron source spectrum**

Neutron source spectrum is given in the Table-2.

**14-4 Experimental data**

Numerical data are given in Table-21. Measured spectrum and the calculated ones with MCNP code are shown in the Fig.19. The MCNP calculations were performed with FSXLIB-J3 and ENDL-85 for cobalt.

**15 Tungsten**

**15-1 Pile**

Sample: Tungsten metal powder, 118.6 kg

Chemical composition

C	12 ppm	N	< 3 ppm
Fe	45 ppm	O	230 ppm
S	12 ppm	Si	< 10 ppm

Container: 40 cm stainless steel vessel (Type-II)

Apparent density: 4.43 g/cm<sup>3</sup>

Sample thickness: 0.8 mean free paths for 14 MeV neutrons

**15-2 Date of experiment**

Jul. 9, 1987

**15-3 Neutron source spectrum**

Neutron source spectrum is given in the Table-2.

**15-4 Experimental data**

Numerical data are given in Table-22. Measured spectrum and the calculated ones with MCNP code are shown in the Fig.20. The MCNP calculations were performed with FSXLIB-J3 and ENDL-85 for tungsten.

## References

- 1) C. Ichihara et al.: *Proc. International Conference on Nuclear Data for Science and Technology (Mito, Japan)*, 1988
- 2) C. Ichihara et al.: *Proc. Second Specialists' Meeting on Nucl. Data for Fusion Reactors (1991)*, JAERI-M 91-062(1991)
- 3) K. Sumita, et al.: *Proc. 12th SOFT*, Vol.1, (1982)
- 4) A. Takahashi, et al.: *OKTAVIAN Report*, C-83-02(1983)
- 5) J. F. Briesmeister ed.: *MCNP-A General Monte Carlo Code for Neutron and Photon Transport*, LA-73966-M, Rev.2, (1986)
- 6) K. Kosako, et al.: *FSXLIB-J3: MCNP Continuous Energy Cross Section Library Based on JENDL-3*, JAERI-M 91-187(1991)
- 7) K. Shibata, et al.: *Japanese Evaluated Nuclear Data Library, Version-3 - JENDL-3 -*, JAERI 1319(1990)
- 8) R. Howerton, et al.: *Evaluated Nuclear Cross Section Library*, UCRL-50400 Vol.4

Fig. 1 Experimental arrangement in the OKTAVIAN Facility

Fig. 2 61 cm diameter vessel (Type-I)

Fig. 3 40 cm diameter vessel (Type-II)

Fig. 4 60 cm diameter vessel (Type-III)

Fig. 5 28 cm diameter vessel (Type-IV)

Fig. 6 Experimental and calculated spectra from LiF 61 cm pile

Fig. 7 Experimental and calculated spectra from TEFLON 40 cm pile

Fig. 8 Experimental and calculated spectra from Al 40 cm pile

Fig. 9 Experimental and calculated spectra from Si 60 cm pile

Fig. 10 Experimental and calculated spectra from Ti 40 cm pile

Fig. 11 Experimental and calculated spectra from Cr 40 cm pile

Fig. 12 Experimental and calculated spectra from Mn 61 cm pile

Fig. 13 Experimental and calculated spectra from Co 40 cm pile

Fig. 14 Experimental and calculated spectra from Cu 61 cm pile

Fig. 15 Experimental and calculated spectra from As 40 cm pile

Fig. 16 Experimental and calculated spectra from Se 40 cm pile

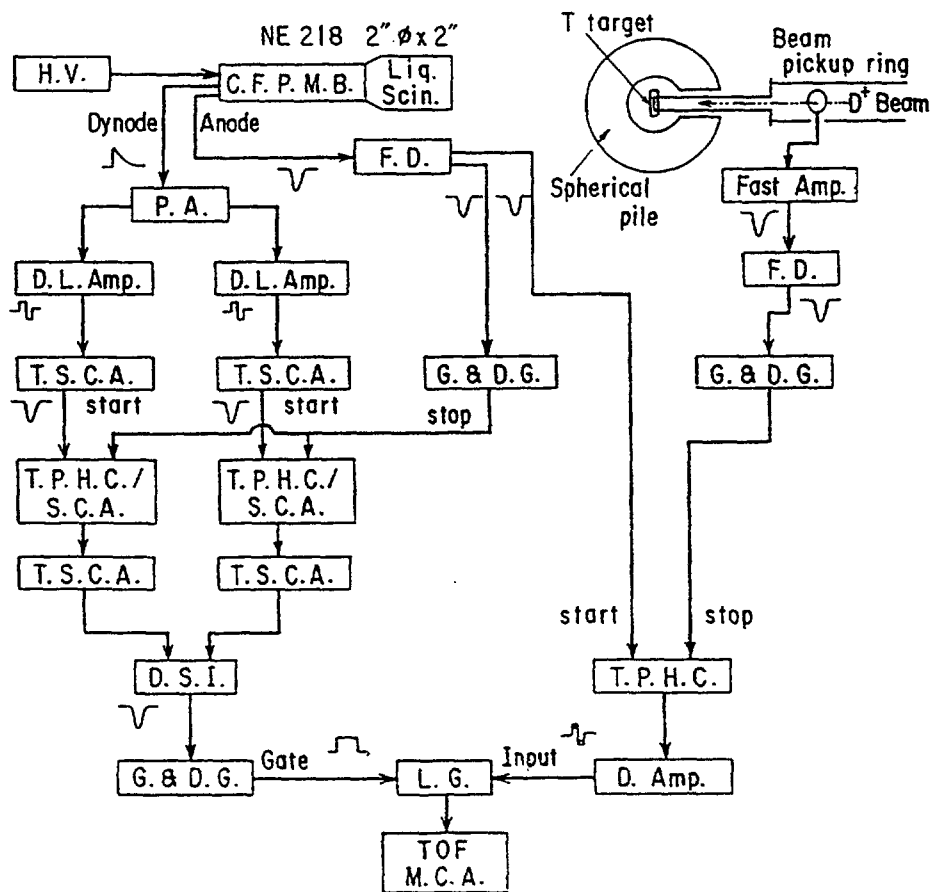
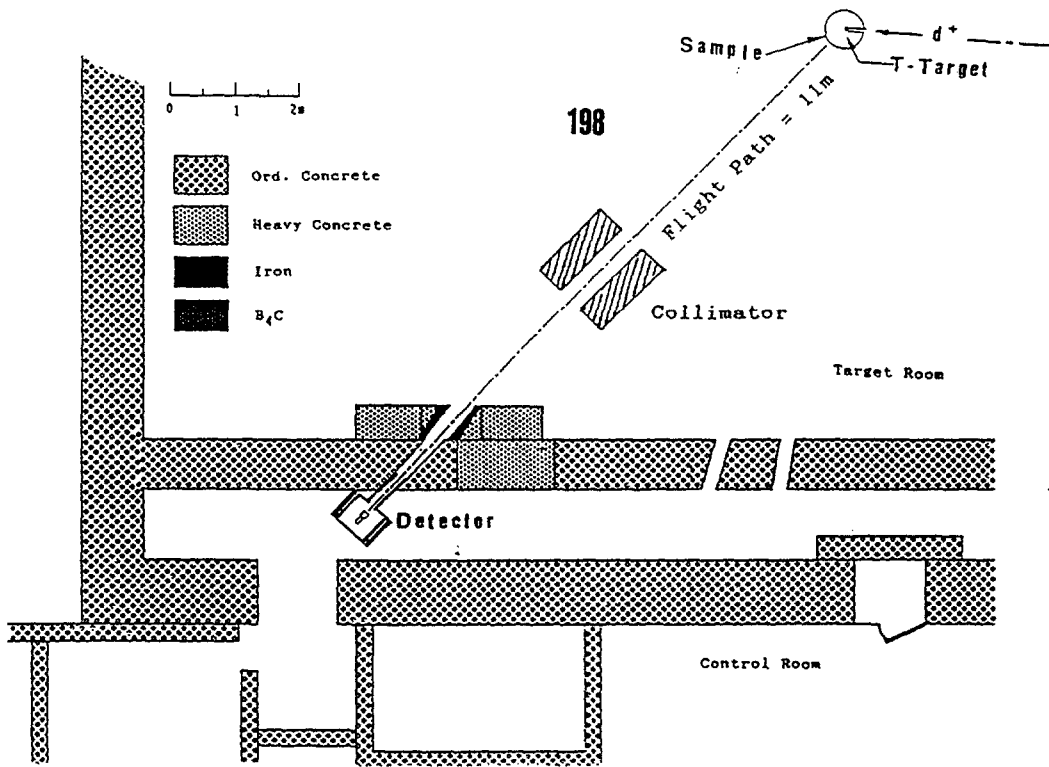
Fig. 17 Experimental and calculated spectra from Zr 61 cm pile

Fig. 18 Experimental and calculated spectra from Nb 28 cm pile

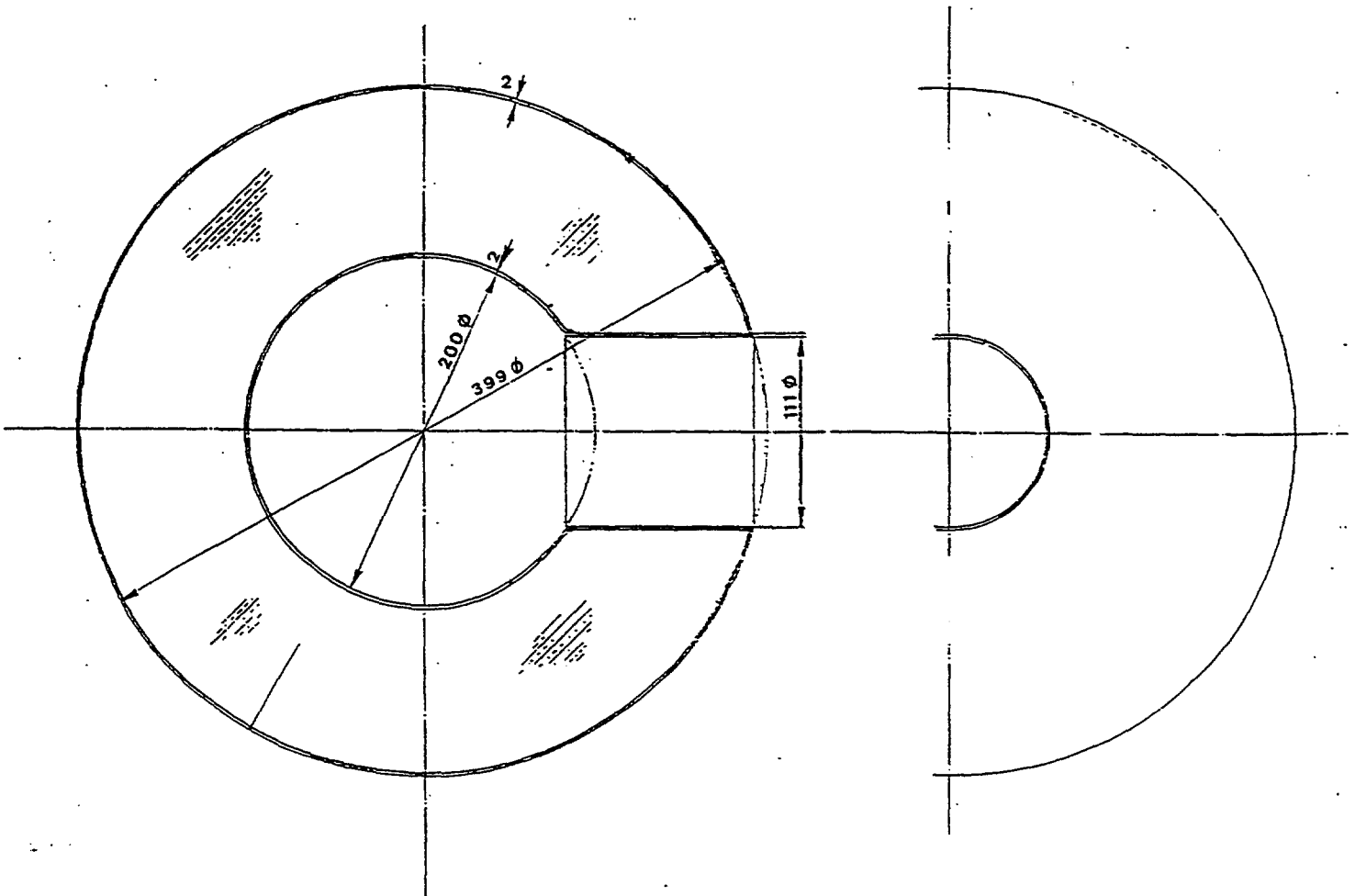
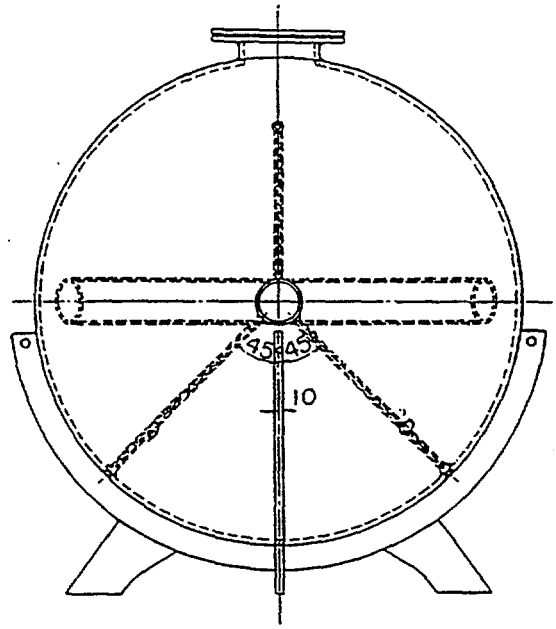
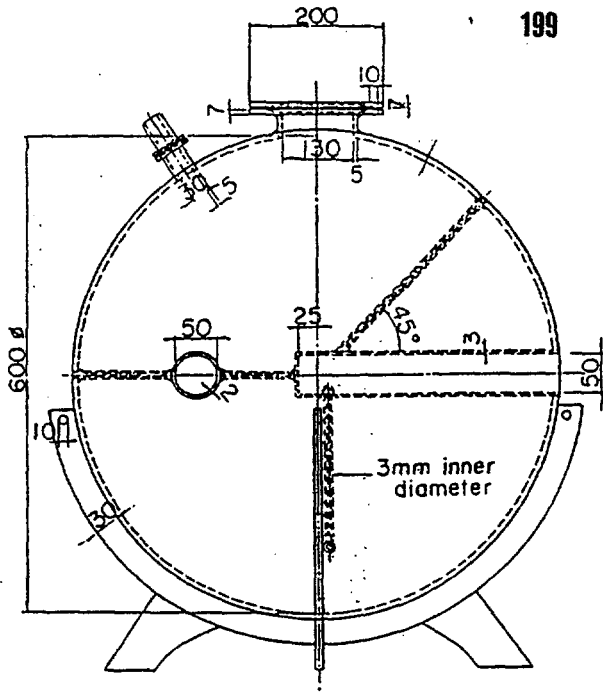
Fig. 19 Experimental and calculated spectra from Mo 61 cm pile

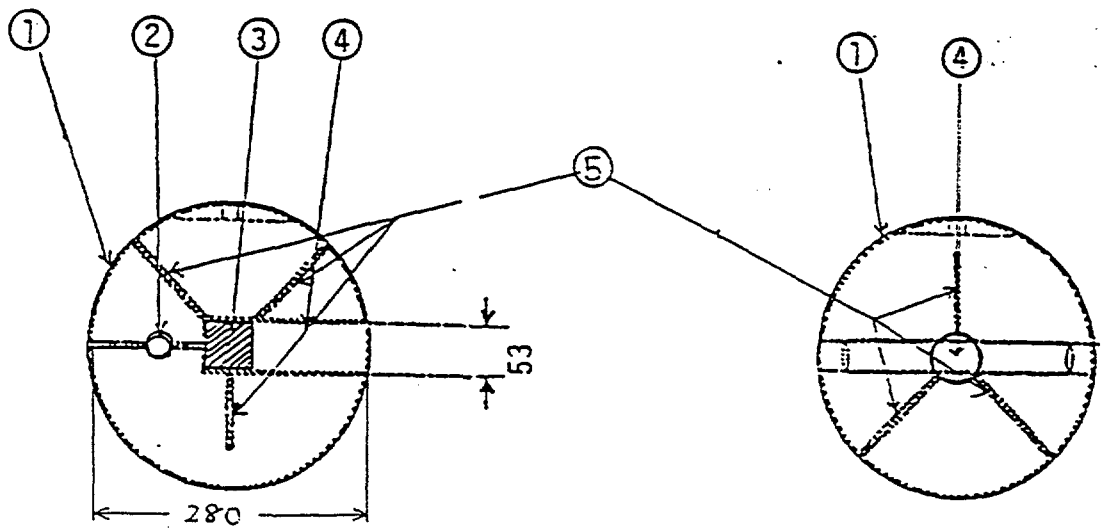
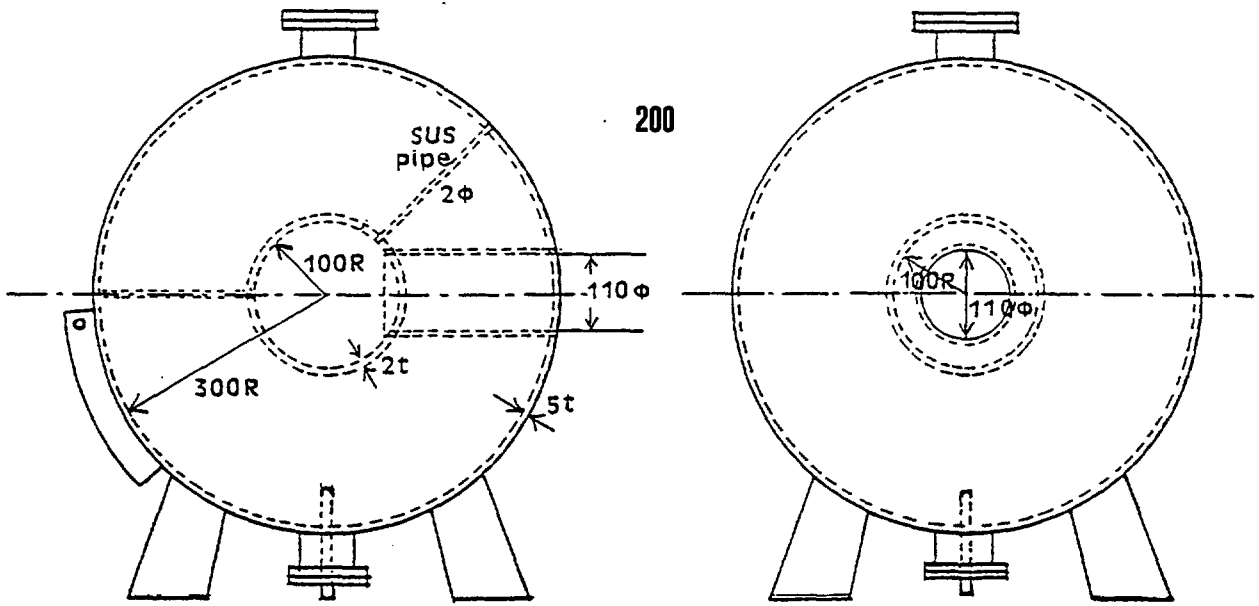
Fig. 20 Experimental and calculated spectra from W 40 cm pile

Table-2 Neutron source spectrum for LiF, Mn, Cu, Mo and W

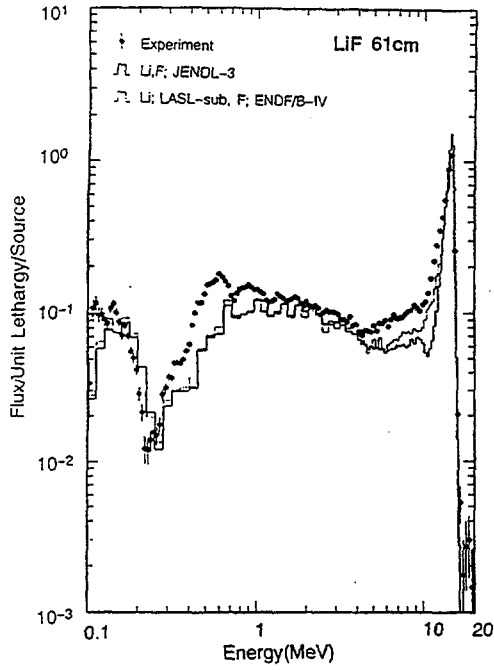


Measuring system for organic liquid scintillation detector

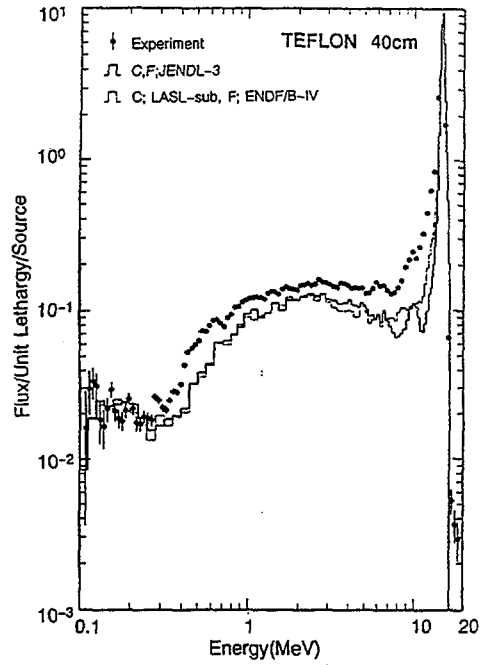




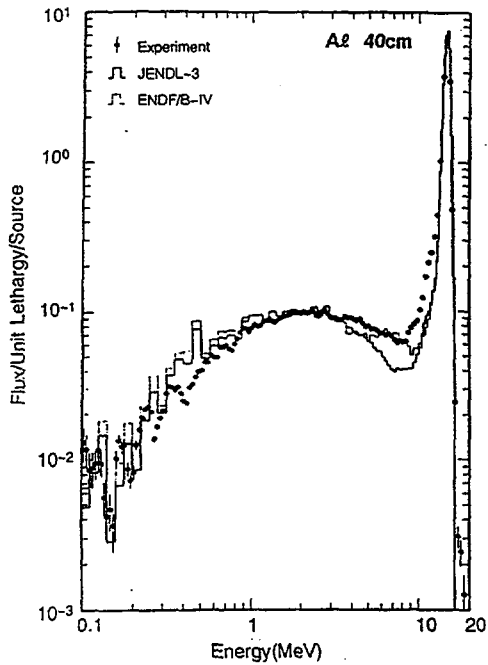
0:8737e140.873.c:129e140j3.mca.c:144e140.mca.  
 EMAX,EMIN= 20 to .1 MeV: FMAX,FMIN= 10 . .001



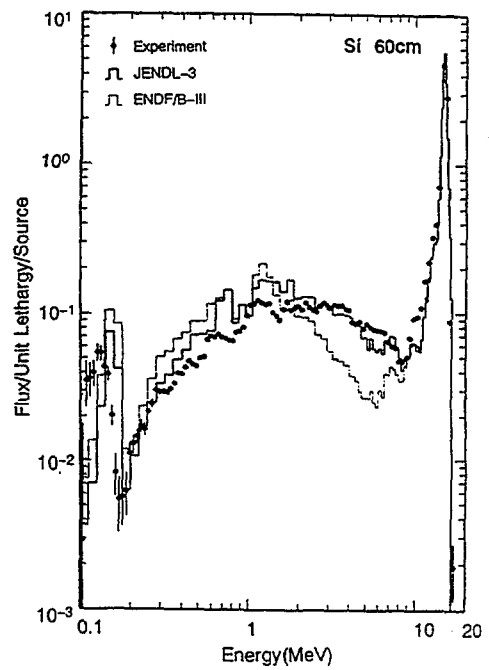
0:8737e140.873.c:129e140j3.mca.c:144e140.mca.  
 EMAX,EMIN= 20 to .1 MeV: FMAX,FMIN= 10 . .001



0:887e140.887.c:129e140j3.mca.c:144e140.mca.  
 EMAX,EMIN= 20 to .1 MeV: FMAX,FMIN= 10 . .001

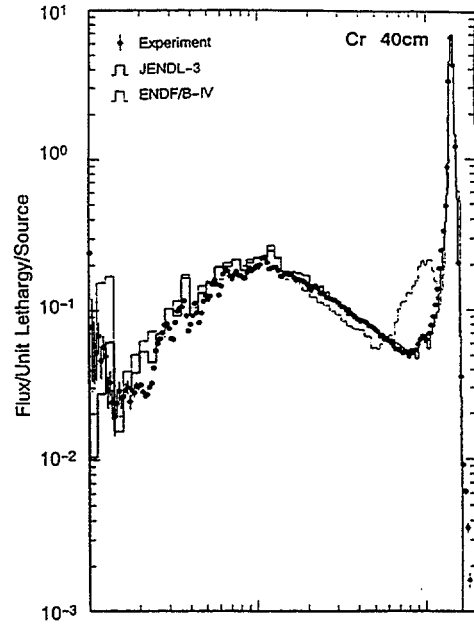
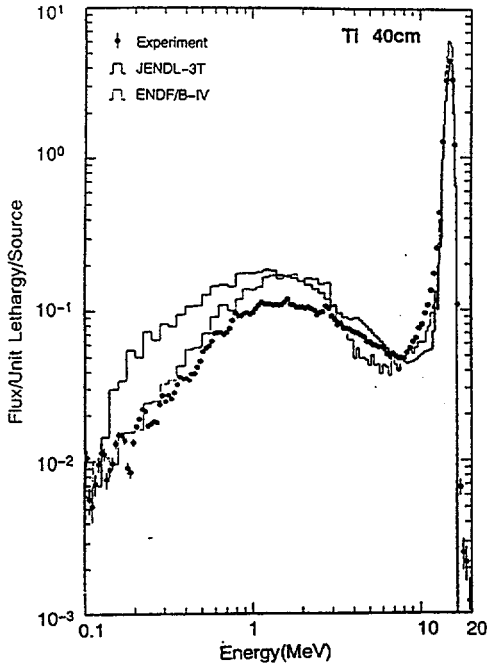


0:887e140.887.c:129e140j3.mca.c:144e140.mca.  
 EMAX,EMIN= 20 to .1 MeV: FMAX,FMIN= 10 . .001



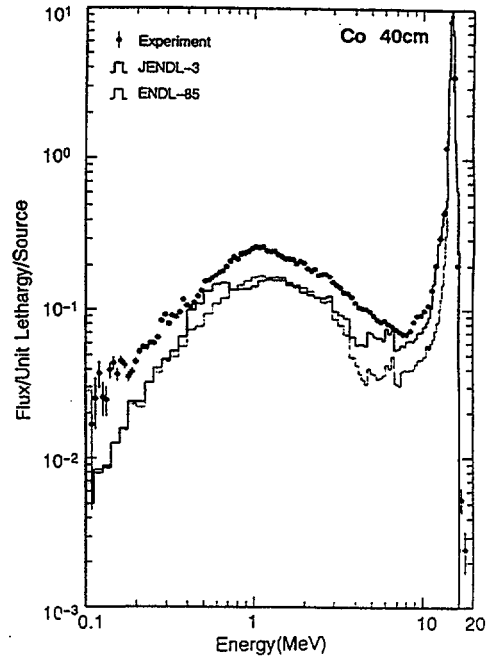
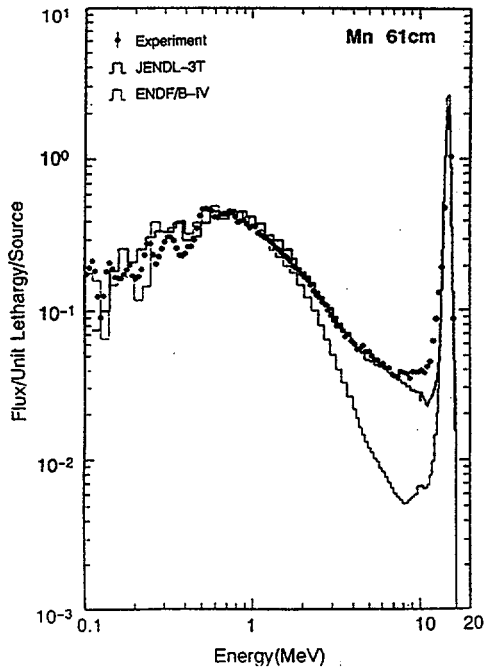
h:388Vcr40.868.c:j3Vcr40j3.mca.c:ead185Vcr40a.mca.  
 EMAX,EMIN= 20 to .1 MeV: PMAX,PMIN= 10 . .001

h:388Vcr40.868.c:j3Vcr40j3.mca.c:ead185Vcr40a.mca.  
 EMAX,EMIN= 20 to .1 MeV: PMAX,PMIN= 10 . .001

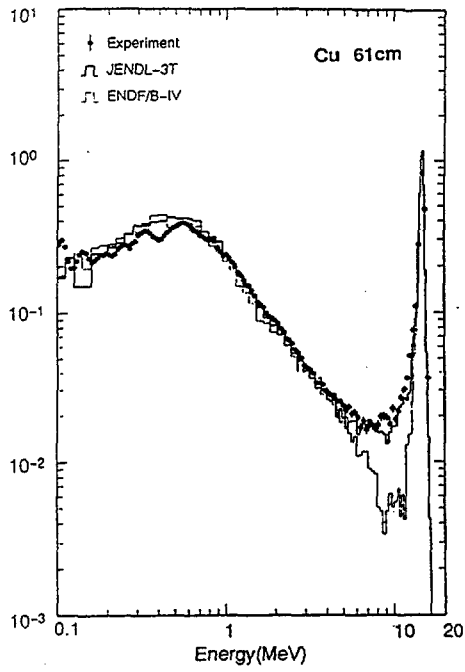


h:377Vmn60.872.c:j3Vmn60j3.mca.c:ead185Vmn60a.mca.  
 EMAX,EMIN= 20 to .1 MeV: PMAX,PMIN= 10 . .001

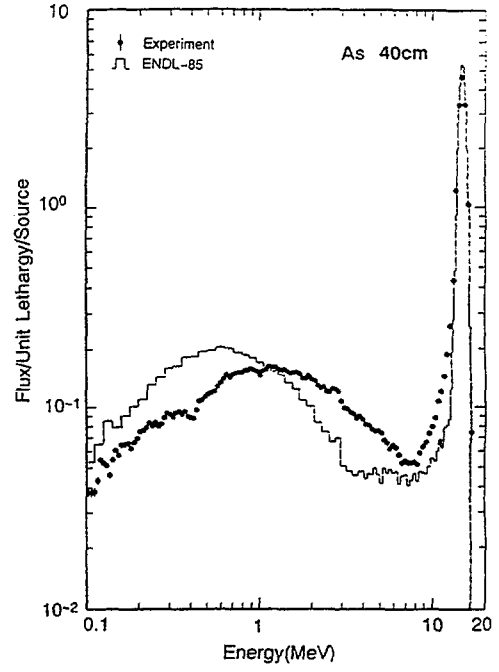
h:377Vmn60.872.c:j3Vmn60j3.mca.c:ead185Vmn60a.mca.  
 EMAX,EMIN= 20 to .1 MeV: PMAX,PMIN= 10 . .001



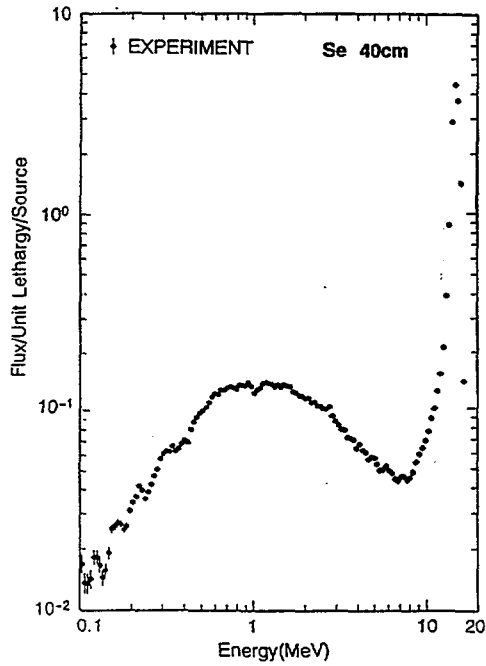
h:177Yr60.877.c1rM13.mca.c1rP4b4.mca.  
 EMAX,EMIN= 20 to .1 MeV: PMAX,PMIN= 10 . .001



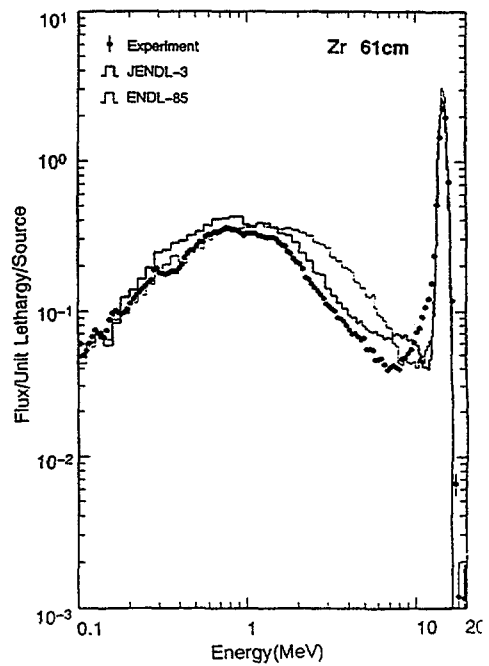
h:177Yr60.888.c1rP85.mca.  
 EMAX,EMIN= 20 to .1 MeV: PMAX,PMIN= 10 . .01



h:177Yr60.888.c1rP85.mca.  
 EMAX,EMIN= 20 to .1 MeV: PMAX,PMIN= 10 . .01

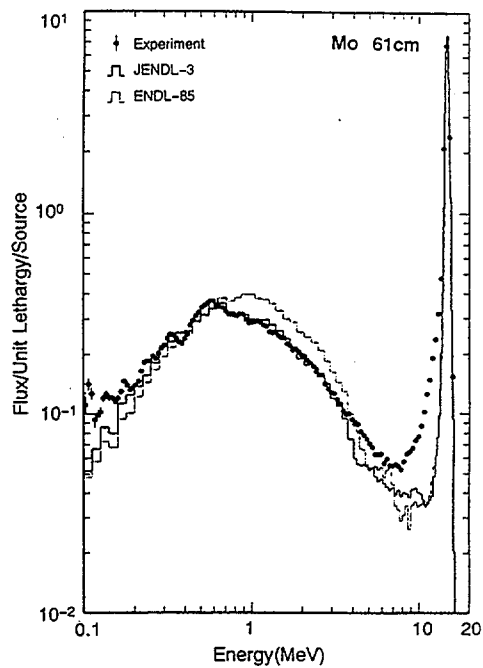
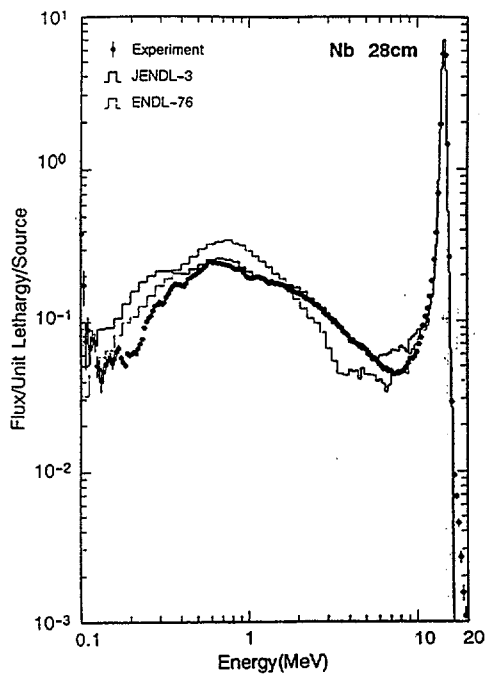


h:177Yr60.888.c1rP85.mca.c1rP85.mca.  
 EMAX,EMIN= 20 to .1 MeV: PMAX,PMIN= 10 . .001

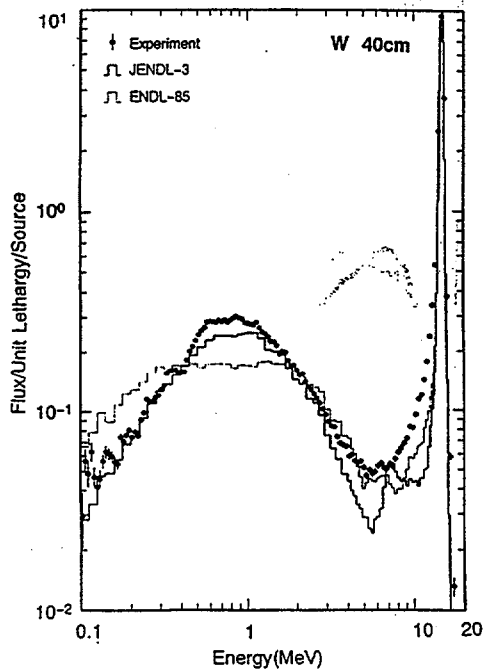


h:\877W40.877.c:\j3W40j3.mca.c:\end185W405.mca.b:\877W405.877.  
 EMAX,EMIN= 20 to .1 MeV; PMAX,PMIN= 10 . .01

b:\877W40.877.c:\j3W40j3.mca.c:\end185W405.mca.b:\877W405.877.  
 EMAX,EMIN= 20 to .1 MeV; PMAX,PMIN= 10 . .01



b:\877W40.877.c:\j3W40j3.mca.c:\end185W405.mca.  
 EMAX,EMIN= 20 to .1 MeV; PMAX,PMIN= 10 . .01



**Title**

Gamma-ray energy spectra emitted from spheres with 14 MeV neutron source.

**Authors**

J.Yamamoto, T.Kanaoka, I.Murata, A.Takahashi and K.Sumita

**Organization, Facility**

Department of Nuclear Engineering, Faculty of Engineering, Osaka University  
2-1 Yamada-oka, Suita, Osaka 565, Japan

**Date and time**

From June, 1987 to September, 1989

**Measured quantities**

Energy spectra of  $\gamma$  rays were measured using a 14 MeV neutron source. The  $\gamma$  rays were produced from  $(n,x\gamma)$  reactions in spheres and emitted from the spherical samples. The measured quantity was a "leakage current spectrum".

**Experimental method**

Gamma-rays were detected with a cylindrical NaI crystal and the energy spectra were obtained from the unfolding process of the  $\gamma$  ray pulse-height spectra, using a response matrix of the NaI detector.

The detector was located at 5.8m distance from the neutron source and counted the  $\gamma$  rays emitted from the sphere. Time spectra of neutrons and  $\gamma$  rays from the sphere were measured simultaneously with the pulse-height spectra by means of a TOF technique. OKTAVIAN was run in the pulsed mode with the repetition frequency of 500 kHz. The pulse width was 3 ns in FWHM and the difference in flight times between the 14 MeV neutrons and the prompt  $\gamma$  rays was about 90 ns from the sphere to the detector. Since those were enough to separate the  $\gamma$  rays from the neutron background in the TOF spectra, the desired

$\gamma$  rays could be discriminated from a neutron background.

#### Neutron source characteristics

Pulses of 14 MeV neutrons were generated by D-T reaction. A 370 GBq TiT target was bombarded with pulsed D+ beam at 243 keV. The following information is available: Energy spectrum of emission neutrons, the neutron yield as a function of emission angle and the production of  $\gamma$  rays at the source.

The neutron energy spectrum was same as that given in Ref.(1). The other information about the emission neutrons is given elsewhere (2). The energy spectrum of  $\gamma$  rays at the source is shown in Fig.1 and the values are as follows.

$\gamma$ ray energy [MeV]	Data [photons/sr./MeV/source neutron]
14.0 - 12.0	0.0
12.0 - 10.0	0.0
10.0 - 9.0	3.8E-5
9.0 - 8.0	7.0E-5
8.0 - 7.5	1.2E-4
7.5 - 7.0	1.5E-4
7.0 - 6.5	2.0E-4
6.5 - 6.0	2.3E-4
6.0 - 5.5	2.3E-4
5.5 - 5.0	3.0E-4
5.0 - 4.5	3.0E-4
4.5 - 4.0	5.0E-4
4.0 - 3.5	5.0E-4
3.5 - 3.0	7.0E-4
3.0 - 2.5	7.0E-4
2.5 - 2.25	8.5E-4
2.25 - 2.00	9.5E-4
2.00 - 1.75	1.0E-3
1.75 - 1.50	1.4E-3
1.50 - 1.38	2.8E-3

1.38 – 1.25	3.8E-3
1.25 – 1.13	4.0E-3
1.13 – 1.00	3.0E-3
1.00 – 0.90	3.5E-3
0.90 – 0.80	7.5E-3
0.80 – 0.70	3.8E-3
0.70 – 0.60	2.3E-3
0.60 – 0.52	5.0E-3
0.52 – 0.50	5.0E-3

- (1)C.Ichihara, et al., "Leakage Neutron Spectra from Various Sphere Piles with 14 MeV Neutrons", this issue.
- (2)J.Yamamoto, et al., "Numerical Tables and Graphs of Leakage Neutron Spectra from Slabs of Typical Shielding Materials with D-T Neutron Source", OKTAVIAN-Report A-8305, Dept. of Nuclear Eng., Osaka University (1983).

#### Material/Geometry/Configuration

The samples in use were Al, Si, Ti, Cr, Mn, Co, Cu, Nb, Mo, W, Pb, LiF and CF<sub>2</sub>(Teflon). All samples were same as those in Ref.(1).

#### Error assessment

The following error sources were included in the errors.

- (a)Uncertainty in monitoring absolute fluxes of the source neutrons.
- (b)Errors of the response matrix.
- (c)Statistical deviation ( $1\sigma$ )

#### References

J.Yamamoto, et al., "γ Ray Emission Spectra from Spheres with 14 MeV Neutron Source", JAERI-M 89-026, 232(1989).

J.Yamamoto, "Integral Experiment on γ Ray Production at OKTAVIAN", JAERI-M 91-062, 118(1991).

### Description of data treatment

The emission spectra were dominated by the  $\gamma$  rays from  $(n,n')$  and  $(n,2n)$  reactions rather than the  $\gamma$  rays from  $(n,\gamma)$  reaction. The data are therefore available to the assessment in the nuclear data for energy distributions of  $\gamma$  rays from non-elastic scattering by high energy neutrons.

### Comments and so forth

Both the leakage spectra of neutron and  $\gamma$  ray can be compared with transport calculations, because of the same condition with regard to the spherical samples and the neutron source. (See Ref.(1))

In the present experiment the period to measure the prompt  $\gamma$  rays from the sphere was 60 to 80 ns after the source neutrons generating, so that it was necessary to compute the  $\gamma$  ray fluxes in the spheres by using time-dependent transport calculations. However, steady state transport calculations were applicable under the compatible condition with the experimental one by a simple method, in which the neutron-mean-emission times from the sphere were investigated as a function of neutron energy to estimate neutron slowing down times in the spheres.

Some examples of calculated emission times are shown in Figs.2 and 3. The calculations were done by MCNP.

In numerical tables of the experimental data, each energy spectrum was normalized in a leakage current flux from a whole surface of the sphere per a source neutron.

### Nuclear data file to be referred

JENDL-3 was used in the analysis mentioned in next term.

### Examples of experimental analysis

MCNP + JENDL-3

Some results are compared with the experimental data in figures.

Input data for a graphite sphere of 30 cm in diameter are as follows.

Configuration is shown in Fig.4 and the result is shown in Fig.5 in comparison with the measured energy spectrum.

TALLY CARD FOR BE EXPERIMENT ANALYSIS BY MCNP JENDL3 (1991,9)

C \*\*\*\*\* CELL CARDS \*\*\*\*\*

```
1 0 -2
2 1 -1.800 -1 2
3 0 -3 1
4 0 3
```

C \*\*\*\*\* SURFACE CARDS \*\*\*\*\*

```
1 SO 15.00
2 SO 4.0
3 SO 621.35
```

C \*\*\*\*\* DATA CARDS \*\*\*\*\*

```
MODE N P
SDEF ERG=D1 POS=0.0 0.0 0.0
IMP:N 1 1 1 0
IMP:P 1 1 1 0
```

C \*\*\* ENERGY BIN FOR SOURCE NEUTRON \*\*\*

```
SI1 H 0.10580E+01 0.11620E+01 0.12750E+01 0.14000E+01 0.15420E+01
0.16980E+01 0.18710E+01 0.20610E+01 0.22700E+01 0.25000E+01
0.27040E+01 0.29240E+01 0.31620E+01 0.34190E+01 0.36990E+01
0.40000E+01 0.41650E+01 0.43370E+01 0.45160E+01 0.47030E+01
0.48970E+01 0.50990E+01 0.53100E+01 0.55290E+01 0.57570E+01
0.59950E+01 0.62420E+01 0.65000E+01 0.67650E+01 0.70410E+01
0.73270E+01 0.76270E+01 0.79380E+01 0.82610E+01 0.85980E+01
0.89490E+01 0.93140E+01 0.96930E+01 0.10089E+02 0.10500E+02
0.10817E+02 0.11143E+02 0.11479E+02 0.11825E+02 0.12182E+02
0.12549E+02 0.12775E+02 0.13005E+02 0.13239E+02 0.13477E+02
0.13720E+02 0.13967E+02 0.14218E+02 0.14474E+02 0.14735E+02
0.15000E+02 0.15270E+02 0.15545E+02 0.15825E+02 0.16110E+02
0.16399E+02
```

C \*\*\*\*\* SOURCE DISTRIBUTION \*\*\*\*\*

SP1 D 0.00000E+00 0.43294E-01 0.32540E-01 0.42945E-01 0.40272E-01  
0.27926E-01 0.34186E-01 0.34042E-01 0.23955E-01 0.31569E-01  
0.43807E-01 0.41738E-01 0.17916E-01 0.17044E-01 0.13307E-01  
0.13417E-01 0.11811E-01 0.11526E-01 0.97991E-02 0.12098E-01  
0.91486E-02 0.87084E-02 0.64650E-02 0.68528E-02 0.59667E-02  
0.62186E-02 0.64940E-02 0.62448E-02 0.55632E-02 0.62477E-02  
0.53803E-02 0.51710E-02 0.55622E-02 0.53794E-02 0.61662E-02  
0.61352E-02 0.68313E-02 0.63205E-02 0.68856E-02 0.80788E-02  
0.76653E-02 0.87169E-02 0.10680E-01 0.10213E-01 0.12114E-01  
0.15459E-01 0.14916E-01 0.14518E-01 0.22867E-01 0.22260E-01  
0.85022E-01 0.82752E-01 0.80572E-01 0.25612E+00 0.24935E+00  
0.24271E+00 0.40968E+00 0.39870E+00 0.38819E+00 0.38627E+00  
0.37601E+00

C \*\*\*\*\* MATERIAL CARDS \*\*\*\*\*

M1 6012.33 1

C \*\*\*\*\* TALLY CARDS \*\*\*\*\*

F21:P 3

C \*\*\*\*\* TIME DISTRIBUTION ( UPPER BOUND ) 1=10 nsec \*\*\*\*\*

T21 10.0889 1.0E4

C \*\*\*\*\* ENERGY BIN \*\*\*\*\*

E21 0.05 0.10 0.15 0.20 0.25 0.30 0.35 0.40 0.45 0.50  
0.55 0.60 0.65 0.70 0.75 0.80 0.85 0.90 0.95 1.00  
1.05 1.10 1.15 1.20 1.25 1.30 1.35 1.40 1.45 1.50  
1.55 1.60 1.65 1.70 1.75 1.80 1.85 1.90 1.95 2.00  
2.05 2.10 2.15 2.20 2.25 2.30 2.35 2.40 2.45 2.50  
2.55 2.60 2.65 2.70 2.75 2.80 2.85 2.90 2.95 3.00  
3.05 3.10 3.15 3.20 3.25 3.30 3.35 3.40 3.45 3.50  
3.55 3.60 3.65 3.70 3.75 3.80 3.85 3.90 3.95 4.00  
4.05 4.10 4.15 4.20 4.25 4.30 4.35 4.40 4.45 4.50  
4.55 4.60 4.65 4.70 4.75 4.80 4.85 4.90 4.95 5.00  
5.05 5.10 5.15 5.20 5.25 5.30 5.35 5.40 5.45 5.50  
5.55 5.60 5.65 5.70 5.75 5.80 5.85 5.90 5.95 6.00  
6.05 6.10 6.15 6.20 6.25 6.30 6.35 6.40 6.45 6.50

6.55 6.60 6.65 6.70 6.75 6.80 6.85 6.90 6.95 7.00  
7.05 7.10 7.15 7.20 7.25 7.30 7.35 7.40 7.45 7.50  
7.55 7.60 7.65 7.70 7.75 7.80 7.85 7.90 7.95 8.00  
8.05 8.10 8.15 8.20 8.25 8.30 8.35 8.40 8.45 8.50  
8.55 8.60 8.65 8.70 8.75 8.80 8.85 8.90 8.95 9.00  
9.05 9.10 9.15 9.20 9.25 9.30 9.35 9.40 9.45 9.50  
9.55 9.60 9.65 9.70 9.75 9.80 9.85 9.90 9.95 10.0

C \*\*\*\*\* CUT OFF CARD \*\*\*\*\*

CUT:N 1.0E+4 1.0E-8 0.01

CUT:P 1.0E+4 1.0E-2 0.01

C \*\*\*\*\* NEUTRON HISTORY \*\*\*\*\*

NPS 1600000

PRINT

Experimental data with errors

\*\*\*\*\*

Al Sphere 40cm 1987.09.25

\*\*\*\*\*

Lower Energy [MeV]	Upper Energy [MeV]	Energy Spectrum [MeV/S.n.]	Error
5.000E-01	6.000E-01	2.025E-01	5.000E-04
6.000E-01	7.000E-01	1.810E-01	5.000E-04
7.000E-01	8.000E-01	1.655E-01	4.000E-04
8.000E-01	9.000E-01	2.199E-01	4.000E-04
9.000E-01	1.000E+00	2.042E-01	4.000E-04
1.000E+00	1.100E+00	1.810E-01	5.000E-04
1.100E+00	1.200E+00	1.364E-01	4.000E-04
1.200E+00	1.300E+00	1.203E-01	4.000E-04
1.300E+00	1.400E+00	1.159E-01	4.000E-04
1.400E+00	1.500E+00	1.033E-01	5.000E-04
1.500E+00	1.600E+00	8.601E-02	6.200E-04
1.600E+00	1.700E+00	8.412E-02	5.200E-04
1.700E+00	1.800E+00	1.108E-01	6.000E-04
1.800E+00	1.900E+00	1.251E-01	6.000E-04
1.900E+00	2.000E+00	9.976E-02	4.200E-04
2.000E+00	2.100E+00	7.944E-02	5.200E-04
2.100E+00	2.200E+00	9.377E-02	7.100E-04
2.200E+00	2.300E+00	1.112E-01	7.000E-04
2.300E+00	2.400E+00	9.630E-02	6.900E-04
2.400E+00	2.500E+00	6.832E-02	1.050E-03
2.500E+00	2.600E+00	5.362E-02	8.800E-04
2.600E+00	2.700E+00	4.855E-02	5.400E-04
2.700E+00	2.800E+00	4.804E-02	9.900E-04
2.800E+00	2.900E+00	5.524E-02	1.010E-03
2.900E+00	3.000E+00	6.851E-02	8.100E-04
3.000E+00	3.100E+00	7.359E-02	8.100E-04
3.100E+00	3.200E+00	6.203E-02	7.500E-04
3.200E+00	3.300E+00	4.470E-02	6.100E-04
3.300E+00	3.400E+00	3.335E-02	6.900E-04
3.400E+00	3.500E+00	2.885E-02	9.100E-04
3.500E+00	3.600E+00	2.788E-02	9.600E-04
3.600E+00	3.700E+00	2.800E-02	9.700E-04
3.700E+00	3.800E+00	2.814E-02	8.600E-04
3.800E+00	3.900E+00	2.828E-02	7.400E-04
3.900E+00	4.000E+00	2.817E-02	9.600E-04
4.000E+00	4.100E+00	2.716E-02	1.220E-03
4.100E+00	4.200E+00	2.539E-02	1.440E-03
4.200E+00	4.300E+00	2.371E-02	2.030E-03
4.300E+00	4.400E+00	2.253E-02	2.610E-03
4.400E+00	4.500E+00	2.190E-02	2.450E-03
4.500E+00	4.600E+00	2.213E-02	1.620E-03
4.600E+00	4.700E+00	2.346E-02	2.550E-03
4.700E+00	4.800E+00	2.536E-02	4.650E-03
4.800E+00	4.900E+00	2.654E-02	5.470E-03
4.900E+00	5.000E+00	2.550E-02	3.830E-03
5.000E+00	5.500E+00	1.596E-02	2.320E-03
5.500E+00	6.000E+00	1.899E-02	1.860E-03
6.000E+00	6.500E+00	1.630E-02	1.360E-03
6.500E+00	7.000E+00	6.569E-03	2.461E-03
7.000E+00	7.500E+00	1.641E-02	2.300E-03
7.500E+00	8.000E+00	4.856E-03	1.785E-03
8.000E+00	8.500E+00	9.137E-03	1.409E-03
8.500E+00	9.000E+00	5.316E-03	6.960E-04
9.000E+00	9.500E+00	1.660E-03	5.890E-04
9.500E+00	1.000E+01	3.036E-03	4.050E-04
1.000E+01	1.050E+01	1.489E-03	2.410E-04
1.050E+01	1.100E+01	6.201E-04	1.409E-04

\*\*\*\*\*  
 Si Sphere 40cm 1987.09.26  
 \*\*\*\*\*

Lower Energy [MeV]	Upper Energy [MeV]	Energy Spectrum [MeV/S.n.]	Error
5.000E-01	6.000E-01	1.846E-01	6.000E-04
6.000E-01	7.000E-01	1.583E-01	6.000E-04
7.000E-01	8.000E-01	1.234E-01	5.000E-04
8.000E-01	9.000E-01	1.447E-01	5.000E-04
9.000E-01	1.000E+00	1.368E-01	5.000E-04
1.000E+00	1.100E+00	1.113E-01	7.000E-04
1.100E+00	1.200E+00	9.339E-02	5.200E-04
1.200E+00	1.300E+00	9.897E-02	5.800E-04
1.300E+00	1.400E+00	1.001E-01	5.000E-04
1.400E+00	1.500E+00	8.920E-02	7.000E-04
1.500E+00	1.600E+00	8.325E-02	8.000E-04
1.600E+00	1.700E+00	1.081E-01	6.000E-04
1.700E+00	1.800E+00	1.601E-01	8.000E-04
1.800E+00	1.900E+00	1.512E-01	8.000E-04
1.900E+00	2.000E+00	8.648E-02	5.300E-04
2.000E+00	2.100E+00	4.784E-02	6.700E-04
2.100E+00	2.200E+00	4.142E-02	9.500E-04
2.200E+00	2.300E+00	3.984E-02	9.000E-04
2.300E+00	2.400E+00	3.550E-02	9.100E-04
2.400E+00	2.500E+00	3.186E-02	1.430E-03
2.500E+00	2.600E+00	3.158E-02	1.200E-03
2.600E+00	2.700E+00	3.426E-02	7.600E-04
2.700E+00	2.800E+00	3.896E-02	1.370E-03
2.800E+00	2.900E+00	4.033E-02	1.360E-03
2.900E+00	3.000E+00	3.466E-02	1.110E-03
3.000E+00	3.100E+00	2.756E-02	1.170E-03
3.100E+00	3.200E+00	2.470E-02	1.090E-03
3.200E+00	3.300E+00	2.512E-02	8.800E-04
3.300E+00	3.400E+00	2.622E-02	1.030E-03
3.400E+00	3.500E+00	2.660E-02	1.310E-03
3.500E+00	3.600E+00	2.577E-02	1.290E-03
3.600E+00	3.700E+00	2.431E-02	1.280E-03
3.700E+00	3.800E+00	2.292E-02	1.160E-03
3.800E+00	3.900E+00	2.131E-02	1.020E-03
3.900E+00	4.000E+00	1.901E-02	1.360E-03
4.000E+00	4.500E+00	1.811E-02	1.240E-03
4.500E+00	5.000E+00	1.892E-02	2.400E-03
5.000E+00	5.500E+00	1.750E-02	3.150E-03
5.500E+00	6.000E+00	9.814E-03	2.557E-03
6.000E+00	7.000E+00	1.616E-02	2.130E-03
7.000E+00	8.000E+00	1.044E-02	2.320E-03
8.000E+00	9.000E+00	4.279E-03	1.348E-03
9.000E+00	1.000E+01	4.596E-03	7.420E-04
1.000E+01	1.100E+01	2.011E-03	2.210E-04

\*\*\*\*\*  
 Si Sphere 60cm 1987.07  
 \*\*\*\*\*

Lower Energy [MeV]	Upper Energy [MeV]	Energy Spectrum [MeV/S.n.]	Error
3.000E-01	4.000E-01	3.171E-01	1.100E-03
4.000E-01	5.000E-01	2.046E-01	1.200E-03
5.000E-01	6.000E-01	2.024E-01	1.200E-03
6.000E-01	7.000E-01	2.642E-01	1.200E-03
7.000E-01	8.000E-01	2.235E-01	1.000E-03
8.000E-01	9.000E-01	1.737E-01	1.000E-03
9.000E-01	1.000E+00	1.673E-01	9.000E-04
1.000E+00	1.100E+00	1.877E-01	1.400E-03
1.100E+00	1.200E+00	1.775E-01	1.000E-03
1.200E+00	1.300E+00	1.490E-01	1.200E-03
1.300E+00	1.400E+00	1.452E-01	1.100E-03
1.400E+00	1.500E+00	2.002E-01	1.400E-03
1.500E+00	1.600E+00	2.768E-01	1.700E-03
1.600E+00	1.700E+00	2.157E-01	1.400E-03
1.700E+00	1.800E+00	1.129E-01	1.400E-03
1.800E+00	1.900E+00	7.780E-02	1.480E-03
1.900E+00	2.000E+00	7.483E-02	1.050E-03
2.000E+00	2.100E+00	7.143E-02	1.280E-03
2.100E+00	2.200E+00	6.256E-02	1.780E-03
2.200E+00	2.300E+00	5.549E-02	1.730E-03
2.300E+00	2.400E+00	5.570E-02	1.870E-03
2.400E+00	2.500E+00	6.197E-02	2.840E-03
2.500E+00	2.600E+00	7.099E-02	2.260E-03
2.600E+00	2.700E+00	7.256E-02	1.360E-03
2.700E+00	2.800E+00	6.235E-02	2.710E-03
2.800E+00	2.900E+00	5.096E-02	2.610E-03
2.900E+00	3.000E+00	4.654E-02	2.040E-03
3.000E+00	3.100E+00	4.716E-02	2.380E-03
3.100E+00	3.200E+00	4.806E-02	2.290E-03
3.200E+00	3.300E+00	4.650E-02	1.880E-03
3.300E+00	3.400E+00	4.326E-02	2.070E-03
3.400E+00	3.500E+00	4.034E-02	2.880E-03
3.500E+00	3.600E+00	3.816E-02	3.400E-03
3.600E+00	3.700E+00	3.663E-02	3.530E-03
3.700E+00	3.800E+00	3.548E-02	2.860E-03
3.800E+00	3.900E+00	3.412E-02	2.080E-03
3.900E+00	4.000E+00	3.316E-02	3.030E-03
4.000E+00	4.500E+00	3.524E-02	2.590E-03
4.500E+00	5.000E+00	3.200E-02	4.740E-03
5.000E+00	5.500E+00	2.468E-02	6.310E-03
5.500E+00	6.000E+00	1.774E-02	5.460E-03
6.000E+00	6.500E+00	2.177E-02	4.500E-03
6.500E+00	7.000E+00	2.841E-02	6.830E-03
7.000E+00	7.500E+00	1.684E-02	6.270E-03
7.500E+00	8.000E+00	1.946E-02	5.280E-03
8.000E+00	8.500E+00	1.683E-03	4.963E-03
8.500E+00	9.000E+00	2.284E-02	4.910E-03
9.000E+00	9.500E+00	1.723E-03	5.981E-03
9.500E+00	1.000E+01	2.039E-02	6.670E-03
1.000E+01	1.050E+01	1.288E-03	5.512E-03
1.050E+01	1.100E+01	1.078E-02	4.330E-03

\*\*\*\*\*  
 Ti Sphere 40cm 1987.09.26  
 \*\*\*\*\*

Lower Energy [MeV]	Upper Energy [MeV]	Energy Spectrum [/MeV/S.n.]	Error
5.000E-01	6.000E-01	2.639E-01	6.000E-04
6.000E-01	7.000E-01	3.119E-01	6.000E-04
7.000E-01	8.000E-01	2.299E-01	5.000E-04
8.000E-01	9.000E-01	1.903E-01	5.000E-04
9.000E-01	1.000E+00	2.267E-01	5.000E-04
1.000E+00	1.100E+00	3.149E-01	8.000E-04
1.100E+00	1.200E+00	3.934E-01	6.000E-04
1.200E+00	1.300E+00	2.654E-01	6.000E-04
1.300E+00	1.400E+00	1.617E-01	5.000E-04
1.400E+00	1.500E+00	1.787E-01	7.000E-04
1.500E+00	1.600E+00	1.888E-01	8.000E-04
1.600E+00	1.700E+00	1.478E-01	6.000E-04
1.700E+00	1.800E+00	1.048E-01	7.000E-04
1.800E+00	1.900E+00	8.068E-02	8.200E-04
1.900E+00	2.000E+00	6.858E-02	5.100E-04
2.000E+00	2.100E+00	6.272E-02	6.600E-04
2.100E+00	2.200E+00	5.657E-02	9.300E-04
2.200E+00	2.300E+00	5.111E-02	8.800E-04
2.300E+00	2.400E+00	4.970E-02	8.800E-04
2.400E+00	2.500E+00	5.086E-02	1.410E-03
2.500E+00	2.600E+00	5.447E-02	1.200E-03
2.600E+00	2.700E+00	5.876E-02	7.600E-04
2.700E+00	2.800E+00	5.790E-02	1.340E-03
2.800E+00	2.900E+00	5.167E-02	1.360E-03
2.900E+00	3.000E+00	4.599E-02	1.100E-03
3.000E+00	3.100E+00	4.261E-02	1.130E-03
3.100E+00	3.200E+00	3.979E-02	1.070E-03
3.200E+00	3.300E+00	3.736E-02	8.500E-04
3.300E+00	3.400E+00	3.549E-02	9.600E-04
3.400E+00	3.500E+00	3.426E-02	1.230E-03
3.500E+00	3.600E+00	3.341E-02	1.220E-03
3.600E+00	3.700E+00	3.206E-02	1.220E-03
3.700E+00	3.800E+00	3.033E-02	1.100E-03
3.800E+00	3.900E+00	2.926E-02	9.700E-04
3.900E+00	4.000E+00	2.936E-02	1.360E-03
4.000E+00	4.200E+00	3.001E-02	1.320E-03
4.200E+00	4.400E+00	2.619E-02	2.160E-03
4.400E+00	4.600E+00	1.893E-02	2.270E-03
4.600E+00	4.800E+00	1.839E-02	3.510E-03
4.800E+00	5.000E+00	2.203E-02	4.640E-03
5.000E+00	5.200E+00	2.046E-02	3.370E-03
5.200E+00	5.400E+00	1.551E-02	6.590E-03
5.400E+00	5.600E+00	1.601E-02	2.730E-03
5.600E+00	5.800E+00	1.774E-02	4.900E-03
5.800E+00	6.000E+00	1.458E-02	3.670E-03
6.000E+00	7.000E+00	1.230E-02	2.170E-03
7.000E+00	8.000E+00	1.107E-02	2.380E-03
8.000E+00	9.000E+00	8.202E-03	1.431E-03
9.000E+00	1.000E+01	4.622E-03	7.990E-04
1.000E+01	1.100E+01	2.541E-03	3.760E-04

\*\*\*\*\*  
 Cr Sphere 40cm 1987.07  
 \*\*\*\*\*

Lower Energy [MeV]	Upper Energy [MeV]	Energy Spectrum [MeV/S.n.]	Error
3.000E-01	4.000E-01	3.118E-01	7.000E-04
4.000E-01	5.000E-01	2.426E-01	7.000E-04
5.000E-01	6.000E-01	2.289E-01	7.000E-04
6.000E-01	7.000E-01	2.653E-01	7.000E-04
7.000E-01	8.000E-01	2.439E-01	6.000E-04
8.000E-01	9.000E-01	1.847E-01	6.000E-04
9.000E-01	1.000E+00	1.652E-01	6.000E-04
1.000E+00	1.100E+00	1.993E-01	7.000E-04
1.100E+00	1.200E+00	2.911E-01	6.000E-04
1.200E+00	1.300E+00	3.086E-01	7.000E-04
1.300E+00	1.400E+00	1.781E-01	6.000E-04
1.400E+00	1.500E+00	8.858E-02	7.100E-04
1.500E+00	1.600E+00	6.908E-02	8.300E-04
1.600E+00	1.700E+00	5.855E-02	6.400E-04
1.700E+00	1.800E+00	5.379E-02	6.800E-04
1.800E+00	1.900E+00	5.306E-02	7.500E-04
1.900E+00	2.000E+00	5.115E-02	5.800E-04
2.000E+00	2.100E+00	5.037E-02	6.500E-04
2.100E+00	2.200E+00	4.927E-02	8.700E-04
2.200E+00	2.300E+00	4.579E-02	8.400E-04
2.300E+00	2.400E+00	4.241E-02	9.400E-04
2.400E+00	2.500E+00	4.034E-02	1.380E-03
2.500E+00	2.600E+00	3.836E-02	1.110E-03
2.600E+00	2.700E+00	3.648E-02	6.800E-04
2.700E+00	2.800E+00	3.708E-02	1.330E-03
2.800E+00	2.900E+00	4.043E-02	1.300E-03
2.900E+00	3.000E+00	4.272E-02	9.600E-04
3.000E+00	3.100E+00	4.087E-02	1.090E-03
3.100E+00	3.200E+00	3.636E-02	1.080E-03
3.200E+00	3.300E+00	3.256E-02	8.900E-04
3.300E+00	3.400E+00	3.056E-02	9.400E-04
3.400E+00	3.500E+00	2.952E-02	1.300E-03
3.500E+00	3.600E+00	2.865E-02	1.530E-03
3.600E+00	3.700E+00	2.749E-02	1.580E-03
3.700E+00	3.800E+00	2.577E-02	1.330E-03
3.800E+00	3.900E+00	2.409E-02	1.030E-03
3.900E+00	4.000E+00	2.348E-02	1.350E-03
4.000E+00	4.100E+00	2.414E-02	1.800E-03
4.100E+00	4.200E+00	2.523E-02	2.250E-03
4.200E+00	4.300E+00	2.588E-02	3.010E-03
4.300E+00	4.400E+00	2.542E-02	3.510E-03
4.400E+00	4.500E+00	2.337E-02	2.990E-03
4.500E+00	4.600E+00	1.982E-02	1.940E-03
4.600E+00	4.700E+00	1.566E-02	3.690E-03
4.700E+00	4.800E+00	1.259E-02	6.380E-03
4.800E+00	4.900E+00	1.229E-02	7.210E-03
4.900E+00	5.000E+00	1.537E-02	4.920E-03
5.000E+00	5.500E+00	2.539E-02	3.140E-03
5.500E+00	6.000E+00	1.121E-02	2.580E-03
6.000E+00	6.500E+00	1.618E-02	1.670E-03
6.500E+00	7.000E+00	1.440E-02	2.730E-03
7.000E+00	7.500E+00	8.613E-03	2.529E-03
7.500E+00	8.000E+00	8.949E-03	2.054E-03
8.000E+00	8.500E+00	4.834E-03	1.861E-03
8.500E+00	9.000E+00	5.793E-03	1.442E-03
9.000E+00	9.500E+00	1.244E-03	1.622E-03
9.500E+00	1.000E+01	3.757E-03	1.743E-03
1.000E+01	1.050E+01	1.319E-04	1.445E-03
1.050E+01	1.100E+01	1.554E-03	1.152E-03

\*\*\*\*\*  
Mn Sphere 60cm 1987.06  
\*\*\*\*\*

Lower Energy [MeV]	Upper Energy [MeV]	Energy Spectrum [MeV/S.n.]	Error
5.000E-01	6.000E-01	2.442E-01	6.300E-03
6.000E-01	7.000E-01	1.431E-01	2.500E-03
7.000E-01	8.000E-01	1.401E-01	1.100E-03
8.000E-01	9.000E-01	1.805E-01	5.000E-04
9.000E-01	1.000E+00	1.460E-01	3.000E-04
1.000E+00	1.100E+00	9.851E-02	5.100E-04
1.100E+00	1.200E+00	8.547E-02	1.000E-03
1.200E+00	1.300E+00	7.995E-02	1.600E-03
1.300E+00	1.400E+00	7.166E-02	1.340E-03
1.400E+00	1.500E+00	6.640E-02	5.600E-04
1.500E+00	1.600E+00	6.275E-02	1.410E-03
1.600E+00	1.700E+00	5.628E-02	1.800E-03
1.700E+00	1.800E+00	5.080E-02	1.520E-03
1.800E+00	1.900E+00	4.776E-02	1.050E-03
1.900E+00	2.000E+00	4.381E-02	6.700E-04
2.000E+00	2.100E+00	3.987E-02	7.700E-04
2.100E+00	2.200E+00	3.866E-02	1.120E-03
2.200E+00	2.300E+00	3.851E-02	1.460E-03
2.300E+00	2.400E+00	3.610E-02	1.810E-03
2.400E+00	2.500E+00	3.196E-02	1.810E-03
2.500E+00	2.600E+00	2.901E-02	1.180E-03
2.600E+00	2.700E+00	2.785E-02	5.700E-04
2.700E+00	2.800E+00	2.689E-02	9.100E-04
2.800E+00	2.900E+00	2.515E-02	1.300E-03
2.900E+00	3.000E+00	2.307E-02	1.670E-03
3.000E+00	3.100E+00	2.134E-02	1.940E-03
3.100E+00	3.200E+00	2.024E-02	1.850E-03
3.200E+00	3.300E+00	1.962E-02	1.230E-03
3.300E+00	3.400E+00	1.908E-02	1.040E-03
3.400E+00	3.500E+00	1.821E-02	2.630E-03
3.500E+00	3.600E+00	1.684E-02	4.110E-03
3.600E+00	3.700E+00	1.522E-02	4.500E-03
3.700E+00	3.800E+00	1.385E-02	3.300E-03
3.800E+00	3.900E+00	1.310E-02	1.250E-03
3.900E+00	4.000E+00	1.303E-02	3.230E-03
4.000E+00	4.500E+00	1.166E-02	2.150E-03
4.500E+00	5.000E+00	6.997E-03	2.122E-03
5.000E+00	5.500E+00	7.462E-03	2.314E-03
5.500E+00	6.000E+00	8.395E-03	1.444E-03
6.000E+00	6.500E+00	3.611E-03	9.850E-04
6.500E+00	7.000E+00	8.556E-03	1.059E-03
7.000E+00	7.500E+00	1.266E-03	8.560E-04
7.500E+00	8.000E+00	3.423E-03	6.490E-04
8.000E+00	8.500E+00	1.867E-03	5.420E-04
8.500E+00	9.000E+00	1.175E-03	3.190E-04
9.000E+00	9.500E+00	1.364E-03	2.020E-04
9.500E+00	1.000E+01	1.034E-03	1.540E-04
1.000E+01	1.050E+01	3.320E-04	8.230E-05
1.050E+01	1.100E+01	1.135E-04	3.250E-05

\*\*\*\*\*  
 Co Sphere 40cm 1987.07  
 \*\*\*\*\*

Lower Energy [MeV]	Upper Energy [MeV]	Energy Spectrum [MeV/S.n.]	Error
2.000E-01	3.000E-01	1.681E-01	9.000E-04
3.000E-01	4.000E-01	3.046E-01	9.000E-04
4.000E-01	5.000E-01	2.485E-01	9.000E-04
5.000E-01	6.000E-01	2.007E-01	7.000E-04
6.000E-01	7.000E-01	2.250E-01	8.000E-04
7.000E-01	8.000E-01	2.181E-01	7.000E-04
8.000E-01	9.000E-01	1.927E-01	7.000E-04
9.000E-01	1.000E+00	1.933E-01	7.000E-04
1.000E+00	1.100E+00	2.054E-01	7.000E-04
1.100E+00	1.200E+00	1.764E-01	6.000E-04
1.200E+00	1.300E+00	1.512E-01	7.000E-04
1.300E+00	1.400E+00	1.362E-01	6.000E-04
1.400E+00	1.500E+00	1.019E-01	7.000E-04
1.500E+00	1.600E+00	7.746E-02	7.900E-04
1.600E+00	1.700E+00	6.857E-02	6.800E-04
1.700E+00	1.800E+00	5.999E-02	6.600E-04
1.800E+00	1.900E+00	5.309E-02	6.800E-04
1.900E+00	2.000E+00	4.879E-02	6.300E-04
2.000E+00	2.100E+00	4.534E-02	6.700E-04
2.100E+00	2.200E+00	4.342E-02	7.800E-04
2.200E+00	2.300E+00	4.279E-02	8.000E-04
2.300E+00	2.400E+00	4.197E-02	8.800E-04
2.400E+00	2.500E+00	4.041E-02	1.010E-03
2.500E+00	2.600E+00	3.791E-02	8.200E-04
2.600E+00	2.700E+00	3.477E-02	6.900E-04
2.700E+00	2.800E+00	3.190E-02	1.000E-03
2.800E+00	2.900E+00	2.991E-02	9.400E-04
2.900E+00	3.000E+00	2.873E-02	8.100E-04
3.000E+00	3.100E+00	2.804E-02	9.800E-04
3.100E+00	3.200E+00	2.757E-02	9.800E-04
3.200E+00	3.300E+00	2.695E-02	8.200E-04
3.300E+00	3.400E+00	2.600E-02	8.300E-04
3.400E+00	3.500E+00	2.494E-02	1.140E-03
3.500E+00	3.600E+00	2.394E-02	1.400E-03
3.600E+00	3.700E+00	2.280E-02	1.430E-03
3.700E+00	3.800E+00	2.142E-02	1.190E-03
3.800E+00	3.900E+00	2.008E-02	9.400E-04
3.900E+00	4.000E+00	1.911E-02	1.140E-03
4.000E+00	4.200E+00	1.851E-02	1.310E-03
4.200E+00	4.400E+00	1.757E-02	1.780E-03
4.400E+00	4.600E+00	1.478E-02	1.180E-03
4.600E+00	4.800E+00	1.229E-02	2.720E-03
4.800E+00	5.000E+00	1.263E-02	2.660E-03
5.000E+00	5.200E+00	1.552E-02	2.530E-03
5.200E+00	5.400E+00	1.633E-02	4.420E-03
5.400E+00	5.600E+00	1.238E-02	1.930E-03
5.600E+00	5.800E+00	8.061E-03	3.060E-03
5.800E+00	6.000E+00	7.517E-03	3.079E-03
6.000E+00	6.500E+00	9.080E-03	9.080E-04
6.500E+00	7.000E+00	9.394E-03	1.115E-03
7.000E+00	7.500E+00	4.306E-03	9.360E-04
7.500E+00	8.000E+00	4.850E-03	7.490E-04
8.000E+00	8.500E+00	2.359E-03	6.300E-04
8.500E+00	9.000E+00	2.359E-03	3.340E-04
9.000E+00	9.500E+00	6.343E-04	3.008E-04
9.500E+00	1.000E+01	1.250E-03	2.940E-04
1.000E+01	1.050E+01	2.130E-04	2.535E-04
1.050E+01	1.100E+01	7.436E-04	2.225E-04

\*\*\*\*\*  
 Cu Sphere 60cm 1987.06  
 \*\*\*\*\*

Lower Energy [MeV]	Upper Energy [MeV]	Energy Spectrum [MeV/S.n.]	Error
5.000E-01	6.000E-01	1.380E+00	4.300E-02
6.000E-01	7.000E-01	8.962E-01	1.700E-02
7.000E-01	8.000E-01	8.176E-01	7.000E-03
8.000E-01	9.000E-01	9.066E-01	2.600E-03
9.000E-01	1.000E+00	8.468E-01	1.700E-03
1.000E+00	1.100E+00	6.704E-01	2.100E-03
1.100E+00	1.200E+00	5.573E-01	4.000E-03
1.200E+00	1.300E+00	4.923E-01	6.200E-03
1.300E+00	1.400E+00	4.327E-01	5.000E-03
1.400E+00	1.500E+00	3.661E-01	2.100E-03
1.500E+00	1.600E+00	2.952E-01	5.500E-03
1.600E+00	1.700E+00	2.413E-01	7.100E-03
1.700E+00	1.800E+00	2.109E-01	6.000E-03
1.800E+00	1.900E+00	1.951E-01	4.100E-03
1.900E+00	2.000E+00	1.805E-01	2.400E-03
2.000E+00	2.100E+00	1.637E-01	2.800E-03
2.100E+00	2.200E+00	1.470E-01	4.100E-03
2.200E+00	2.300E+00	1.314E-01	5.500E-03
2.300E+00	2.400E+00	1.187E-01	7.000E-03
2.400E+00	2.500E+00	1.100E-01	7.000E-03
2.500E+00	2.600E+00	1.043E-01	4.600E-03
2.600E+00	2.700E+00	1.001E-01	2.000E-03
2.700E+00	2.800E+00	9.698E-02	3.420E-03
2.800E+00	2.900E+00	9.421E-02	5.180E-03
2.900E+00	3.000E+00	9.031E-02	6.610E-03
3.000E+00	3.100E+00	8.453E-02	7.360E-03
3.100E+00	3.200E+00	7.791E-02	6.770E-03
3.200E+00	3.300E+00	7.213E-02	4.330E-03
3.300E+00	3.400E+00	6.788E-02	3.850E-03
3.400E+00	3.500E+00	6.496E-02	1.008E-02
3.500E+00	3.600E+00	6.245E-02	1.597E-02
3.600E+00	3.700E+00	5.997E-02	1.764E-02
3.700E+00	3.800E+00	5.770E-02	1.300E-02
3.800E+00	3.900E+00	5.597E-02	4.750E-03
3.900E+00	4.000E+00	5.494E-02	1.218E-02
4.000E+00	4.500E+00	4.869E-02	8.390E-03
4.500E+00	5.000E+00	2.953E-02	8.000E-03
5.000E+00	5.500E+00	3.094E-02	8.520E-03
5.500E+00	6.000E+00	2.406E-02	4.900E-03
6.000E+00	6.500E+00	2.093E-02	3.200E-03
6.500E+00	7.000E+00	1.397E-02	3.110E-03
7.000E+00	7.500E+00	1.564E-02	2.330E-03
7.500E+00	8.000E+00	1.047E-02	1.560E-03
8.000E+00	8.500E+00	3.402E-03	1.241E-03
8.500E+00	9.000E+00	6.043E-03	6.560E-04
9.000E+00	9.500E+00	1.134E-03	4.260E-04
9.500E+00	1.000E+01	7.879E-04	2.452E-04
1.000E+01	1.050E+01	1.124E-03	1.640E-04
1.050E+01	1.100E+01	2.081E-04	7.030E-05

\*\*\*\*\*  
 Nb Sphere 28cm 1987.06.21  
 \*\*\*\*\*

Lower Energy [MeV]	Upper Energy [MeV]	Energy Spectrum [MeV/S.n.]	Error
5.000E-01	6.000E-01	6.126E-01	8.300E-03
6.000E-01	7.000E-01	3.887E-01	3.300E-03
7.000E-01	8.000E-01	3.372E-01	1.500E-03
8.000E-01	9.000E-01	3.758E-01	7.000E-04
9.000E-01	1.000E+00	3.547E-01	5.000E-04
1.000E+00	1.100E+00	2.833E-01	6.000E-04
1.100E+00	1.200E+00	2.129E-01	1.200E-03
1.200E+00	1.300E+00	1.793E-01	1.800E-03
1.300E+00	1.400E+00	1.634E-01	1.500E-03
1.400E+00	1.500E+00	1.482E-01	6.000E-04
1.500E+00	1.600E+00	1.305E-01	1.600E-03
1.600E+00	1.700E+00	1.131E-01	2.100E-03
1.700E+00	1.800E+00	1.014E-01	1.700E-03
1.800E+00	1.900E+00	9.516E-02	1.200E-03
1.900E+00	2.000E+00	9.162E-02	7.500E-04
2.000E+00	2.100E+00	8.976E-02	8.500E-04
2.100E+00	2.200E+00	8.674E-02	1.230E-03
2.200E+00	2.300E+00	7.921E-02	1.640E-03
2.300E+00	2.400E+00	6.840E-02	2.070E-03
2.400E+00	2.500E+00	5.853E-02	2.080E-03
2.500E+00	2.600E+00	5.181E-02	1.370E-03
2.600E+00	2.700E+00	4.774E-02	6.500E-04
2.700E+00	2.800E+00	4.509E-02	1.020E-03
2.800E+00	2.900E+00	4.301E-02	1.530E-03
2.900E+00	3.000E+00	4.087E-02	1.960E-03
3.000E+00	3.100E+00	3.813E-02	2.210E-03
3.100E+00	3.200E+00	3.466E-02	2.070E-03
3.200E+00	3.300E+00	3.098E-02	1.350E-03
3.300E+00	3.400E+00	2.774E-02	1.200E-03
3.400E+00	3.500E+00	2.535E-02	3.030E-03
3.500E+00	3.600E+00	2.387E-02	4.760E-03
3.600E+00	3.700E+00	2.309E-02	5.250E-03
3.700E+00	3.800E+00	2.272E-02	3.870E-03
3.800E+00	3.900E+00	2.243E-02	1.420E-03
3.900E+00	4.000E+00	2.197E-02	3.640E-03
4.000E+00	4.500E+00	1.639E-02	2.500E-03
4.500E+00	5.000E+00	9.383E-03	2.402E-03
5.000E+00	5.500E+00	1.081E-02	2.590E-03
5.500E+00	6.000E+00	8.120E-03	1.502E-03
6.000E+00	6.500E+00	6.642E-03	1.002E-03
6.500E+00	7.000E+00	4.718E-03	1.006E-03
7.000E+00	7.500E+00	4.308E-03	7.880E-04
7.500E+00	8.000E+00	2.145E-03	5.740E-04
8.000E+00	8.500E+00	2.807E-03	4.810E-04
8.500E+00	9.000E+00	8.306E-04	2.942E-04
9.000E+00	9.500E+00	1.202E-03	2.010E-04
9.500E+00	1.000E+01	3.918E-04	1.567E-04
1.000E+01	1.050E+01	4.331E-04	1.131E-04
1.050E+01	1.100E+01	2.169E-04	5.372E-05

Mo Sphere 60cm 1987.06

Lower Energy [MeV]	Upper Energy [MeV]	Energy Spectrum [MeV/S.n.]	Error
5.000E-01	6.000E-01	5.591E-01	1.080E-02
6.000E-01	7.000E-01	3.766E-01	4.200E-03
7.000E-01	8.000E-01	3.860E-01	1.700E-03
8.000E-01	9.000E-01	4.088E-01	6.000E-04
9.000E-01	1.000E+00	3.071E-01	4.000E-04
1.000E+00	1.100E+00	2.165E-01	4.000E-04
1.100E+00	1.200E+00	1.811E-01	9.000E-04
1.200E+00	1.300E+00	1.623E-01	1.400E-03
1.300E+00	1.400E+00	1.442E-01	1.200E-03
1.400E+00	1.500E+00	1.288E-01	5.000E-04
1.500E+00	1.600E+00	1.135E-01	1.300E-03
1.600E+00	1.700E+00	9.452E-02	1.640E-03
1.700E+00	1.800E+00	7.849E-02	1.348E-03
1.800E+00	1.900E+00	6.932E-02	9.100E-04
1.900E+00	2.000E+00	6.412E-02	5.900E-04
2.000E+00	2.100E+00	6.046E-02	6.900E-04
2.100E+00	2.200E+00	5.673E-02	9.800E-04
2.200E+00	2.300E+00	5.220E-02	1.280E-03
2.300E+00	2.400E+00	4.776E-02	1.600E-03
2.400E+00	2.500E+00	4.416E-02	1.620E-03
2.500E+00	2.600E+00	4.100E-02	1.070E-03
2.600E+00	2.700E+00	3.765E-02	5.200E-04
2.700E+00	2.800E+00	3.422E-02	7.900E-04
2.800E+00	2.900E+00	3.133E-02	1.150E-03
2.900E+00	3.000E+00	2.936E-02	1.520E-03
3.000E+00	3.100E+00	2.812E-02	1.800E-03
3.100E+00	3.200E+00	2.711E-02	1.720E-03
3.200E+00	3.300E+00	2.593E-02	1.100E-03
3.300E+00	3.400E+00	2.458E-02	9.200E-04
3.400E+00	3.500E+00	2.331E-02	2.450E-03
3.500E+00	3.600E+00	2.218E-02	3.820E-03
3.600E+00	3.700E+00	2.086E-02	4.150E-03
3.700E+00	3.800E+00	1.906E-02	3.000E-03
3.800E+00	3.900E+00	1.681E-02	1.060E-03
3.900E+00	4.000E+00	1.446E-02	2.970E-03
4.000E+00	4.200E+00	1.181E-02	3.980E-03
4.200E+00	4.400E+00	1.102E-02	2.800E-03
4.400E+00	4.600E+00	1.184E-02	2.500E-03
4.600E+00	4.800E+00	1.079E-02	3.920E-03
4.800E+00	5.000E+00	8.580E-03	1.871E-03
5.000E+00	5.500E+00	7.651E-03	2.181E-03
5.500E+00	6.000E+00	4.846E-03	1.278E-03
6.000E+00	6.500E+00	6.191E-03	8.500E-04
6.500E+00	7.000E+00	3.833E-03	8.740E-04
7.000E+00	7.500E+00	3.266E-03	7.050E-04
7.500E+00	8.000E+00	2.567E-03	5.300E-04
8.000E+00	8.500E+00	1.749E-03	4.410E-04
8.500E+00	9.000E+00	1.296E-03	2.710E-04
9.000E+00	9.500E+00	9.457E-04	1.895E-04
9.500E+00	1.000E+01	3.341E-04	1.601E-04
1.000E+01	1.050E+01	6.341E-04	1.053E-04
1.050E+01	1.100E+01	1.515E-04	4.950E-05

\*\*\*\*\*  
 W Sphere 40cm 1987.11  
 \*\*\*\*\*

Lower Energy [MeV]	Upper Energy [MeV]	Energy Spectrum [MeV/S.n.]	Error
3.000E-01	4.000E-01	1.420E-01	3.000E-04
4.000E-01	5.000E-01	1.019E-01	3.000E-04
5.000E-01	6.000E-01	1.104E-01	2.000E-04
6.000E-01	7.000E-01	1.494E-01	3.000E-04
7.000E-01	8.000E-01	1.283E-01	2.000E-04
8.000E-01	9.000E-01	1.072E-01	2.000E-04
9.000E-01	1.000E+00	1.074E-01	2.000E-04
1.000E+00	1.100E+00	1.137E-01	2.000E-04
1.100E+00	1.200E+00	1.037E-01	2.000E-04
1.200E+00	1.300E+00	8.927E-02	2.700E-04
1.300E+00	1.400E+00	7.513E-02	2.600E-04
1.400E+00	1.500E+00	6.712E-02	2.700E-04
1.500E+00	1.600E+00	6.409E-02	2.900E-04
1.600E+00	1.700E+00	6.050E-02	2.600E-04
1.700E+00	1.800E+00	5.554E-02	2.600E-04
1.800E+00	1.900E+00	5.191E-02	2.700E-04
1.900E+00	2.000E+00	4.947E-02	2.500E-04
2.000E+00	2.100E+00	4.716E-02	2.600E-04
2.100E+00	2.200E+00	4.489E-02	2.800E-04
2.200E+00	2.300E+00	4.251E-02	2.800E-04
2.300E+00	2.400E+00	3.970E-02	2.900E-04
2.400E+00	2.500E+00	3.642E-02	3.300E-04
2.500E+00	2.600E+00	3.327E-02	2.900E-04
2.600E+00	2.700E+00	3.080E-02	2.500E-04
2.700E+00	2.800E+00	2.889E-02	3.200E-04
2.800E+00	2.900E+00	2.714E-02	3.100E-04
2.900E+00	3.000E+00	2.537E-02	2.700E-04
3.000E+00	3.100E+00	2.354E-02	3.000E-04
3.100E+00	3.200E+00	2.164E-02	3.000E-04
3.200E+00	3.300E+00	1.974E-02	2.600E-04
3.300E+00	3.400E+00	1.792E-02	2.600E-04
3.400E+00	3.500E+00	1.626E-02	3.300E-04
3.500E+00	3.600E+00	1.478E-02	3.800E-04
3.600E+00	3.700E+00	1.345E-02	3.900E-04
3.700E+00	3.800E+00	1.222E-02	3.400E-04
3.800E+00	3.900E+00	1.120E-02	2.700E-04
3.900E+00	4.000E+00	1.048E-02	3.200E-04
4.000E+00	4.100E+00	9.991E-03	4.270E-04
4.100E+00	4.200E+00	9.499E-03	5.370E-04
4.200E+00	4.300E+00	8.719E-03	6.660E-04
4.300E+00	4.400E+00	7.607E-03	6.960E-04
4.400E+00	4.500E+00	6.430E-03	5.410E-04
4.500E+00	4.600E+00	5.466E-03	4.220E-04
4.600E+00	4.700E+00	4.880E-03	7.940E-04
4.700E+00	4.800E+00	4.757E-03	1.225E-03
4.800E+00	4.900E+00	4.945E-03	1.305E-03
4.900E+00	5.000E+00	5.061E-03	8.550E-04
5.000E+00	5.500E+00	3.586E-03	5.960E-04
5.500E+00	6.000E+00	2.673E-03	4.880E-04
6.000E+00	6.500E+00	2.548E-03	2.790E-04
6.500E+00	7.000E+00	1.277E-03	3.730E-04
7.000E+00	7.500E+00	1.651E-03	3.420E-04
7.500E+00	8.000E+00	9.984E-04	2.980E-04
8.000E+00	8.500E+00	1.113E-03	2.650E-04
8.500E+00	9.000E+00	4.566E-04	1.861E-04
9.000E+00	9.500E+00	4.841E-04	1.894E-04
9.500E+00	1.000E+01	2.774E-04	1.971E-04
1.000E+01	1.050E+01	3.672E-05	1.720E-04
1.050E+01	1.100E+01	1.371E-04	1.412E-04

Pb Sphere 40cm 1987.11

Lower Energy [MeV]	Upper Energy [MeV]	Energy Spectrum [MeV/S.n.]	Error
6.000E-01	7.000E-01	6.386E-02	6.190E-03
7.000E-01	8.000E-01	5.678E-02	2.380E-03
8.000E-01	9.000E-01	7.840E-02	6.100E-04
9.000E-01	1.000E+00	6.535E-02	2.000E-04
1.000E+00	1.100E+00	4.269E-02	2.100E-04
1.100E+00	1.200E+00	3.377E-02	3.400E-04
1.200E+00	1.300E+00	3.107E-02	4.600E-04
1.300E+00	1.400E+00	2.835E-02	3.700E-04
1.400E+00	1.500E+00	2.564E-02	2.000E-04
1.500E+00	1.600E+00	2.423E-02	4.200E-04
1.600E+00	1.700E+00	2.425E-02	5.500E-04
1.700E+00	1.800E+00	2.478E-02	4.900E-04
1.800E+00	1.900E+00	2.392E-02	3.600E-04
1.900E+00	2.000E+00	2.157E-02	2.200E-04
2.000E+00	2.100E+00	1.946E-02	2.100E-04
2.100E+00	2.200E+00	1.780E-02	3.200E-04
2.200E+00	2.300E+00	1.599E-02	4.400E-04
2.300E+00	2.400E+00	1.511E-02	5.700E-04
2.400E+00	2.500E+00	1.687E-02	5.800E-04
2.500E+00	2.600E+00	2.064E-02	4.000E-04
2.600E+00	2.700E+00	2.281E-02	1.900E-04
2.700E+00	2.800E+00	2.048E-02	3.200E-04
2.800E+00	2.900E+00	1.503E-02	5.200E-04
2.900E+00	3.000E+00	1.006E-02	6.200E-04
3.000E+00	3.100E+00	7.349E-03	5.930E-04
3.100E+00	3.200E+00	6.336E-03	4.840E-04
3.200E+00	3.300E+00	5.976E-03	3.640E-04
3.300E+00	3.400E+00	5.771E-03	3.750E-04
3.400E+00	3.500E+00	5.690E-03	7.600E-04
3.500E+00	3.600E+00	5.744E-03	1.231E-03
3.600E+00	3.700E+00	5.791E-03	1.444E-03
3.700E+00	3.800E+00	5.662E-03	1.161E-03
3.800E+00	3.900E+00	5.352E-03	5.060E-04
3.900E+00	4.000E+00	4.994E-03	8.320E-04
4.000E+00	4.200E+00	4.587E-03	1.288E-03
4.200E+00	4.400E+00	4.271E-03	9.750E-04
4.400E+00	4.600E+00	3.869E-03	7.240E-04
4.600E+00	4.800E+00	3.150E-03	1.100E-03
4.800E+00	5.000E+00	2.796E-03	5.080E-04
5.000E+00	5.500E+00	1.653E-03	5.400E-04
5.500E+00	6.000E+00	1.040E-03	3.200E-04
6.000E+00	6.500E+00	1.147E-03	2.220E-04
6.500E+00	7.000E+00	1.103E-03	1.930E-04
7.000E+00	7.500E+00	4.657E-04	1.426E-04
7.500E+00	8.000E+00	3.516E-04	1.086E-04
8.000E+00	8.500E+00	3.173E-04	9.390E-05
8.500E+00	9.000E+00	1.219E-04	5.730E-05
9.000E+00	9.500E+00	2.174E-04	3.890E-05
9.500E+00	1.000E+01	1.072E-04	2.490E-05
1.000E+01	1.050E+01	5.485E-05	1.940E-05
1.050E+01	1.100E+01	2.378E-05	1.000E-05

\*\*\*\*\*

LiF Sphere 40cm 1987.06

\*\*\*\*\*

Lower Energy [MeV]	Upper Energy [MeV]	Energy Spectrum [MeV/S.n.]	Error
5.000E-01	6.000E-01	2.606E-01	6.300E-03
6.000E-01	7.000E-01	1.303E-01	2.500E-03
7.000E-01	8.000E-01	1.259E-01	1.100E-03
8.000E-01	9.000E-01	1.480E-01	4.000E-04
9.000E-01	1.000E+00	1.274E-01	3.000E-04
1.000E+00	1.100E+00	1.008E-01	4.000E-04
1.100E+00	1.200E+00	1.025E-01	9.000E-04
1.200E+00	1.300E+00	1.226E-01	1.500E-03
1.300E+00	1.400E+00	1.288E-01	1.200E-03
1.400E+00	1.500E+00	1.006E-01	4.000E-04
1.500E+00	1.600E+00	6.201E-02	1.350E-03
1.600E+00	1.700E+00	3.994E-02	1.700E-03
1.700E+00	1.800E+00	3.388E-02	1.360E-03
1.800E+00	1.900E+00	3.465E-02	8.650E-04
1.900E+00	2.000E+00	3.617E-02	5.400E-04
2.000E+00	2.100E+00	3.452E-02	6.400E-04
2.100E+00	2.200E+00	2.983E-02	9.200E-04
2.200E+00	2.300E+00	2.582E-02	1.250E-03
2.300E+00	2.400E+00	2.519E-02	1.620E-03
2.400E+00	2.500E+00	2.758E-02	1.670E-03
2.500E+00	2.600E+00	3.022E-02	1.120E-03
2.600E+00	2.700E+00	2.966E-02	4.800E-04
2.700E+00	2.800E+00	2.524E-02	7.500E-04
2.800E+00	2.900E+00	1.997E-02	1.190E-03
2.900E+00	3.000E+00	1.693E-02	1.590E-03
3.000E+00	3.100E+00	1.651E-02	1.860E-03
3.100E+00	3.200E+00	1.728E-02	1.770E-03
3.200E+00	3.300E+00	1.795E-02	1.110E-03
3.300E+00	3.400E+00	1.797E-02	9.500E-04
3.400E+00	3.500E+00	1.748E-02	2.580E-03
3.500E+00	3.600E+00	1.682E-02	4.050E-03
3.600E+00	3.700E+00	1.617E-02	4.400E-03
3.700E+00	3.800E+00	1.537E-02	3.190E-03
3.800E+00	3.900E+00	1.427E-02	1.080E-03
3.900E+00	4.000E+00	1.305E-02	3.070E-03
4.000E+00	4.500E+00	1.362E-02	2.100E-03
4.500E+00	5.000E+00	1.337E-02	2.030E-03
5.000E+00	5.500E+00	1.171E-02	2.220E-03
5.500E+00	6.000E+00	6.479E-03	1.116E-03
6.000E+00	6.500E+00	4.436E-03	7.570E-04
6.500E+00	7.000E+00	3.308E-03	7.880E-04
7.000E+00	7.500E+00	2.820E-03	6.360E-04
7.500E+00	8.000E+00	1.950E-03	4.830E-04
8.000E+00	8.500E+00	1.935E-03	4.070E-04
8.500E+00	9.000E+00	8.525E-04	2.534E-04
9.000E+00	9.500E+00	8.657E-04	1.765E-04
9.500E+00	1.000E+01	4.385E-04	1.515E-04
1.000E+01	1.050E+01	3.208E-04	9.910E-05
1.050E+01	1.100E+01	1.246E-04	4.790E-05

\*\*\*\*\*

CF2 Sphere 40cm 1987.07

\*\*\*\*\*

Lower Energy [MeV]	Upper Energy [MeV]	Energy Spectrum [MeV/S.n.]	Error
2.000E-01	3.000E-01	6.650E-02	4.400E-04
3.000E-01	4.000E-01	1.318E-01	4.000E-04
4.000E-01	5.000E-01	1.142E-01	4.000E-04
5.000E-01	6.000E-01	9.011E-02	3.900E-04
6.000E-01	7.000E-01	1.199E-01	4.000E-04
7.000E-01	8.000E-01	1.461E-01	4.000E-04
8.000E-01	9.000E-01	1.099E-01	3.000E-04
9.000E-01	1.000E+00	8.152E-02	3.800E-04
1.000E+00	1.100E+00	9.708E-02	4.300E-04
1.100E+00	1.200E+00	1.253E-01	4.000E-04
1.200E+00	1.300E+00	1.225E-01	4.000E-04
1.300E+00	1.400E+00	8.449E-02	3.800E-04
1.400E+00	1.500E+00	5.035E-02	4.000E-04
1.500E+00	1.600E+00	3.696E-02	4.500E-04
1.600E+00	1.700E+00	3.523E-02	3.900E-04
1.700E+00	1.800E+00	3.896E-02	4.000E-04
1.800E+00	1.900E+00	4.255E-02	4.200E-04
1.900E+00	2.000E+00	3.834E-02	3.800E-04
2.000E+00	2.100E+00	2.962E-02	4.000E-04
2.100E+00	2.200E+00	2.421E-02	4.700E-04
2.200E+00	2.300E+00	2.401E-02	4.800E-04
2.300E+00	2.400E+00	2.762E-02	5.400E-04
2.400E+00	2.500E+00	3.092E-02	6.300E-04
2.500E+00	2.600E+00	2.905E-02	5.300E-04
2.600E+00	2.700E+00	2.287E-02	4.400E-04
2.700E+00	2.800E+00	1.765E-02	6.200E-04
2.800E+00	2.900E+00	1.601E-02	6.100E-04
2.900E+00	3.000E+00	1.679E-02	5.500E-04
3.000E+00	3.100E+00	1.806E-02	6.300E-04
3.100E+00	3.200E+00	1.865E-02	6.400E-04
3.200E+00	3.300E+00	1.811E-02	5.900E-04
3.300E+00	3.400E+00	1.701E-02	6.200E-04
3.400E+00	3.500E+00	1.672E-02	7.500E-04
3.500E+00	3.600E+00	1.779E-02	8.700E-04
3.600E+00	3.700E+00	1.915E-02	9.000E-04
3.700E+00	3.800E+00	1.963E-02	8.000E-04
3.800E+00	3.900E+00	1.969E-02	6.800E-04
3.900E+00	4.000E+00	2.157E-02	7.500E-04
4.000E+00	4.100E+00	2.777E-02	9.600E-04
4.100E+00	4.200E+00	3.779E-02	1.230E-03
4.200E+00	4.300E+00	4.642E-02	1.490E-03
4.300E+00	4.400E+00	4.749E-02	1.500E-03
4.400E+00	4.500E+00	3.982E-02	1.120E-03
4.500E+00	4.600E+00	2.822E-02	9.100E-04
4.600E+00	4.700E+00	1.851E-02	1.700E-03
4.700E+00	4.800E+00	1.338E-02	2.660E-03
4.800E+00	4.900E+00	1.254E-02	2.730E-03
4.900E+00	5.000E+00	1.454E-02	1.730E-03
5.000E+00	5.500E+00	1.614E-02	1.270E-03
5.500E+00	6.000E+00	5.416E-03	1.041E-03
6.000E+00	6.500E+00	6.630E-03	5.740E-04
6.500E+00	7.000E+00	3.436E-03	7.680E-04
7.000E+00	7.500E+00	4.963E-03	6.750E-04
7.500E+00	8.000E+00	6.290E-04	5.857E-04
8.000E+00	8.500E+00	3.458E-03	5.240E-04
8.500E+00	9.000E+00	1.123E-03	3.450E-04
9.000E+00	9.500E+00	7.546E-04	3.384E-04
9.500E+00	1.000E+01	9.663E-04	3.498E-04
1.000E+01	1.050E+01	2.017E-04	2.984E-04
1.050E+01	1.100E+01	2.381E-04	2.521E-04

Ms. Magrine AVEDIKIAN  
NESI-INIS  
A-2418

---

Nuclear Data Section  
International Atomic Energy Agency  
P.O. Box 100  
A-1400 Vienna  
Austria

e-mail, INTERNET: SERVICES@IAEAND.IAEA.OR.AT  
e-mail, BITNET: RNDS@IAEA1  
fax: (43-1) 20607  
cable: INATOM VIENNA  
telex: 1-12645 atom a  
telephone: (43-1) 2060-21710

---

online: TELNET or FTP: IAEAND.IAEA.OR.AT  
username: IAEANDS for interactive Nuclear Data Information System  
username: NDSOPEN for FTP file transfer

---